OPTICAL DATA STORAGE CENTER
University-Industry Cooperative Research

Annual Report: March 15, 1991

Optical Sciences Center
University of Arizona
Tucson, Arizona

OPTICAL DATA STORAGE CENTER
University-Industry Cooperative Research

Annual Report: March 15, 1991

Optical Sciences Center
University of Arizona
Tucson, Arizona

FROM THE DIRECTOR

This is our fourth annual report, prepared for our sponsors on the occasion of their Spring meeting in Tucson at the Viscount Suite Hotel on April 24 & 25. It summarizes progress on current research projects and proposed plans for their continuation. A new proposal on signal processing, submitted by Max Liu of the Electrical and Computer Engineering Dept., is also included. Preprints appear as appendices.

ODSC is currently under its first five-year "Sunset Review" by the Provost's Office, in conformance with policies established many years ago by the Board of Regents. (We are assured that these reviews are simply "management tools" that imply nothing sinister.) I have submitted the required "Self-Study" report, describing the Center's accomplishments, revenues and expenditures for the five-year period beginning July 1, 1985 and ending June 30, 1990. (You may remember that the Regents formally established ODSC in October, 1985, and IBM initiated funding the same month.) In conformance with Regents' policy, a committee of three (external to ODSC) was appointed to review us. That committee, composed of Peter Franken and Don Hillman of OSC and Gary Eckhardt of IBM, has submitted its report to R. R. Shannon, OSC Director. He will complete the process by writing his own report to the Provost.

A useful result of the review process is the bibliography of papers, presentations, dissertations, theses and invention disclosures produced by ODSC researchers to date. This bibliography, included as Appendix O of this report, is impressive. It includes 93 refereed articles, 73 papers in Proceedings and/or Digests of meetings, 48 unpublished presentations, 8 dissertations, 10 theses, 7 invention disclosures and 2 patent applications.

Mat Watson, who has been working with Pierre Meystre on direct-overwrite modeling, expects to complete his dissertation in the next few months. He has been collaborating with Mark Schultz of DSSC, CMU. Mat's model and Mark's experimental results seem to be converging, though final results are not yet in. The turnaround time on the University's Convex computer has degenerated to 24 hours for the dynamical model. It has become a laborious process, one that is causing Pierre to lose interest. As noted in his summary of progress and plans, he would like to put his energies into more fundamental studies of the limits of optical recording. Because of the depth and extent of his knowledge of quantum optics, I think he should be encouraged. We await your views at the meeting.

Arne Funkenbusch says that 3M should complete its arrangement to support Neal Armstrong's corrosion/passivation work by mid April. 3M executives have signed the appropriate papers, but the

lawyers were still looking things over in mid March. Arne is insisting that these are open, basic studies. I trust his demands will be met.

John Simonds of NSIC will attend our upcoming meeting and will participate in the "blue laser" ATP meeting the afternoon of April 25 and the morning of April 26. I have taken the liberty of inviting Martin Fejer of Stanford University to that meeting. He has been the major contributor to the quasi-phasematched doubling in $LiNbO_3$ waveguides at Stanford. His perspective should be valuable to all participants. We're looking forward to a lively meeting. This is something new for all of us, and it will be a challenge to make it work effectively.

George Lawrence plans to leave the University at the end of this semester. As the most inventive of the faculty who have participated in ODSC, we will sorely miss him. He plans to devote full time to the pursuit of his consulting business and the continuing development and support of his modeling software program, GLAD. We wish him abundant success.

We look forward to meeting with you next month.

J.J. Burke
March 15, 1991

TABLE OF CONTENTS

SECTION 1. SUMMARY REPORTS

DIRECT OVERWRITE MODELING

P. Meystre, H. Fu, and M. Watson

PROGRESS

The direct overwrite modeling efforts have concentrated on the collaboration recently initiated with the Carnegie-Mellon University (CMU) group, with the goal of testing our code against the direct overwrite experiments performed at Pittsburgh. We received a direct overwrite sample (GdTbFe) from M. Schultz of CMU, together with its thermal parameters and a description of the experimental conditions under which direct overwrite was achieved. The magnetization and coercivity of this sample were measured by T. Wu and R. Hajjar of M. Mansuripur's group, while domain collapse and expansion measurements were performed by B. Bernaki and M. Watson, who used them to calculate the wall energy.

M. Schultz was also given access to our computer, so that he can remotely log on and run our thermal code. Specifically, he is using this code to fit experimental data obtained in dynamic writing to determine the film's thermal constants. The close collaboration between M. Watson and M. Schultz is expected to lead to a better understanding of both the experimental results and the theory, and to improve the predictive value of our modeling efforts.

We also continued to work on alternative direct-overwrite schemes using microwave fields, in particular on the "adiabatic following" scheme. In this scheme three magnetic fields acting on the domain to be overwritten are required: 1) a strong dc field ($H_0 \simeq 5$ kOe) perpendicular to the film plane; a perpendicular anisotropy field ($H_{ani} \simeq 1$ kOe) inherent in the MO film; and an in-plane rf field ($H_{rf} \simeq 50$ Oe). We showed by numerical modeling that, for sufficiently weak damping, a domain in a single-layer disk can be switched to a desired direction by properly chirping the frequency of the microwave magnetic field. The model we used is a single-dipole model; the dynamics are governed by the Landau-Lifshitz-Gilbert equation.

We also simulated the direct-overwrite scheme in a two-dimensional model which consists of, for example, 19 × 19 dipoles, each representing a small volume in MO film. This model is more realistic than the single-dipole model, since it allows interactions between dipoles. We found that, to achieve direct overwrite, the exchange coupling constant of the MO film should be high enough (the stiffness constant $A_x = 2 - 5 \times 10^{-7}$ erg/cm), that the dipoles in the domain to be overwritten move uniformly. This knowledge is useful for choosing the MO film suitable to this direct-overwrite scheme.

An essential element required by both this scheme and a related scheme proposed by M. Mansuripur is a rf source producing on the order of 10 mW of microwave power. We are investigating several approaches to this problem. A promising approach uses the mixing of optical fields (which could be provided by diode lasers) at a metal-insulator-metal (MIM) tip. Another possibility might be to use a waveguide that is shorted in the vicinity of the domain. Dong et al. [J. Appl. Phys. 64, 3602 (1988)], in particular, were able to generate a 360-Oe, 500-MHz microwave magnetic field in a 4 μm $\times$ 4 μm area with a 0.4-W microwave input.

PLANS

Looking to the future, we plan to extend our ODSC-related work to study the fundamental limits of optical data storage, a goal we have had in mind for some time but had put on the back burner while we addressed more practical questions. In particular, we want to investigate the roles that will be played in data storage by exciting developments in quantum optics and in the emerging field of quantum noise engineering that have taken place in the last few years.

The ultimate (optical) memory will consist of a single atom or a few atoms, switched between two states, "0" and "1", by a very weak perturbation (probably at the quantum level). The state of the memory will also be measured with one or a few photons. Thus, both the write and read steps will be quantum mechanical. A number of questions come to mind. What will quantum fluctuations do to the memory? Will a tailored reservoir (such as those used in inhibited spontaneous emission and sub-Poissonian diode lasers) help? How important is quantum tunneling between the two states of the memory and how can it be controlled? What about the measurement-induced diffusion between the two states due to measurement back-action? Can we use back-action evading and quantum nondemolition techniques to avoid this difficulty? And ultimately, what are the fundamental quantum limits to information storage and retrieval, if any?

Although these questions may seem far-fetched, they represent the state of the art in quantum optics and electronics, both theoretically and experimentally. In particular, it is now clear that sub-Poissonian diode lasers, already demonstrated at NTT, will be commercially introduced in the near future. This opens the way to subshot-noise detection schemes and signal-to-noise ratios which will surely find their way into data storage technology. Universities are the place of choice to carry out this kind of research. Within the framework of ODSC and with concomitant industrial feedback, we should be in a

unique position to rapidly and efficiently translate these new fundamental developments into technological advances.

MAGNETOOPTIC SUPERLATTICE THIN-FILMS: FABRICATION, STRUCTURAL AND MAGNETIC CHARACTERIZATION

C. M. Falco, B. N. Engel, C. D. England, and R. A. Van Leeuwen

PROGRESS

This past quarter has brought significant progress in our studies of MBE-grown Co/Pd superlattices. We have used a variation of the seeded epitaxy techniques recently published by IBM (Lee, Farrow, Lin, Marinero, and Chien) for growing Co/Pd in different crystal orientations. We have now grown a series for each orientation [111], [100], and [110]. By varying the Co thickness, we have been able to determine the dependence of the interface anisotropy on crystal face.

Very large anisotropies were observed in several of the superlattices, preventing saturation along the hard direction in fields as high as 55 kOe. For these samples, the moderate fields (≈ 20 kOe) available in conventional torque magnetometers make determination of the anisotropy constants difficult with this method. Instead, we have employed a technique that involves analyzing the magnitude and curvature of the hard axis magnetization as a function of applied field. Saturation of the spins in the hard direction is not required, allowing an accurate determination of the anisotropy energy in easily obtainable fields. It can be shown that for a uniaxial magnetic system

$$\frac{H}{M} = \frac{2K_1}{M_s^2} + \frac{4K_2}{M_s^4}M^2 \qquad (1)$$

where H is the applied field, M is the magnetization measured along the hard-axis, M_s is the saturation magnetization (determined from the easy-axis loop), and K_1 and K_2 are the effective anisotropy constants. Hence, plotting H/M *vs.* M^2 yields a linear behavior, with the anisotropy constants deducible from the slope and intercept. The total effective uniaxial anisotropy, K_u, is then determined from $K_1 + K_2$. We have verified the results obtained from this technique by making direct comparisons to torque magnetometry for several samples, and find agreement to better than 10%.

To remove the effects of hysteresis and obtain a single hard-axis magnetization curve for the above analysis, the two sections of each hysteresis loop were averaged at constant magnetization values. The validity of this averaging was confirmed by comparison to "anhysteretic" curves measured for a few of the samples. Above the coercive field, excellent agreement with Equation 1 was observed for all but one of the samples ($d_{Co} = 8$ Å, [110]). As discussed in more detail below, because of the complicating

effect of an additional cubic anisotropy, the shape of the hysterisis curve for this one sample did not lend itself to the above analysis, so the anisotropy energy for this sample was determined by torque magnetometry. Figure 1 displays the hard-axis magnetization measured to high field of a strongly perpendicular superlattice (d_{Co} = 2 Å, [111]). The solid curve is a fit to equation 1, demonstrating excellent agreement over the entire range. The anisotropy energy density in Co/Pd superlattices can be modelled phenomenologically by the inclusion of an interface contribution, proportional to $1/d_{Co}$, and a volume term, independent of d_{Co}. This volume contribution includes the magneto-crystalline, magneto-elastic, and shape-induced anisotropies associated with the crystal structure and geometry. The anisotropy energy per Co volume can be written as

$$K_u^{Co}d_{Co} = (K_v^{eff} - 2\pi M_s^2)d_{Co} + 2K_s \qquad (2)$$

where K_v^{eff} is the sum of the magneto-crystalline and magneto-elastic contributions, $2\pi M_s^2$ is the demagnetizing energy density of a sheet of Co spins, and K_s is the interface or surface anisotropy energy density. The factor of two in this last term accounts for the two interfaces per magnetic layer. In this convention, $K_u > 0$ for a perpendicular easy-axis.
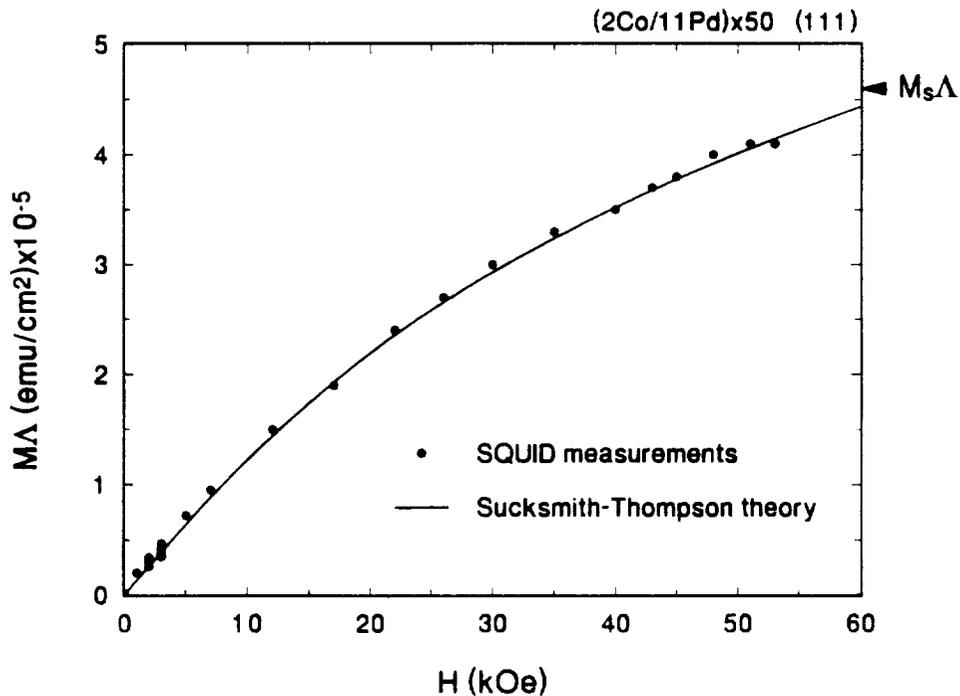
Figure 1. Hard-axis magnetization measured to high field of a strongly perpendicular superlattice (d_{Co} = 2 Å, [111]).

From Equation 3, the product $K_u^{Co}d_{Co}$ is linear in d_{Co} with a slope of $(K_V^{eff}-2\pi M_s^2)$ and an intercept of $2K_s$. This quantity, $K_u^{Co}d_{Co} = K_u^{tot}\Lambda$, is directly determined from the hard-axis magnetization curves of our superlattices, $M(H)\Lambda$, and Equation 2. Figure 2 displays $K_u^{Co}d_{Co}$ versus d_{Co} for all three crystal orientations and the polycrystalline multilayers. The behavior is linear for all sets of samples as suggested by Equation 3.

Uniaxial Anisotropy
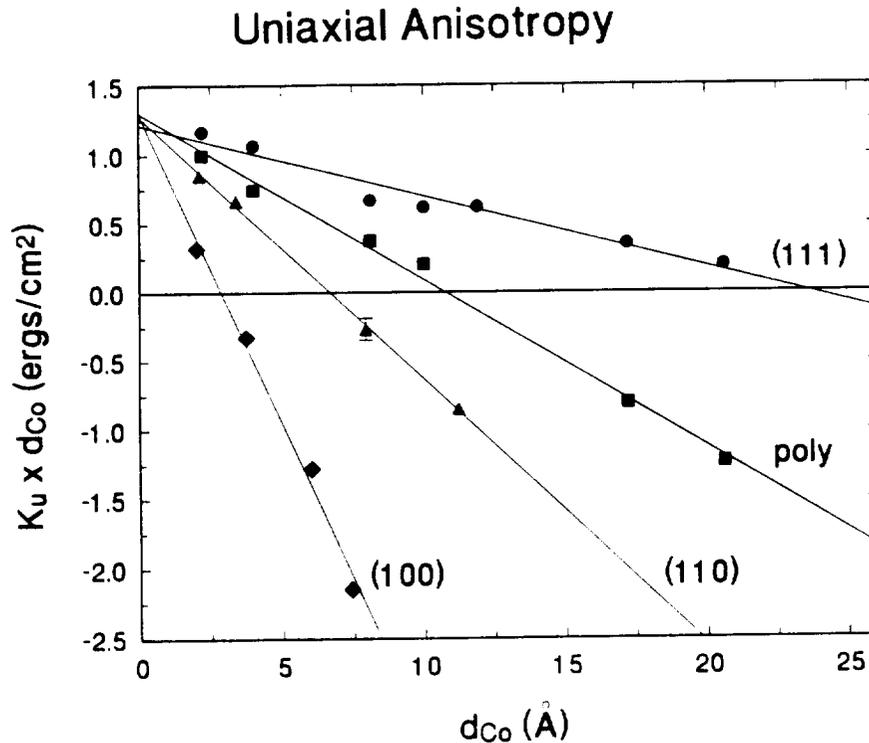
Figure 2. $K_u^{Co}d_{Co}$ versus d_{Co} for all three crystal orientations and the polycrystalline multilayers.

The most striking feature of Figure 2 is the convergence of all curves to a single intercept, $2K_s$. These results show the contribution of the Co-Pd interface to the anisotropy, *independent* of crystal orientation, is $K_s = 0.63 \pm 0.05$ ergs/cm². However, as would be expected, growth along the different crystal axes produces different magneto-crystalline and magneto-elastic contributions. The large variations with d_{Co} of the total anisotropy energy are solely a result of greatly different volume contributions as indicated by the slopes of the fits.

The most strongly perpendicular superlattices are the (111) series, which show a crossover to in- plane behavior at $d_{Co} = 24$ Å. Because the [111] direction (c-axis for hcp) is the easy-axis for a bulk Co crystal, the magneto-crystalline contribution can aid the perpendicular anisotropy for films oriented

along this direction. Correcting for the shape anisotropy ($2\pi M_s^2 = 1.27 \times 10^7$ ergs/cm^3) gives an effective volume anisotropy of $K_V^{eff} = 7.7 \pm .1 \times 10^6$ ergs/cm^3. This value is about 20% larger than the magneto-crystalline anisotropy for a bulk, single-crystal of hcp Co (6.3×10^6 ergs/cc), suggesting a strain-induced, magneto-elastic contribution.

The anisotropy measurements of our polycrystalline samples agree well with other similarly-prepared multilayers reported in the literature, and show a crossover to in-plane behavior at $d_{Co} = 11$ Å. To within our experimental precision, there is no evidence of an effective volume contribution other than the shape anisotropy for these films.

In sharp contrast to the (111) superlattices, the (100) films show a crossover to in-plane behavior between one and two atomic layers of Co; $d_{Co} = 3$ Å. This crossover is consistent with measurements of Co/Pd (100) superlattices grown on NaCl. In view of the large strain deduced from x-ray diffraction, this very large in-plane volume anisotropy, $K_V^{eff} = -3.2 \times 10^7$ ergs/cm^3, probably is of magneto-elastic origin.

The (110) superlattices display an intermediate behavior, with a crossover of 7 Å. Because of the rectangular symmetry of the (110) face, we observe an additional cubic anisotropy when the spins are tipped into the film plane. Hence, for the perpendicular superlattices, care was taken to align this cubic axis along the magnetic field for proper determination of the uniaxial anisotropy from the hard-axis loops. This cubic anisotropy also complicates the hard-axis loop shape for the $d_{Co} = 8$ Å sample, where the uniaxial contribution is small. Torque magnetometry was therefore used to determine the anisotropy for this superlattice.

These results are surprising. That the interface anisotropy is independent of crystal structure implies that this phenomenon is an intrinsic property of the Co/Pd interface. The large variations in volume anisotropies, together with evidence of large amounts of strain from x-ray diffraction, call into question the role of strain in interface anisotropy. Theoretical attention to this question is needed.

This work was presented in an invited paper by B. N. Engel at the March American Physical Society Meeting in Cincinnati.

PLANS

We have completed the integration of the *in situ* SMOKE chamber with the MBE machine and will begin our studies on magnetic monolayers. Our discovery that the interface anisotropy is independent of crystal structure suggests a pursuit of electronic effects may prove more fruitful.

CHARACTERIZATION FACILITY FOR MAGNETOOPTIC MEDIA

M. Mansuripur, H. Fu, R. Hajjar, B. Bernacki, F.L. Zhou, R. Uber, T. Wu and J.K. Erwin

OBJECTIVES

Our objectives are as follows.

- To measure the hysteresis loop, Kerr rotation angle, anisotropy energy constant, Hall voltage and magnetoresistance of thin-film magnetooptic media using our loop tracer. This equipment has a maximum field capability of 21 kOe, and can measure the temperature dependence of the media's magnetic properties in the range of 57 K to 475 K.

- To measure the wavelength dependence of the Kerr rotation angle and ellipticity for thin-film media, using our magneto-optic spectrometer. The spectrometer operates over wavelengths ranging from 350 nm to 1100 nm.

- To measure the hysteresis loop, coercivity and remanent magnetization, saturation magnetization, and anisotropy energy constant for thin-film magnetic media using our vibrating sample magnetometer (VSM). The VSM, purchased through an equipment grant from the National Science Foundation, was installed the spring of 1990. The range of temperatures available for characterizing samples is 77 K to 1000 K, with a maximum magnetic field of 12 kOe.

- To perform static read/write/erase experiments on thin-film magnetooptic media using our static test station. The test station is a commercial polarized-light microscope that has been modified to include a laser diode, electromagnet, temperature-controlled stage, and a television camera, all under computer control.

- To perform dynamic read/write/erase experiments, using a commercial tester. Our Nakamichi OMS 1000 test station was donated by the Data General Corporation the summer of 1989.

- To integrate the existing models of magnetization, magnetooptic effects, coercivity, and anisotropy in an interactive and user-friendly environment. Furthermore, to analyze the characterization data obtained in the various experiments, using this modeling package.

PROGRESS

Magnetooptic Media Characterization

A large number of Co/Pd, Co/Pt, TbFe and TbFeCo samples were characterized during the past several months. Preliminary results of this work are summarized in appendices A, B, and C. Appendix A contains results of magnetooptic Kerr measurements, Hall effect, VSM, and

magnetoresistance measurements. Appendix B describes the wavelength-dependent characteristics of the magnetooptic media. Appendix C is devoted to fractal analysis of domain-boundary jaggedness. In Appendix C, we describe the results of the spectral method of fractal analysis and compare them with the ruler method, which has been reported in previous ODSC reports. Agreement between the two methods is excellent. One advantage of the spectral method is that it allows samples that usually break up into multiple domains (and, thus, do not comply with the requirements of the ruler method) to be measured just as easily.

During this period we upgraded our magnetooptic spectrometer by placing the magnet and the monochromator under computer control. The system is now fully automated and a complete set of measurements (consisting of Kerr rotation angle, ellipticity, and reflectivity versus wavelength in the range of λ from 350 nm to 1100 nm) for a sample can be performed in less than one hour.

The loop tracer also was upgraded. A new sample holder was built to allow rapid measurements of optical and magnetic properties at and above room temperature. The old sample holder is now used only for low-temperature measurements. Exchange of the samples in the cryogenic holder was rather time consuming and, since in many cases one does not need the low-temperature results, we decided to build the new holder for rapid, everyday measurements. The electronic circuits and computer interface were upgraded. We now have a much more sensitive Kerr looper than at any time in the past. The addition of a quarterwave plate to the system has enabled us to measure the ellipticity at the operating wavelength of λ = 6328 Å as well.

Magnetooptic Ellipsometer

Construction of a new ellipsometer has been completed. This system operates at λ = 6328 Å and has a variable angle of incidence from 20° to 88°. Amplitude and phase of the reflection coefficients at oblique incidence are measured by this system. A computer program then converts these data to characteristics (dielectric tensor, thickness, refractive index, etc.) of the sample under consideration. The computer program is powerful and allows analysis of complex samples (such as multilayers) as well as of simple thick films.

Connection Machine Simulations

An invited paper on the coercivity of wall motion was published in the *Journal of the Magnetic Society of Japan*. A reprint is included in this report (see Appendix D). More recent results not yet

published are included as Appendix E. These results describe the trapping of domain walls at the boundary between various patches, where the exchange interaction is weak.

The process of thermomagnetic recording in amorphous ferromagnetic films is now simulated on the connection machine. Interesting nucleation and growth patterns have been observed. The results will be presented at the ODSC board meeting in April. A paper based on this work is being prepared for presentation at the MORIS Conference in Tokyo.

Analysis of Noise in Magnetooptical Readout

A chapter on noise was written for the optical storage course offered to our students at the Optical Sciences Center. Because some of the material in this chapter is new and could be useful to persons working in this area, we have included a copy of this material as Appendix F. One of the main focuses of this document is separation of noise into various components according to the source of noise, and identifying the component of noise that corresponds to "magnetic" fluctuations. Fractal analysis of the media ultimately is related to the noise that arises from such magnetic fluctuations, whether they are on an erased track or on the boundary of recorded domain (i.e., domain-wall jaggedness).

PLANS

The ellipsometer will be fully automated and used to characterize the dielectric tensor of the various magnetooptic media, especially the Co/Pt and Co/Pd superlattice films for which this information is presently unavailable.

F. L. Zhou is building a large database for the wavelength-dependence of the magnetooptic coefficients. His task in the coming year will be to try to relate the observed phenomena to the band structure of the materials. His goal is to construct phenomenological models that will explain the existing data and that will have predictive capabilities.

R. Hajjar and T. Wu are working on models that will enable them to relate their large volume of data to the basic structural/magnetic properties of the media. Their data include temperature dependencies of saturation magnetization, anisotropy constants, Hall voltage, magnetoresistance, and magnetooptic Kerr angle. Some of the models on which they are concentrating are based on the mean-field theory, Stoner-Wohlfarth theory of magnetization reversal, and Mott theory of magnetoresistance.

B. Bernacki will compare his fractal dimension data with noise figures obtained from the dynamic tester. Extracting the relevant noise figure from the dynamic noise measurements has proved to be a

complicated task. What exactly corresponds to "magnetic noise" in magnetooptical readout systems is a subject that we have explored in Appendix F. We shall continue this effort and, with help from Komag (D. Treves is sending us fully characterized disks for fractal analysis), we hope to shed some light on the very important issue of magnetic noise.

R. Giles of Boston University will continue collaborating with us on the connection machine simulations. We are finally in a position to dynamically simulate the thermomagnetic write/erase process and to study the influence of the various sources of coercivity (i.e., inhomogeneities and defects) on the character of recorded domains (jaggedness' dynamics of domain formation process, etc.). This is very exciting work and the level of interest in it is, in part, demonstrated by the invitation we received to write a paper for the *Japanese Journal of the Magnetic Society* (see Appendix D) and by the invitation to speak at the upcoming MORIS Conference in Tokyo.

DYNAMIC TESTBED LABORATORY AND MICROOPTICS

T. Milster, K. Erwin, F. Froehlich, J. Kann, J. Treptau, H. Tang, M. Shi-Wang, and N. Wong

OBJECTIVE

Our objectives are: 1) to measure performance of media and optical systems, using the dynamic testbed; 2) to model optical systems to predict performance; and 3) to investigate new components that have potential for improving performance.

PROGRESS

This quarter we have learned a great deal about our testbed and the differential focus servo. We presented four papers, two concerning modeling efforts, one addressing the differential focus servo, and one describing our curved-substrate microlens. In addition, two invention disclosures were generated from the microoptics work.

Testbed

We have been analyzing our differential servo method. A paper summarizing our results, entitled "Differential spot-size focus servo," was presented at the ODS conference in Colorado Springs this year. The paper is attached as Appendix G. In brief, cross talk from the tracks into the focus error signal is reduced by a factor of three. However, we discovered a false FES from sector marks that passed through the differential circuitry. We are investigating methods for minimizing this effect. Our diffraction models are being used to study cross talk and alignment sensitivities.

We tried using the AMC tester to measure CNR on some grooved Chinese phase-change disks. Two major problems were encountered. The erase/write power requirements of the medium are too high and the tracking error signal is too low. We believe the low tracking error signal arises from very shallow grooves. We tried modifying the dynamic testbed to meet the erase/read requirements, but the tracking signal was still too low. Measurements of diffraction patterns conclude that the groove depth is considerably shallower than that for several MO disks in our inventory.

To allow us to test grooveless disks, a new actuator is being implemented into the dynamic testbed. A pinning-loop servo is included in this actuator so that mechanical coupling from the focus actuator does not influence the tracking actuator. H. Tang has been building the necessary circuits.

Work on the clock and data recovery board continues. A circuit is nearly completed, and is in the process of being debugged. J. Kann is performing this task. He is interested in communication systems, and will be testing some high-speed fiber links for the Navy over the next year.

Modeling

We presented two papers resulting from our modeling work. Both papers were presented at OE-LASE '91 this year.

In the first paper, entitled "Measurement of laser spot quality," we analyzed several ways of measuring spot quality and various figures of merit. Several important points relating to data storage were illustrated. First, results from knife-edge scans and actual spot profiles differ because of integration of the differentiated knife-edge signal. Second, width measurements are not by themselves adequate to describe spot quality. This is because the central lobe is constrained by pupil filling for small amounts of aberration and, for larger amounts of aberration, width measurements are difficult to interpret. Third, the most sensitive measure of spot quality is the Strehl ratio. The Strehl ratio is difficult to measure directly, but it may be approximated by averaging encircled energy found from x and y scans of a knife-edge scanner. This proceedings paper is attached as Appendix H.

The second paper, entitled "Laser beam modeling in optical storage systems," discusses general concepts of modeling ODS systems, and will serve as an introductory chapter in J. Treptau's thesis. His work in developing the model will be completed this spring. He must complete the ray-trace analysis portion and its integration with the rest of the model. The package will be consolidated and delivered to NASA Langley. A copy of the paper is attached as Appendix I.

M. Shi-Wang is using the model to analyze our differential focus servo. He has made several modifications to the model necessary for studying our system. We are attempting to understand cross talk, which has turned out to be a challenging task. Shi-Wang will continue using the model to understand dynamic performance with multiple beams as part of his dissertation work.

Microoptics

We are interested in two areas of microoptics. We are developing a microoptic beam deflector, and we are continuing our research in fabrication of micro-Fresnel lenses (MFLs) on curved substrates. This work has resulted in two invention disclosures. In addition, a paper entitled "Microoptic lens for

data storage" was presented at the ODS conference in Colorado Springs this year. A copy of the paper is attached as Appendix J.

The deflection system consists of a pair of identical binary lenslet arrays. Table I is an overview of the system constraints and deflector requirements. Figure 1 is a diagram of one array, and Fig. 2 illustrates how the array will be used to deflect a beam. Table II lists construction parameters for the array. N. Wong is working on design details, efficiency calculations, and the effect in the far field from diffraction off lenslet edges. As part of our plan for next year, we hope to fabricate the lens at a commercial facility. Wong will test the deflector as part of her master's thesis.

Table I. Overview of deflection system parameters.

INPUT BEAM SIZE (diameter)	4.3 mm
OUTPUT BEAM SIZE	4.3 mm
WAVELENGTH	830 $\pm$20 nm
RANGE OF DEFLECTION ANGLES	$\pm$1.6°
FIELD ANGLE	$\pm$0.5°
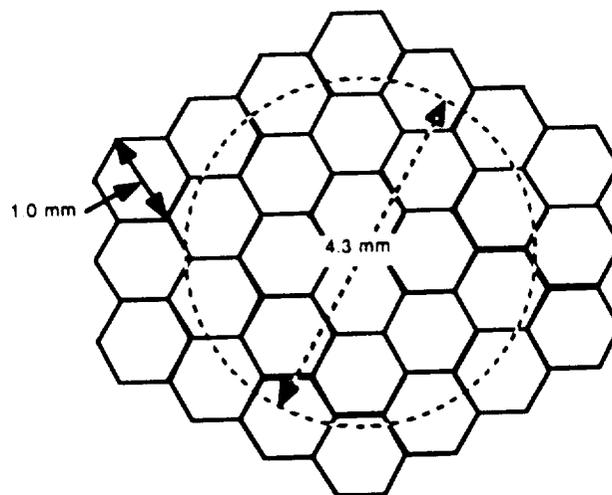
Figure 1. Diagram of one beam deflector array.
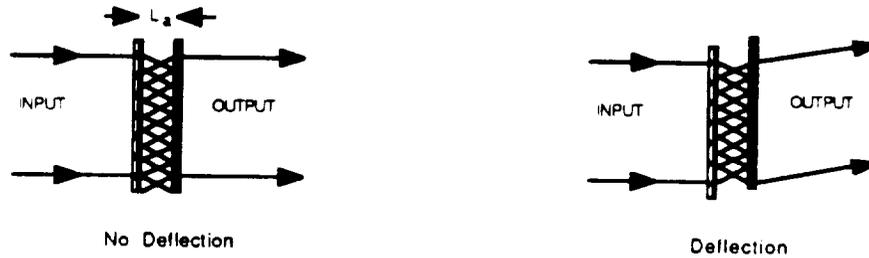
Figure 2. Beam deflection is achieved by translating one array with respect to the other.

Table II. Construction parameters for the array.

LENSLETS	F/5
FOCAL LENGTH	5.0 mm
LENSLET SHAPE	hexagonal
LENSLET SIZE	1.0 mm
ARRAY SIZE	5 × 5 elements
# OF LEVELS	8
MINIMUM FEATURE SIZE	1.04 μm
MAXIMUM ARRAY TRANSLATION	120 μm
LENGTH OF SYSTEM	10 mm
THEORETICAL EFFICIENCY	78.8%

We have shown that a curved substrate is necessary to achieve wide-field-of-view microoptics with a single lens. Previously, we attempted to fabricate MFLs on hollow glass microspheres. The processing steps were difficult, but they served to verify the concept. An alternative approach is being studied by F. Froehlich. It is the subject of an invention disclosure in preparation.

We plan to create the MFL pattern on the thin-film substrate using an electron-beam writer or conventional photolithography. We have recently acquired a scanning electron microscope from IBM that will be converted for use as an e-beam writer. Currently we are overhauling the vacuum system, and the instrument will be operating as a SEM shortly. Conversion for e-beam writing will occur later in the year.

PLANS

Over the next year we plan to build a new optical head for the dynamic testbed, test a microoptic beam deflector, investigate more completely our differential focus servo, look at multiple-beam servos, and build more microoptics.

The design for the new head for our dynamic testbed is shown in Fig. 3. The new head is more versatile than the present design. It includes a relay lens for transferring the pupil, a deflection system to test our microoptic beam deflector, and separate data and servo paths. The relay system transfers the back focal plane of the laser diode collimating lens to the front focal plane of the optical disk's objective lens, making the entire optical head doubly telecentric. The telecentric condition allows easier implementation of laser array sources, controls magnification versus defocus at the disk plane, and controls magnification versus defocus at the detector planes. Separate servo and data paths allow testing of new data-detection techniques while maintaining focus and tracking. Likewise, new servo ideas can be implemented without affecting the data channel. Tolerancing of the new system is being completed in CODE V by N. Wong. The off-the-shelf optics are relatively inexpensive.
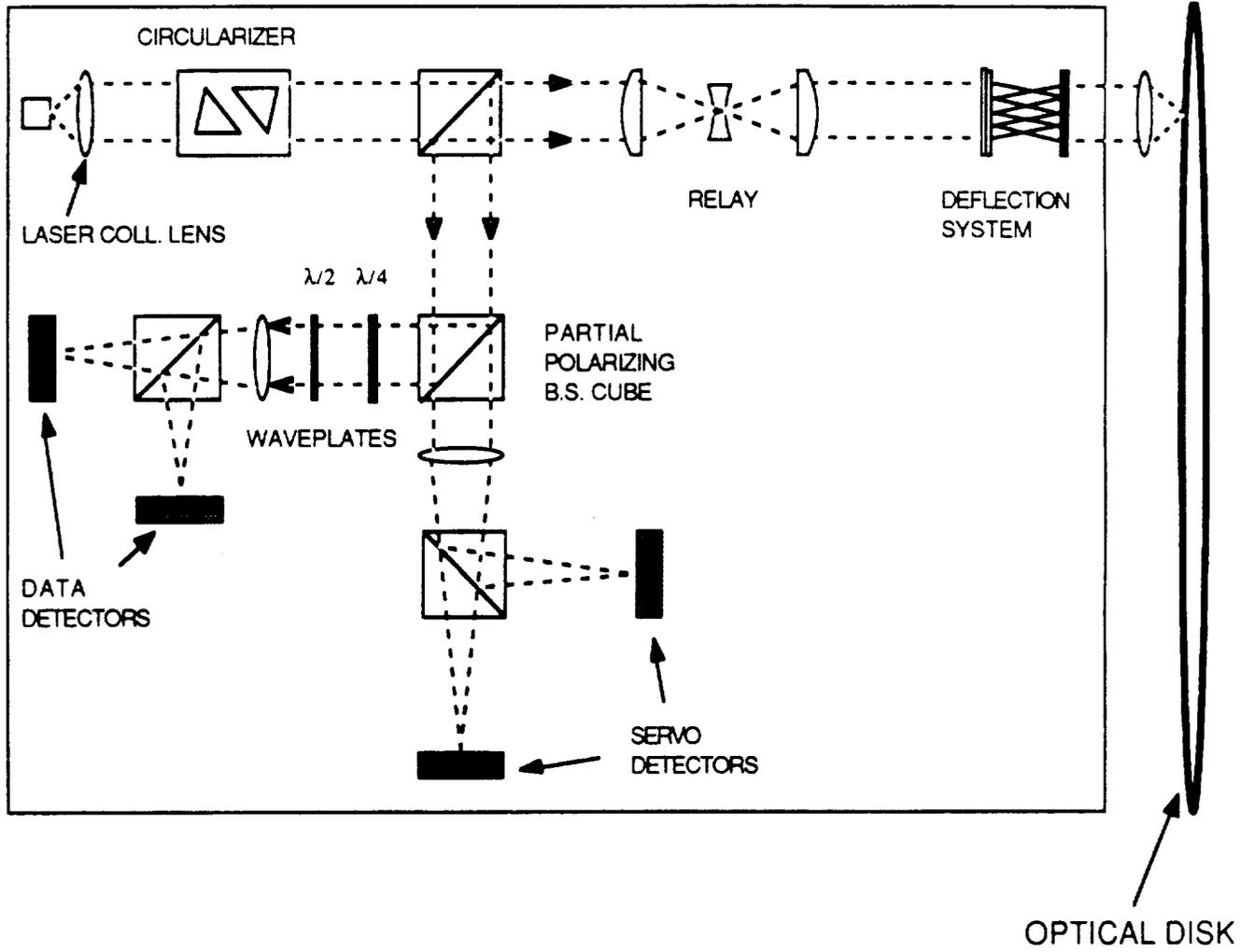
Figure 3. Layout of new head design for the dynamic testbed.

MeV ION-BEAM ANALYSIS OF OPTICAL DATA STORAGE FILMS

J. A. Leavitt, L. C. McIntyre Jr., Z. Lin and B. Dezfouly-Arjomandy

OBJECTIVES

Our objectives are threefold: 1) to accurately characterize optical data storage films by MeV ion-beam analysis (IBA) for ODSC collaborators; 2) to develop new and/or improved analysis techniques; and 3) to expand the capabilities of the IBA facility itself.

Using $^1H^+$, $^4He^+$ and $^{15}N^{++}$ ion beams in the 1.5 to 10 MeV energy range from a 5.5 MV Van de Graaff accelerator, we determine film thickness (in atoms/cm^2), stoichiometry, impurity concentration profiles and crystallize structure by Rutherford backscattering (RBS), high-energy backscattering, channeling, nuclear reaction analysis (NRA) and proton induced X-ray emission (PIXE). Most of these techniques are discussed in detail in ODSC Annual Report (February 17, 1987), p. 74. The PIXE technique is discussed in this report.

PROGRESS

Film Characterization

From March 1, 1990, to March 1, 1991, we provided a total of 225 equivalent backscattering analyses of thin films provided by ODSC collaborators; Table 1 indicates the distribution.

Table 1. Total number of analyses of thin films from ODSC collaborators.

Period	Falco	Mansuripur	Gibson	Armstrong	Total
3/1/90 - 6/1/90	54	2	6	—	62
6/1/90 - 9/1/90	36	—	—	2	38
9/1/90 - 12/1/90	77	15	—	—	92
12/1/90 - 3/1/91	16	17	—	—	33
Total	183	34	6	2	225

For Falco (with Engel, England and van Leeuwen): we performed extensive channeling studies on 15 Pd/Co multilayers on crystalline (110) GaAs, 8 rotating RBS analyses, 2 carbon depth profile studies and 45 ordinary RBS analyses of these multilayers. We also provided RBS analyses of the following: 8 Co/Ag/Pd/PdCo films, 6 Pd/Au films and 1 each Cu/Co, B/Pd, B/Ag films.

J. A. Leavitt et al.

For Mansuripur (with Hajjar, Wu, and Shieh of IBM): we performed RBS analyses of 15 TbCo, 16 GdCo, and 3 TbFeCo films. For Gibson (with Cornett): we performed 6 RBS analyses of ZrOF and Sm/TbFeCo films. For Armstrong (with Lee): we performed RBS analyses of FeTbCoTa and FeTbCoZr films.

In the majority of the RBS analyses, we used ^{4}He beam energies greater than 3.5 MeV to reduce overlap of signals from different elements; we applied our deconvolution programs to reduce the effect of the remaining overlaps. In most of these cases, we provided complete analyses of the data (with uncertainties), including film stoichiometry ($\leq$ 1%), elemental areal densities in atoms/cm^2 ($\pm$3%), and impurity profiles.

Technique Development

During the past year, we developed reliable methods for depth profiling hydrogen in films with a limiting sensitivity of about 0.1%. The NRA method, using 6 to 10 MeV ^{15}N^{++} analysis beams, is discussed in detail in the June 15, 1990, ODSC Quarterly Report. This method has high near-surface depth resolution ($\sim$ 100 Å). The second method, utilizing protons forward scattered by incident ^{4}He$^+$ ions, is briefly described in the March 15, 1990, ODSC Annual Report; this method has low near-surface depth resolution ($\sim$ 700 Å), but requires much less beam time than the NRA method.

We also have improved our channeling techniques in connection with the extensive studies of epitaxial growth in Falco's Pd/Co multilayers; see the September 15, 1990, ODSC Quarterly Report for detailed discussion.

We have returned to our program of measuring non-Rutherford cross sections for the backscattering of ^{4}He ions incident on light elements. We have preliminary measurements of ^{4}He-^{10}B, ^{4}He-^{11}B cross sections at the backscattering angle of 170° for ^{4}He energies 1-3 MeV. The motivation for this work may be found in the preprint (Appendix C) in the December 15, 1990, ODSC Quarterly Report.

We attempted to adjust our Penning ion source assembly to produce ^{4}He^{++} ions so we can run with up to 10 MeV ^{4}He^{++} analysis beams; we were unable to separate the ^{4}He^{++} ions from H$_2$$^+$ ions.

We have continued to develop computer programs for data deconvolution, simulation and analysis. The program for analyzing the forward-scattered proton data for hydrogen depth-profiling has been overhauled and improved.

Facility Development

The major facility development during the past year has been the installation of a PIXE system for analyzing trace elements by proton-induced X-ray emission. This technique is capable of detecting impurity elements at levels of parts per million (ppm) or even parts per billion (ppb), in favorable cases. The PIXE effort has been a joint project with Prof. Q. Fernando (University of Arizona, Department of Chemistry), who provided the Si(Li) X-ray detector and the funds to construct the beam-line and target chamber. We provided the design, construction, assembly and testing of the system.

We obtained our first PIXE data at 5:07 p.m., March 1, 1991; PIXE data for a sample containing arsenic are shown in Fig. 1. The sample was made by drying 50 μliters of an aqueous solution containing 10 ppm As spread over a ¼ in. diameter circle on a KAPTON substrate; the As areal density was 1.2-by-10^{16} atoms/cm^2. The As K_α and K_β X-ray lines produced by X-rays emitted following ejection of inner shell electrons by incident protons are prominently displayed. Acquisition time for these data was 5 minutes. It is clear that even smaller As concentrations may be easily measured.

We are now prepared to make measurements of trace elements present in ODSC films. We will give a more detailed discussion of the PIXE technique in a later report.
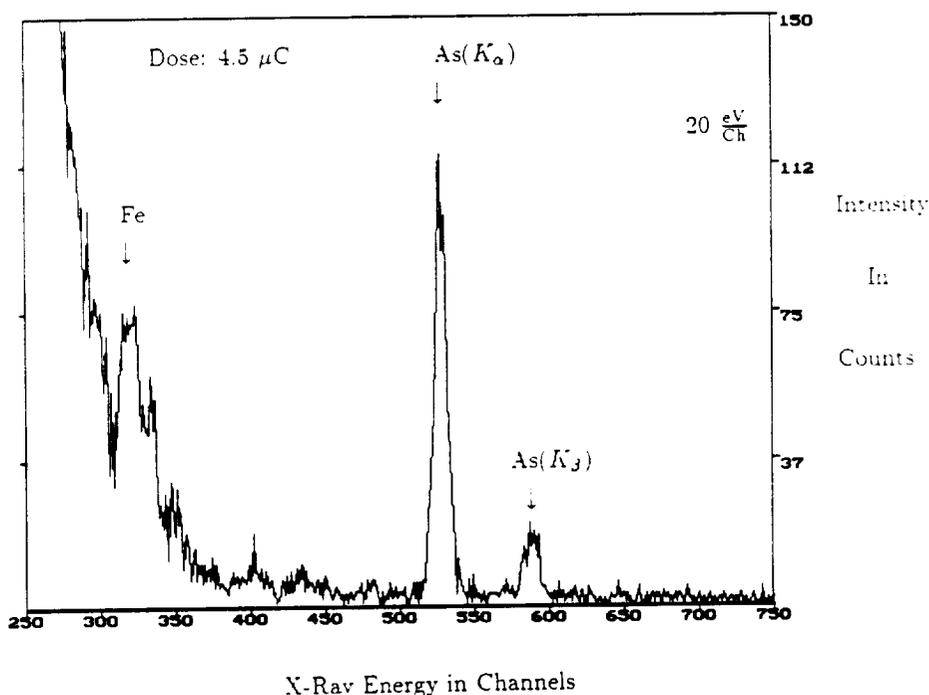
Figure 1. A portion of the PIXE spectrum of the As-doped sample. The incident proton beam energy was 2.0 MeV.

Other

During October and November 1990 we conducted a 10-hour seminar on ion-beam analysis techniques for faculty and students. The initial enrollment was 29 students.

Graduate student B. Dezfouly-Arjomandy received his Ph.D. in December 1990 and is currently employed as a postdoctoral research associate at the University of Pennsylvania Department of Physics. His dissertation is titled "Hydrogen Depth Profiling using the 6.385 MeV Resonance in the ^{1}H(^{15}N, $\alpha\gamma$)^{12}C Nuclear Reaction." Z. Lin has taken Dezfouly-Arjomandy's place on the ODSC project. Lin is developing (α,p) and (p,γ) nuclear reaction analysis techniques for depth profiling light elements in, or on, heavy substrates.

PLANS

During the next year, we plan the following: to continue characterizing ODS films for ODSC collaborators (we expect some interest in the newly installed PIXE technique); to acquire experience in using the PIXE technique; to continue measuring non-Rutherford cross sections for scattering of ^{4}He incident on light elements (specifically B and N) in the 1-to-5 MeV energy range; and to continue work on using (α,p) and (p,γ) nuclear reactions to depth profile light elements in a more massive matrix.

We plan no major facility development during the next year; we wish to develop expertise in using the PIXE technique. During the *following* year, we *may* attempt installation of a micro-beam facility that would enable us to examine spots of the order of 1 μm in size.

1990 PUBLICATIONS

1.   J.A. Leavitt, L.C. McIntyre Jr., M.D. Ashbaugh, J.G. Oder, Z. Lin and B. Dezfouly-Arjomandy, "Cross sections for 170.5° backscattering of ^{4}He from oxygen for ^{4}He energies between 1.8 and 5.0 MeV," Nucl. Instr. Meth. B **44**, 260 (1990).

2.   J.A. Leavitt and L.C. McIntyre Jr., "High energy ^{4}He backscattering," in *High Energy and Heavy Ion Beams in Materials Analysis*, J.R. Tesmer, C.J. Majjiore, M. Nastasi, J.C. Barbour and J.W. Mayer, eds. (Materials Research Society, Pittsburgh, 1990) pp. 129-138.

3.   L.C. McIntyre Jr., J.A. Leavitt, M.D. Ashbaugh, B. Dezfouly-Arjomandy, Z. Lin, J.G. Oder, R.F.C. Farrow and S.S.P. Parkin, "Detection and depth profiling of ^{19}F using resonances in the ^{19}F(α,p)^{22}Ne reaction," Nucl. Sci. Tech. (China) **1**, 56 (1990).

4.   J.A. Leavitt and L.C. McIntyre Jr., "Non-Rutherford ^{4}He cross sections for ion beam analysis," Bull. Am. Phys. Soc. **35**, 1695 (1990), and Nucl. Instr. Meth. B.

CHARACTERIZATION OF METAL MULTILAYER MEDIA: ANALYSIS OF THE OXIDATION OF Pd/Co MULTILAYERS

N. R. Armstrong, P. A. Lee, and J. L. Danziger

OBJECTIVES

Interest in the magnetooptic properties of modulated metal multilayers has grown recently, due to the discovery of perpendicular magnetism in particular systems. While waiting for samples of FeTbCo,X from our sponsors, we have attempted to use x-ray photoelectron spectroscopy (XPS) to characterize interfacial interactions in these modulated structures. Research this quarter focused on the study of metal multilayer systems of Pd/Co supplied by C. Falco's group. Our goals in these studies were to use angle-resolved XPS and electron energy loss spectroscopy (EELS) to characterize changes in the XPS lineshapes of Co and/or Pd (as compared to bulk Co and/or Pd) in these structures, which result from their interactions. In addition, we can study the extent of and effect of oxidation in these materials. The principal characterization tool has been XPS. XPS allows us compare the lineshapes under varying conditions and to monitor the effects of oxidation (with O_2 and H_2O) of these metal multilayers, or optical media, or clean metal surfaces, over distances up to about 100 Å. Low-takeoff-angle (or grazing) XPS, which allows for analysis of the materials in the uppermost surface region only (the top 10 Å - 20 Å), was also used.

PROGRESS

Progress over the last quarter has been good. Characterization of the corrosion and oxidation of FeTbCo media samples has been slowed somewhat, as we have exhausted our supply of samples. Our goal in this area remains to understand the mechanistic role of modifiers, such as Zr or Ta, on FeTbCo media surfaces, with media samples supplied by the sponsors. We believe that by studying the molecular mechanism for oxide formation of these materials we can gain some insight into the protective properties of fourth-element modifiers, and some predictive understanding that will guide the development of new media. These studies are expected to continue very soon, as we expect to receive new samples in the near future.

Table I describes the Pd/Co metal multilayer samples provided by C. Falco's group. Each sample is a Pd/Co multilayer, with a Pd cap layer and Pd starting layer, deposited on Ag deposited on textured (111) Silicon. Samples M43, M44, M45, and M46 were all studied after exposure to the atmosphere for

an extended period of time, while sample M51 was characterized immediately after fabrication (less than five minutes of exposure to atmosphere).

Table 1. Description of metal multilayer samples provided by C. Falco.

Sample No.	Pd Layer Thickness Å	Co Layer Thickness Å	N (Bilayers)
M43	11	2	50
M44	11	4	30
M46	11	6	20
M45	11	8	15
M51	11	2	50

Figure 1 shows a representative XPS (normal) full scan, from 0 to 1000 eV binding energy, for sample M46. (Similar scans are seen for all other samples.) The Pd (3d) peaks can be seen at 335 eV, and the Co (2p) peaks can be seen at 781 eV. Other Pd and Co XPS and Auger peaks can also be seen. Also seen is a large amount of contamination in the form of oxygen (O(1s)) at 532 eV and carbon (C(1s)) at 284 eV. Larger oxygen and carbon peaks (relative to the Pd and Co peaks) are seen with grazing XPS. This suggests that much of the oxygen and carbon is localized at the surface.
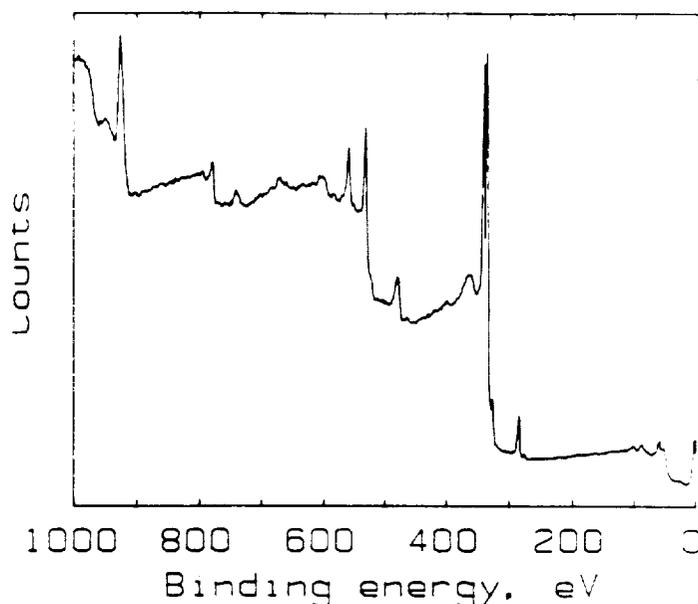

Figure 1. XPS spectrum of a full scan of sample M46, showing the presence of oxygen (1s) (532 eV binding energy) and carbon (1s) (284 eV) on the surface along with the Pd (3d) (335 eV) and Co (2p) (781 eV) peaks.

Figures 2a through 2d show the normal and grazing XPS of representative Co (2p) peaks for samples M46 and M51 respectively. The normal XPS of sample M46, which was exposed to the atmosphere for an extended period of time, shows some oxidation of the Co peak. More extensive oxidation is seen in the near-surface region with grazing XPS, as the Co peak, which was near 778 eV, shifts to a higher binding energy. Surprisingly, sample M51, which was exposed to atmosphere for only a short time, behaves in much the same manner as sample M46. The normal XPS of the Co peak shows some oxidation of Co. Grazing XPS of sample M51, like sample M46, shows (although less conclusively because of the low signal-to-noise ratio) more extensive oxidation of the Co in the surface region. Figure 2e and 2f show the Co peaks for sample M46 (normal and grazing XPS respectively), after sputtering (low-energy argon sputtering) of the surface. Sputtering significantly reduces the surface oxidation present, even in the near-surface region, as shown with the grazing XPS in Figure 2f.

Table II displays a comparison of the Pd/Co, O/Pd, and O/Co ratios for the samples as computed using peak areas from normal XPS and grazing XPS. One result worth noting is that the Pd/Co ratio decreases in the samples as the Co layer thickness increases (progressing from sample M43 - M46, the Pd layer thickness remains at 11 Å, while the Co layer thickness increases from 2 Å to 8 Å). This result shows that these XPS techniques can qualitatively monitor changes in thickness of these multilayers.

Table II. A comparison of the Pd/Co, O/Pd, and O/Co ratios for the various samples, computed using peak areas from normal XPS and grazing XPS. Samples M43 - 46 showed significant oxidation of the Co. Sputtering of sample M46 (M46S) reduced the oxide present on the Co. The Co was not seen to be oxidized for the fresh sample (M51) although significant oxygen was present.

| Sample	XPS	NOTES	Pd/Co	O/Pd	O/Co
M43	Normal	Co oxidized	5.15	2.16	11.15
M43	Grazing	Co oxidized	4.62	3.88	17.90
M44	Normal	Co oxidized	3.71	2.18	8.07
M44	Grazing	Co oxidized	3.89	2.73	10.63
M46	Normal	Co oxidized	3.55	1.90	6.74
M46	Grazing	Co oxidized	3.13	2.27	7.10
M45	Normal	Co oxidized	2.79	2.30	6.40
M45	Grazing	Co oxidized	2.32	3.92	9.10
M51	Normal	Fresh sample, Co oxidized	5.44	1.90	10.37
M51	Grazing	Fresh sample, Co oxidized	5.17	2.32	12.01
M46S	Normal	Sputtered, Co not oxidized	1.11	1.23	1.37
M46S	Grazing	Sputtered, Co not oxidized	1.07	1.41	1.52

N. R. Armstrong et al.
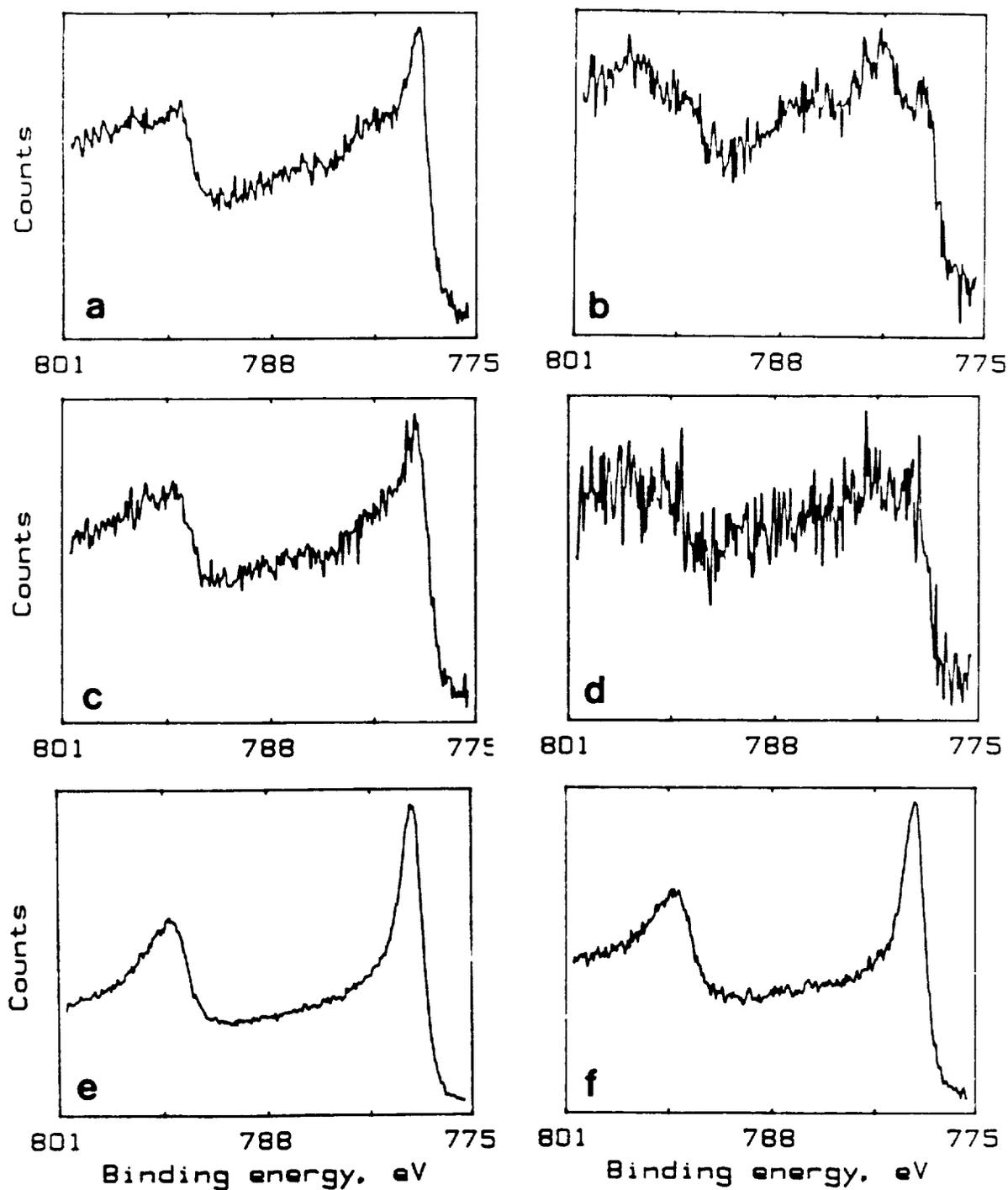
Figure 2. XPS of the Co (2p) peaks for (a) a representative older sample, M46 (normal XPS); (b) sample M46 (grazing XPS); (c) the fresh sample, M51 (normal XPS); (d) sample M51 (grazing XPS); (e) sample M46 after sputtering (normal XPS); and (f) M46 after sputtering (grazing XPS).

The most significant results from these studies are that the Co is significantly oxidized in samples M43 through M46 and M51, and that the Pd/Co ratio decreases when grazing XPS is used instead of normal XPS. These two results suggest that Co or a Co-oxide layer is the outermost layer. These films were made with a Pd cap layer, however, so it is apparent that the Co has migrated to the surface. This finding can be explained as follows. If an 11-Å Pd layer was the outermost layer, the Pd/Co ratio should increase when grazing XPS is used. The XPS electron escape depth for these materials is only on the order of 20 Å for normal XPS, and would be even smaller for grazing XPS. In addition, the relationship between XPS intensity and depth is an exponential, not a linear, relationship, so the surface species is accentuated. Because the Pd/Co ratio decreases, even for a 2-Å Co layer under Pd, the Co layer must be on top. One possibility is that pinholes in the Pd layer allow for oxidation of the underlying Co layer, and this oxidation causes Co to migrate toward the surface.

Surprisingly, sample M51, placed immediately into the ultrahigh vacuum environment for XPS analysis, with minimal exposure to atmosphere after fabrication, behaved similar to the older samples. Results for this sample suggest that some mixing of the outermost layers of these modulated structures may occur during fabrication. Low-angle x-ray scattering of these samples clearly shows that a modulated structure exists. It is plausible that the deeper layers maintain their structure, resulting in the x-ray pattern, while mixing may occur in the outermost layers. Further studies of these modulated structures, directly after fabrication (as with sample M51) are needed to study the oxidation and layer mixing which may occur during fabrication, and to reach more definitive conclusions about the nature of interfacial interactions in these structures.

APPLICATION OF HOLOGRAPHIC OPTICAL ELEMENTS TO MO READ/WRITE HEADS

R. K. Kostuk, T. Fujita, E. Campbell, C. Haggans, and C.-W. Han

OBJECTIVES

Our objectives are to determine the theoretical and practical performance limits of holographic optical elements (HOEs) formed in various recording materials, and to evaluate magnetooptic read/write head designs which use these components.

PROGRESS

Rigorous Hologram Modeling and Verification

Advances in coupled-wave models for both volume and surface-relief gratings and in verification of these models were made during this period. The volume-hologram model effort concentrated on including coordinate transformations for the polarization of the reconstruction beam. This situation exists for focusing elements with high numerical apertures. Data from experimental 0.55-NA holographic objectives were compared to theoretical calculations for an element with the same physical parameters, and were in good agreement. To perform this comparison, it was necessary to incorporate many of the material properties of the emulsion and changes to these properties that occur during processing. This capability is an extremely useful design feature of this model. A paper summarizing some aspects of these results is attached (Appendix K).

Work is proceeding on a modification to the surface-relief grating program, to allow modeling diffraction from a volume grating having an index modulation that varies with grating depth. This modification would allow an accurate evaluation of the performance of gratings formed in DCG.

Calculated data from the surface-relief grating model were compared to efficiency and polarization values measured from photoresist gratings in our lab, and to experimental and theoretical data previously reported in the literature. The values are quite sensitive to the grating relief profile, making conclusive validation of the model difficult. Better methods for quantifying the relief profile will have to be developed. If the model is correct, however, it indicates that grating fabrication tolerances will have to be controlled to a reasonably high degree. During the next period we will again be emphasizing improvements to our polarization and profile measuring techniques.

Planarized Head Designs and Hologram Fabrication

Several investigations are underway to demonstrate the feasibility of making a free-space (as opposed to guided waveguide) planarized optical head. This approach has the advantage of using lithography to accurately define the locations of multiple components to reduce alignment requirements, but does not suffer from some of the restrictions of single-mode waveguide structures.

Two fabrication methods are being pursued. One uses multiple lithographically defined gratings directly, and the other uses a lithographically formed grating as a master to produce an object beam for recording in a volume-hologram material. The latter method will allow recording higher grating spatial frequencies necessary for polarization-selective components. Currently we are studying the effects of copying and reconstructing multiple components into the volume material at two different wavelengths. Although this approach works for single elements, we are not sure if it can be extended to cascaded gratings.

A Karl Suss mask aligner suitable for fabricating gratings with $< 0.4 \, \mu m$ resolution was obtained through a National Science Foundation equipment grant, and is currently being brought into operation. Two e-beam mask sets were also received from AT&T, and will be used for initial characterization of this instrument and for the etching process. After initial evaluation, new masks will be designed for defining optical wavefronts for the copying process.

In addition to the above investigation, Dr. Teruo Fujita, a visitor to our lab from Mitsubishi, has been assembling a specialized test instrument which will readily accept the holographic elements made in our lab. This debrought into operation. Two e-beam mask sets were also received from AT&T, and will be used for initial characterization of this instrument and for the etching process. After initial evaluation, new masks will be designed for defining optical wavefronts for the copying process.

In addition to the above investigation, Dr. Teruo Fujita, a visitor to our lab from Mitsubishi, has been assembling a specialized test instrument which will readily accept the holographic elements made in our lab. This derease the efficiency by optimizing the development process.

A surplus humidity and temperature chamber was also identified during this period. We plan to use this chamber to control gelatin curing, an important parameter for obtaining consistent results.

PLANS

During the next quarter we will continue our efforts to extend and verify our models, to improve hologram fabrication, and to implement designs using planarized substrate-mode holographic elements. We have also reached an acceptable agreement with the DuPont Company to utilize their holographic photopolymer, and we plan to conduct a preliminary evaluation of this material for fabricating volume holograms.

SOL-GEL WAVEGUIDE AND GRATING FABRICATION

B. Zelinski, R. Roncone, L. Weisenbach, C. Schneiker, J. O'Kelly and J. Burke

OBJECTIVES

The overall goal of this research is to develop wet chemical techniques to synthesize low loss SiO_2-TiO_2 planar waveguides and planar waveguides with surface relief structures. To achieve this goal three short-term objectives currently are being pursued: 1) development of coating solution chemistries and processing techniques that will reliably produce quality planar waveguides; 2) investigation of the theoretical and experimental aspects of loss in these waveguides; and 3) development of suitable solutions and techniques for embossing surface features into planar waveguides.

PROGRESS AND PLANS

Waveguide Synthesis

During the last several months we have directed work toward improving the overall optical quality of the deposited sol-gel films. After spinning, the films often contained radial streaks (or striae) and mottling on a macroscopic scale. We have continued to investigate the roles of solution chemistry and surface leveling agents (SLAs) in removing these surface flaws. Our studies continue to support earlier observations that simplifying the film chemistry to reduce the number of different solvents reduces the extent of striae formation. This new chemistry is based almost entirely on ethanol and the ethoxides as metal cation sources; however, some preliminary loss data suggest that attenuation in the ethoxide-based solutions may be larger than in the earlier mixed-solvent solutions.

We have continued to use SLAs to minimize striae formation. SLAs are surface-active molecules, such as fluoromodified monomers, that segregate to high surface tension areas and that eliminate surface tension gradients. We have significantly reduced overall levels of surface undulations (striae) using SLAs. This is seen clearly in Figure 1. Figure 1a shows the surface striae that are present in a typical SiO_2-TiO_2 film. Notice that the striae have a spacing of about 50 μm and a peak to trough height of about 20 nm to 30 nm. Figure 1b shows the surface topography of a film generated using the same solution but with the addition of 0.02 wt% 3M-FC171 SLA. The surface striae have been significantly reduced. The surface topography varies by about 5 nm, which is approaching the noise level of the profilometer.

Effect of Surface Leveling Agent

Waveguide Topography

(a)

Waveguide Topography

(b)
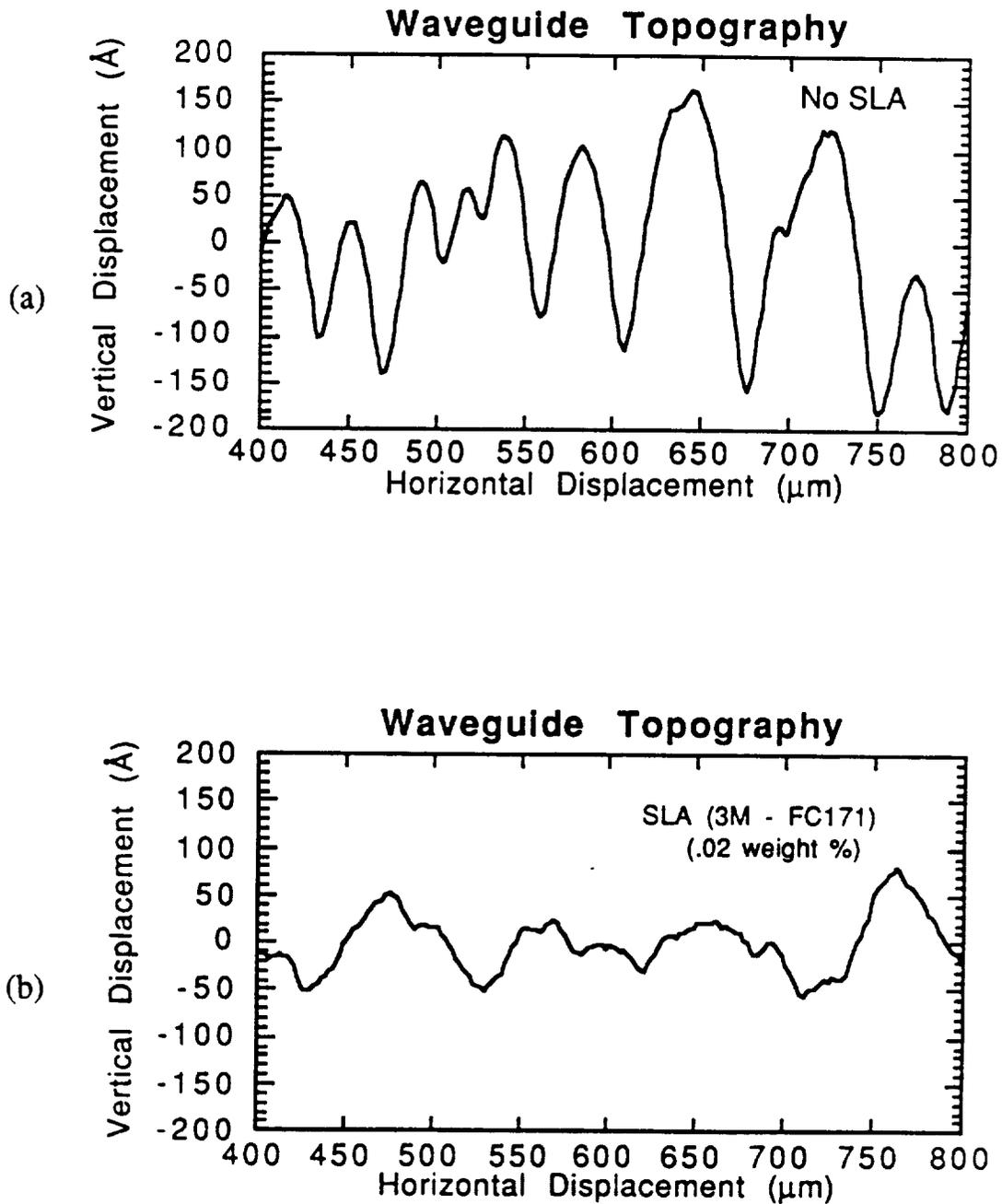
Figure 1. (a) The striae, or surface undulations, present in a typical sol-gel planar waveguide as revealed by surface profilometry; b) the reduction in peak-to-trough heights of the surface striae achieved by adding SLAs to the sol-gel solution before spin coating.

Now that the waveguide loss system is operating fully we plan to investigate extensively the relationship between film processing and attenuation. This work will assess the lower limits of loss that are possible in films generated by the sol-gel process. We will vary several parameters including overall film composition (to include ternary and quaternary compositions) and the relative amounts of water and alkoxide in the solution. We also will quantify the effects of striae and mottling on film attenuation.

Waveguide Loss System

The Automated Loss Measurement System is now operating fully. The system consists of a slit-scanned PMT moving across the modal streak that has been imaged by a coherent fiber bundle. Voltages, corresponding to intensities at 160 μm (or 80 μm) intervals along the streak are time-averaged in a digital oscilloscope for 2 seconds to 8 seconds, and subsequently are sent to a computer. The raw data are multiplied by a calibration factor (see below) and are processed to yield waveguide loss in dB/cm. Rudimentary plotting and graphic displays are included in this automated system.

Since our primary concern is to be able to measure variations in waveguide losses induced by variations in processing, repeatability of the loss measurement system is critical. To ensure repeatability, interferometric alignment of the waveguide and fiber bundle (to achieve parallelism) is employed. Consecutive scans of the same modal streak yield loss values repeatable to better than 1%. Consecutive measurements of the same modal streak, when the fiber bundle is repositioned between trials, yield losses repeatable to better than 4%.

The fiber bundle/PMT slit alignment was calibrated with a 2000 C Black Body source. With a known uniform light source, we determined both the transmission fluctuations of the fiber bundle (i.e. intensity [voltage] fluctuations in output vs. lateral distance along the bundle), misalignment (non-parallelism) of the fiber bundle and PMT (evident in a slope of light intensity vs. lateral distance along the bundle). From these data, multiplicative calibration factors for each measurement location were incorporated into the controlling software.

We can now systematically study attenuation in sol-gel waveguides to pinpoint processing techniques that yield low-loss planar films. In addition, we can begin comparing experimental and theoretical film losses to validate the scattering models.

Waveguide Scatter Theory

We have continued our work on the first-order boundary perturbation waveguide surface scatter model of Ames and Hall. When this model is completed (the spring meeting is the target date), and is used with the completed volume-scatter model, we will be able to predict the total surface and volume loss contributions of asymmetric slab waveguides, and the tolerable microstructural dimensions (surface and volume) required to achieve a desired attenuation.

Embossing

Work during the past quarter has focused on characterizing the new pneumatic embossing press (see December 15, 1990, report for description). We have concentrated on: 1) identifying usable pressure ranges; 2) identifying optimum pre-emboss bake times; 3) investigating the effects of line contact embossing; and 4) comparing photoresist masters to ion-milled glass masters.

We have determined optimum embossing pressures and pre-emboss bake times. Additionally, the ion-milled master gratings consistently produced better embossed gratings than the photoresist masters. We are now investigating the cause of this and we are trying to obtain more uniform embossed gratings over about a 2.5 mm^2-by-2.5 mm^2 region.

We will continue to optimize our processing techniques to routinely and repeatably emboss uniform waveguide gratings. We will investigate coating the master with carbon or Au/Pd to reduce the interaction of the ion-milled master grating with the sol-gel film.

GRATINGS AND WAVEGUIDES: MODELING AND VALIDATION

L. Li, K. Bates, G. Ma, and N. Ramanujam, J. Burke

OBJECTIVE

Our immediate objective is to understand the limitation of guided-wave and grating-coupler devices in their application to optical data storage heads. Our long-range goal is to develop and validate design codes for integrated optic devices.

PROGRESS AND PLAN

Focusing Grating Coupler

K. Bates continued to work on the focusing grating coupler (FGC) project, concentrating on three areas: construction optics, reconstruction optics, and holographic construction. He improved the FGC construction optics by incorporating a superior spatial filter collimator assembly into the optical system, and he designed and built a mechanical fixture to make optical alignment and sample positioning easier. In addition, he performed a number of iterations to find a suitable reconstruction source, ultimately using a Pencom 780 nm light pen, provided by IBM Tucson. He then characterized the wave-front quality and output wavelength of this source. Finally, working closely with L. Li, he is learning how to make holographic gratings in photoresist.

Ideally the FGC should be very weak, such that the grating aperture is uniformly illuminated. The last FGC we made (reported at the last IAB meeting), had a large decay rate so that most of the guided light coupled out of the waveguide in the first quarter of the grating aperture. It is extremely difficult to work with, and to measure, very thin photoresist films. In principle, using ion-beam etching techniques, we can obtain arbitrarily shallow gratings. However, because our supply of waveguides was limited, and because at the beginning of this year our new ion-beam source was not characterized, we continued trying to make better FGCs in photoresist. The results were not satisfactory. Now we know better the characteristics of our new ion beam source, and Dr. J. Revelli of Kodak has kindly provided some sputtered 7059 glass waveguides, so we are ready to attempt to produce some ion-beam-etched FGCs. Several test etchings of FGCs into glass slides have been made. They show promising signs that uniform and shallow FGCs can be achieved. We expect to have some results by the upcoming IAB meeting.

Ion-exchanged Waveguide

Since the last quarter, N. Ramanujam has continued to work on the fabrication and characterization of single-mode planar waveguides by K^+-ion exchange in soda-lime glass. An unexpected problem--cracking of the dishes used to contain the KNO_3 melt--was resolved. The quality of waveguides was improved by varying certain fabrication parameters (diffusion time and temperature), and the scattering loss was measured to be 1.0 - 1.5 dB/cm for single-mode (TE) guides. Work on optimizing these parameters is ongoing. Fabrication of shallow buried guides, made by purely thermal migration of K^+-ions (exchange with K^+-ions followed by a second exchange with Na^+-ions) was attempted, but the results have not yet been successful. Finally, the experimental setup for refractive-index profile characterization of single guides, based on a refraction method, is being completed, and results should be available soon.

Waveguide Modeling by FEM

G. Ma continues to work on the numerical modeling of optical waveguides and waveguide gratings by finite-element methods. Professor Cangellaris of the ECE department is teaching him some novel techniques to handle the boundary conditions of the open waveguide structure. Development of the FEM computer program is underway.

Grating Fabrication

The long-awaited saddle field atom (ion) beam source was finally operational in mid February. The source has been run maintenance free for more than 25 hours with C_2F_6 gas, with no signs of deterioration in operating conditions. (The conventional Kaufman ion beam source must be cleaned every two to three hours when working with C_2F_6 gas.) To use the atom beam source efficiently, a careful characterization is necessary, which includes determination of the etch rates at different beam voltages and currents, at different beam angles, and for different materials (soda-lime glass, fused silica, Sol-Gel films, etc.) K. Erwin is working on this task and plans to finish in one or two months.

Although complete characterization of the source has yet to be completed, L. Li's preliminary characterization work has enabled him to make etched gratings for the current needs of the group. Several linear gratings were etched into 7059 glass waveguides (provided by Kodak) as input couplers for K. Bates's FGC project. Etched gratings were also supplied to C. Schneiker as masters in his grating embossing experiment. Work is ongoing to etch gratings into Sol-Gel film waveguides made by

R. Roncone and his coworkers, and into K^+-ion exchanged waveguides made by N. Ramanujam. Those two waveguides are candidates for waveguides in our future FGC work.

Now that the atom beam source is finally working, L. Li will concentrate on the variable-groove-depth grating project proposed a year ago, and on the grating groove polishing project proposed last October. He will continue to help K. Bates in the FGC work, and occasionally provide gratings to the other members of the group (hopefully, this task will be transferred to someone soon). One major problem with the variable-groove-depth project is that the electronic chip on the precision, vacuum-compatible, stepper-motor-driven linear translation stage is vulnerable to high-voltage arcing in the vacuum when the atom source is operating. Li will solve this problem with K. Bates's help.

SECTION 2. PROPOSALS

SIGNAL PROCESSING TECHNIQUES FOR OPTICAL DATA STORAGE

M. M.-K. Liu

ABSTRACT

High density is a key advantage that optical data storage has over other storage technologies. To increase the density, the spatial resolution in writing and reading should be increased. Therefore, reducing the laser spot size or the diffraction limit is very important. As the spot size is reduced, jitter becomes important. Jitter is the random deviation from original marks, and has various causes, such as noise. Because jitter may not be reduced at the same rate as can the laser spot size, jitter becomes more important as density increases.

Compared to magnetic recording, an understanding of the jitter characteristics and the use of signal processing techniques in optical recording are limited. In response, we have recently studied a jitter model and several signal processing techniques. Initial simulation results indicate that the processing techniques are effective in reducing jitter. *The objectives of this proposal are to quantify the jitter characteristics in more detail and to verify the performance of the signal processing techniques experimentally.*

INTRODUCTION

High density is a key advantage of optical data storage, and research activity has focused on this property. The use of shorter wavelengths from a laser source is one critical thrust towards achieving high density storage by reducing the laser spot size or the diffraction limit. However, the use of smaller laser spot sizes alone cannot yield high density because another critical limiting factor, *jitter* (the random deviation from original mark widths) exists in every optical data storage system. Jitter can be caused by noise, fluctuation of rotational speeds, disk material jaggedness, and intersymbol interference. As storage density increase, jitter becomes more important, because the degree of jitter may not be reduced at the same rate as storage density increases.

Therefore, a clear understanding of jitter characteristics and a good combination of signal processing techniques are of fundamental importance in the pursuit of higher storage density. As jitter is reduced to its minimum, data can be stored in its highest spatial resolution.

Although optical recording and magnetic recording have many similarities, such as the two-state modulation (i.e., two magnetic polarization states in saturated magnetic recording and magnetooptical--

MO--recording), the understanding of jitter characteristics and the use of signal processing techniques in optical recording are relatively limited. There are many distinct physical characteristics peculiar only to optical recording. For example, in optical recording the channel is not inherently a differential (or AC coupling) channel as it is in magnetic recording. It can be a low-pass channel[2,3] if the basic Kerr effect[4] is used in M-O systems.* Also, the jitter characteristics in optical recording due to media noise, photon-shot noise, and intersymbol interference during the write and read processes are quite different from that in magnetic recording.

In this proposal, we will focus on pulse width modulation (PWM), where information is stored through modulating sizes of sequential marks alternating in magnetic polarization or in material structure. In PWM, jitter or mark size deviation is the key factor that results in error detection. We have studied a jitter model and several signal processing techniques to reduce the error rate.[1] These processing techniques can be integrated in a single chip by advanced VLSI technology. Initial simulation results have been obtained and the signal processing techniques are found to be effective.

PAST WORK AND NEW APPROACH

Traditionally, in detecting a mark size in a PWM readback signal, the peak detection technique is used.[3,6] In peak detection, a peak will be first generated at the recorded mark boundary if the channel is differential, such as that in magnetic recording. A detected peak or the derivative of a step function can be either positive or negative, depending on the step transition at the mark boundary. From these peaks, a readback clock will be generated by a phase lock loop (PLL),[6] and this clock provides the necessary detection "timing window" in recovering the original data. As a result, from the positions of the timing windows within which peaks fall, original mark sizes can be recovered and the original data can be decoded. Based on this detection approach, various equalization techniques have been used to improve the detection accuracy. In general, equalization techniques are used either to preshift the peaks (write equalization) or to reduce detected peak widths. The latter is call pulse slimming (read equalization).[7-10]

In this proposal, a different approach is taken to retrieve the stored data. Instead of generating a readback clock and timing window to identify the position of each peak, time marks are first quantized from the readback signal. To quantize a time mark, a high-speed counter driven by a high-speed clock

---

*It can also be a differential channel if the edge detection is used instead.[5]

is used. A triggering signal is used to reset the counter and to latch the counter output to the register. This triggering signal can be derived from the same peak-detection technique described above if the channel is differential, or it can derived by a simple threshold detection with threshold adaptation if necessary. An integer proportional to the time mark size will be generated for each mark. Therefore, this quantization step transforms the readback signal from time marks to amplitude marks. With these quantized marks, various digital signal processing techniques can be used to equalize and recover the original mark sizes.

There are two important advantages of this quantization approach. First, it converts an analog signal of temporal marks to a discrete digital signal. As a result of this conversion, time domain noise (or jitter) is at the same time converted to amplitude domain noise, and digital signal processing can be used to recover the original data. For example, an increase in size of a temporal mark has a strong correlation with the decrease of its adjacent temporal mark. Two simple signal processing techniques, called Differential Interleaving Detection (DID) and Additive Interleaving Detection can be used to take advantage of this strong correlation.[1] The second advantage of this approach is it allows us to use the VLSI technology in implementing and integrating various equalization, detection, and demodulation algorithms. For example, the intersymbol interference (ISI) in the signal can be strongly nonlinear. This nonlinear ISI can be easily programmed in digital signal processing algorithms for cancellation.

One may point out one disadvantage of this new approach: the added quantization error. However, if the clock is fast enough, this quantization error is negligible. For example, if the clock has a period of one nsec and mark sizes are multiples of 100 nsec,** we have a signal-to-noise ratio of SNR $= 10\log_{10}(100^2/(1/12)) = 50.8$ db.[11] Therefore, this quantization error is practically insignificant compared to other noise such as thermal and media noise. With 16 bits in quantization, mark sizes can be as long as 65.5 μsec or 655 times of 100 nsec, which is sufficient for most modulation codes.

RESEARCH IMPACTS

The success of the proposed research will enable us: 1) to effectively integrate the proposed signal processing techniques with other techniques such as modulation and error correction codes; and 2) to realize these techniques in practical systems. With a better understanding of jitter characteristics and with

---

** If we assume the disk linear velocity is 4 m/sec, this 100 nsec time unit corresponds to 400 nm mark unit. For a system using (2,7) RLL code, the minimum mark size is 1.2 μm. If we compare this with a typical diffraction limit at 1 μm, this 100 nsec is a reasonable assumption.

the use of signal processing techniques, we will be able to find additional modulation codes and error correction codes that can maximize the density at a specified bit error rate. The best modulation and error correction codes will be those that can best match the jitter characteristics and take advantage of the proposed signal processing techniques.

In addition to modulation and error correction codes, more complicated detection techniques, such as the maximum likelihood (ML) method and the Viterbi algorithm, can be used to decrease the error rate further. These additional techniques can be used in addition to the proposed signal processing techniques whenever the storage density can be further improved.

From recent state-of-the-art reports for both the magnetic and optical recording technologies,[12] the linear density of SONY's magnetooptical (1989) systems is 950 bits/mm or 1 μm per bit. This is quite close to the diffraction limit with a typical laser diode at a wavelength of 890 nm. Therefore, success of the proposed work in signal processing becomes very important and can help real system implementation based on the VLSI technology to achieve higher storage densities.

WORK PLAN

The proposed work will be based on the study described in Ref. 1, where a jitter model and several signal processing techniques have been proposed. Work is planned over a two-year period and consists of two tasks: (1) quantification of the statistical jitter distribution of each jitter source in real systems; and (2) experimental verification of the proposed signal processing techniques.

Quantification of Jitter Distribution

In the first year, we will first quantify three types of jitter: noise jitter, bit-shift jitter, and intersymbol-interference jitter.[1] Currently, we have a time interval analyzer (TIA) and digital scopes that allow us to measure a time mark with resolution to one nsec. The TIA is programmable in a way that helps to identify each jitter source. For example, we can repeat the measurement of a given mark many times to get the jitter distribution in the read process, or we can repeat the measurement of a sequence of marks many times and take an average to get the jitter distribution in the write process. We can further use different data patterns to investigate the jitter distribution in the write process. We can further use different data patterns to investigate the ISI jitter in both the write and read processes. This jitter quantification step is tedious but is very important and requires extreme carefulness. Our experience in measurement[13] has prepared us for this step.

Verification of the Signal Processing Techniques

In the second year, we will use the jitter distribution and build necessary circuits to quantize and process the temporal marks. This step will help us to verify the proposed techniques and provide us with the information for making necessary modifications. We expect to see significant improvement in storage capacity at the end of this second step.

REFERENCES

1. M. K. Liu, "Jitter model and signal processing techniques for pulse width modulation optical recording," to appear in IEEE International Conference on Communications, Denver, June 1991.

2. R. Karabed and P. Siegel, "Even mark modulation for optical recording," pp. 1628-1632, Proceedings of ICC, 1989.

3. R. Wood, "Magnetic and optical storage systems: opportunities for communications technology," pp. 1605-1612, Proceedings of ICC, 1989.

4. M. J. Freiser, "A survey of magnetooptic effects," IEEE Trans.Magnetics, pp. 152-161, June 1968.

5. M. Mansuripur, "Detecting transition regions in magneto-optical disk systems," Appl. Phys. Lett., pp. 716-717, 21 Aug. 1989.

6. H. Burkhardt, "Phase detection with run-length-limited codes," IBM Technical Disclosure Bulletin, Vol. 24, No. 1B, p. 683, June 1981.

7. G. V. Jacoby, "Signal equalization in digital magnetic recording," IEEE Trans. on Magnetics, pp. 302-305, Sept. 1968.

8. R. C. Schneider, "An improved pulse-slimming method for magnetic recording," IEEE Trans. on Magnetics, pp. 1240-1241, Sept. 1975.

9. R. C. Schneider, "Write equalization in high-linear-density magnetic recording," IBM J. of Res. and Develop., pp. 563-568, Nov. 1985.

10. P. Sutardja, "A Post-Compensation Scheme for Peak Detect Channel," Proceeding of Intermag, 1990.

11. B. P. Lathi, Chapter 3 of *Modern Digital and Analog Communication Systems*, 2nd Ed., Holt, Rinehart, and Winston, 1989.

12. R. Wood, "Magnetic megabits," IEEE Spectrum, pp. 32-38, May 1990.

13. M. M.-K. Liu, "Experiments for Future High Density Optical Data Storage," paper presented in Optical Data Storage meeting, University of Arizona, Tucson, April 1990.

SECTION 3. APPENDICES

52

Appendix A
Characterization of Magneto-Optical Media

$P_ \ 18$

Roger A. Hajjar , *Te-ho Wu* and M. Mansuripur

Optical Sciences Center

University of Arizona

Tucson, AZ 85721

$A \times 556$

Amorphous rare earth-transition metal (RE-TM) alloys and compositionally modulated *TM TM* films (prepared in the laboratories of the ODSC sponsors) are characterized in terms of their magnetic, magneto-optic and galvanomagnetic properties. The loop tracer, vibrating sample magnetometer (VSM), and the Rutherford Backscattering facility (RBS) have been used to characterize and analyze the various properties of these magneto-optical storage media.

The loop tracer consists of a 21 kGauss electromagnet (4" diameter pole piece, 2" gap). The magnet has a rotating stage that allows its field to be applied both perpendicular to and in the plane of the sample. Samples of up to 1" in diameter can be analyzed in a cryogenic dewar cycling temperatures from 80 K to 475 K. The DC differential detection technique is used to measure the magneto-optical Kerr effect at the 633 nm HeNe wavelength. Ellipticity can also be measured with the insertion of a quarter-wave-plate. The magnetic properties such as coercivity and anisotropy constants at various temperatures are determined form the perpendicular and in-plane measurements of the polar Kerr effect[1] (KE). Galvanomagnetic and transport properties such as the Hall effect (HE), magnetoresistance (MR) and resistivity are measured with two mutually orthogonal pairs of point contacts at the sample surface[2].

a) Co/Pt Films : The *Co/Pt* films were prepared by Dr. *C-J*. Lin of IBM Almaden Research Center. These are multilayered films consisting of alternating ultrathin *Co* and *Pt* layers. The films were deposited by *e*-beam evaporation from *Co* and *Pt* sources onto glass substrates[3]. The periodicity and crystallographic structures were obtained by *X*-ray diffraction analyses and the composition was measured by both XRF and RBS. The total thickness of these films was nominally set to 30 nm where the **thickness** of the *Pt* layer was set to about 1.0 nm and the thickness of the *Co* layer varied from 0.2nm to 0.4 nm.

All samples show perpendicular magnetic anisotropy and rectangular hysteresis loop in perpendicular magnetic fields. Figures 1 through 4 show the various chracteristics of these films versus *Co* thickness. The remanent Kerr angle and Hall resistivity at room temperature are displayed in Fig. 1. Figure 2 shows the saturation magnetization M_s obtained from the VSM hysteresis loops and $\Delta\rho/\rho$ longitudinal obtained from the MR measurement when the field is in the plane of the sample. The value of $\Delta\rho/\rho$ is obtained from the peak of the longitudinal MR curve as shown in

Appendix A

Fig. 5. The linear trend of θ_k, ρ_H, M_s and $\Delta\rho/\rho$ (longitudinal peak) correlate with the increase of Co content in these films. From the magnetization data we find that the effective Co moment is around 1750 emu/cc which is considerably enhanced relative to that of bulk cobalt. This enhancement is believed to be due to the stretching of the cobalt lattice which makes it more atomic like (atomic spin polarization of Co is about twice as large as that of bulk Co)[4]. There is little evidence that Pt is polarized as far as we can tell from the Ms data. Evidently, more data points are needed in order to give a quantitative assesment of the Pt polarization.

Figure 3 displays the nucleation coercivity (H_c) and anisotropy field (H_k) for these films. Both H_c and H_k can be determined from four different measurements, namely : Kerr, Hall, VSM and MR measurements with the applied field being either perpendicular to or in the plane of the sample. The nucleation coercivity can be obtained from KE, HE or VSM hysteresis loops. We can also obtain Hc from the perpendicular MR measurement as illustrated in Figs. 7 and 8. The linear part of the curve in Fig. 8 has a negative slope of 3.1×10^{-8} per Oersted, which has its origin in the s-d scattering phenomenon as interpreted by Mott[5]. The peaks centered around the coercive field are caused by the scattering of the conduction electrons from the magnetization within the domain walls. These walls cause the resistivity to increase provided that their magnetic moments, while in the plane of the film, are also parallel to the direction of the current. Thus the height of the peaks in Fig. 8 is a measure of the volume fraction covered by the domain walls, while the width of the peaks corresponds to the transition region observed in the vicinity of H_c in the hysteresis loop.

The anisotropy field is determined from the initial part of the KE or HE in-plane measurement[1] (Fig. 6). Also, H_k can be roughly determined from the perpendicular and in-plane VSM measurement by extrapolating the intercept of the in-plane measurement with the saturation part of the hysteresis loop as shown in Fig. 9. H_k is also obtained from the longitudinal MR measurement as shown in Fig. 5. In this measurement, the sample is first saturated along the easy axis. The initial increase of resistivity with the applied field is due to the alignment of magnetization with the field. The maximum of $\Delta\rho/\rho$ (longitudinal) is reached at $H = H_k$. Once the magnetization and the field have been aligned, further increases in H cause a linear decrease of $\Delta\rho/\rho$ which, as mentioned before, is related to the s-d scattering. As shown in Fig. 3, the anisotropy field decreases with increasing cobalt layer thickness. As expected, H_k decreases from a positive value towards negative values, corresponding to an in-plane easy axis of magnetization for thick cobalt layers. A rough extrapolation shows that the crossing point between the perpendicular and in plane anisotropy regimes lies at about 0.7 nm of Co. For ultrathin Co (< 0.25 nm), the anisotropy field is reduced mainly due to the island-like formation of the Co layers that become discontinuous.

Figure 4 shows the magnitude of the slope due to s-d scattering obtained from the perpendicular MR measurement (see Fig. 8). The data obtained correlate to a certain extent with the total thickness of one period over the thickness of cobalt, $(t_{Co} + t_{Pt})/t_{Co}$. Note that for pure cobalt, where this ratio is equal to 1, the slope obtained is 3×10^{-8} per Oersted.

We have also measured the electrical resistivity using the Van der Pauw technique[6]. The resistivity reflects the character of the interfaces in superlattices. For reference, the resistivity of a thick (sputtered) cobalt sample (175 nm-thick) was found to be 14 $\mu\Omega.cm$, and those of pure *Pd* and *Pt* films (sputtered) were around 17 $\mu\Omega.cm$. The typical room temperature resistivity for a multilayer film is in the range of 30 - 60 $\mu\Omega.cm$. From this behaviour, we can assume that multilayers with abrupt interfaces should have a resistivity intermediate to those of the constituent metals while mixed interfaces will have resistivities as much as a factor of 10 higher. For the samples studied here, the *Co/Pt* films (30 nm-thick) have a typical resistivity of 45 $\mu\Omega.cm$, while similar *Co/Pd* samples (see next paragraph) have a resistivity of 37 $\mu\Omega.cm$. Adopting the above argument, we attribute the larger resistivity of the *Co/Pt* films to interfacial mixing between platinum and cobalt layers, and conclude that *Co/Pd* films have sharper interfaces.

b) Co/Pd Films : A series of Co/Pd multilayer films were fabricated by Dr. Charles Brucker of Kodak Research Laboratories. These are sputtered *Co* (0.2 nm)/*Pd* (.9 nm) films with thicknesses ranging from 5.5 nm to 87.5 nm. Figures 10 - 13 display the thickness-dependence of the magnetic, magneto-optic, and galvanomagnetic properties of these samples at room temperature. The Kerr rotation angle Θ_k measured from the film side is remarkably enhanced around 11 nm of thickness. This enhancement is due to optical interference between the rays reflected from the film surface and those reflected at the interface between film and substrate; the enhancement is *not* related to the multilayer structure of the film. Even though the concept of Kerr effect enhancement due to optical interference is well known, we revisit this topic for the sake of completeness.

Consider a magneto-optic film sandwiched between two mediums of indices n_1 and n_3. The MO layer has two indices of refraction denoted by n_2^+ and n_2^-, corresponding to left and right circularly polarized light. Knowing that linearly polarized light may be decomposed into left and right circular polarization, we write the Fresnel coefficients as :

$$r_1^{(\pm)} = \frac{n_2^{(\pm)} - n_1}{n_2^{(\pm)} + n_1}$$

for reflection off the top surface of the MO layer and :

$$r_2^{(\pm)} = \frac{n_3 - n_2^{(\pm)}}{n_3 + n_2^{(\pm)}}$$

for the reflection off the bottom surface of the MO layer. Assuming multiple reflections within the MO layer, we obtain a general expression of the total reflectivity as follows :

$$r^{(\pm)} = \frac{r_1^{(\pm)} + r_2^{(\pm)} \exp(-i\delta^{(\pm)})}{1 + r_1^{(\pm)} r_2^{(\pm)} \exp(-i\delta^{(\pm)})}$$

where $\delta^{(\pm)} = 4\pi\, n_2^{(\pm)} \times thickness/\lambda$. Calculation of Kerr rotation angle and ellipticity from the above equation is straightforward[7]. Figure 14 shows a calculated curve of Θ_k and ϵ_k versus film thickness. The magneto-optic refractive indices (at $\lambda = 790$ nm) are obtained from the literature for the film structure $Co(0.2\text{nm})/Pd(0.9\text{nm})$ with a total thickness of 50 nm.

The electrical resistivity is displayed in Fig. 12 and shows a rapid increase for thicknesses below 16.5 nm. This increase in resistivity can be explained by the change in the film morphology, namely the film growth from an island structure to a continuous structure[8]. The change in the film morphology can also be observed in the magnetic properties such as the anisotropy, coercivity and saturation magnetization where a sharp decrease is observed below 16.5 nm (see Figs. 11 and 13). Note that, as expected, the Hall resistivity in Fig. 10 is independent of the magneto-optical interference effects discussed above and is closely related to the resistivity data. It can be shown[9] that $\rho_h \propto \gamma\rho^2$, where the coefficient γ is related to the spin-orbit coupling and goes to zero in the absence of spin-orbit coupling. Good agreement is obtained by fitting the data with the theory.

The s-d slope observed in these films is significantly larger than in Co/Pt films of approximately the same structure as shown in Figs. 15 and 16. This might be attributed to three different phenomena : The d-band structure of cobalt is becoming steeper and closer to the Fermi level (see reference 4), the induced magnetic polarization of Pd, or the extreme proximity of the Pd Fermi level to the edge of the d-band.

c) **TbFeCo Films** : A study of the thermomagnetic properties of TbFeCo films is currently underway. These are films of variable Tb content (ranging from 22.5% to 28%), and were prepared at the IBM Almaden Research Center. The films are deposited onto quartz substrates and consist of a quadrilayer structure of AlCr with an MO layer sandwiched between two dielectric SiN layers.

Figure 17 displays the saturation magnetization M_s versus temperature for these films. Figure 18 shows the T_{comp} and M_s as a function of Tb content. The sum of the anisotropy energy constants K_1 and K_2 at room temperature is displayed in Fig. 19. These parameters are obtained from the in-plane Kerr measurement[1]. The apparent reduction of K_u (i.e., $K_1 + K_2$) at the compensation point is not real, but is due to the fact that the maximum field strength in our experiment ($\simeq 21$ KOe) is insufficient to tilt the magnetization away from the perpendicular direction.

Figure 20 shows a typical set of perpendicular and in-plane Kerr effect measurement results for the TbFeCo samples. The bottom frame in Fig. 20 shows the fitting of the normalized in-plane data to the theoretical model (normalization is by the height of the hysteresis loop); it is from this kind of fitting that the anisotropy constants K_1 and K_2 are determined.

Plots of the remanent Kerr angle and coercivity, obtained from the hysteresis loops, are shown in Fig. 21. We are currently measuring the temperature-dependence of the various properties of these films in order to determine their anisotropy constants as function of temperature.

REFERENCES

1   R.A. Hajjar, F.L. Zhou and M. Mansuripur, J.Appl. Phys. **67**, 5328 (1990).

2   R.A. Hajjar, M. Mansuripur and *H*-P.D. Shieh, to appear in J. Appl. Phys. (1991).

     R.A. Hajjar, M. Mansuripur and *H*-P.D. Shieh, presented at MMM'90, to appear in J. Appl. Phys., April 1991.

3   C.-J. Lin and H.V. Do, IEEE MAG **26**, 1700 (1990).

4   R. H. Victora and J.M. Maclaren, "Calculated Magnetic and Electronic Properties of *Co/Pd* Superlattices", (unpublished Report).

5   N. F. Mott, Proc. Roy. Soc. A, (London) **153**, 699 (1936) and **56**, 368 (1936).

6   L. J. Van der Pauw, Philips Rev. **20**, 220 (1958).

7   M. Born and E. Wolf, "Principles of Optics", 6th edition, Pergamon Press.

8   S. Hachimoto,Y. Ochiai and K. Aso, J. Appl. Phys. **67**, 4429 (1990).

9   R. Karplus and J.M. Luttinger, Phys. Rev. **95**, 1154 (1954).

Appendix A
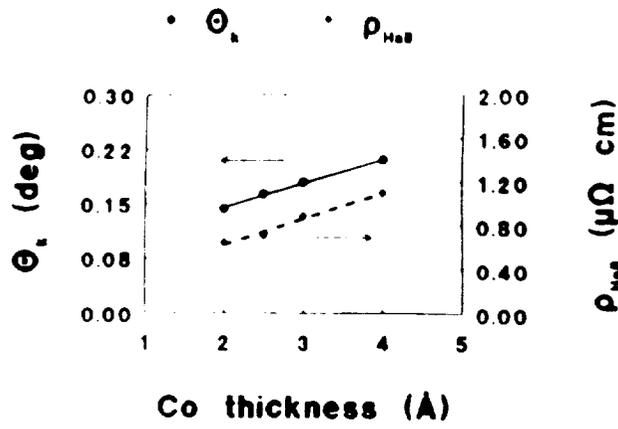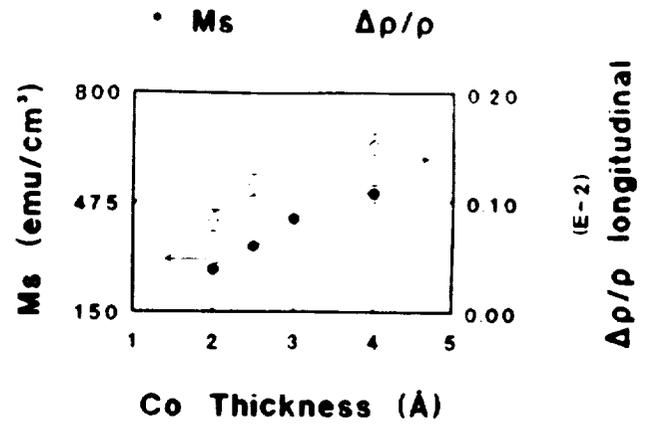
Fig. 1

Fig. 2
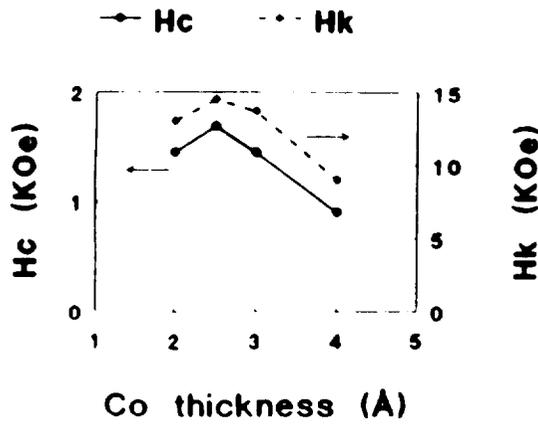
Fig. 3
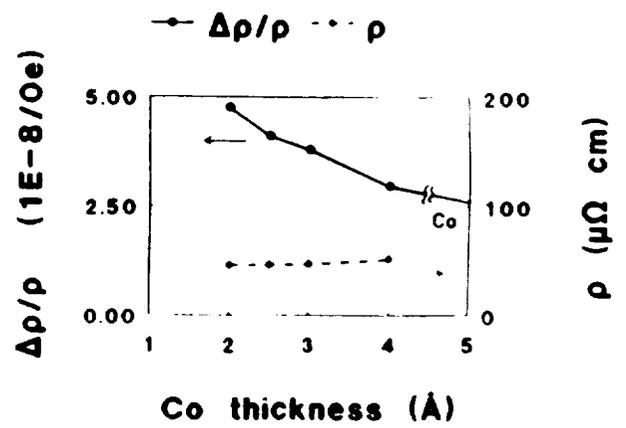
Fig. 4

LONGITUDINAL
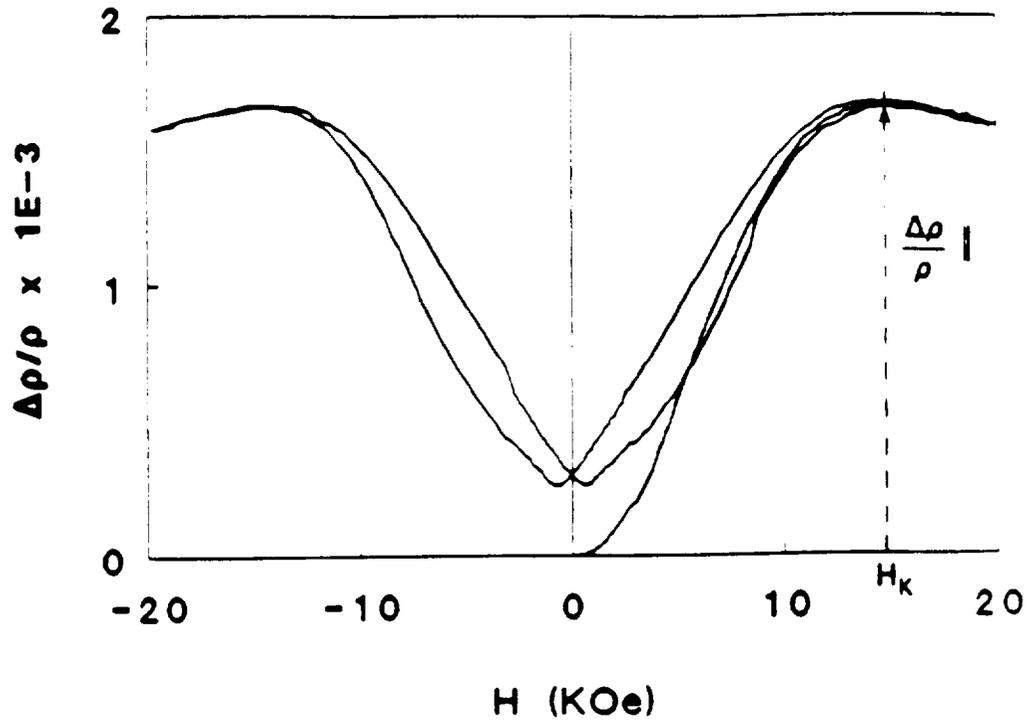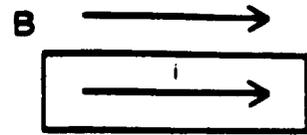
Fig. 5
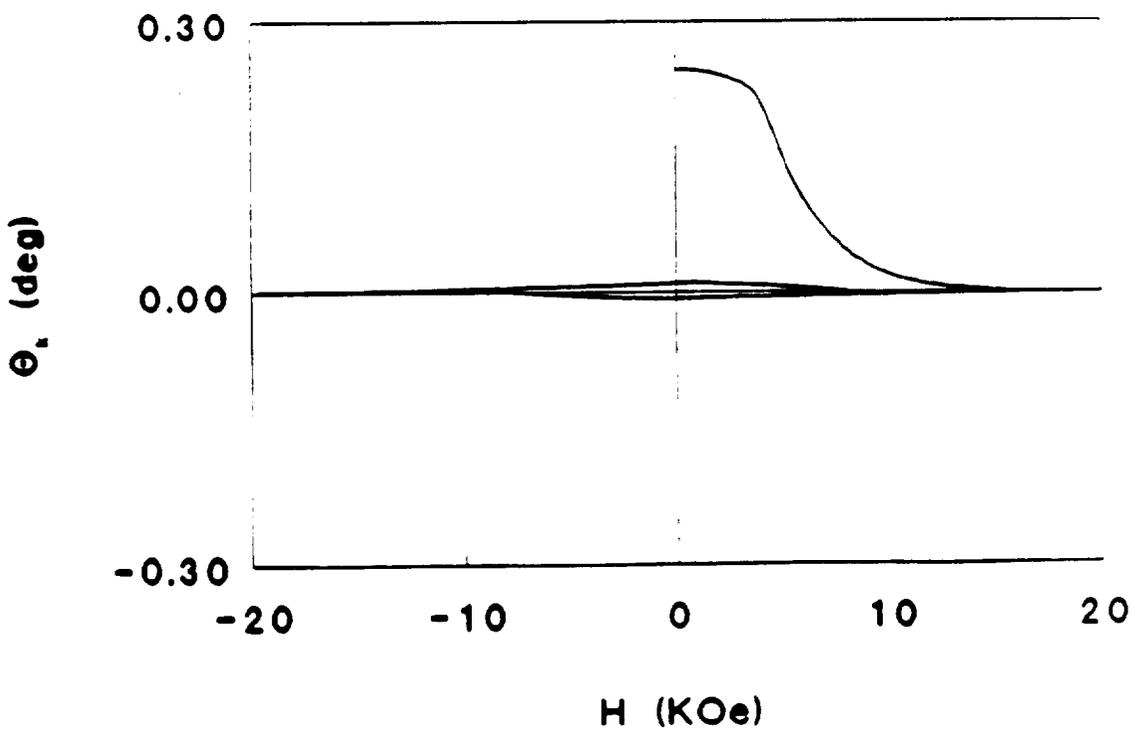
Fig. 6

PERPENDICULAR B

Fig. 7

Fig. 8
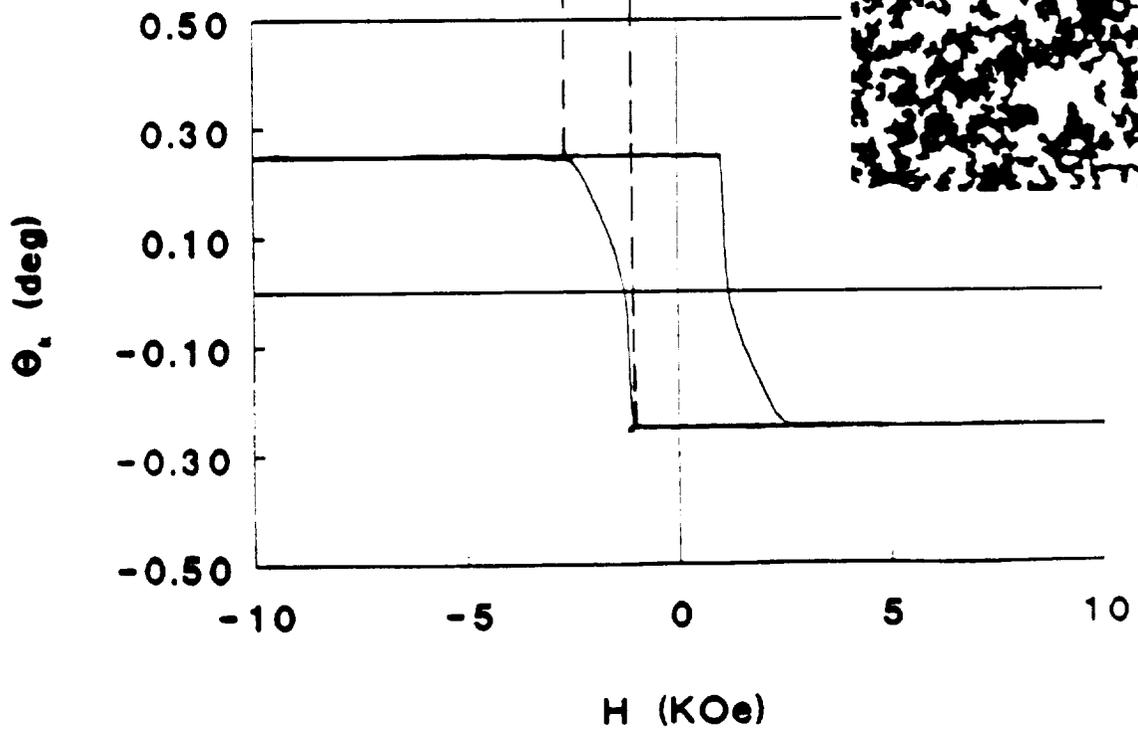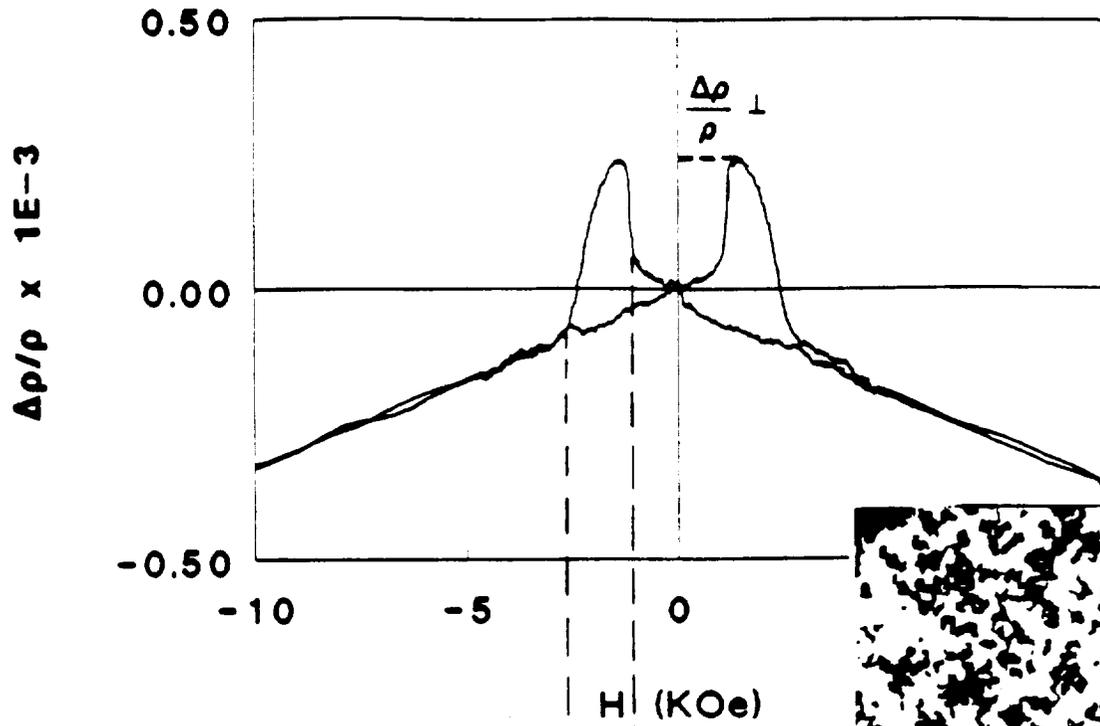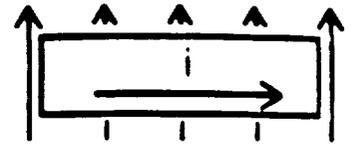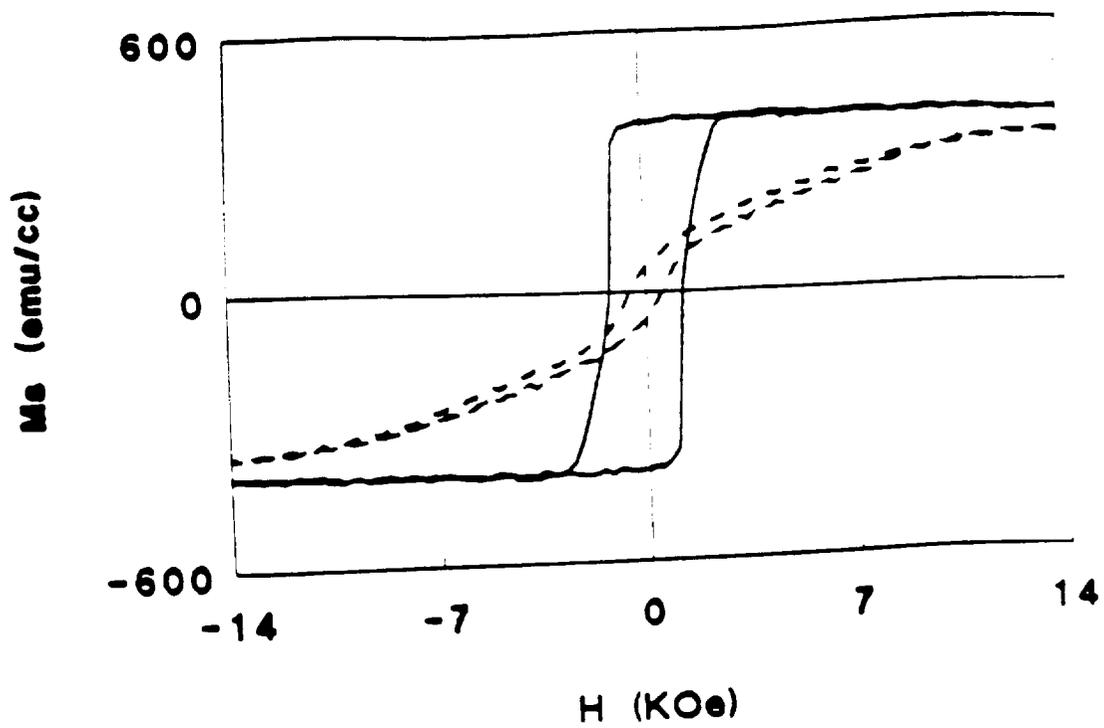
Fig. 9
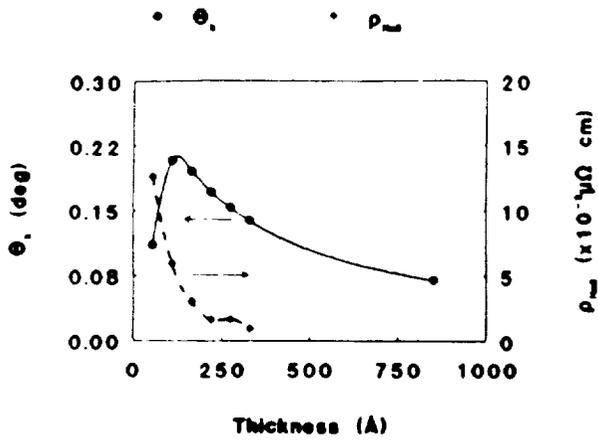
Fig. 10

Fig. 11

Fig. 12
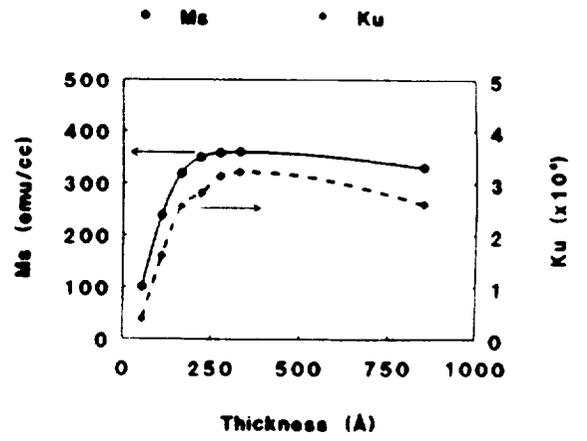
Fig. 13

Fig. 14

Appendix A
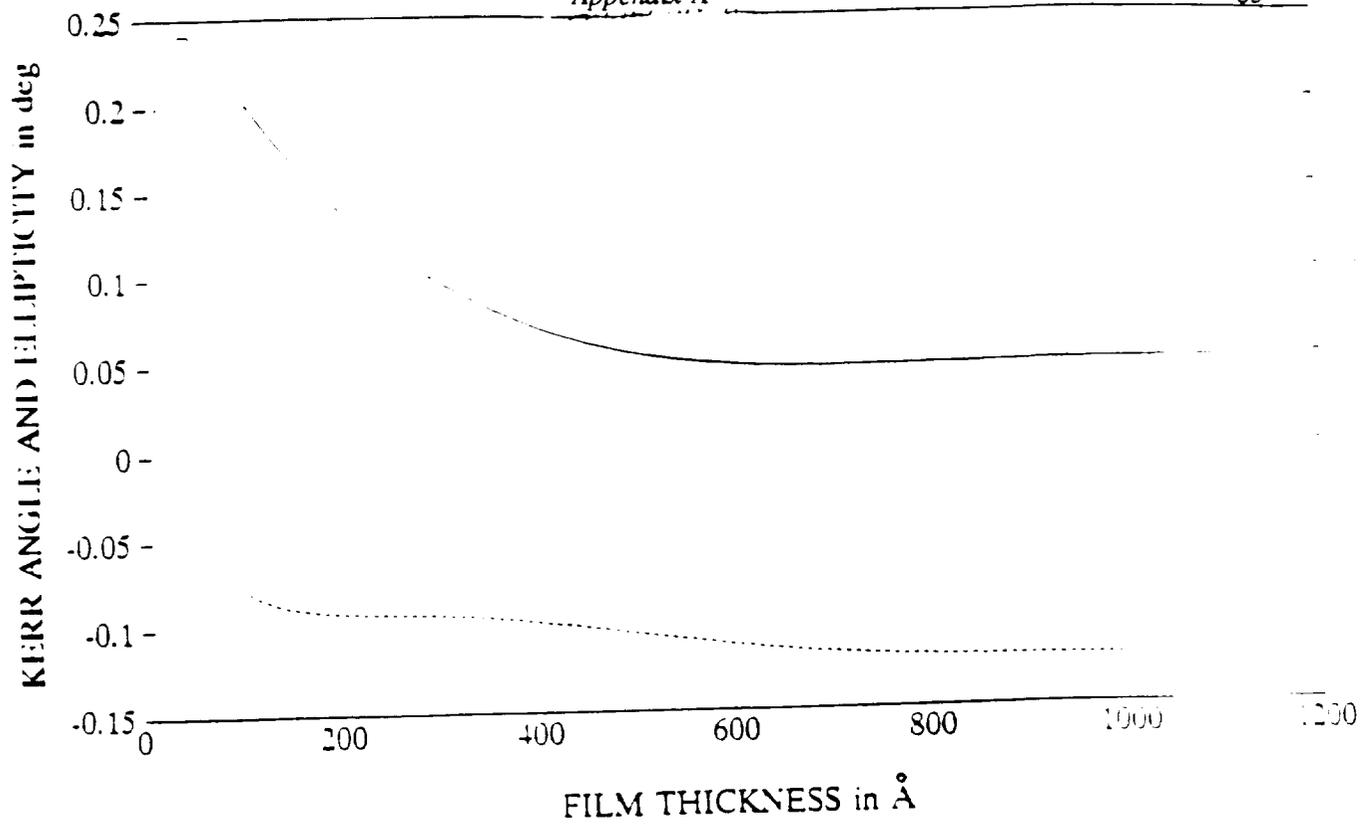
Co(2Å)/Pt(10Å) x 25 (300Å)
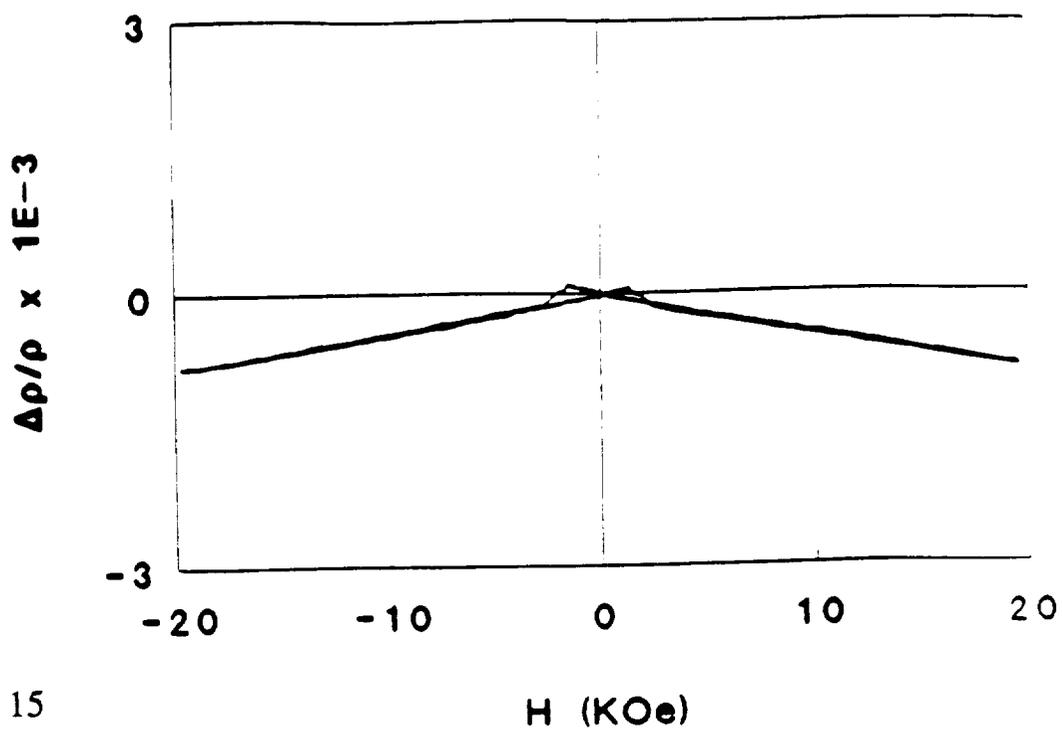
Fig. 15

Co(2Å)/Pd(9Å) x 30 (330Å)

Fig. 16

Ms Vs Temperature
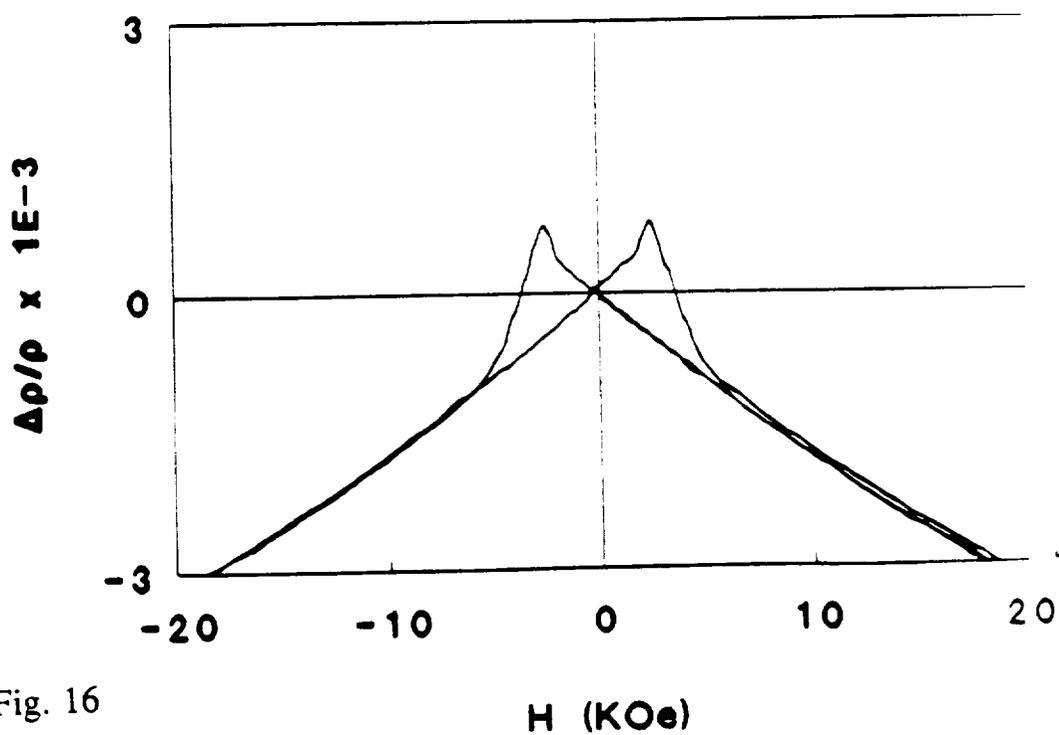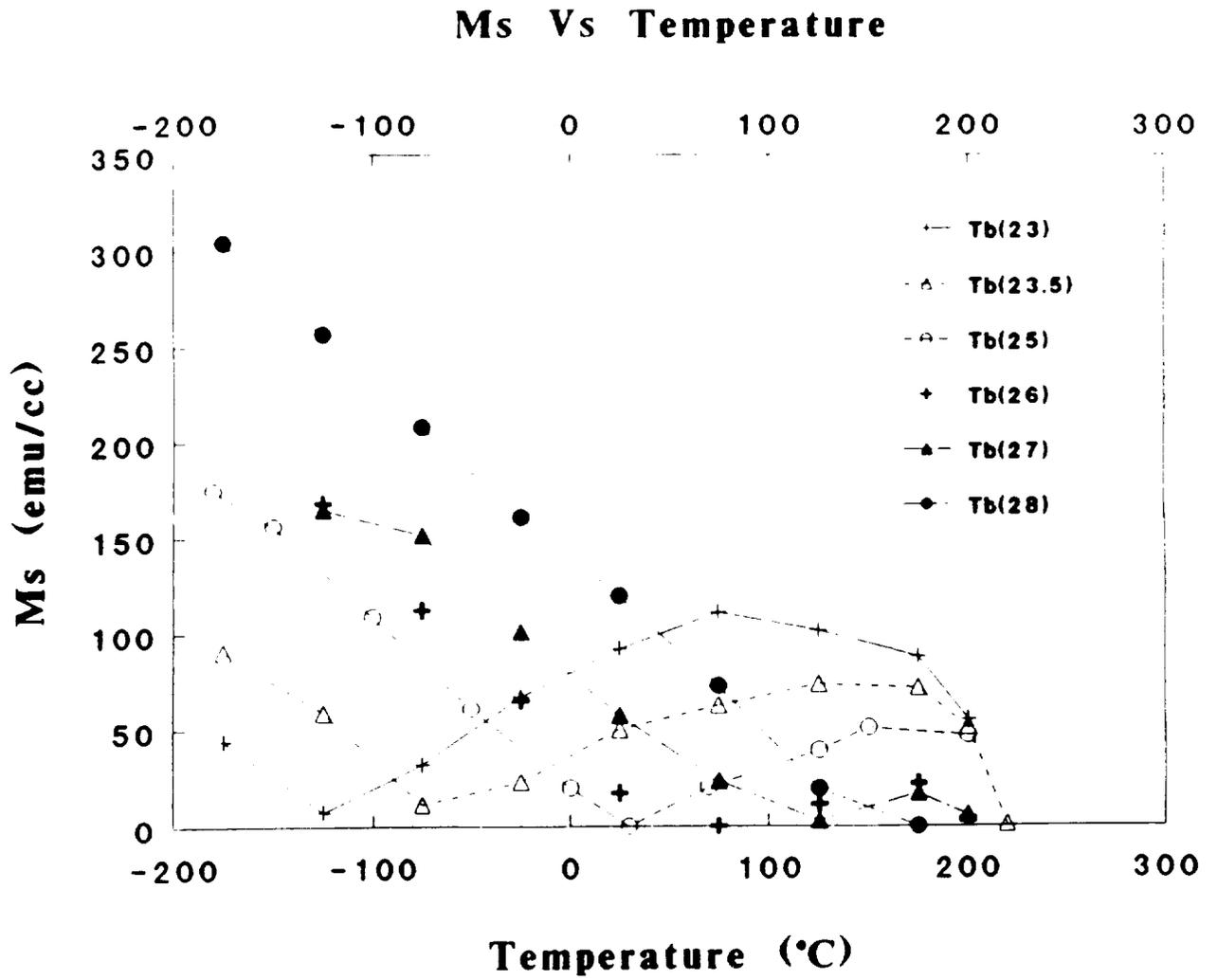
Fig. 17

T$_{Comp}$ and Ms vs Tb at. %

● T$_{Comp}$ ▲ Ms (AT RT)
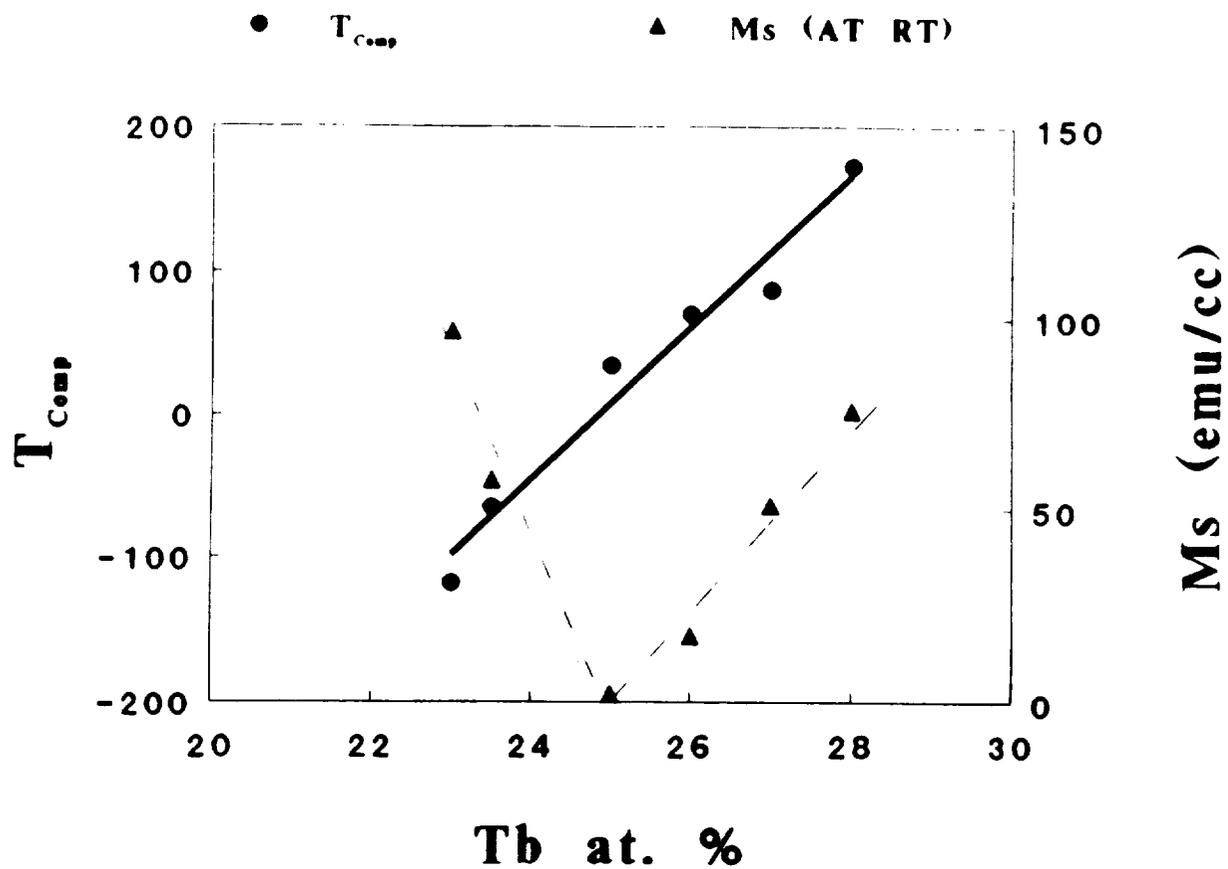
Tb at. %

Fig. 18

K_1 and K_u vs Tb at. %
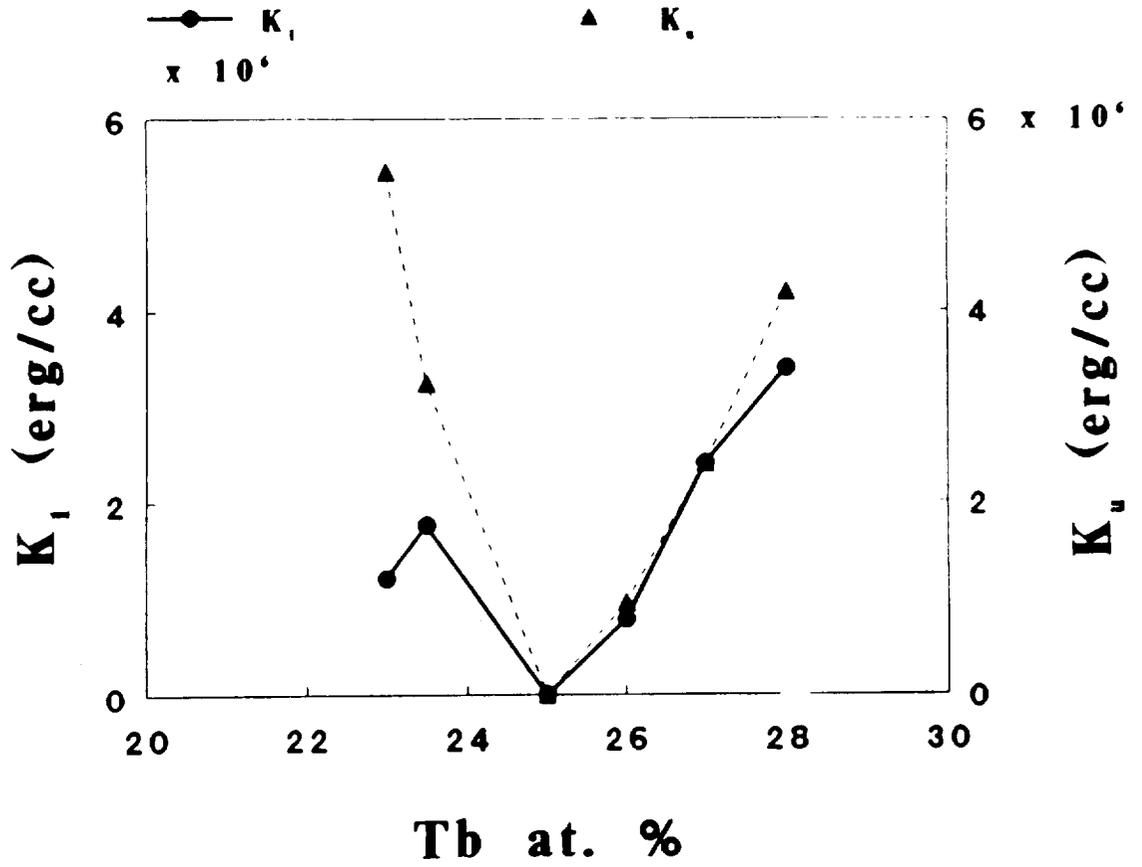
Fig. 19
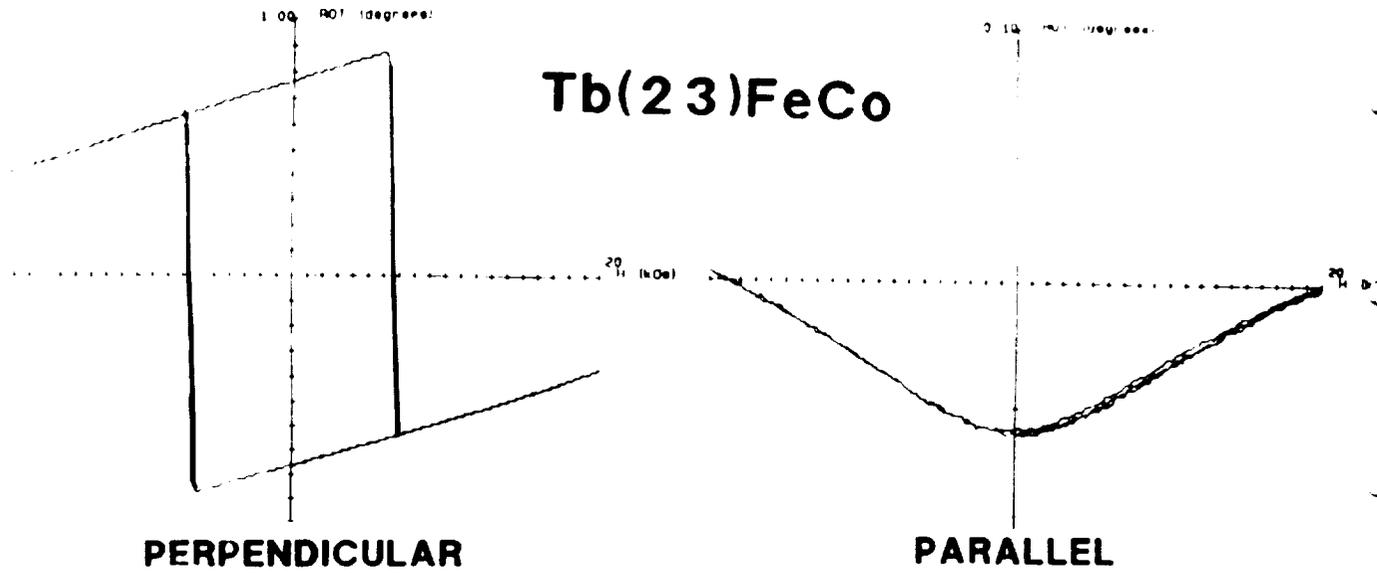
Tb(23)FeCo

PERPENDICULAR   PARALLEL

Experimental and theoretical data

*experimental
−theoretical
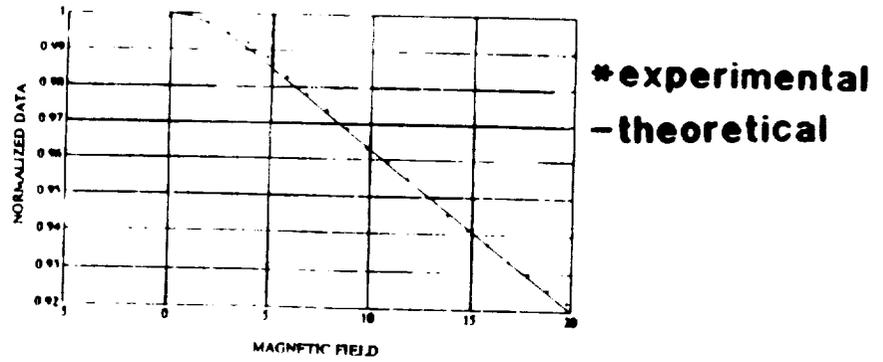
Fig. 20

Θ_k and Hc vs Tb at. %

Fig. 21

Appendix A
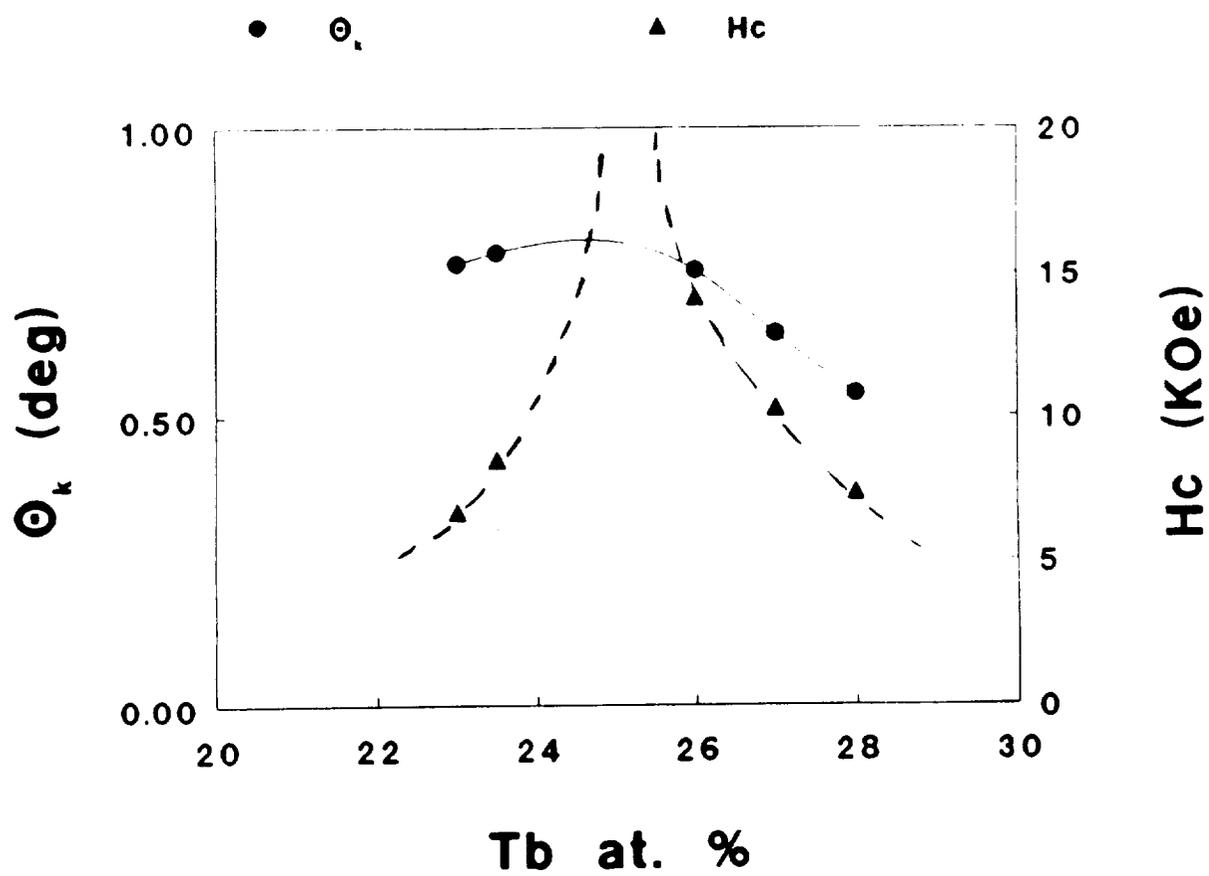
N9 2 - 14904

WAVELENGTH DEPENDENCIES OF THE KERR ROTATION

AND ELLIPTICITY FOR THE MAGNETO-OPTICAL RECORDING MEDIA

Feng Lei Zhou, J. Kevin Erwin, and M. Mansuripur

Optical Sciences Center, University of Arizona, Tucson, AZ 85721

I. INTRODUCTION

Amorphous rare earth-transition metal alloys are the conventional media of erasable optical storage. Recently there has been a flurry of activity in the area of thin film superlattice-type structures, such as Co/Pt and Co/Pd, suggesting that these materials may be used in second generation devices. In both cases, understanding the wavelength dependence of the megneto-optical Kerr rotation and ellipticity is important for the application of these media, as magneto-optical recording has the potential for higher data density at short wavelengths. Also understanding the physics of the magnetooptical interactions is dependent on the availability of accurate measurements of the spectral characteristics of the Kerr rotation and ellipticity[1,2]. In this paper we will present wavelength dependence measurements of Co/Pd and Co/Pt superlattice samples with different compositions. We will explore the relationship between the composition, and magneto-optical spectra. The induced magnetization in the Pt of Co/Pt or in the Pd of Co/Pd samples plays an important role in the magneto-optical activity[3] and it will be discussed for the samples we measured. In section II we present the experimental set up and describe the samples we used. In section III the measurement results of one Co/Pt

sample and a series of Co/Pd samples are discussed. Finally we present conclusions in section IV.

II. Experimental Procedure and Samples

Kerr rotation, ellipticity and reflectivity are measured simultaneously by a novel method of Kerr spectroscopy[1]. The spectral range of measuring system is from 350 nm to 1100 nm and the whole operation is fully automatic. The resolution of the system is about ± 0.005 degrees for Kerr rotation and ± 0.01 degrees for ellipticity.

The Co/Pd samples we used here are made by a sputtering process and have film thicknesses from 5.5 nm to 33 nm. They have a layer structure of 0.2 nm Co and 0.9 nm Pd. All of them are sputtered on glass substrates and have no overcoating. The measurements are done from both the film side and substrate side. All the samples have square hysteresis loops and have coercivity fields between 0.3 KOe and 2.5 KOe. A domain can be written on the 33nm thick samples. Table 1 shows the full list of all the Co/Pd samples. For the Co/Pt sample the composition of the sample is .4 nm Co and 1 nm Pt with a total thickness of 19.1 nm. It has no dielectric overcoating. The hysteresis loop is square for this sample and the coecivity field is 1.5 KOe. Good domains can be written on the sample. Disks made of this sample have a CNR value of 53.5 dB (with dielectric coating). The substrate material is glass.

III. Measurement Results and Discussions

The wavelength dependence of the Kerr rotation, ellipticity and reflectivity always consist of two contributions: one is the interference of the overcoating, the film and the substrate and the other is the electronic structure of the material. The interference effect has been known for years[4] and it plays an important role in enhancement of the magneto-optical signal in practice. To investigate the effect of the electronic structure of the materials, we need to separate these two effects. The material properties are determined by the dielectric tensor while the interference depends on the overcoating, the film and the substrate. For superlattice Co/Pt and Co/Pd samples without dielectric overcoating, it is well known that for samples thinner than 50 nm, there is enough light transmitting through the superlattice film, and the interference effect due to the substrate needs to be taken into account. The spectra for these types of samples are a combination of the substrate interference and the electronic structure of the materials. While for samples with more than 50 nm thickness, the absorption of the materials allows little or no light to transmit through the substrate. Therefore there is no interference effect from the substrate, and the spectra is determined by the electronic structure of the materials only.

The wavelength dependence curves of Kerr rotation, ellipticity and reflectivity for sample 4 of Co(2)/Pd(9) samples are shown in the Fig. 1. This sample is quite thin and the interference has a strong effect on the spectra. This is a typical figure for all the Co(2)/Pd(9) samples we measured in this paper. From this curve we can see some interesting characteristics. The reflectivity curve has a dip between 750 nm and 850 nm range while the Kerr rotation and the ellipticity curves also have a bump and dip respectively in the same range. These phenomena arise from the fact that when more light is trapped in the film, it gives more internal bouncing back and forth, and reflection and the magneto-optical Kerr rotation grows bigger. The ellipticity is quite large and it is negative for very short wavelengths and it becomes positive for longer wavelengths. The error bars on the curves are generated by standard deviation calcualation of several measurements. Fig. 2 is the Kerr rotation curves for all the 6 Co/Pd samples. There are

several points we can draw from this figure. All the samples have similar wavelength dependent shapes and the difference is that the peak Kerr rotation position shifts from about 400 nm for the 33 nm thick film to about 540 nm for the 5.5 nm thick film. This peak shift is purely interference effect and it only depends on the refractive index and absorption coefficient of the material. For 150 nm thick film, there is no interference effect andthe Kerr rotation peak is located at a wavelength less than 350 nm as shown in the Fig. 7 of Ref. 1. The Kerr rotation vs. film thickness for each wavelength can also be seen in this figure. For wavelength below 560 nm the Kerr rotation peak is at thickness of 16.5 nm (curve 3) while for wavelength above 560 nm value, the peak is at thickness of 11 nm (curve 2). The two curves in the Fig. 3 is the Kerr rotation vs. film thickness curve for wavelength of 450 nm and 750 nm respectively. The phenomenon that the peak of Kerr rotation vs. film thickness shifts to thicker film thickness as the wavelength decreases can be explained quanlitatively by interference. For a fixed refractive index n and absortion coefficient k material, as film thickness increases, the corresponding anti-reflection wavelength will decrease and the anti-reflection wavelength is also the peak Kerr rotation wavelength for the reason that the Kerr rotation is inversely proportional to the reflectivity.

Fig. 4 is the ellipticity curves for all the Co/Pd samples. For film thickness increase from 5.5 nm to 33 nm, the ellipticity curve shifts upwards with a little tilt downwards on the long wavelength side. Fig. 5 is the reflectivity curves for all the Co/Pd samples. It is clear that the reflectivity curves are similar for all the different thickness samples and the value increases as the film thickness increases. The interference effect is less pronounced in the reflectivity curves, and only the small drop of relative values on the short wavelength side gives the indication of interference effect. For applications the parameter with more direct relation to the signal-noise-ratio is called the Figure Of Merit (FOM) and it is defined as $\sqrt{R}\sqrt{\theta_k^2 + \epsilon_k^2}$. The wavelength dependence of the FOM for all the Co/Pd samples are plotted in the Fig. 6. From the curves we can see that they

all have the same shape and all the FOM peak at about the same wavelength of 480 nm. The highest FOM for all the wavelength between 350 nm and 1050 nm is the film with 16.6 nm thickness.

We also measured all the Co/Pd samples from the substrate side. The Kerr rotation, ellipticity, reflectivity, and figure of merit curves are shown in Fig. 7, 8, 9, and 10 respectively. From these figures we can see clearly that the interference effect is much smaller than the results from the film side. The reason is that from the substrate side there is a much better index match between the glass and the first layer of the M-O film than from the film side measurement case, in which the matching is between the air and the first layer of the M-O film. The Kerr rotations are higher from the substrate side due to the lower reflectivities from this side. The above differences are purely optical effect and magnetic properties are the same.

Fig. 11 is the Kerr rotation, ellipticity and reflectivity measurement for the Co/Pt sample. Compared with the Co/Pd smples, the Kerr rotation wavelength dependence shape is quite different, which indicates the different inter-layer interactions for these two types of materials. The Kerr rotation values of the Co/Pt sample are much larger than the Co/Pd samples with the same Co content of Co/Pd sample 6. It is very interesting to notice that the wavelength dependence of reflectivity is very similar for the Co/Pt and Co/Pd samples, which indicates that their refractive index and absorption coefficients have similar wavelength dependence.

IV. Conclusions

The wavelength dependence of Kerr rotation, ellipticity and reflectivity for Co/Pd and Co/Pt superlattice samples are measured with a new technique. The series results of differernt thickness of Co/Pd samples clearly show the interference effect on the spectra.

The clear understanding of of the interference effect cleared the way for further investigating the material properties. By getting the wavelength dependence of the refractive index and absorption coefficient and together with the Kerr rotation and ellipticity results, the dielectric tensor can be calculated and the physical properties can be studied directly. Comparing the spectral dependence of the two Co/Pd samples and the Co/Pt samples, we can see that the interactions between the Co layers and the Pd layers are very strong and the magneto-optical properties for the superlattice samples are determined by these inter-layer interactions.

References

1.   F. L. Zhou, J. K. Erwin and M. Mansuripur, to appear in J. Appl. Phys (1991)

2.   D. Weller and W. Reim, Appl. Physics A, 49, 599 (1989)

3.   E. R. Moog, J. Zak, and S. D. Bader, to appear in J. Appl. Phys. (1991)

4.   G. A. N. Connell, Appl. Phys. Lett., 40(3), 212 (1982)

Table 1

| Sample	1	2	3	4	5	6
Composition Co/Pd	2/9	2/9	2/9	2/9	2/9	2/9
Number of Layers	5	10	15	20	25	30
Total Thickness (nm)	5.5	11	16.5	22	27.5	33

Co(2)/Pd(9), 22 nm
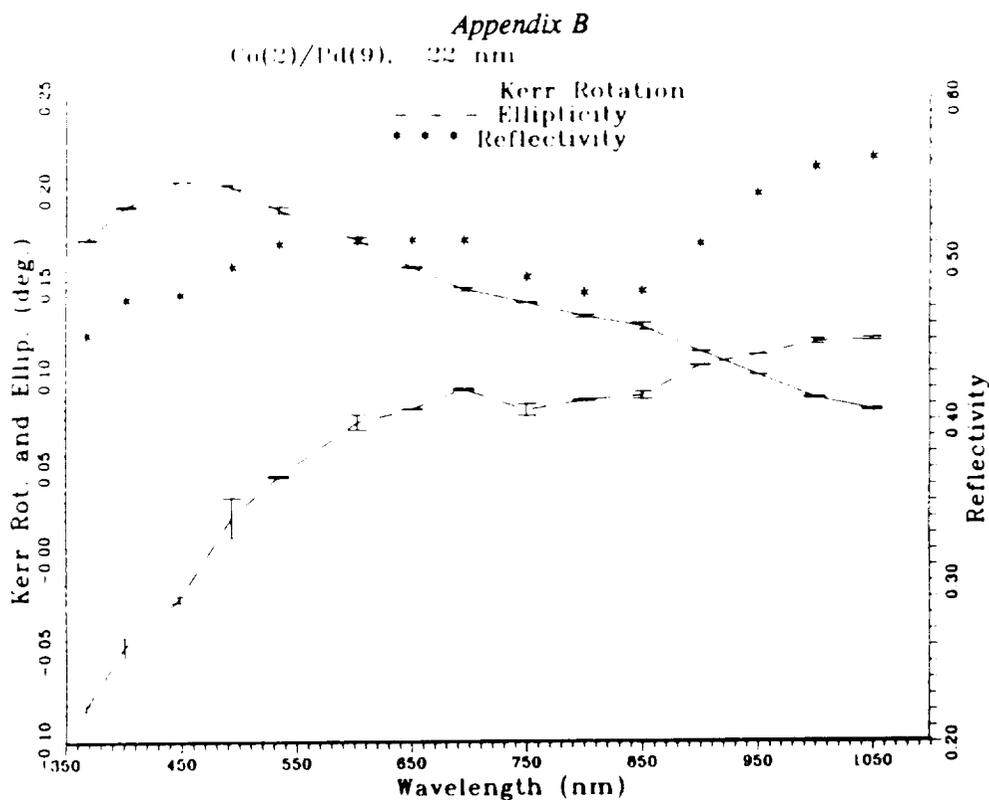
Figure 1. Wavelength dependence of Kerr rotations, ellipticity and reflectivity for Co/Pd sample 4. Solid line is Kerr rotation curve, dashed line is the ellipticity curve, and the "" is the reflectivity curve.

Co(2)/Pd(9), FILM SIDE
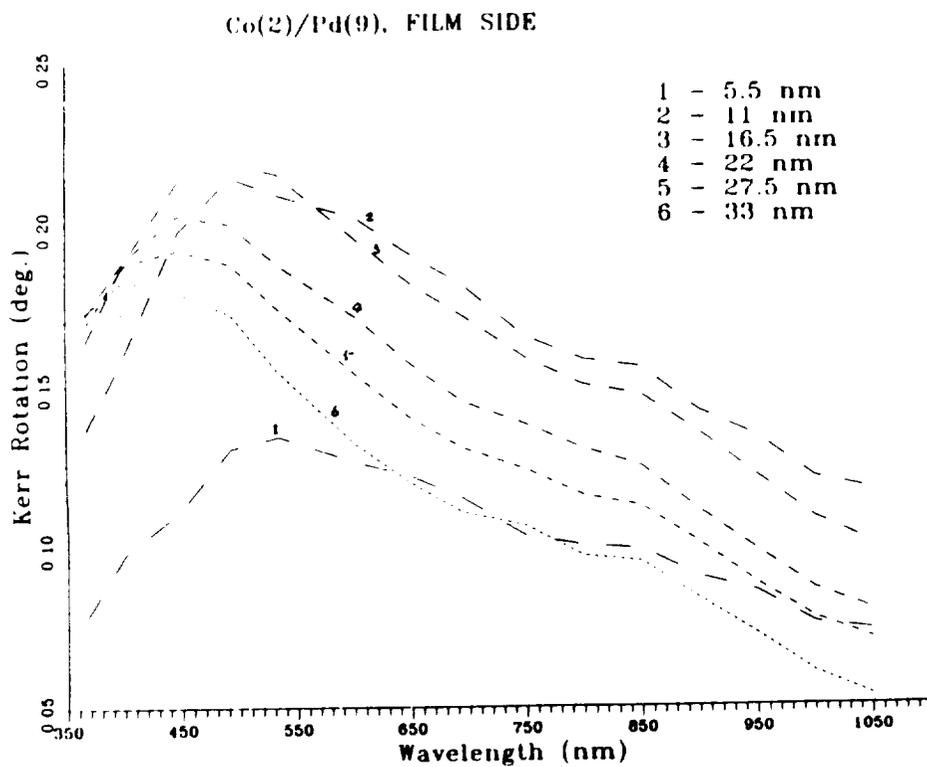
Figure 2. Wavelength dependence of Kerr rotations for the 6 Co/Pd samples, measured from the film side.
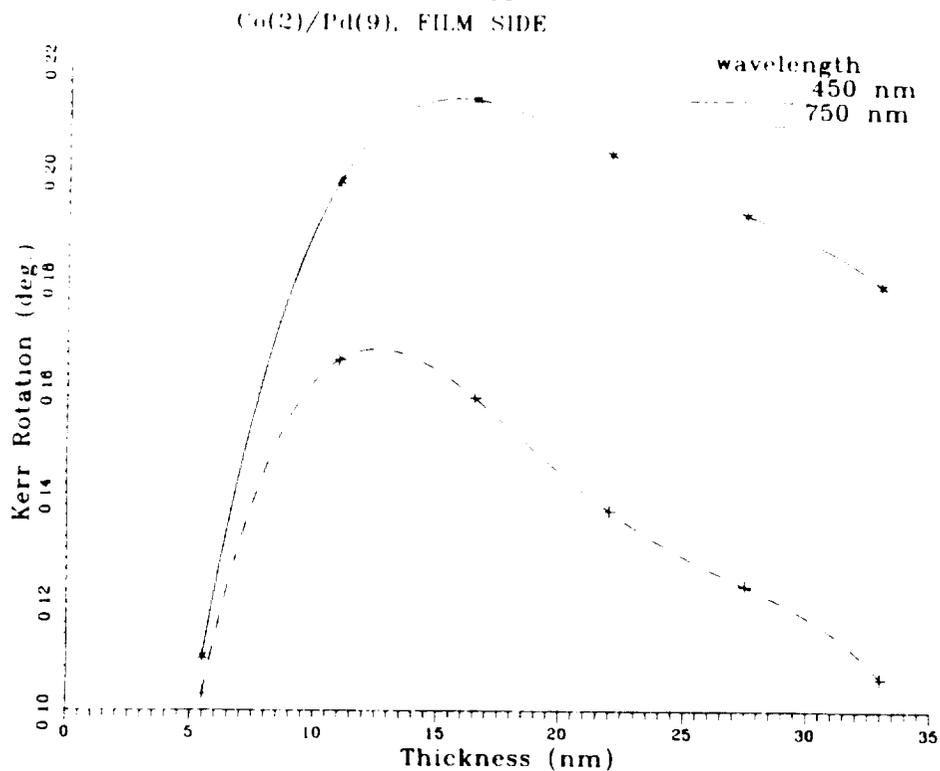
Co(2)/Pd(9). FILM SIDE

Figure 3. Thickness dependence of Co/Pd samples. Solid line is for 450 nm wavelength and dashed line is for the 750 nm wavelength.
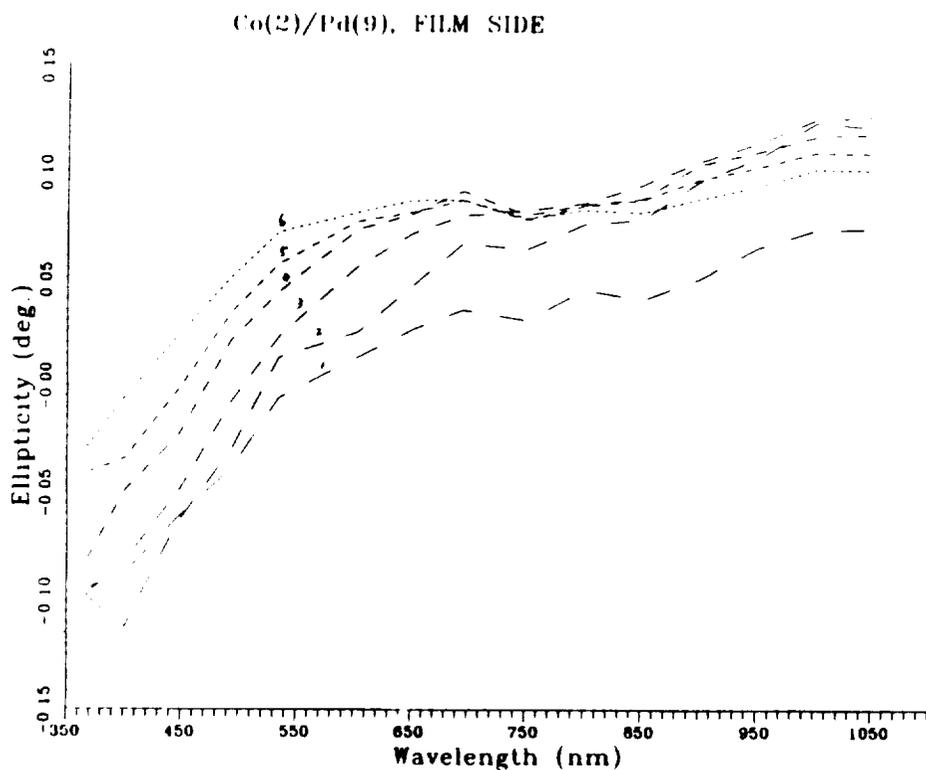
Co(2)/Pd(9). FILM SIDE

Figure 4. Wavelength dependence of ellipticity for the 6 Co/Pd samples, measured from the film side.
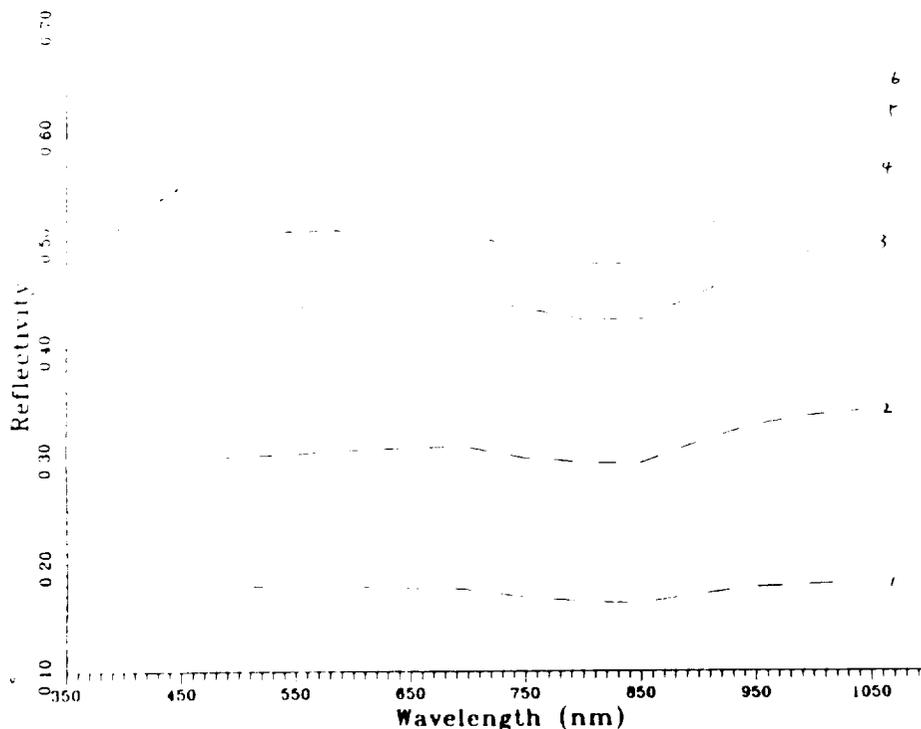
Co(2)/Pd(9), FILM SIDE

Figure 5. Wavelength dependence of reflectivity for the 6 Co/Pd samples, measured from the film side.

Co(2)/Pd(9), FILM SIDE

```
1 - 5.5 nm
2 - 11 nm
3 - 16.5 nm
4 - 22 nm
5 - 27.5 nm
6 - 33 nm
```
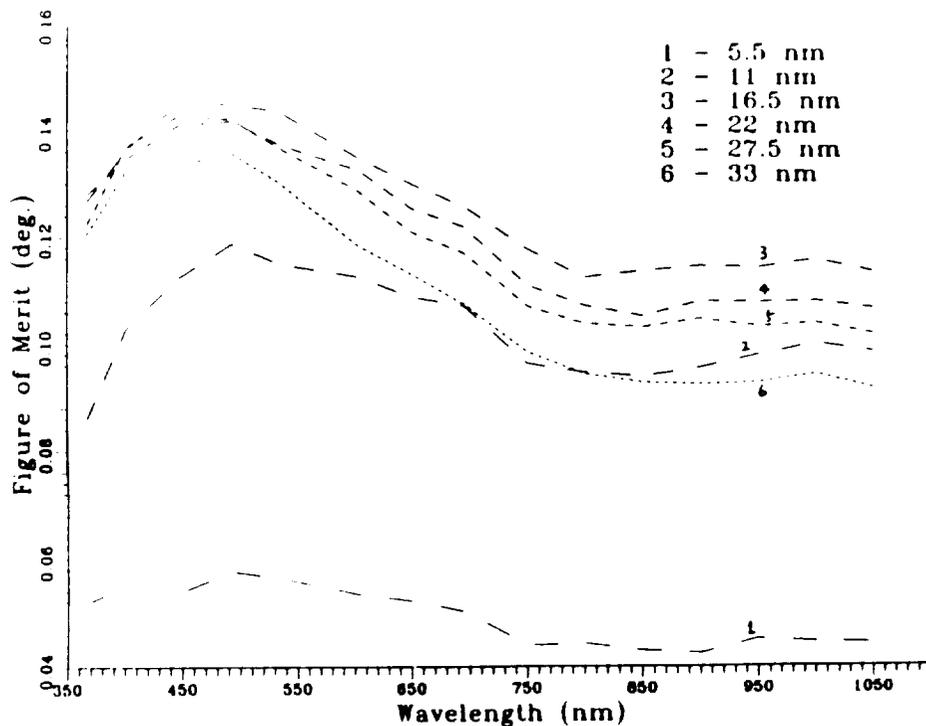
Figure 6. Wavelength dependence of figure of merit for the 6 Co/Pd samples, measured from the film side.

Co(2)/Pd(9). SUBSTRATE SIDE
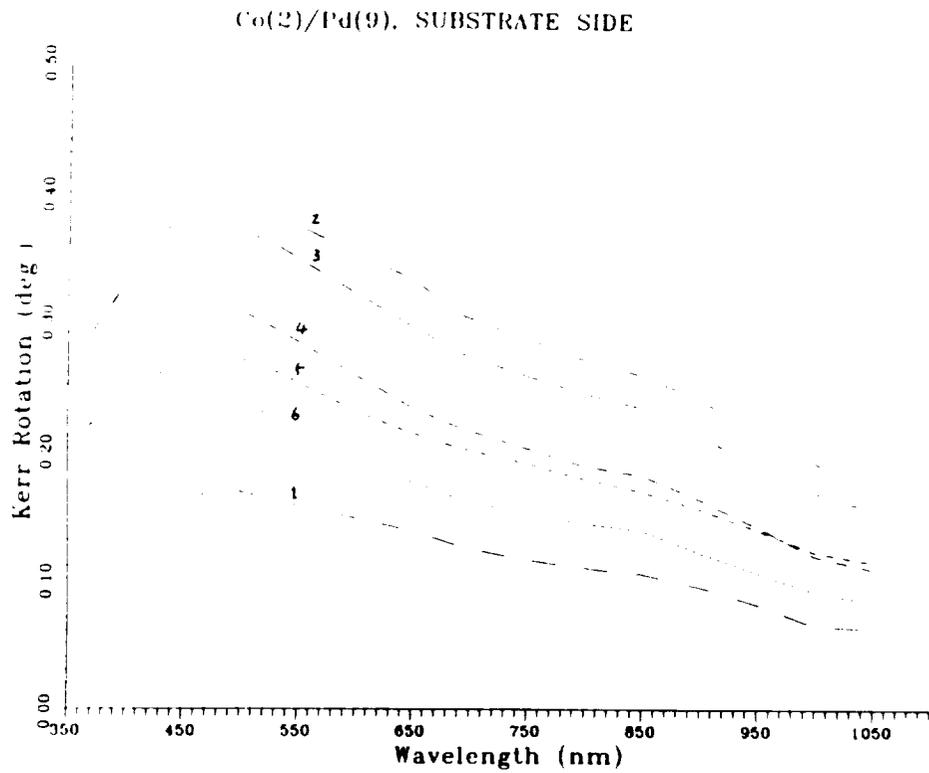
Figure 7. Wavelength dependence of Kerr rotation for the 6 Co/Pd samples, measured from the substrate side.

Co(2)/Pd(9), SUBSTRATE SIDE
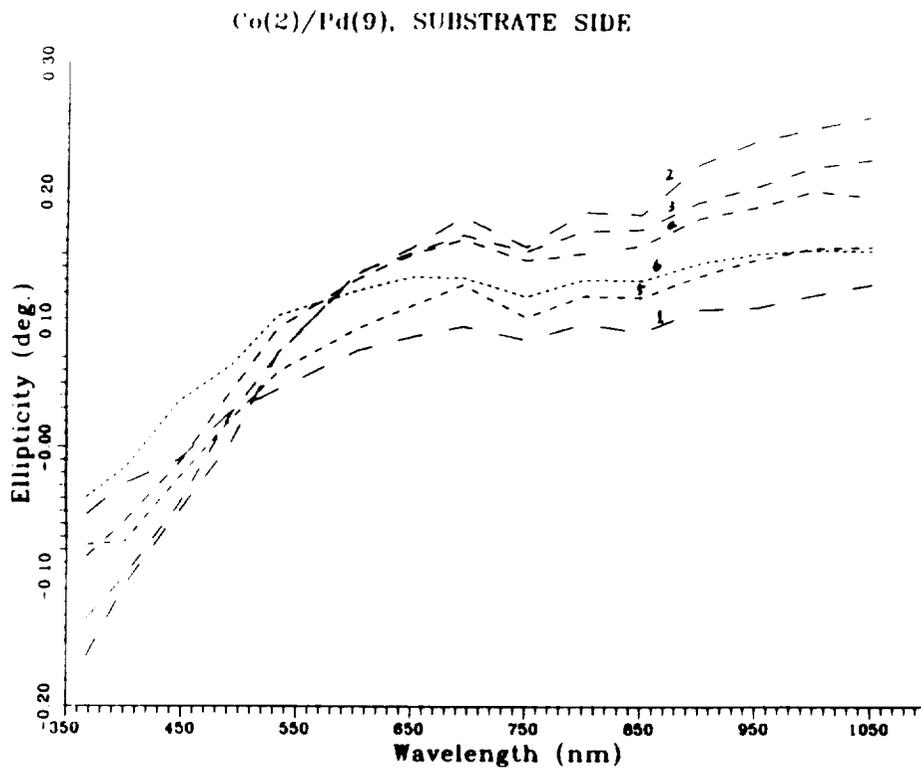
Figure 8. Wavelength dependence of ellipticity for the 6 Co/Pd samples, measured from the substrate side.

Co(2)/Pd(9), SUBSTRATE SIDE
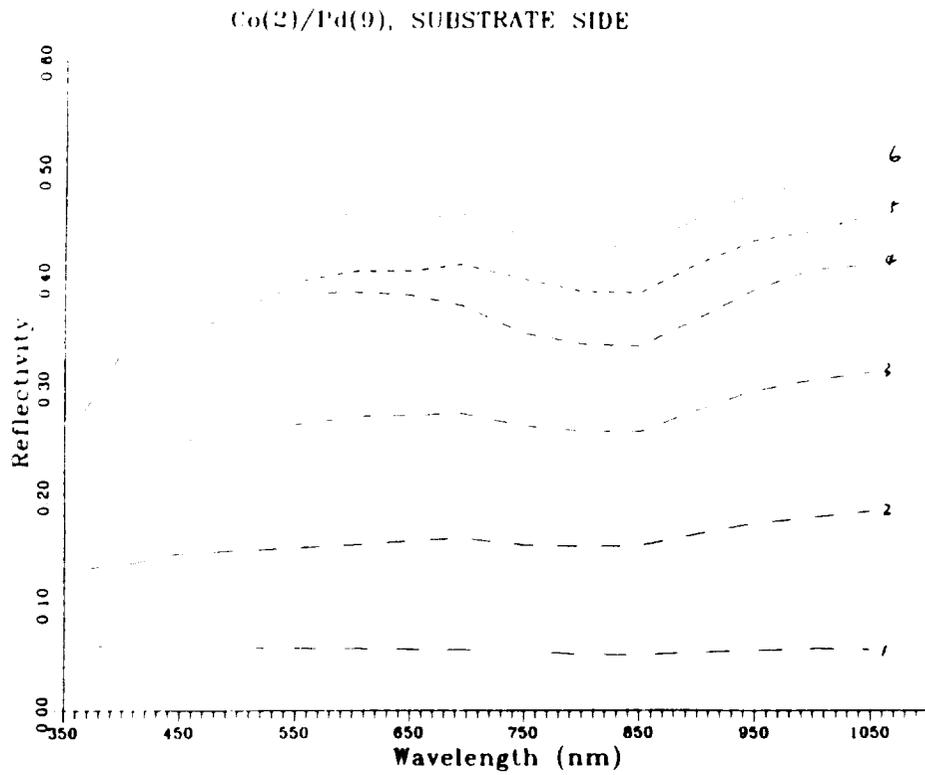
Figure 9. Wavelength dependence of reflectivity for the 6 Co/Pd samples, measured from the substrate side.

Co(2)/Pd(9), SUBSTRATE SIDE
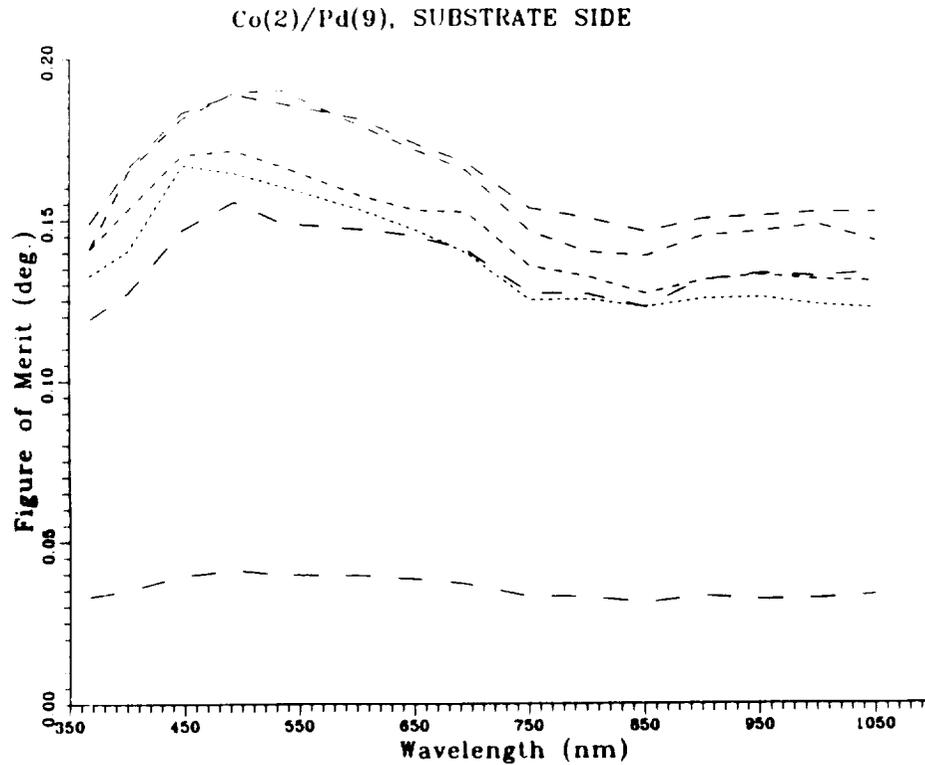
Figure 10. Wavelength dependence of figure of merit for the 6 Co/Pd samples, measured from the substrate side.

Appendix B

Co(1)/Pt(10), 19.1 nm
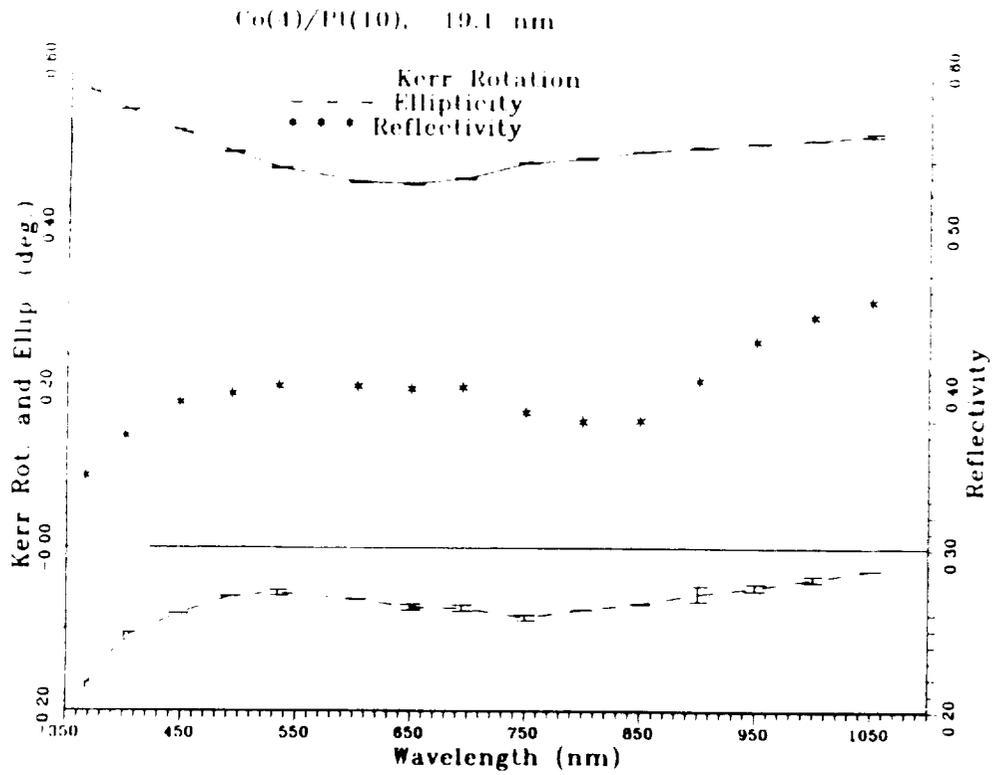

Figure 11. Wavelength dependence of Kerr rotation, ellipticity and reflectivity for Co/Pt sample. Solid line is Kerr rotation curve, dashed line is the ellipticity curve, and the "" is the reflectivity curve.

COMPARISON OF DIFFERENT FRACTAL DIMENSION MEASURING ALGORITHMS FOR RE-TM M-O FILMS

Bruce E. Bernacki and M. Mansuripur

N92-14905

I. INTRODUCTION

As outlined in an earlier paper[1], noise in magneto-optical (M-O) recording devices is classed as that which is system-related (laser, electronic, and shot noise), and that which is media-related. Media noise is rooted in the magnetic and M-O properties of the recording media. The measure of the fractal dimension, D, for domain boundaries was proposed to investigate media noise and its relation to the microstructure and micromagnetics of thin films. Some of the possible sources of domain boundary jaggedness, and hence, different measures of D, might include structural/magnetic inhomogenieties as well as competition between domain wall energy and demagnetization.

Earler work concentrated on the conceptually simple divider method for measuring the fractal dimension, D, of binary images of M-O domains, both circular and line. To review this method, recall Richardson's[2] comparisons of the measurements of the coastlines of Europe. He discovered that when the boundary was measured with rulers of different lengths, substantially different values for the coastline length resulted. If the logarithm of the boundary as a function of ruler length was plotted versus the logarithm of ruler length, the points lay on a line of constant slope, m, that was related to D, the fractal dimension in the following way:

$$D = 1 - m.$$

However, certain films, notably, those which are nucleation-dominated, do not produce images that are particularly well conditioned for application of the divider method. Also, domain structure can occur within the interior of the major domain wall, and this is not measured by the divider method. A two-dimensional technique is clearly required. Two such 2-D techniques that can be employed are the amplitude spectrum method, and the box counting method.

The amplitude method (or power spectrum method) is based on Fourier methods. Using the same binary (or even grey-level) image, the 2-D FFT is computed, with only the amplitude of each frequency component of interest. Then, these frequency amplitudes are averaged for each integer frequency component to form an array of radial wave vectors. The log of amplitude components is then plotted versus the log of the radial wave vectors. A least squares line fit results provides the slope of the line, and D is calculated using the following relationship:

$$D = E + 3.2 + m$$

where E is the Euclidean dimension. The value of one (1) is used for the value of E so that this techniqe can be compared with the divider method.

The box counting method is probably the simplest technique of all. After the binary image is gotten, one slides squares with edge size ϵ through the image. If the box contains any of the domain pixels, the count for the number of boxes is incremented. A plot of the logarithm of image area as a function of box area versus the logarithm of the edge dimension is plotted, and a line fitted to determine its slope. The fractal dimension, D, is then calculated using the equation

$$D = 1 + m.$$

The box counting method was not used in this study.[3]

II. EXPERIMENT

For a group of seven (7) different amorphous, RE-TM magneto-optical thin films, fives images were recorded with different domain radii for each sample, ranging from approximately 40 μm to 120 μm. Then, the fractal dimension, D, for each expansion was measured and averaged using two measurement techniuqes: the divider method, and amplitude spectrum method. An additional metric was utilized, which is termed the local fractal dimension, or local D. In this measurement, a window is moved through the data, and then D is calculated for each window. That is, for a 10 component window, one calculates D for data points 1 through 10, then 2 through 11, 3 through 12, and so on. An average and standard deviation are then found for the data. Typically, the local D is used as a figure of merit to rank the goodness of one's fractal measuring algorithm, with a perfect result being a horizontal line. Here, it is used to compare the average D against that calculated for a specific range of data that was selected after examination of the log-log plot for both techniques. In this way, a less skewed measure of D might be possible, since the influence of the experimenter is greatly reduced. The data for these seven samples is summarized in Table 1. As can be seen in the table, there is good agreement between the local D, and that calculated for a narrow band of data. Figure 1 graphically compares the two approaches of narrowband and average of local D for the two fractal algorithms. In Fig. 1, the sample number corresponds to the numbering in

Table 1. Figure 2 shows representative images of each sample. Figures 3 and 4 are examples of the log-log plots for the divider method and amplitude spectrum method, respectively.

III. CONCLUSION

In general, it appears that either the divider technique or amplitude spectrum technique may be used interchangeably to measure the D inherent in domain wall structure of ideal images. However, some caveats must be observed for best results.

The divider technique is attractive for its simplicity and relatively modest computation requirements. But, it is sensitive to noise, in that noise pixels that touch the domain boundary are interpreted as being part of the boundary, skewing the measurment. Also, it is not useful in measuring nucleation-dominated films or domains that have significant amounts of structure within the interior of the domain wall.

The amplitude spectrum method is more complex, and less intuitive than the divider method, and somewhat more expensive to implement computationally. However, since the camera noise tends to be white, the noise can be avoided in the measurement of D by avoiding that portions of the curve that is flat (due to the white noise) when the least squares line is fit to the plot. Also, many image processing software packages include an FFT facility, while the user will most likely have to write his own edge extraction routine for the divider method. The amplitude spectrum method is a true two-dimensional technique that probes the interior of the domain wall, and in fact, can measure arbitrary clusters of domains. It can also be used to measure grey-level images, further reducing processing steps needed to threshhold the image.

Appendix C

REFERENCES

1. B.E. Bernacki and M. Mansuripur, *J. Apl. Phys.*, **69** (1), 1991.

2. B.B. Mandelbrot, *The Fractal Geometry of Nature* (W.H. Freeman, New York, 1983).

3. The box counting method is not sensitve to the structure in domain walls for binary images of domains that are predominately black. This is due to the small precentage of the total image that the domain wall represents, and thus is dwarfed by the dominant morphology, which is that of a round black domain.

Table 1

SAMPLE No.	Ruler ⟨D⟩ Local ⟨D⟩	Spectral ⟨D⟩ Local ⟨D⟩
1 12990G $Tb_{18.3}Fe_{74.5}Ar_{7.2}$	$1.293 \pm .027$ $1.279 \pm .011$	$1.288 \pm .022$ $1.309 \pm .024$
2 12490B $Tb_{28.1}Fe_{71.9}$	$1.281 \pm .040$ $1.284 \pm .050$	$1.272 \pm .047$ $1.318 \pm .031$
3 12990B $Tb_{24.1}Fe_{76.0}$	$1.095 \pm .005$ $1.086 \pm .007$	$1.129 \pm .011$ $1.113 \pm .019$
4 12990A $Tb_{22.5}Fe_{77.6}$	$1.015 \pm .006$ $1.016 \pm .006$	$1.037 \pm .003$ $1.045 \pm .012$
5 830 $Tb_{17.2}Fe_{60.3}Co_{7.4}Ar_{15.2}$	$1.051 \pm .006$ $1.052 \pm .009$	$1.054 \pm .009$ $1.081 \pm .009$
6 821 $Tb_{23.4}Fe_{57.6}Co_{8.5}Ar_{10.5}$	$1.149 \pm .014$ $1.151 \pm .018$	$1.099 \pm .011$ $1.134 \pm .003$
7 819 $Tb_{22.9}Fe_{58.4}Co_{9.4}Ar_{9.3}$	$1.163 \pm .024$ $1.187 \pm .041$	$1.118 \pm .030$ $1.188 \pm .081$

TABLE 1.
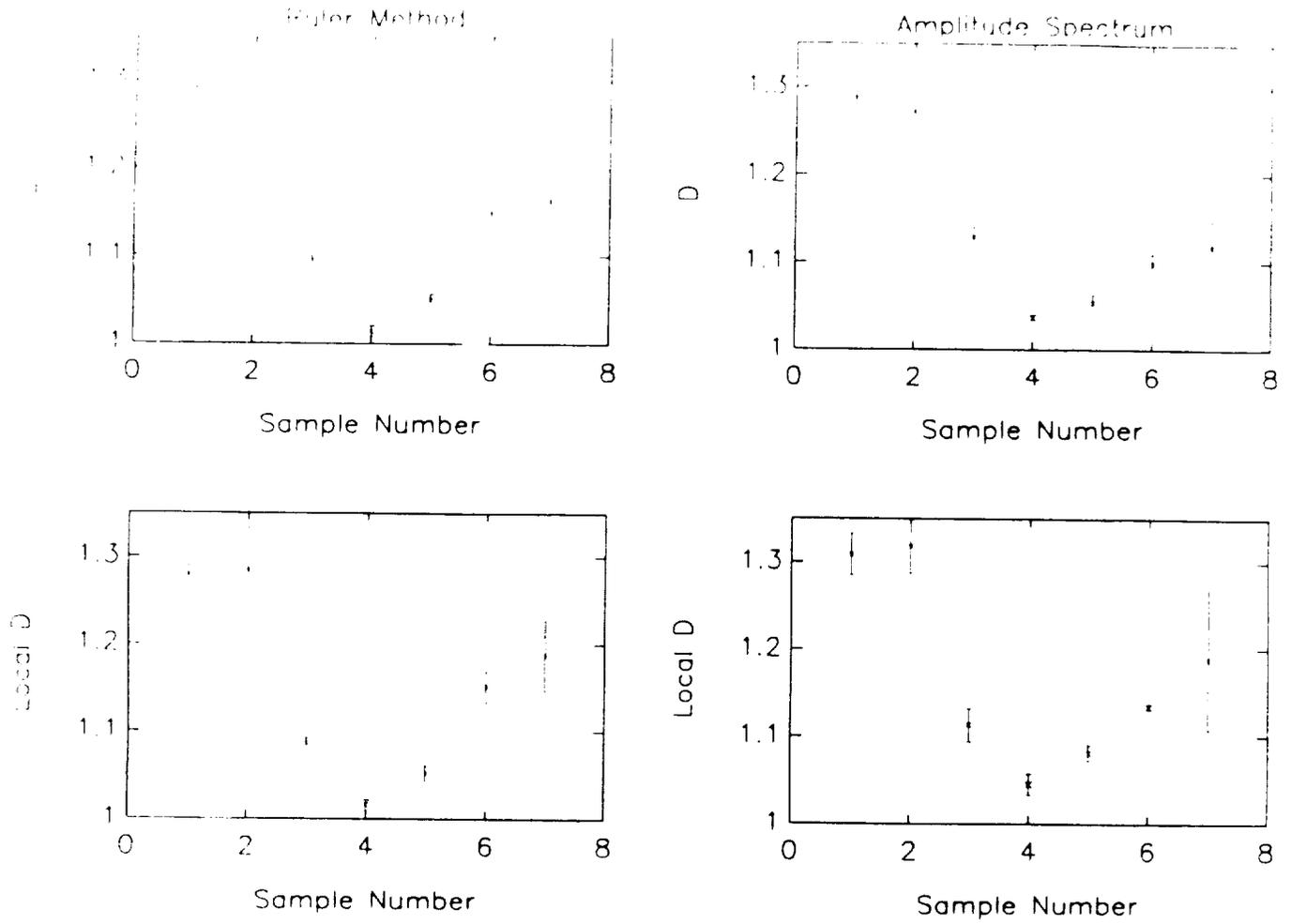
Fig. 1

Figure 2. Example images of samples used in the comparison study.
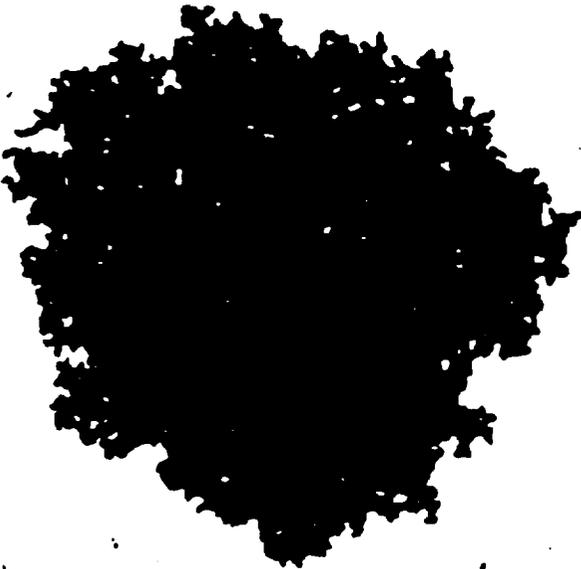
12990A
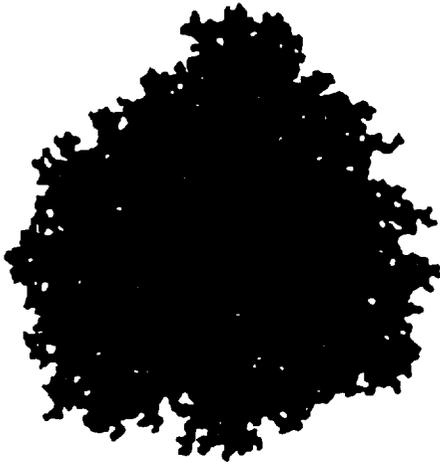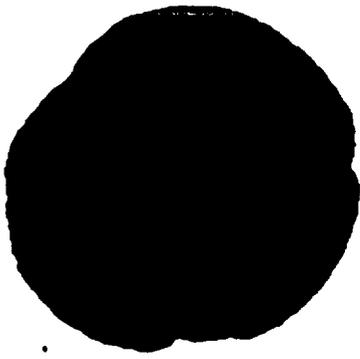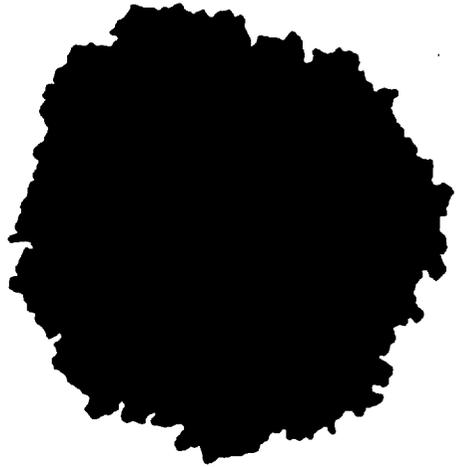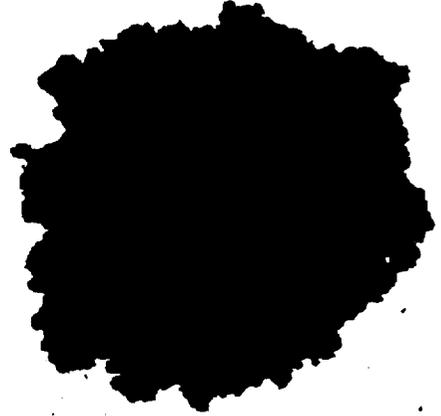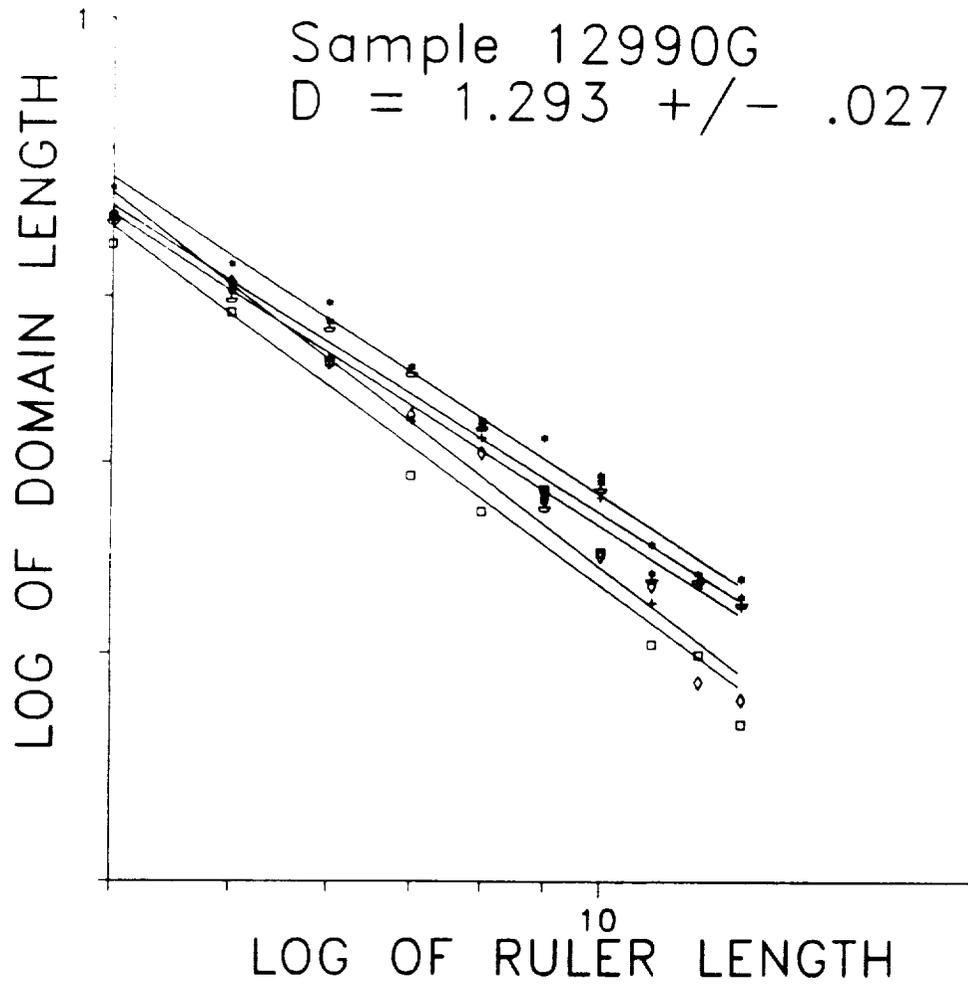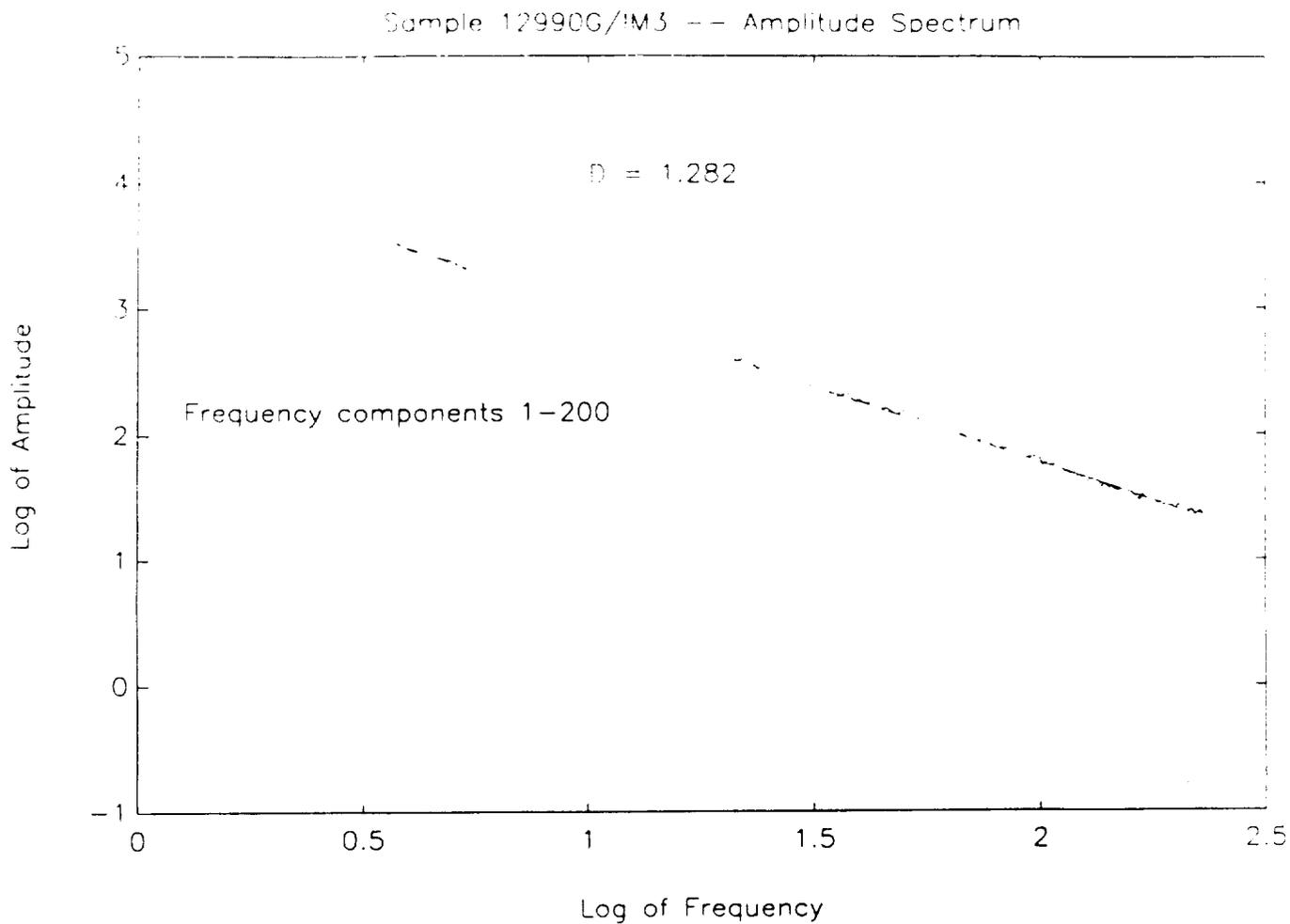
12990B

819

12490B

821

12990G

830

Fig. 3

Sample 12990G/!M3 -- Amplitude Spectrum

D = 1.282

Frequency components 1-200

Fig. 4

Appendix C

Review ✕✕✕✕✕✕✕✕✕✕✕✕✕✕✕✕✕✕✕✕ Micromagnetics

Coercivity of Domain Wall Motion in Thin Films of Amorphous Rare Earth–Transition Metal Alloys

M. Mansuripur,* R. C. Giles** and G. Patterson**

*Optical Sciences Center. University of Arizona. Tucson. Arizona 85721
**College of Engineering. Boston University. Boston. Massachusetts 02215

Computer simulations of a two-dimensional lattice of magnetic dipoles are performed on the Connection Machine. The lattice is a discrete model for thin films of amorphous rare earth-transition metal alloys, which have application as the storage media in erasable optical data storage systems. In these simulations the dipoles follow the dynamic Landau-Lifshitz-Gilbert equation under the influence of an effective field arising from local anisotropy. near-neighbor exchange. classical dipole-dipole interactions. and an externally applied field. Various sources of coercivity. such as defects and or inhomogeneities in the lattice, are introduced and the subsequent motion of domain walls in response to external fields is investigated.

Key words: coercivity. magnetization reversal

1. Introduction

Magnetization reversal in thin films of amorphous rare earth–transition metal (RE-TM) alloys is of considerable importance in erasable optical data storage.[1~13] The success of thermomagnetic recording and erasure depends on the reliable and repeatable reversal of magnetization in micron-size areas within the storage medium. A major factor usually encountered in descriptions of the thermomagnetic process is the coercivity of the magnetic medium. Coercivity, however, is an ill-defined concept generally used in the phenomenology of bulk reversal, but its usefulness and relevance to the phenomena occurring on the spatial/temporal scales of thermomagnetic recording are seriously in doubt. To begin with. there is the problem of distinguishing nucleation coercivity from the coercivity of wall motion. Then there is the question of speed and uniformity of motion as the wall expands beyond the site of its origination. Finally one must address the issues of

stability and erasability—also intimately related to coercivity—in a framework wide enough to allow the consideration of local instability and partial erasure. It is fair to say that the existing models and or theories of coercivity[14~31] are generally incapable of handling the problems associated with thermomagnetic recording and erasure. In our view. the natural vehicle for conducting theoretical investigations in this area is dynamic computer simulations based on the fundamental concepts and equations of micromagnetics. We have conducted several such studies in the past[32~35] and have succeeded in clarifying some of the issues involved in the nucleation stage of the magnetization reversal process. Also treated in these studies were the dynamics of wall motion in homogeneous media. The purpose of the present paper is to investigate the coercivity of wall motion at the submicrometer scale and in the presence of defects and or inhomogeneities, using large scale computer simulations.

The simulations were performed for a two dimensional hexagonal lattice of magnetic dipoles following the Landau-Lifshitz–Gilbert equation.[36] In addition to interacting with an externally applied field. the dipoles were subject to effective fields arising from local uniaxial anisotropy. nearest neighbor exchange. and long range dipole-dipole interactions. Details of the micromagnetic model have been previously published[32, 37~39] and will not be repeated here. Suffice it to say that the massive parallelism of the Connection Machine on which these simulations were performed. together with the fast Fourier transform algorithm[37, 38] which was used to compute the demagnetizing field. enabled us to accurately simulate a large (256 · 256) hexagonal lattice of dipoles.

J. Mag. Soc. Japan. Vol. 15, No. 1. 1991

17

Since the lattice constant was chosen to be 10Å in these simulations, the total area of the lattice corresponds to a section of the magnetic film with dimensions L_x = 0.256 μm, L_y = 0.222 μm. Periodic boundary conditions were imposed on the lattice in both X and Y directions, but the film thickness along Z was finite and the magnetization distribution in this direction was assumed to be uniform.

In a previous paper where nucleation of reverse-magnetized domains was under consideration, it was shown that the fields required to initiate the reversal process in a uniform material are generally higher than those observed in practice. Various submicron-size "defects" were then introduced in the magnetic state of the lattice and the values of nucleation coercivity corresponding to different types, sizes, and strengths of these "defects" were computed. Voids, for instance, were found to have an insignificant effect on the value of the nucleation field, but reverse-magnetized seeds, formed and stabilized in areas with large local anisotropy, could substantially reduce the nucleation coercivity. Similarly, the presence of spatial variations in the magnetic parameters of the material, such as random axis anisotropy, was found to affect the coercivity of nucleation.

Random spatial fluctuations and structural/magnetic defects also create barriers to domain wall motion. These barriers are overcome only when sufficiently large magnetic fields (in excess of the so-called wall motion coercivity) are applied. Simulations reveal that wall coercivity in amorphous RE-TM alloy films is generally less than the corresponding nucleation coercivity. This finding is in agreement with the experimentally observed square shape of the hysteresis loops in these media. The strength of wall coercivity, of course, depends on the type and size of fluctuations and/or defects. The results reported in the next section are intended to clarify some of these relationships.

Magnetization-pattern-displays in this paper utilize a color coding scheme. Since the magnitude of the magnetization vector M will be fixed throughout the lattice, the *Color Sphere* is used to represent its local orientation. The Color Sphere is white at its
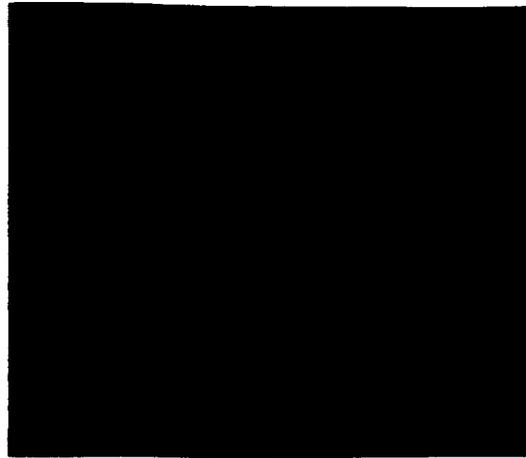
Fig. 1 The *Color Circle* is used to encode the direction of magnetization in the plane of the lattice. In this scheme a red pixel is associated with local magnetization direction along $-X$, light green corresponds to $-Y$, blue to $-X$, and purple to $-Y$. When a vector is not completely in the plane of the lattice, but has a perpendicular component along $-Z$ (or $-Z$), its associated color is obtained by mixing the color of its in-plane component with a certain amount of white (or black), the strength of white (or black) depending on the magnitude of the vertical component. A vector fully aligned with the $-Z$ direction is shown by a white pixel, while a vector in the $-Z$ direction is displayed as black.

north pole, black at its south pole, and covers the visible spectrum on its equator in the manner shown in Fig. 1. As one moves from the equator to the north pole on a great circle, the color pales, *i.e.*, it mixes with increasing amounts of white, until it becomes white at the pole. Moving towards the south pole has the opposite effect as the color mixes with increasing amounts of black. Thus, when the magnetization vector at a given site is perpendicular to the plane of the lattice and along the positive (negative) Z axis, its corresponding pixel will be white (black). For M in the plane of the lattice the pixel is red when pointing along $-X$, light green along $-Y$, blue along $-X$, and purple along $-Y$. In the same manner, other orientations of M map onto the corresponding color on the Color Sphere.
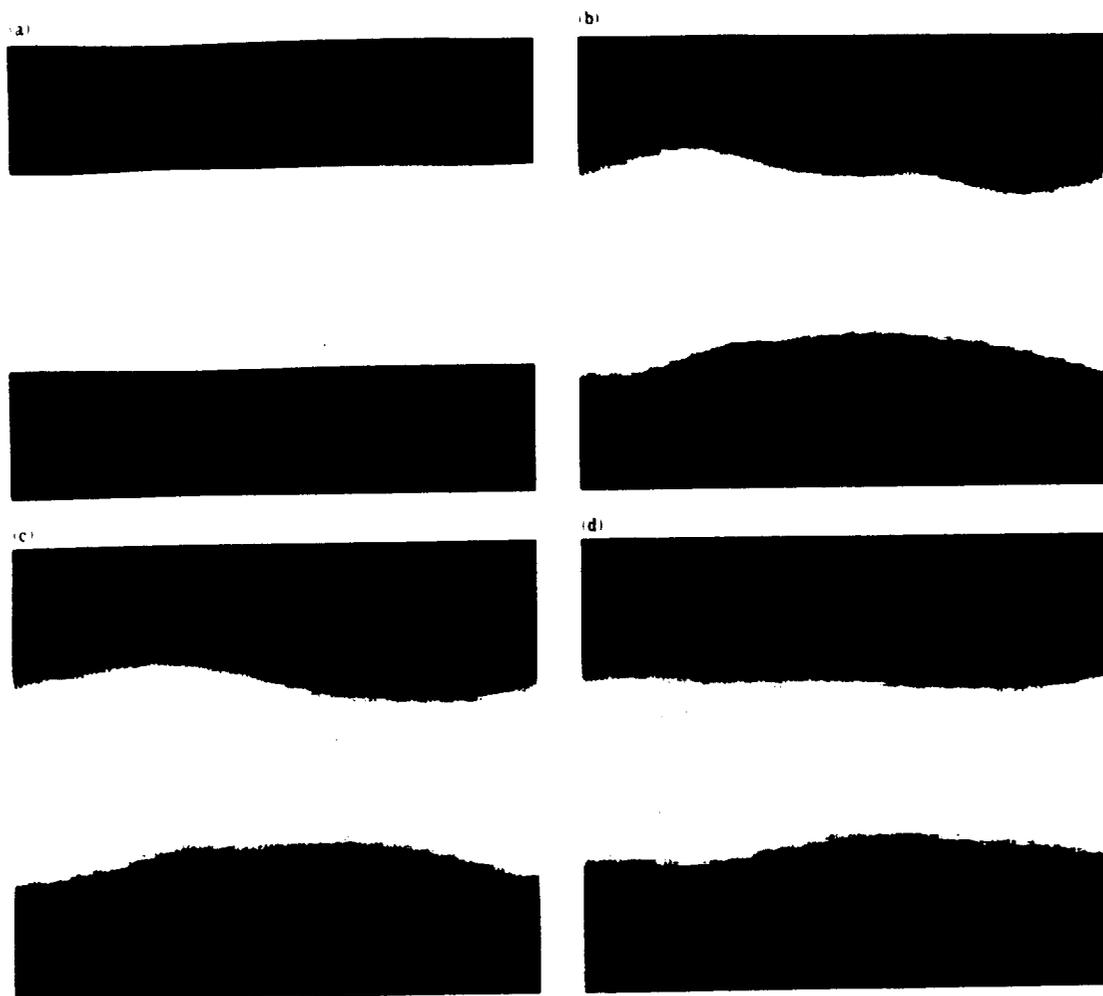
Fig. 2 Formation of domain walls in a medium with random axis anisotropy (cone angle $\Theta = 45°$) and in the absence of an applied field. (a) Dipoles in the white region are initialized along $+Z$, while dipoles in the dark region are initialized along $-Z$. (b) The state of the lattice at $t = 0.8$ ns. Each wall contains three vertical Bloch lines (VBLs) at this stage. (c) The state of the lattice at $t = 1.7$ ns. The number of VBLs has not changed since the previous frame, but they have moved along the walls. (d) The steady state of the lattice at $t = 4.56$ ns. The number of VBLs in each wall is still three.

2. Structure and Motion of Domain Walls

The following set of parameters (used in all simulations reported in this paper) are typical of amorphous films of TbFeCo used in magneto-optical recording: saturation magnetization $M_s = 100$ emu/cm^3, anisotropy energy constant $K_u = 10^6$ erg/cm^3, exchange stiffness coefficient $A_x = 10^{-7}$ erg/cm, film thickness $h = 500$Å, damping coefficient $\alpha = 0.5$, and gyromag-

netic ratio $\gamma = -10^7$ Hz/Oe. In subsequent discussions the term "random axis anisotropy" is meant to imply that the anisotropy axes of the lattice are distributed randomly and independently among the lattice cells (or among various groups of these cells). By keeping the deviation angle θ of the anisotropy axis from Z below a certain maximum angle Θ, the random assignment of axes preserves the perpendicular nature of the overall anisotropy. Thus θ is

19
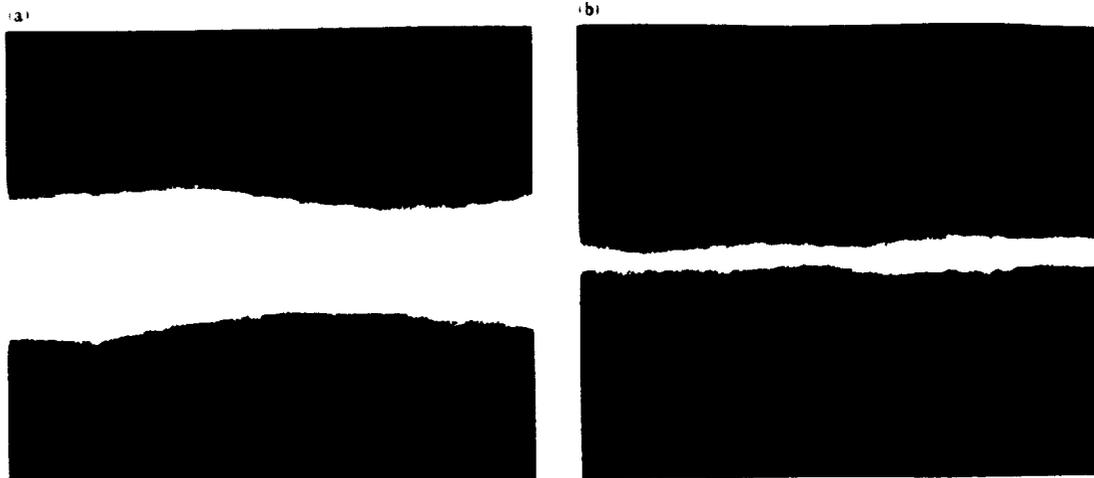
Fig. 3 Collapse of the stripe domain depicted in Fig. 2(d) under the external field $H_t = 1000$ Oe. Frames (a) and (b) show the state of the lattice at $t = 0.96$ ns and $t = 3.58$ ns, respectively.

**Fig. 4** Patchy lattice with 346 patches. Colors are used solely for the purpose of identification of different patches, otherwise they have no meaning or significance.

selected with equal probability from the values in the interval [0, Θ]; for brevity, Θ will be referred to as the *cone angle* in this paper. No constraints are imposed on the distribution of the azimuthal angle ϕ and its values are therefore selected (also randomly and independently) from the interval [0, 360°]. It is perhaps worth mentioning at this point that the random assignment of the axes of anisotropy to individual dipoles does not automatically result in rapid

variations of the direction of magnetization in space. In fact, the strong exchange field in our simulations gives rise to a smooth distribution of the magnetization vector across the lattice, even when large cone angles are involved.

Figure 2 shows the structure of domain walls in a uniform medium with the aforementioned set of parameters. The lattice for this set of simulations had random axis anisotropy over individual cells with a cone angle of $\Theta = 45°$, that is, the axis of local anisotropy was selected randomly for each cell of the lattice with $\theta \in [0, 45°]$, $\phi \in [0, 360°]$, and the values of θ and ϕ chosen for one cell were independent of those selected for all the other cells. Initially the central band of the lattice was magnetized in the $-Z$ direction while the remaining part was magnetized in the $-Z$ direction, as shown in Fig. 2(a). When the lattice was allowed to relax for 0.8 ns, the pattern in Fig. 2 (b) was obtained. Notice that there are three vertical Bloch lines (2π VBLs) in each wall and that the walls are no longer straight. By allowing the lattice to relax for another 0.9 ns we obtained the pattern of Fig. 2(c), which shows significant VBL movements along the walls. Finally, Fig. 2(d) shows the steady state situation at $t = 4.56$ ns. Both walls are now straightened considerably, but the number of VBLs in each wall has not changed; no amount of relaxation can unwind a 2π Bloch line.

A perpendicular field H_z 200 Oe. applied to the state of Fig. 2(d), moves the walls somewhat closer to each other, but fails to eliminate them. The force of demagnetization apparently opposes the external field in collapsing the reverse-magnetized stripe. The domain will collapse, however, under an applied field of H_z 1000 Oe, as shown in Fig. 3. Frames (a) and (b) in this figure correspond, respectively, to t 0.96 ns and t 3.58 ns, where t is the elapsed time since the application of the field. Although not shown in this figure, the walls proceeded to collide and annihilated each other at a later time.

In the above example the randomness in the lattice parameters is clearly too weak to cause significant coercivity for the wall motion. To remedy this problem, we increased the fluctuations' correlation length by introducing large patches, that is, patches whose dimensions are large compared to the width of the domain wall. Figure 4 shows a typical lattice covered with 346 patches of random shape and size. These patches were created by selecting at random a number of lattice sites as seeds, and growing outward from them (in a random fashion) until every site in the lattice belonged to one patch or another. By assigning different attributes to different patches one can thus create spatial variations in the structure magnetic properties of the lattice over length ales comparable to the average patch size.

Figure 5(a) shows a stripe of reverse magnetization in the patchy lattice of Fig. 4. For the sake of clarity, the boundaries of the patches are highlighted in the figure. Each patch is assigned an axis of anisotropy, randomly and independently of all the other patches, with a cone angle of $\Theta = 45°$. The walls in Fig. 5 are somewhat more jagged than those in Fig. 2, where the patches were essentially the size of an individual lattice cell. Under an applied field of $H_z = -1.5$ kOe the walls in Fig. 5(a) moved slightly and then came to equilibrium as shown in Fig. 5(b). A plot of $\langle M_z \rangle$, the average magnetization of the lattice along the Z axis, *versus* time is shown in Fig. 5(c). This plot indicates that the initial $\langle M_z \rangle$, which is slightly above zero, has increased to about 20% of its saturation value in the first 0.5 ns after the application of the field, but has stopped growing at the point. Compare this

situation with that depicted in Figs. 2 and 3, where 1 kOe of field was sufficient to annihilate the walls. Clearly it is the presence of patches and not the demagnetizing force which is responsible for blocking the wall motion. Thus the wall motion coercivity has increased as a result of increased correlation among the local easy axes. When the field was further increased to H_z 2 kOe, it became possible to push the walls beyond the barriers and force them to collide and disappear. (Because of the periodic boundary condition, the walls collide after wrapping around the lattice.) Figure 5(d) shows an advanced state of domain expansion under the 2 kOe field (t 1.154 ns). Note that the lower wall has remained almost intact, while the upper wall has moved substantially. The plot of M_z *versus* time in Fig. 5(e) starting with the application of the 2 kOe field reveals that the movement is slow in the beginning, as the field struggles to overcome the pinning of the walls. Once released, the wall moves rapidly for a period of about 1 ns until either another pinning occurs or the demagnetization force begins to push the walls apart (remember the periodic boundary condition). In any event, the motion slows down at $t = 1.2$ ns and the growth rate of M_z drops by nearly a factor of 2. The walls, however, continue to move out, wrap around at the boundary, and eventually annihilate.

In order to understand the effect of patch size on coercivity, we repeated the preceding simulation for another lattice which had the same set of parameters as the lattice in Fig. 5, but whose total number of patches had increased to 1300. Again we found that $H_z = 1.5$ kOe could not move the walls significantly, but that $H_z = 2$ kOe could. It is probably safe, therefore, to assert that the average size of the patch does not affect the coercivity in a substantial way, so long as it is larger than the characteristic width of the domain wall in the given medium.

Figure 6(a) shows another strip of reverse magnetization in the patchy lattice of Fig. 4. This time, however, a few of the patches have been made void by assigning the value of zero to their magnetic parameters. These void patches are shown as gray regions in the figure. (No special property is assumed
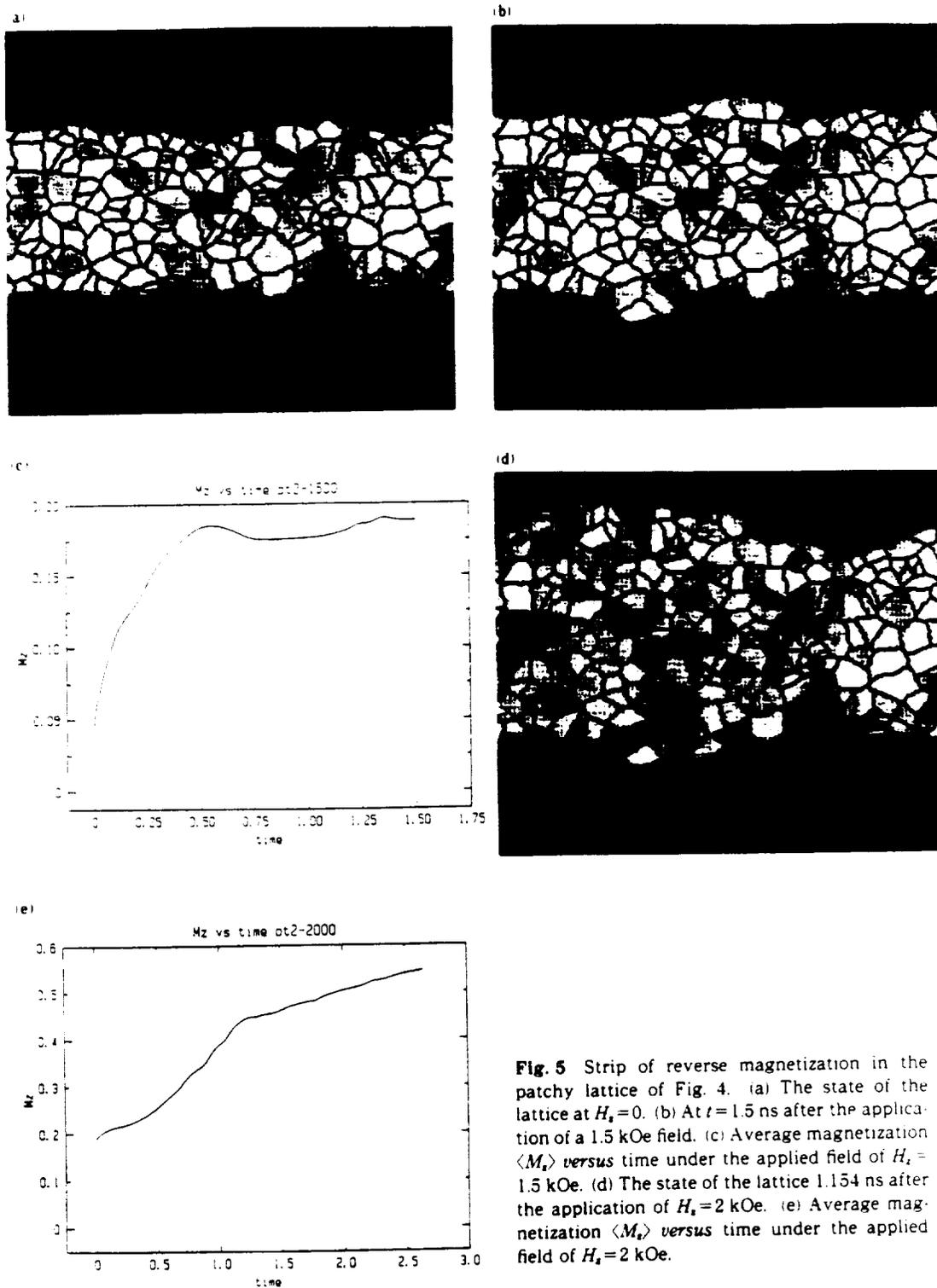
Fig. 5 Strip of reverse magnetization in the patchy lattice of Fig. 4. (a) The state of the lattice at $H_a=0$. (b) At $t=1.5$ ns after the application of a 1.5 kOe field. (c) Average magnetization $\langle M_t \rangle$ *versus* time under the applied field of $H_t=1.5$ kOe. (d) The state of the lattice 1.154 ns after the application of $H_a=2$ kOe. (e) Average magnetization $\langle M_t \rangle$ *versus* time under the applied field of $H_a=2$ kOe.

(a)

(b)

(c)

Energy vs. time hkl-a-0
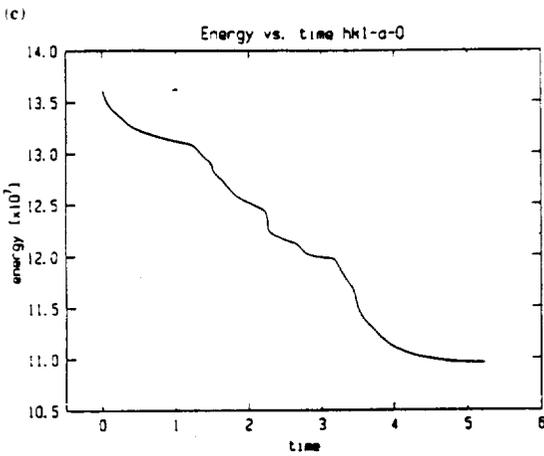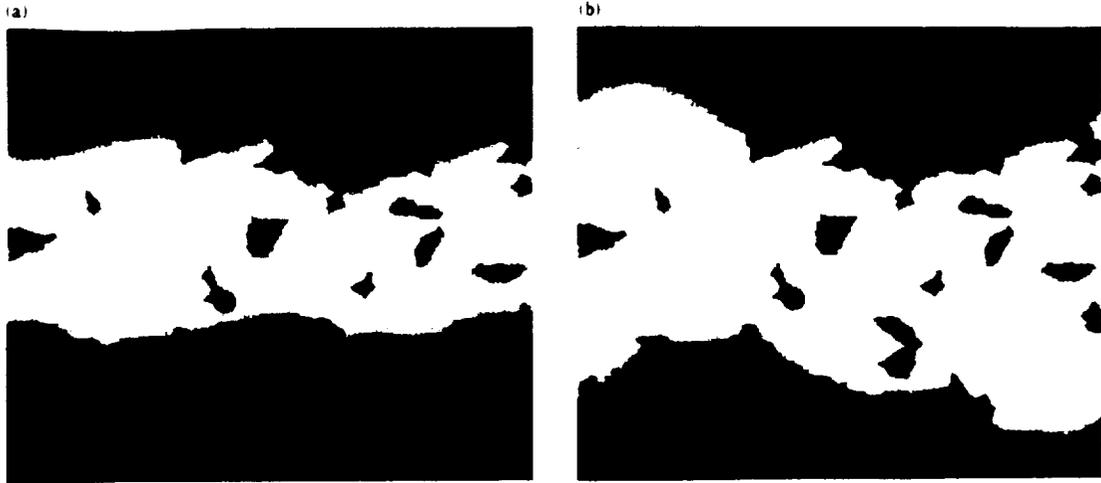
Fig. 6 Strip of reverse magnetization in a patchy lattice with voids. (a) At $H_a = 0$. (b) After $t = 5$ ns under the applied field of $H_a = 1.5$ kOe. (c) Total magnetic energy *versus* time under $H_a = 1.5$ kOe.
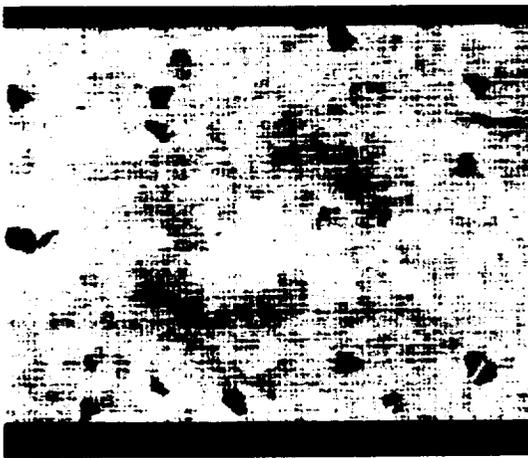
Fig. 7 Lattice with 662 patches, of which 24 are "defective". A normal patch is assigned anisotropy axis within a cone of $\Theta = 10°$ from the perpendicular direction, whereas the easy axis of a defective patch is nearly in the plane of the lattice. The color coding scheme depicts the direction of anisotropy for the individual patches.
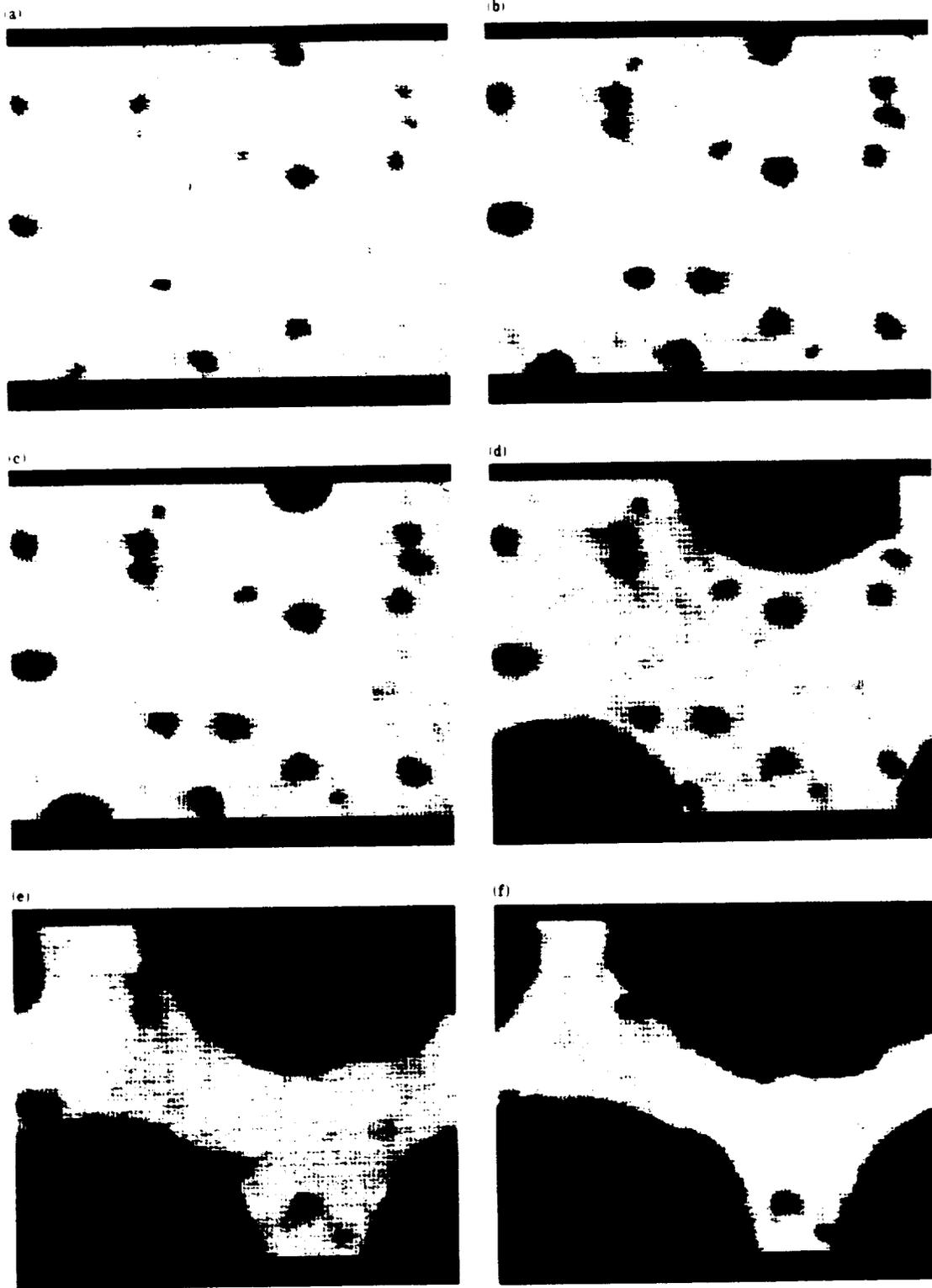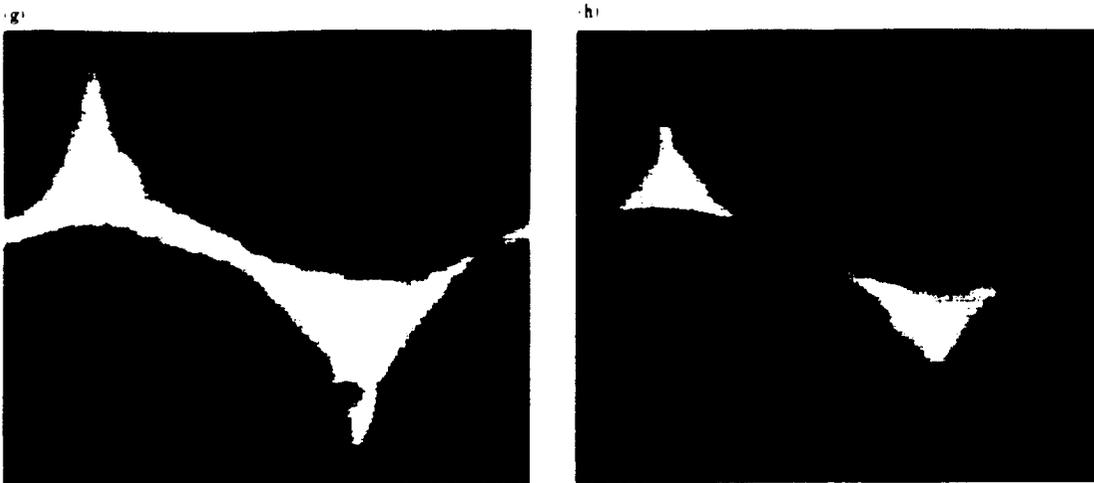
Fig. 8 Magnetization distribution in the patchy lattice of Fig. 7. (a) The remanent state at $H_z = 0$. (b) The steady state under $H_z = -8900$ Oe. The remaining frames show the time evolution of the lattice under $H_z = -8920$ Oe. (c) At $t = 0.24$ ns the reversal is underway with a nucleus forming in the lower left corner. The periodic extension of this nucleus in the upper right corner of the lattice is also visible. (d) At $t = 0.72$ ns. (e) At $t = 1$ ns. (f) At $t = 1.08$ ns. (g) At $t = 1.248$ ns. (h) At $t = 1.32$ ns.

for the dipoles at the void boundaries, their magnetic parameters being the same as those elsewhere in the lattice. Of course no exchange field is exerted on the boundary dipoles from the neighboring cells on the void side, and the magnetic charges that accumulate on the void boundaries are automatically accounted for when the demagnetizing field is computed.) The remaining patches are all identical in their magnetic properties except for the value of the anisotropy constant K_u which fluctuates randomly and independently from patch to patch. (The standard deviation of these fluctuations is 20% of the average value of K_u.) No other spatial variations in the parameters have been assumed and, in particular, all axes of anisotropy are perpendicular (i.e., $\Theta = 0$).

The walls in Fig. 6(a) have automatically adjusted themselves to minimize their lengths by attaching to the voids in the neighborhood. Minimization of length is tantamount to minimization of total wall energy and is therefore favored by the magnetic system under consideration. Figure 6(b) shows the state of the lattice under an applied field of $H_z = +1.5$ kOe at $t \simeq 5$ ns. Apparently, the walls have continued to seek voids to attach onto, while expanding in

response to the external field. Figure 6(c) is a plot of the total magnetic energy of the lattice during this growth period. It is marked by slow declines, characteristic of continuous wall motion, and rapid drops, corresponding to detachments from or attachments to the voids. It is thus observed that void-like defects in real media can create jagged domain boundaries, increase the coercivity of wall motion, and cause discontinuities in the propagation process.

As another example consider the case of a patchy lattice with a different kind of "defect". The 662 patches in this case were divided into two groups as shown in Fig. 7. The first group, consisting of 638 patches, were assigned nearly-perpendicular axes of anisotropy, as has been our practice so far. Each one of the patches in this group was assigned an axis, randomly and independently of the others, with a cone angle of $\Theta = 10°$. The second group of 24 patches were assigned axes of anisotropy that were nearly parallel to the plane of the lattice. The randomly and independently chosen values of θ and ϕ for these patches belonged to the intervals $[80°, 90°]$ and $[0, 360°]$, respectively. (In the color-coded distribution of the anisotropy axes shown in Fig. 7, the

(a)

(b)

(c)

(d)
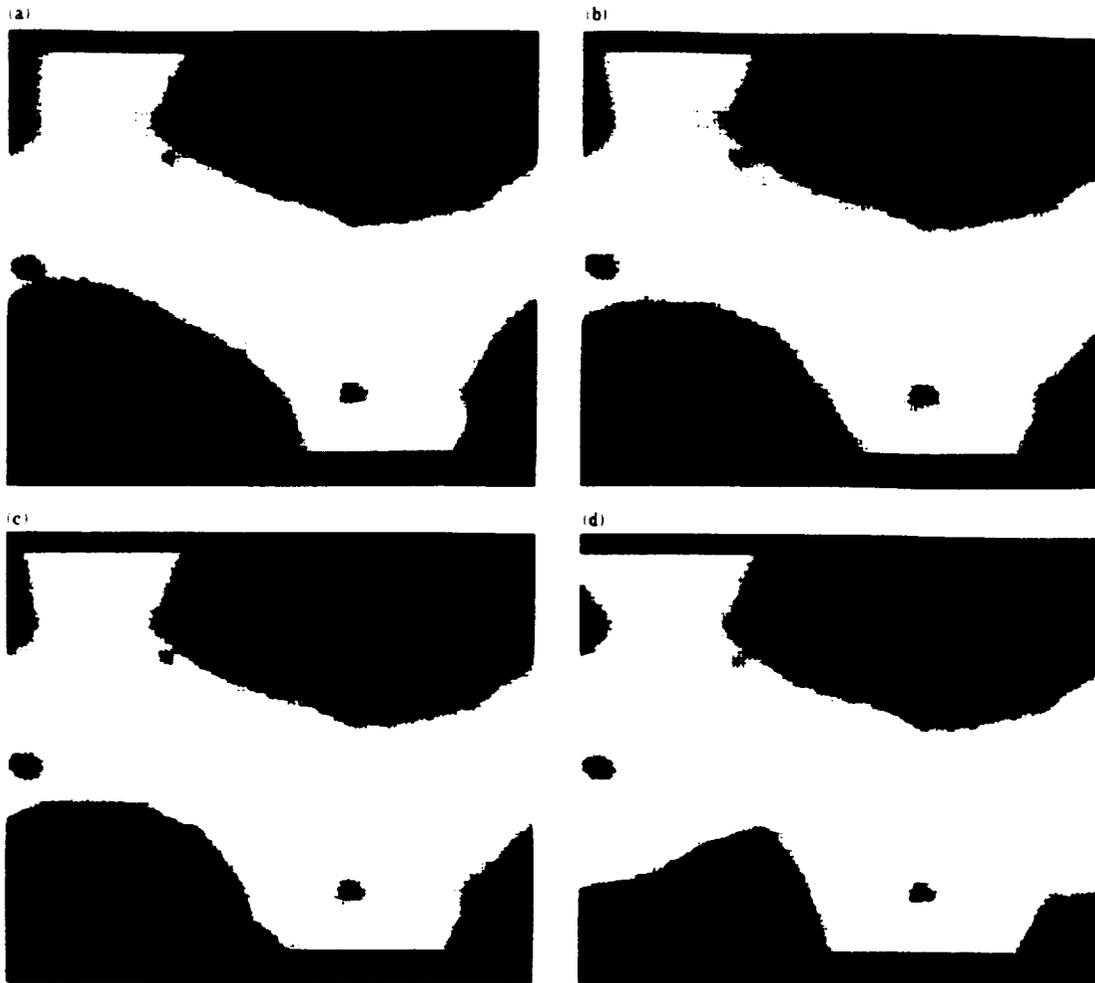
Fig. 9 Evolution of the magnetization state of Fig. 8(e) after the removal of the external field. (a) $t = 0.44$ ns. (b) $t = 1.12$ ns. (c) $t = 1.16$ ns. (d) $t = 5.83$ ns.

patches with prominent colors are those with nearly in-plane axes.) The remaining parameters of the lattice were the same as before. In the following discussion this lattice shall be referred to as "the lattice with in-plane defects".

The entire lattice with in-plane defects was initially saturated along the $+Z$ axis and then allowed to relax in zero field, until the remanent state of magnetization, shown in Fig. 8(a), was arrived at. The strong exchange interaction has clearly forced the magnetization of the in-plane patches towards the $-Z$ axis, but the tendency towards the plane is still visible in some areas. We subjected the remanent

state to a reverse-magnetizing external field along $-Z$, and searched for the critical magnitude of this field that would initiate the reversal process. The critical field for nucleation was found to be 8910 Oe. It is important to note that in the absence of the in-plane patches the same sample had a nucleation coercivity close to 18 kOe. The in-plane regions, therefore, facilitate the nucleation process. In Fig. 8 (b) we show the pattern of magnetization distribution under an applied field $H_z = -8900$ Oe, which is only slightly weaker than the critical field. The defects are seen to have been pushed toward the plane, yet the field is not quite strong enough to

(a)

```
pt4-r24-relax.dot: E and Mz
```


(b)

```
pt4-r24-relax.dot: Exch and Anis
```


(c)

```
pt4-r24-relax.dot: Demag and Mz
```
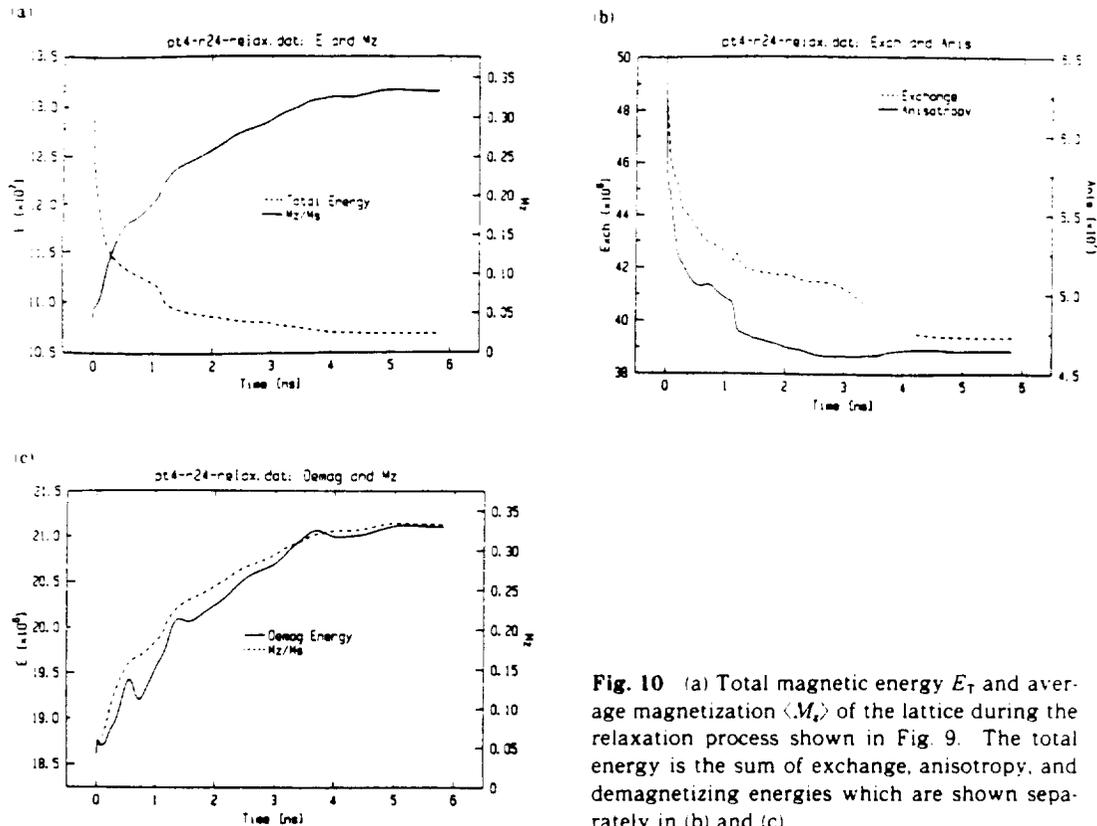
Fig. 10 (a) Total magnetic energy E_T and average magnetization $\langle M_z \rangle$ of the lattice during the relaxation process shown in Fig. 9. The total energy is the sum of exchange, anisotropy, and demagnetizing energies which are shown separately in (b) and (c).

cause them to reverse. When the field was raised to $H_z = -8920$ Oe, the reversal began, as the time evolution series in Figs. 8(c) to 8(h) shows. First the defect at the lower left corner of the lattice (with its periodic extension at the upper right) nucleated. Then the nucleus grew until the entire sample was reverse-magnetized. Note how the defects seem to attract the domain wall as it approaches them, and then try to pin the wall to prevent its further progress. The applied field, however, is strong enough to overcome the pinning of the wall and bring the reversal to completion. A hysteresis loop with high squareness is the hallmark of this type of reversal.

In order to investigate the pinning process and the phenomenon of wall coercivity, we took the state of the lattice in Fig. 8(e) as the initial state for another simulation and set the external field to zero. Note that because of the periodic boundary condition im-

posed on the hexagonal lattice, the several black regions in Fig. 8(e) are in fact different pieces of one and the same reverse-magnetized domain. This (roughly circular) domain must begin to collapse immediately after the removal of the external field. The reason for the collapse is that the domain wall energy density of the material $(\sigma_w = 4\sqrt{A_x K_u} = 1.265$ erg/cm^2) is greater than the demagnetizing energy density at the wall $(\sim 6\pi h M_s^2 = 0.943$ erg/cm^2) and, therefore, energy minimization favors the shrinking of the domain. Figure 9 shows the time evolution of the shrinking process, with frames (a) to (d) corresponding to $t = 0.44$ ns, 1.12 ns, 1.16 ns, and 5.83 ns after the external field is reset to zero. In the absence of defects the collapse would have been complete, but in the present situation after an initial period of shrinking, the defects trap the domain wall and prevent its collapse. Note in Fig. 9(c), for instance, how
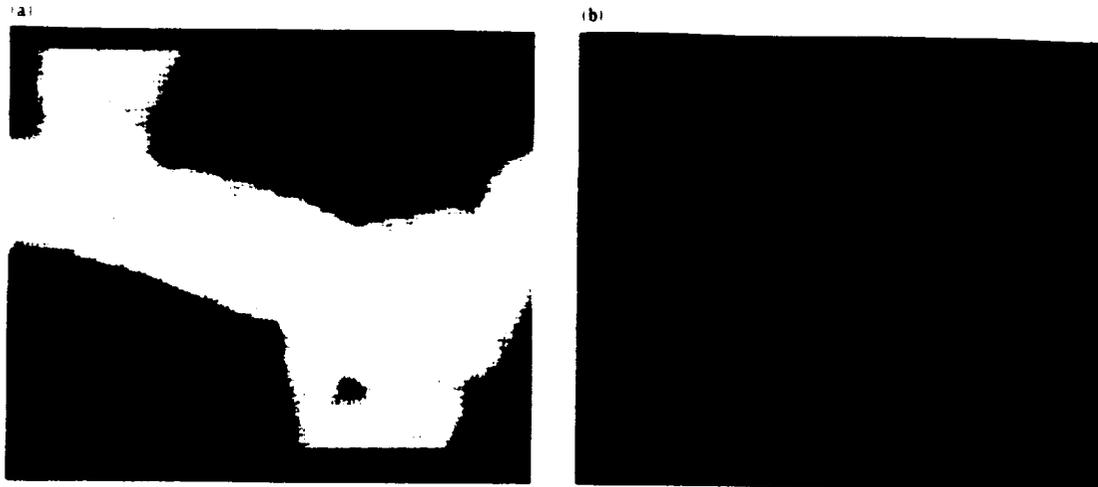
Fig. 11 (a) Magnetization distribution pattern corresponding to the relaxation of the state in Fig. 8(f) under zero applied field. The steady state shown here is obtained after 4 ns of relaxation. (b) Dot product of the initial state of magnetization shown in Fig. 8(f) and the final (relaxed) state shown in Fig. 11(a). The color coding scheme for this figure which is different from that used elsewhere in the paper is described in the text.

the defect in the lower central part of the lattice attracts the wall and keeps it pinned there afterwards. Therefore, like the other types of defect described in previous examples, defects with in-plane anisotropy are likely responsible for the observed wall coercivity of the RE-TM media. A comparison of Fig. 9(d) with Fig. 7 clearly indicates that the domain is fully anchored on a number of defects. The fact that the domain in Fig. 9(d) is stable has practical significance in data storage applications, since it provides one possible mechanism for the stability of very small thermomagnetically recorded marks.

Figure 10 shows plots of energy E and average magnetization $\langle M_z \rangle$ during the relaxation process depicted in Fig. 9. As expected, the total energy E_{TOT} of the system decreases in time, while the average magnetization along Z increases. A sudden jump in the curve of energy (such as the one at $t \simeq 1.14$ ns) is an indicator of the capture of the wall by a defect. Plots of the various components of energy in Figs. 10 (b) and 10(c) show that the exchange and anisotropy energies of the system generally decrease with time, while the demagnetizing energy increases. This is to be expected of course in the present situation since,

as was pointed out earlier, during relaxation the total length of the domain wall must decrease.

Finally, starting from the state of Fig. 8(f), we show in Fig. 11 the result of relaxation under zero applied field. The magnetization pattern in Fig. 11(a) is the steady state of the lattice obtained after 4 ns of relaxation. The reverse domain here is somewhat larger than the one in Fig. 9(d), simply because it started from a larger initial domain. The jaggedness of the wall in Fig. 11(a) is particularly striking. Figure 11 (b) shows the difference between the initial state in Fig. 8(f) and the final relaxed state in Fig. 11(a), using a different color coding scheme. What is depicted here is the dot product between the magnetization directions of the initial and final states: each pixel represents a scalar value in the interval $[-1, -1]$ corresponding to the dot product of the two unit vectors. In this coloring scheme -1 corresponds to purple, -1 to red, and the values in between are mapped continuously to the color wheel of Fig. 1. Figure 11(b) clearly shows the nonuniform motion of the wall during zero-field relaxation. While some regions of the wall have not moved at all, others have travelled by as much as a few hundred angstroms. In general, the wall seems to have remained pinned on

28

several defects. while regions of the wall in between those defects have relaxed toward a state of minimum energy. Once again, the observed behavior confirms that small patches of material with in-plane anisotropy are effective in capturing and stabilizing the small domains.

3. Concluding Remarks

Hypothetical mechanisms of wall coercivity in thin films of amorphous rare earth-transition metal alloys were examined in this paper. Using computer simulations. we found that regions as small as a few hundred angstroms in diameter. with certain deviations of their structure magnetic attributes from the rest of the film. could trap domain walls and cause significant changes in the value of the coercive field. Values of the coercive field obtained by simulation are comparable to those observed in practice. Whether or not these hypothetical sources exist in real materials is a question whose answer must await further progress in experimental "nanomagnetics". Among the existing tools for observation of the magnetic state in thin films. Lorentz Electron Microscopy[40] and Magnetic Force Microscopy[41] have the potential to clarify this situation in the near future.

Acknowledgements

References

1) P. Hansen and H. Heitmann. *IEEE Trans. Magn.* **MAG-25**. 1390 (1989).

2) P. Chaudhari, J. J. Cuomo and R. J. Gambino. *Appl. Phys. Lett.*, **22**, 337 (1973).

3) R. J. Gambino, P. Chaudhari and J. J. Cuomo. AIP Conf. Proc. No. **18**. Pt. 1. pp. 578-592 (1973).

4) T. Chen. D. Cheng and G. B. Charlan. *IEEE Trans. Magn.* **MAG-16**, 1194 (1980).

5) Y. Mimura. N. Imamura and T. Kobayashi. *IEEE Trans. Magn.* **MAG-12**. 779 (1976).

6) Y. Mimura. N. Imamura. T. Kobayashi. A. Okada and Y. Kushiro. *J. Appl. Phys.*, **49**. 1208 (1978).

7) F. E. Luborsky. *J. Appl. Phys.*, **57**. 3592 (1985).

8) H. Tsujimoto. M. Shouji. A. Saito. S. Matsushita and Y.

9) G. A. N. Connell. R. Allen and M. Mansuripur. *J. Appl. Phys.*, **53**. 7759 (1982).

10) M. Urner-Wille. P. Hansen and K. Witter. *IEEE Trans. Magn.* **MAG-16**, 1188 (1980).

11) T. C. Anthony. J. Burg. S. Naberhuis and H. Birecki. *J. Appl. Phys.*, **59**. 213 (1986).

12) Y. Sakurai and K. Onishi. *J. Magn. Magn. Materials*, **35**. 183 (1983).

13) P. Wolniansky. S. Chase. R. Rosenvold. M. Ruane and M. Mansuripur. *J. Appl. Phys.*, **60**. 346 (1986).

14) E. C. Stoner and E. P. Wohlfarth. *Phil. Trans. Roy. Soc.*, **A240**. 599 (1948).

15) D. O. Smith. *J. Appl. Phys.*, **29**. 264 (1958).

16) E. M. Bradley and M. Prutton. *J. Electronics and Control*, **6**. 81 (1959).

17) S. Middelhoek. PhD Thesis. University of Amsterdam (1961).

18) R. Harris. M. Plischke and M. J. Zuckermann. *Phys. Rev. Lett.*, **31**. 160 (1973).

19) R. Harris. S. H. Sung and M. J. Zuckermann. *IEEE Trans. Magn.* **MAG-14**. 725 (1978).

20) R. Friedberg and D. I. Paul. *Phys. Rev. Lett.*, **34**. 1234 (1975).

21) D. I. Paul. *Phys. Lett.*, **64A**. 485 (1978).

22) D. I. Paul. *J. Appl. Phys.*, **53**. 2362 (1982).

23) B. K. Middelton. "Magnetic Thin Films and Devices". in "Active and Passive Thin Film Devices". ed. by T. J. Coutts. Academic Press. New York (1978). Chapter 11.

24) A. Sukiennicki and E. Della Torre. *J. Appl. Phys.*, **55**. 3739 (1984).

25) K. Ohashi. H. Tsuji. S. Tsunashima and S. Uchiyama. *Jpn. J. Appl. Phys.*, **19**. 1333 (1980).

26) K. Ohashi. H. Takagi. S. Tsunashima. S. Uchiyama and T. Fujii. *J. Appl. Phys.*, **50**. 1611 (1979).

27) M. C. Chi and R. Alben. *J. Appl. Phys.*, **48**. 2987 (1977).

28) J. M. D. Coey. *J. Appl. Phys.*, **49**. 1646 (1978).

29) J. M. D. Coey and D. H. Ryan. *IEEE Trans. Magn.* **MAG-20**. 1278 (1984).

30) E. Callen. Y. J. Liu and J. R. Cullen. *Phys. Rev. B.* **16**. 263 (1977).

31) R. C. O'Handley. *J. Appl. Phys.*, **62**. R15 (1987).

32) M. Mansuripur. *J. Appl. Phys.*, **63**. 5809 (1988).

33) M. Mansuripur and T. W. McDaniel. *J. Appl. Phys.*, **63**. 3831 (1988).

34) M. Mansuripur and R. Giles. *Computers in Physics*. **4**. 291 (1990).

35) R. Giles and M. Mansuripur. submitted to *Computers in Physics*.

36) A. P. Malozemoff and J. C. Slonczewski. "Magnetic Domain Walls in Bubble Materials". Academic Press. New York (1979).

37) M. Mansuripur and R. Giles. *IEEE Trans. Magn.* **MAG-24**. 2326 (1988).

38) M. Mansuripur. *J. Appl. Phys.*, **66**. 3731 (1989).

39) M. Mansuripur and M. F. Ruane. *IEEE Trans. Magn.* **MAG-22**. 33 (1986).

40) C. J. Lin and D. Rugar. *IEEE Trans. Magn.* **MAG-24**.

2311 1988
41   D Rugar, H. J. Mamin and P Guthner. *Appl. Phys. Lett.*, 55 2588 1989

[Received October 15. 1990]

Masud MANSURIPUR

1977 BSEE in Electrical Engineering at Arya-Mehr University of Technology (Tehran, Iran).

1978 MS in Electrical Engineering at Stanford University.

1980 MS in Mathematics at Stanford University.

1981 PhD in Electrical Engineering at Stanford University. During and after his graduate studies, he worked at the Xerox Palo Alto Research Center on erasable optical data storage materials and systems.

1982 Joined as a member of the faculty of the Electrical Engineering Department in Boston University.

1988 Joined as Associate Professor of the Optical Sciences Center in the University of Arizona.

Present: Associate Professor of the Optical Sciences Center in the University of Arizona. Member of the Institute of Electrical and Electronics Engineers (IEEE) and Optical Society of America (OSA).

Research Field: Studies on magnetic and optical properties of amorphous materials with emphasis on thin film and multilayer structures. Computer simulations of micromagnetics and domain wall dynamics. Developing novel experimental methods for studying magnetic and optical properties of materials.

Roscoe C. GILES

1970 BA in Physics at the University of Chicago

1975 PhD in Physics at Stanford University. Worked as post doctoral fellow in theoretical particle physics at the Stanford Linear Accelerator Center and at the Center for Theoretical Physics at MIT and has been Assistant Professor of Physics at MIT

Present: Professor of the Electrical, Computer and Systems Engineering Department of Boston University. Member of the Boston University Center for Computational Science. Member of the American Physical Society, Sigma Xi, and Phi Beta Kappa.

Research Field: Large scale computer simulations of magnetic materials and on molecular dynamics. Developing massively parallel algorithms and applications.

George PATTERSON

1987 BS in Physics at MIT

Present: Doctoral student in the Department of Physics at Boston University

Research Field: Supercomputer simulations of magnetic materials. Simulations of rare earth-transition metal alloys and analysis of three dimensional topological structures in magnetic materials for vertical Bloch line memories.

N92-14907

Effect of Patch Borders on Coercivity in Amorphous Rare Earth-Transition Metal Thin Films

G. Patterson*, H. Fu[†], R. Giles* and M. Mansuripur[†]

*College of Engineering, Boston University, Boston, Massachusetts 02215

[†]Optical Sciences Center, University of Arizona, Tucson, Arizona 85721

1 Motivation

The coercivity at the micron scale is a very important property of magneto-optical media [1, 2]. It is a key factor that determines the magnetic domain wall movement and domain reversal. In this report we discuss how the coercivity is influenced by a special type of patch borders. Patch formation is a general phenomenon in growth processes of amorphous rare-earth-transition-metal thin films [3]. Different patches may stem from different seeds and the patch borders are formed when they merge. Though little is known about the exact properties of the borders, we may expect that the exchange interaction at the patch border is weaker than that within a patch, since there is usually a spatial gap between two patches. This is the practical background of our work.

2 The System

Our computer simulations were performed on a two-dimensinal hexagonal lattice consisting of 37 complete patches with random shape and size. Though we used the same lattice for the results to be represented in Figs. 1 and 2, the patch borders are only highlighted by the grey lines in Fig. 2. Some of the patches appearing in the boundaries of the lattice are actually different parts of the same patch, because of the periodic boundary conditions. Each patch has

its own axis of anisotropy, which is oriented randomly within a cone angle of $\Theta = 45°$ about the perpendicular direction. Since the lattice has an area $0.256\mu m \times 0.222\mu m$, the average dimension of each patch is about 390 Å. This dimension is large in comparison with the width of domain wall ($\simeq 100$ Å) in the present situation.

The following set of parameters were used in the simulations: saturation magnetization $M_s = 100$ emu/cm^3, anisotropy energy density constant $K_u = 10^6$ erg/cm^3, exchange stiffness coefficient within the patches $A_x = 10^{-7}$erg/cm, film thickness $h = 500$ Å, Gilbert damping constant $\alpha = 0.5$, gyromagnetic ratio $\gamma = -10^7$Hz/Oe. Different values are assigned to the stiffness constant A_x at the patch borders. For the five patches containing a reversed domain (see Fig.1), starting from the lower left corner and moving counterclockwise, the stiffness constant on the patch borders are 10 %, 20 %, 50 %, 40 % and 30 % of the nominal value (i.e. 10^{-7} erg/cm). The stiffness constant on all of the remaining patch borders are 50 % times 10^{-7} erg/cm. There are two reasons for setting different exchange constants at the borders. One is that in reality the borders may be different, the other is that we can simulate different cases in a single computer run. The anisotropy constant at the central disk of each reversed domain is 10^7 erg/cm^3 (i.e. 10 times the nominal value of K_u), because otherwise these initial nuclei will not be stable.

3   Results

Fig.1 (a) shows the initial magnetization state. Five reversed domains were artificially built in the above mentioned special patches. The patch borders are not highlighted. Following the direction change in each of the domain wall, we see that the accumulate winding angle is equal to 2π for each domain wall. Now we let this initial magnetic state relax for $t = 0.5$ ns to the remanent state. To make sure that this state is close enough to the equilibrium state, we also made snapshots of the magnetization at $t = 0.3$ ns and 0.4 ns and found no difference between them. The remanent state is illustrated in Fig.1 (b). Now we see that the lower left domain

has two dramatic changes, while the remaining four domains remain more or less unchanged. One change is that the domain expands to the north border of the patch. The reason is that, the domain wall is initially very close to the border which has a very low exchange energy (10 %). Therefore, it sticks to the border, just as a domain wall sticks to a void region [1, 2], to make the minimum wall energy. The other change experienced by this domain is that the winding number becomes zero, i.e. the dipoles in the domain wall region align in the same direction. If there were no border, the winding number would not have been changed, since changing a winding number must experience a stage where anti-parallel dipoles are generated, which corresponds to a higher exchange energy. In the present case of weak exchange coupling, the winding angle can be changed because there is no such energy barrier.

In order to investigate the coercivity of domain wall motion, we applied a magnetic field in the negative z-direction to the lattice. At first, we applied a field of $H_z = -1000$ Oe. Fig.2(a) is a snapshot of the steady state at $t = 1.3$ ns. Here we see that the lower left domain expands to fill the whole patch. This means that, when the reversed domain is near a border with weak exchange interaction, the coercivity of domain wall motion is very low. The reason is that the magnetization outside the patch cannot exert a sufficient exchange force to keep the dipoles inside the patch upwards. At the next stage, we increase the strength of the applied field to $H_z = -1500$ Oe and let the system start from the state of Fig.2(a). Fig.2(b) shows the new steady state at $t = 2.45$ ns. Since the exchange interaction is too weak, the reversed domain in the lower left corner does not influence too much on the magnetization outside the patch. This means that, for the magnetization outside (and near) that patch to reverse, i.e. the domain wall moves beyond the patch, the external field must overcome the nucleation coercivity, but not the wall motion coercivity. To estimate this nucleation coercivity, we neglect the demagnetizing field and the 10 % exchange interaction and consider the patch border as a straight open border. Then it is easy to find out that the critical magnetic field strength to reverse the magnetization at the open border is about 40 % of the anisotropy field. In the present case this critical field is equal to -8 kOe, which is obviously much stronger than what we applied to the film (-1.5

kOe). Therefore, for a patch with weak exchange borders, we can conclude that the inside reversed domain can easily expand to fill the patch, but it is difficult to move beyond the patch border. This picture also applies to the patch whose borders have 20 % exchange constant, see the reversed domain in the lower right corner in Fig.2(b). In contrast to these two cases, the reversed domain in the extreme right with borders of 50 % exchange strength and that in the upper central patch with borders of 40 % exchange strength do not expand too much, because for stronger exchange borders, the coercivity of wall motion is higher.

The reversed domain in the upper left corner whose borders have 30 % exchange strength in Fig.2(b) shows a compromise case. In this case, we see that the coercivity of domain wall motion is less than 1500 Oe and yet, when the domain reaches the borders, the exchange force produced by the reversed domain inside the patch and the external field together makes the domain expand a little bit outside the patch borders. It then stops because the exchange interaction inside a patch is strong and so is the coercivity of domain wall motion. Now we increase the applied field to $H_z = -2000$ Oe and let the system start from the state of Fig.2(b). Fig.2(c)-(e) are snapshots of systems at $t = 0.95$ ns, 1.25 ns and 1.55 ns. Now we see that the applied field is stronger than the coercivity of wall motion and the four domains with relatively stronger exchange interaction borders expand, and until eventually all the lattice is reversed (not shown in the figure). In the process of domain expansion, we see that the domain in the lower left corner does not expand, because the applied field is still weaker than the corresponding nucleation field, i.e. $\simeq -8$ kOe, as was mentioned before.

From this series of simulations we may conclude that the domain in the patch with borders of 30 % exchange strength can expand most easily to the whole lattice, because the exchange strength of the border is not too high to prevent the domain from growing within the patch and it is not too low to prevent the domain from expanding beyond the patch.

References

[1] R. Giles and M. Mansuripur, *Possible sources of coercivity in thin films of amorphous rare earth- transition metal alloys*, Computers in Physics, (1991).

[2] M. Mansuripur, R. Giles and G. Patterson, *Coercivity of domain wall motion in thin films of amorphous rare earth-transition metal alloys*, J. Mag. Soc. Japan. Vol. 15 (1991) pp.17-30.

[3] R. B. Sargent, *Surface diffusion: a computer study of its effects on thin film morpholoy*, Ph.D thesis, Optical Sciences Center, University of Arizona, 1990.

Figure Captions

Fig.1 (a) The initial state has five reversed domains. These domains are located inside patches whose borders have 10 % (lower left), 20 % lower right, 30 % (upper left), 40 % (upper right) and 50 % (middle right) exchange strength. (b) The remanent state after relax from the state (a) for 0.5 ns.

Fig.2 Evolution of the magnetization under an applied field. (a) The steady state under $H_z = -1000$ Oe is reached after $t = 1.3$ ns starting from the state of Fig.1(b). (b) The steady state under $H_z = -1500$ Oe is reached after $t = 2.45$ ns starting from (a). (c)-(e) Evoluiton starting from (b) under $H_z = -2000$ Oe at $t = 0.95$ ns, 1.25 ns and 1.55 ns.

(a)

Fig. 1

(b)

(a)

Fig. 2

(b)

(c)

Fig. 2

(d)

(e)

Fig. 2

N92-14908[119]
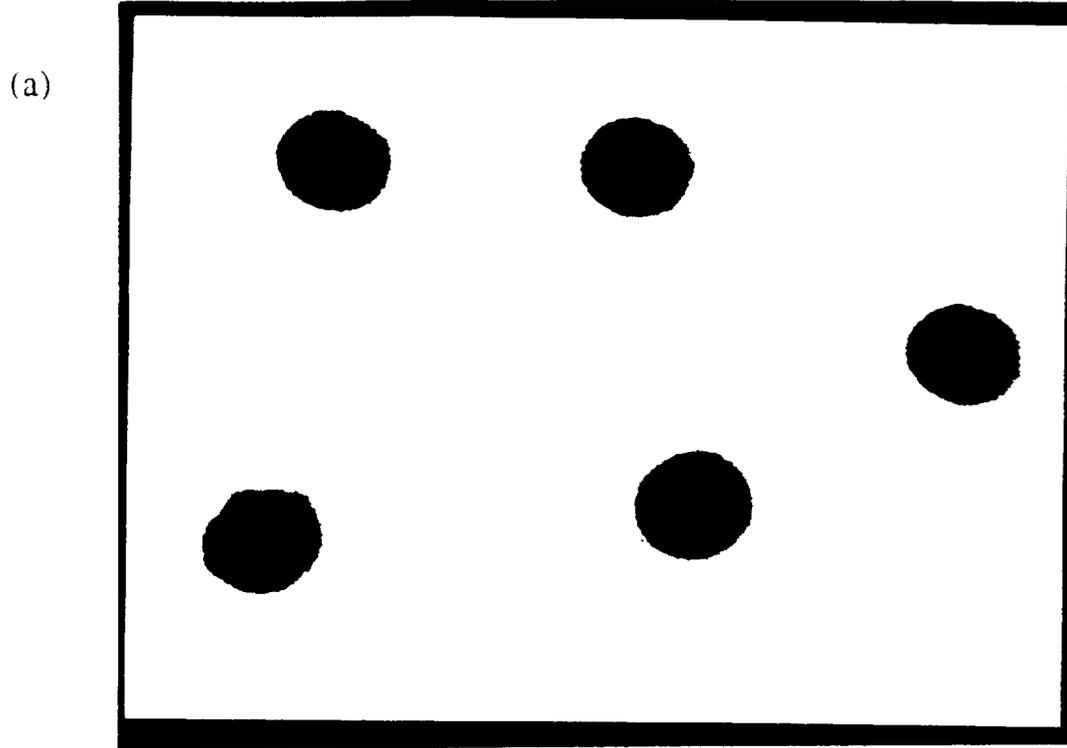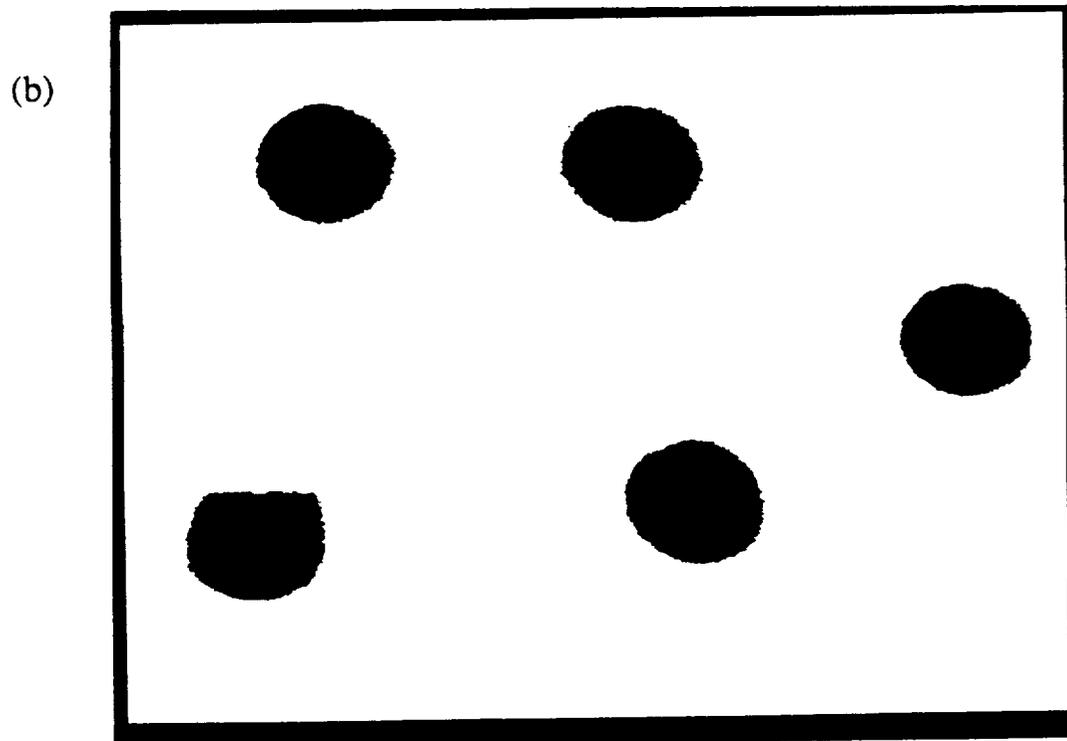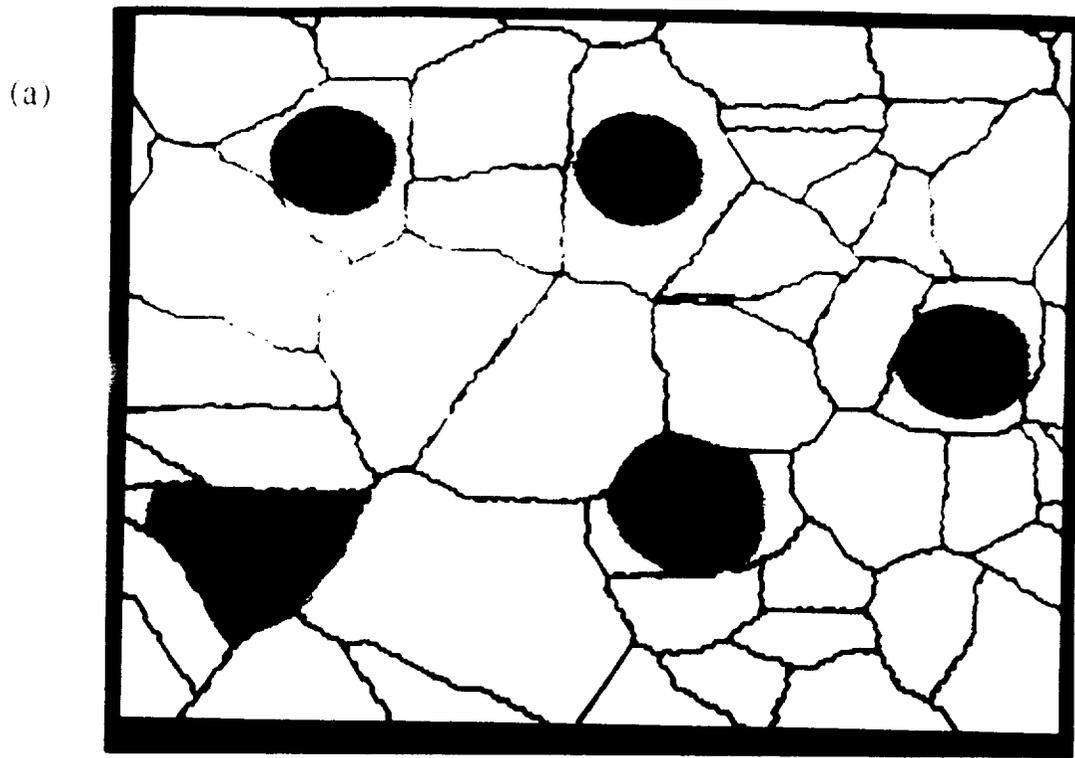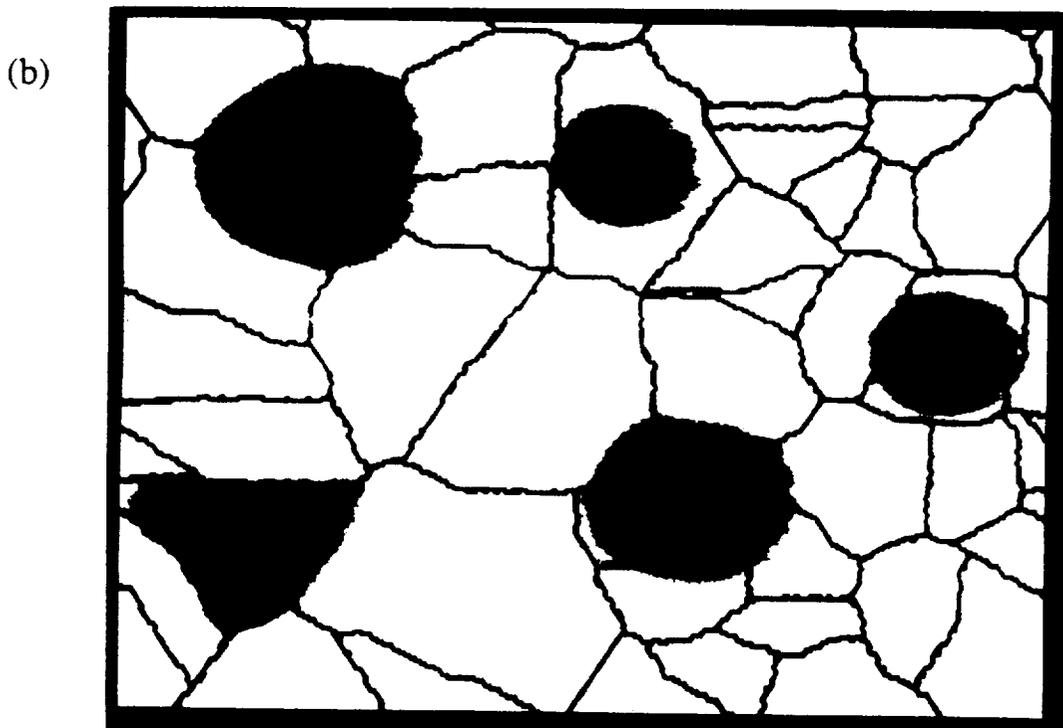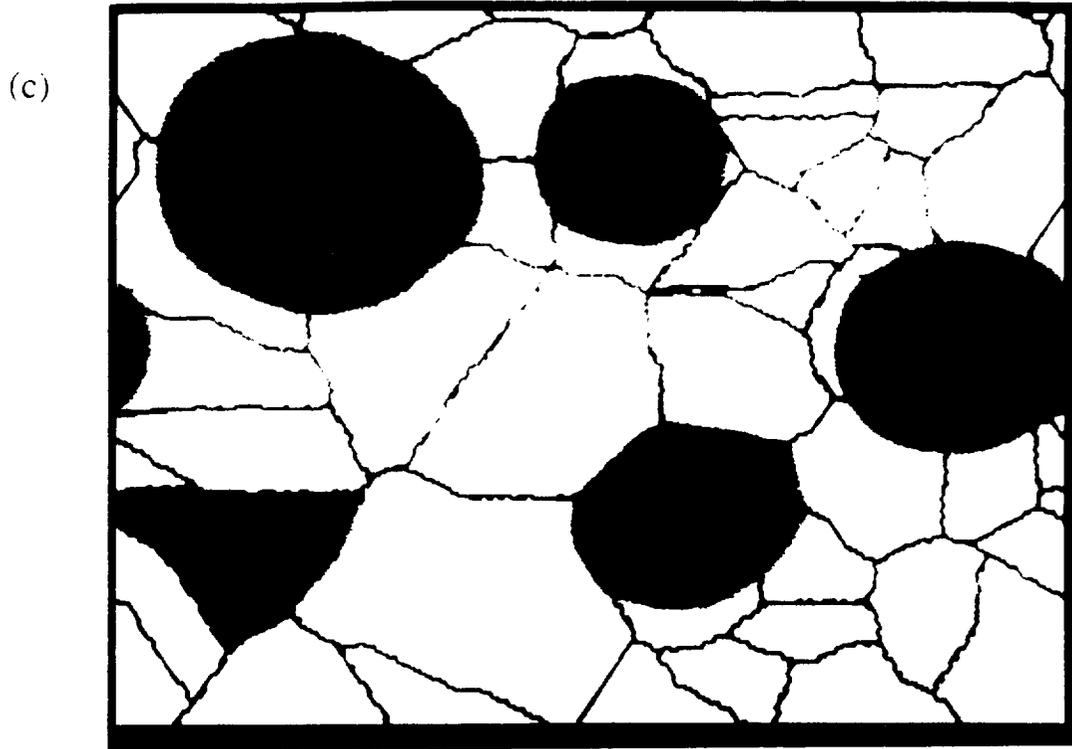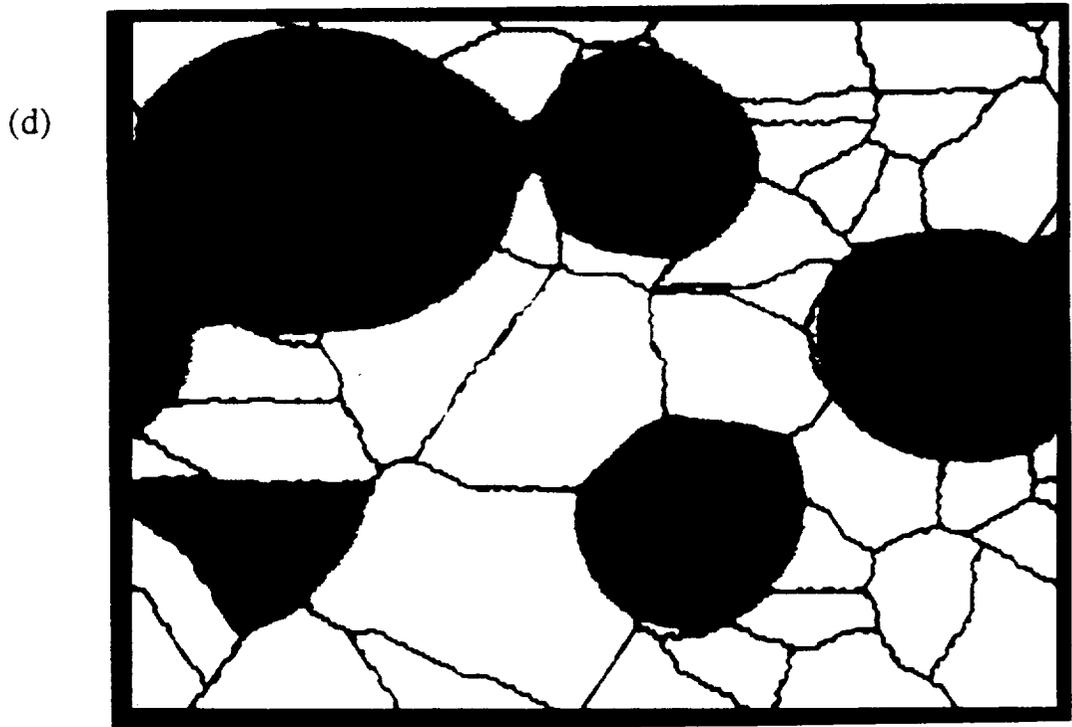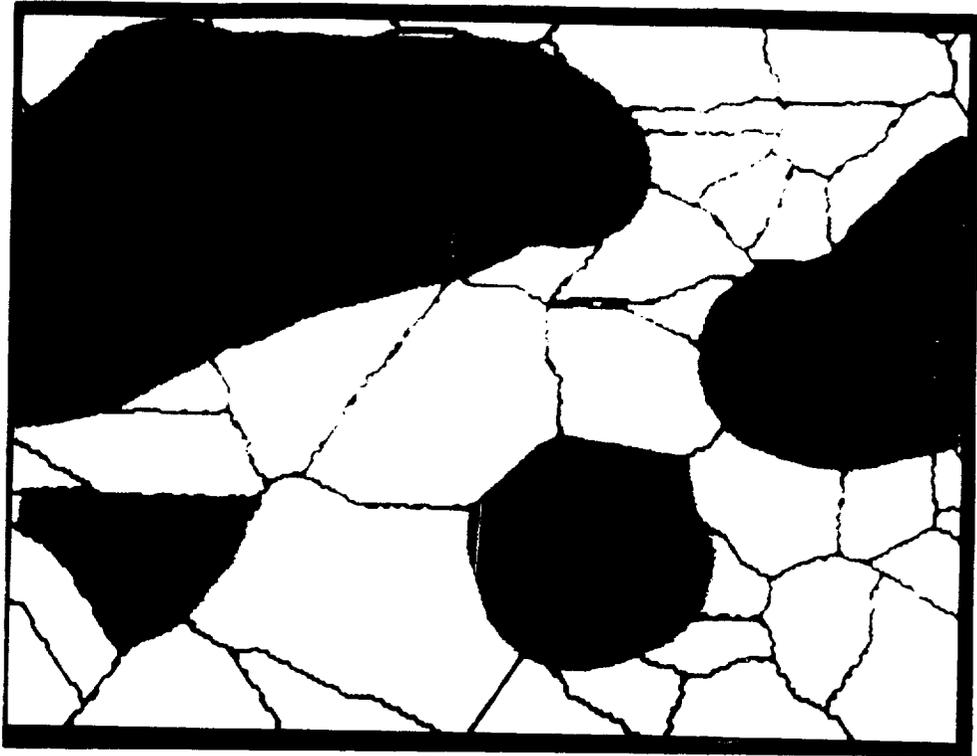
Sources of Noise in Magneto-Optical Readout

M. Mansuripur

Optical Sciences Center

University of Arizona

In this document we analyze the various sources of noise which are often encountered in magneto-optical readout systems. Although the focus is on magneto-optics, most sources of noise are common among the various optical recording systems and one can easily adapt the results of this work to other media and systems. A description of the magneto-optical readout system under consideration is given in Section 1; also described there are the standard methods and the relevant terminology of signal and noise measurement. After these preliminary considerations, the characteristics of thermal noise, which originates in the electronic circuitry of readout, are described in Section 2. In Section 3 we consider the most fundamental of all sources of noise, the shot noise, and give a detailed account of its statistical properties. Shot noise, which is due to random fluctuations in photon arrival times, is an ever-present noise in optical detection. Since the performance of magneto-optical recording devices in use today is approaching the limit imposed by the shot noise, it is important that the reader have a good grasp of this particular source of noise. In Section 4 we describe a model for the laser noise, and present measurement results which yield numerical values for the strength of the laser power fluctuations. Spatial variations of the disk reflectivity and random depolarization phenomena also contribute to the overall level of noise in readout; these and related issues are treated in Section 5. The final section is devoted to numerical simulation results, describing some of the more frequently encountered sources of noise which accompany the recorded waveform itself, namely, jitter noise and signal-amplitude-fluctuation noise.

1. **Preliminaries** : Throughout this chapter, frequent reference will be made to the readout system depicted in Fig. 1. The light source in this system is a semiconductor diode laser which operates at a constant (CW) output power level[†]. The reflected light from the magneto-optical disk consists of a polarization component parallel to the direction of incident polarization X, and a perpendicular component Y, which carries information about the recorded data.

For the purpose of monitoring the laser power fluctuations, the leaky polarizing-beam-splitter directs a small fraction γ^2 of the emitted light towards a photodetector; the output of this detector is fed back to the laser in order to stabilize its radiation level. The light transmitted by the leaky PBS is linearly polarized along X but, upon reflection from the disk, it acquires a Y-component as well. In the return path, the leaky PBS provides the detection module with a fraction γ of the X-component as well as the entire Y-component. The latter is the magneto-optically generated signal which carries the desired information; the former, although barren of such information, is needed in the scheme of differential detection in order to properly extract the data.

To eliminate the ellipticity of the beam, a phase compensator (either quarter-wave plate or adjustable Soleil-Babinet retarder) is employed. A regular PBS, with its axes at 45° to X and Y, together with detectors #1 and #2 comprise a balanced differential detection module. These detectors are low-noise, photodiode/preamplifier integrated circuits whose outputs are fed to a differential amplifier for subtraction and further amplification.

Let us now describe the units of signal and noise which are commonly used in practical measurements. A constant (DC) voltage V or current I is specified in terms of the power P that it delivers to a fixed resistor R, that is, $P = V^2/R$ or $P = RI^2$. The standard value of R is 50 Ω and the power thus measured may be stated either in Watts or in milliWatts. In the logarithmic units known

---

[†] For the purpose of noise reduction in practice the laser drive current is modulated at a frequency in the range of several hundred MHz. Generally, the modulation frequency is well beyond the bandwidth of the detection system and is ignored by the detectors. Signal and noise analysis, therefore, may proceed by ignoring the modulation of the laser and treating its beam as CW.

as deciBell (*dB*) the strength of the signal is defined as $10 \log_{10} P$; if P is in Watts the logarithmic unit is called dBw, and if P is in milliWatts it is known as dBm. For example, the power of a 1 Volt DC signal is 13 dBm, while that of a 1 Amp DC current is 47 dBm. The same rules and definitions apply to single-frequency (AC) signals, provided of course that one remembers that the effective (root-mean-square) amplitude of a sinusoid is $1/\sqrt{2}$ times its maximum amplitude.

When the dimensionless ratio of two quantities such as P_1/P_2 or V_1/V_2 or I_1/I_2 is expressed on the logarithmic scale, the units are specified as *dB*. It must be emphasized that the ratio of powers in *dB* is defined as $10 \log P_1/P_2$, whereas for currents and voltages the correct definition is $20 \log (I_1/I_2)$ and $20 \log (V_1/V_2)$.

If a signal is amplified prior to the measurement, then the gain G must also be taken into account. Generally, when one uses a logarithmic scale, one must subtract the value of $20 \log_{10} G$ from the signal power in order to eliminate the gain factor. It is important here that the gain be dimensionless, that is, voltage be amplified to voltage and current be amplified to current. If, on the other hand, current is amplified to voltage (or vice versa) then the gain must be adjusted to take account of the resistance R. For instance, if the initial noise current has a power of RI^2, after amplification (and conversion to voltage) its power will become G^2I^2/R. Therefore, the proper gain coefficient in this instance is not G but G/R (where R is typically 50 Ω).

Unlike the signal, noise has a broad spectrum and its strength (or power) depends on the bandwidth within which it is being measured. The spectral density of the noise is usually defined as the average noise power delivered to a 50 Ω resistor within a bandwidth of 1 Hz, and is denoted by $R \langle i_n^2 \rangle$ or $\langle v_n^2 \rangle/R$, depending on whether the noise is due to fluctuations of current or voltage. We shall denote the rms noise current by i_n, although formally the appropriate notation is $\sqrt{\langle i_n^2 \rangle}$. Similarly the rms noise voltage shall be denoted by v_n. It is customary in practice to measure the noise power not in a 1 Hz bandwidth, but in a 30 kHz bandwidth, and express the result in dBw or dBm. Thus, a noise current of 10 $pA/\sqrt{Hz}$ will have a power of

$$10 \log_{10}(50 \times 10^{-22} \times 30000) = -158.24 \text{ dBw} = -128.24 \text{ dBm} .$$

Similarly, the measured power of a noise voltage with the spectral density of 1 $nV/\sqrt{Hz}$ will be

$$10 \, \log_{10}(10^{-18} \times 30000/50) = -152.22 \text{ dBW} = -122.22 \text{ dBm} .$$

In the above example, if one assumes that an amplifier with a gain of $G = 100 \; V/A$ is used to convert current to voltage, then the normalized gain G/R will be equal to 2. This means that the noise current must be 6 dB below the level of the noise voltage, as is indeed the case.

2. **Noise in the Electronic Circuitry** : The fluctuating conduction electrons within resistors and transistors of an electronic circuit create a random voltage or current at the circuit's output terminal. When these fluctuations are caused by thermal motion of the electrons the resulting noise is referred to as Johnson noise. A resistor R at an equilibrium temperature T exhibits a noise whose spectrum is flat for practically all frequencies of interest. If the Johnson noise of this resistor is measured within a bandwidth B, the resulting magnitude of the noise current will be

$$< i_{th}^2 > = \frac{4 \, k_B \, T \, B}{R} \; . \tag{1}$$

In the above equation the brackets $\langle \cdot \rangle$ indicate statistical averaging or averaging over time, k_B is Boltzmann's constant $(1.38 \times 10^{-23} \, Joule/^0K)$, T is the absolute temperature (in degrees Kelvin), B is the bandwidth (in Hertz), and R is the resistance (in Ohms). For simplicity's sake we shall denote the root-mean-square value of the noise current by i_{th} instead of $\sqrt{< i_{th}^2 >}$. Since the frequency spectrum of thermal noise is flat, one usually specifies the strength of the noise in a 1 Hz bandwidth. Thus the noise amplitude of a 1 $k\Omega$ resistor at room temperature is about 4 $pA/\sqrt{Hz}$. If the bandwidth of the measuring system happens to be $B = 1$ MHz, then the measured noise current will be 4 nA. The corresponding rms noise voltage is then given by $v_{th} = R \, i_{th} = 4 \, \mu V$.

An amplifier, in addition to multiplying the input noise amplitude by a gain factor, introduces a noise of its own. This is because in transistors, for instance, random generation and recombination of electrons and holes, or the random arrival of these carriers at the collector, create current and voltage fluctuations†.The excess noise of an amplifier is generally characterized by the noise factor F, which is the ratio of the available output noise (including contributions by the amplifier) to the available output noise arising from the input alone [1]. Although every stage of the amplification process

---

† *The* terms *shot noise* and *flicker (or 1/f) noise* are often used in referring to these fluctuations. The $1/f$ noise is limited to the very low frequency range of the spectrum and, for all the practical situations considered in this chapter, it makes negligible contribution to the overall noise level.

contributes to the overall noise level, it is usually the case that the preamplifier (i.e., the first stage) makes the most significant contribution, simply because the noise from this stage is amplified more than that from the following stages. In any event, since the electronic noise is independent of the readout signal, there shall be no need to analyze its various components separately; instead, it shall be treated in its entirety as one source of noise. By measuring the spectrum of noise at the differential output of the system while blocking the laser beam from reaching the detectors (see Fig. 1) one obtains an accurate picture of the total electronic noise contribution.

Another manifestation of the thermal noise is the so-called *dark current* of photodetectors. Within the bulk of the semiconductor crystal constituting a photodiode, some valence electrons are thermally excited into the conduction band, giving rise to a current similar to that generated by photo-induced electrons. Unlike Johnson noise, however, the average value of the dark current is nonzero. Fluctuations of the dark current around its average value are known as dark-current-noise. These fluctuations are very similar to the shot noise which will be described in the next section. For the purpose of analysis, dark current and its associated noise may be treated by adding an equivalent (constant) light power level to the incident power on the photodetector. We will return to this topic at the end of section 3.

3. Shot Noise in Photodetection : Direct detection of optical signals usually entails their conversion into electrical signals by a photodetector. Photodetection is a quantum process whereby incident photons cause the release of electrons, which then go on to produce an electric current. Unfortunately, the photons do not arrive at well-defined instants of time; rather, their arrival times are random. The random arrival of photons at the detector creates fluctuations in the resulting photocurrent, which is generally known as the shot noise [2]. In this section we study properties of the shot noise as casued by coherent light. The basic property of coherent light is that the number of photons arriving during any time interval, say $[t, t + \tau]$, is independent of the number arriving during any other (non-overlapping) interval. If the interval is sufficiently short, then there is either one photon arriving in that interval or there is none at all. Assuming that the incident beam is monochromatic with frequency ν, and that its power at time t is $P_0(t)$, the probability of a single photon arriving during the short interval Δt is given by

$$p\left\{ n = 1, [t, t + \Delta t] \right\} = \frac{P_0(t)\ \Delta t}{h\nu}, \tag{2}$$

where $h\nu$ is the energy of individual photons of frequency ν. Not every photon of course creates one photoelectron. The quantum efficiency η of a photodetector is defined as the probability of a free electron being generated by an incident photon. Thus the chance that one photoelectron is released during the short interval Δt is given by

$$p\left\{ n = 1, [t, t + \Delta t] \right\} = (\eta/h\nu)\ P_0(t)\ \Delta t . \tag{3}$$

Next we derive an expression for the probability that a number n of photoelectrons is produced in the interval $[0, t]$ by the incident laser power $P_0(t)$. The probability of having $n + 1$ electrons in $[0, t + \Delta t]$ is related to the course of events in $[0, t]$ by the fact that either there are n electrons in $[0, t]$, in which case the extra electron is created in $[t, t + \Delta t]$, or there are $n + 1$ electrons in $[0, t]$ and none in $[t, t + \Delta t]$. (Since Δt is assumed very short, the chance of two or more photoelectrons being generated in

$[t, t + \Delta t]$ is ignored.) From Eq. (3) we know the probability for the generation of one electron in a short interval; the probability of having no electrons at all in the same interval is 1 minus the probability of having one electron. Combining these arguments, we arrive at the following equation :

$$p\left\{ n + 1, [0, t + \Delta t] \right\} = p\left\{ n, [0, t] \right\} p\left\{ 1, [t, t + \Delta t] \right\} + p\left\{ n + 1, [0, t] \right\} p\left\{ 0, [t, t + \Delta t] \right\}$$

$$= p\left\{ n, [0, t] \right\} (\eta/h\nu) P_0(t) \, \Delta t + p\left\{ n + 1, [0, t] \right\}\left[1 - (\eta/h\nu) P_0(t) \, \Delta t \right] ,$$

which, after some rearrangements, yields :

$$\frac{d}{dt} p\left\{ n + 1, [0, t] \right\} = (\eta/h\nu) P_0(t)\left\{ p\left\{ n, [0, t] \right\} - p\left\{ n + 1, [0, t] \right\} \right\}. \qquad (4)$$

When there are no electrons in the entire interval, Eq. (4) simplifies to

$$\frac{d}{dt} p\left\{ n = 0, [0, t] \right\} = -(\eta/h\nu) P_0(t) \, p\left\{ n = 0, [0, t] \right\} \qquad (5)$$

whose solution is readily obtained as follows :

$$p\left\{ n = 0, [0, t] \right\} = A \exp\left\{ -(\eta/h\nu) \int_0^t P_0(t) \, dt \right\}.$$

The integration constant A must be equal to 1, since at $t = 0$ the probability of having no electrons must be unity. Therefore,

$$p\left\{ n = 0, [0, t] \right\} = \exp(-A) \qquad (6)$$

where

$$\Lambda = (\eta/h\nu) \int_0^t P_0(t) \, dt \ .$$

(7)

We now replace Eq. (6) in Eq. (4) and calculate $p\left\{ n = 1, [0,t] \right\}$. Afterwards we calculate the probability for $n = 2$, then for $n = 3$, and so on. The general solution is found to be

$$p\left\{ n, [0,t] \right\} = \exp(-\Lambda) \frac{\Lambda^n}{n!} \ .$$

(8)[†]

Several important properties of the shot noise may be derived from the above distribution function. For instance, the average number of photoelectrons generated in $[0,t]$ is

$$<n> = \sum_{n=0}^{\infty} n \, p\left\{ n, [0,t] \right\} = \Lambda \exp(-\Lambda) \sum_{n=0}^{\infty} \frac{\Lambda^n}{n!} = \Lambda$$

That is,

$$\boxed{<n> = (\eta/h\nu) \int_0^t P_0(t) \, dt}$$

(9)

Thus the average number of electrons released in $[0,t]$ is proportional to the total optical energy collected in that time interval. Similarly, the variance of the number of electrons is

$$\sigma_n^2 = <n^2> - <n>^2 = \sum_{n=0}^{\infty} n^2 \, p\left\{ n, [0,t] \right\} - <n>^2 = \sum_{n=0}^{\infty} n^2 \frac{\Lambda^n}{n!} \exp(-\Lambda) - \Lambda^2$$

$$= \exp(-\Lambda) \sum_{n=0}^{\infty} \frac{n \, \Lambda^n}{(n-1)!} - \Lambda^2 = \exp(-\Lambda) \left[\Lambda \sum_{n=0}^{\infty} \frac{\Lambda^n}{n!} + \Lambda^2 \sum_{n=0}^{\infty} \frac{\Lambda^n}{n!} \right] - \Lambda^2 = \Lambda$$

---

† The probability distribution in Eq. (8) is known as the *Poisson distribution*.

Appendix F

The standard deviation σ_n of the number of photoelectrons released in $[0,t]$ is thus given by

$$\sigma_n = \sqrt{(\eta/h\nu) \int_0^t P_0(t)\, dt}$$

(10)

Equations (9) and (10) are very important in the analysis of shot noise insofar as they relate the incident laser power $P_0(t)$ to the strength of the photocurrent signal and the inherent shot noise which accompanies it.

The sensitivity η_s of a photodiode is generally defined as the average photocurrent (in Amperes) produced for 1 Watt of incident power. From Eq. (9),

$$\eta_s = \frac{\eta e}{h\nu}$$

(11)

where $e = 1.6 \times 10^{-19}$ Coulomb is the electronic charge, $h = 6.62 \times 10^{-34}$ erg. sec is Planck's constant, and ν is the frequency of the incident light. For a typical value of $\eta = 0.85$ at $\lambda = 800$ nm, the photodiode sensitivity is found from Eq. (11) to be $\eta_s = 0.55$ A/W. Now, if the signal S and the noise N are defined in terms of the integrated current (instead of the integrated number of electrons), and if the detector sensitivity η_s is used in place of the quantum efficiency η, we find

$$S = e \langle n \rangle = \eta_s \int_0^t P_0(t)\, dt$$

(12)

$$N = e\,\sigma_n = \sqrt{e\,\eta_s \int_0^t P_0(t)\, dt} \; .$$

(13)

Example 1 : Let a 1 mW, 100 ns pulse of laser ($\lambda = 800$ nm) be incident on a photodiode with quantum efficiency $\eta = 0.85$. If the pulse is uniformly integrated, the ratio of signal to noise

(averaged over many repetitions of the experiment) will be :

$$\frac{S}{N} = \frac{\langle n \rangle}{\sigma_n} = \sqrt{(\eta/h\nu) \int_0^t P_0(t)\, dt} = 1.85 \times 10^4 = 85.34 \text{ dB.}$$

This is a healthy signal-to-noise ratio for most practical applications.

Spectral Analysis of Shot Noise : Another characteristic of the shot noise is its power spectrum, which we are about to describe. Let each photoelectron generated within the detector give rise to an output electric current or voltage waveform $h(t)$†. The collective output $\psi(t)$ is thus written as

$$\psi(t) = \sum_i eh(t - t_i) , \tag{14}$$

where e is the electronic charge and t_i is the instant of time at which the i'th electron has been released. Let us confine attention temporarily to that part of $\psi(t)$ which belongs to the finite time interval $[-T, T]$; later, T will be allowed to approach infinity in order to eliminate the consequences of this truncation. The Fourier transform of the truncated $\psi(t)$ is given by

$$\Psi_T(f) = \int_{-T}^{T} \psi(t) \exp(-i2\pi ft)\, dt = e \sum_i \exp(-i2\pi ft_i) \int_{-\infty}^{\infty} h(t) \exp(-i2\pi ft)\, dt$$

$$= e\, H(f) \sum_i \exp(-i2\pi ft_i) . \tag{15}$$

---

† Quite generally, $h(t)$ may describe the response of a cascade of elements from the detector itself to amplifiers, to filters, to signal processing circuitry, so long as all these elements are linear.

$H(f)$ is the Fourier transform of $h(t)$, which is usually referred to as the detection system's transfer function. The power spectral density of $\psi(t)$ is defined as

$$\mathcal{S}_\psi(f) = \underset{T \to \infty}{Lim} \; < \frac{1}{2T} \; |\Psi_T(f)|^2 >, \tag{16}$$

where the brackets signify statistical averaging over all possible output functions $\psi(t)$. In Eq. (16) the normalization by $2T$ ensures that the integral of the spectral density function $\mathcal{S}_\psi(f)$ over the entire range of frequencies remains finite. Now, replacing for $\Psi_T(f)$ from Eq. (15) into Eq. (16) yields

$$\mathcal{S}_\psi(f) = e^2 \; |H(f)|^2 \underset{T \to \infty}{Lim} \; < \frac{1}{2T} \sum_i \sum_j \exp\left[-i2\pi f(t_i - t_j)\right] >. \tag{17}$$

Separating the terms with $i = j$ from those with $i \neq j$, Eq. (17) is rewritten as

$$\mathcal{S}_\psi(f) = e^2 \; |H(f)|^2 \underset{T \to \infty}{Lim} \left\{ (\frac{1}{2T} \sum_i 1) \; + \; < \frac{1}{2T} \underset{i \neq j}{\sum_i \sum_j} \exp\left[-i2\pi f(t_i - t_j)\right] > \right\}. \tag{18}$$

The first bracketed term on the right-hand-side of the above equation is the average number of photoelectrons released in $[-T, T]$. As for the second term, it may be decomposed and expressed as the product of terms containing i and j only, since different electrons are released independently. Thus

$$\mathcal{S}_\psi(f) = e^2 \; |H(f)|^2 \underset{T \to \infty}{Lim} \left\{ \frac{1}{2T} \langle n \rangle \; + \; \frac{1}{2T} \langle n(n-1) \rangle \left| \frac{\left| \int_{-T}^{T} P_0(t) \exp(-i2\pi ft) \, dt \right|^2}{\int_{-T}^{T} P_0(t) \, dt} \right| \right\}. \tag{19}$$

Replacing for $\langle$ n $\rangle$ and $\langle$ n^2 $\rangle$ from Eqs. (9) and (10), we obtain

$$
\mathcal{S}_\psi(f) = |H(f)|^2 \underset{T \to \infty}{\mathcal{L}im} \left\{ \frac{e\eta_s}{2T} \int_{-T}^{T} P_0(t) \, dt + \frac{\eta_s^2}{2T} \left| \int_{-T}^{T} P_0(t) \exp(-i2\pi f t) \, dt \right|^2 \right\}
\tag{20}
$$

Equation (20) is the main result of this section and contains several important pieces of information. First, it shows that the transfer function of the system, $|H(f)|^2$, simply multiplies the total spectrum. Second, the shot noise spectral density (first term on the right-hand-side) is independent of frequency, but proportional to the average incident power. Third, the spectrum of the optical signal $P_0(t)$, aside from the addition of the shot noise and multiplication by $|H(f)|^2$, is fully reproduced within the spectrum of the signal $\psi(t)$.

The power spectral density of the shot noise is flat (i.e., frequency-independent) and is given by

$$
N_{shot}(f) = e\eta_s \langle P_0(t) \rangle .
\tag{21}
$$

In Eq. (21) the brackets are used to indicate time-averaging (as opposed to ensemble averaging). Assuming that the overall gain is unity, the system's bandwidth B may be defined as follows :

$$
B = \frac{1}{2} \int_{-\infty}^{\infty} |H(f)|^2 \, df .
\tag{22}
$$

The factor 1/2 in this equation is due to $H(f)$ having both positive and negative frequency components. The total (integrated) shot noise power within a given bandwidth then becomes

$$
< i_{shot}^2 > = \int_{-B}^{B} N_{shot}(f) \, df = 2e\eta_s \langle P_0(t) \rangle B .
\tag{23}
$$

The total signal power is the integral of its spectral density over the entire frequency range. Assuming that the system transfer function $H(f)$ does not enhance, attenuate, or otherwise modify the spectrum of $P_0(t)$, we write

$$\text{Signal Power} = \eta_s^2 \lim_{T \to \infty} \int_{-\infty}^{\infty} \frac{1}{2T} \left| \int_{-T}^{T} P_0(t) \exp(-i2\pi ft) \, dt \right|^2 df$$

$$= \eta_s^2 \lim_{T \to \infty} \frac{1}{2T} \int_{-T}^{T} P_0^2(t) \, dt$$

$$= \eta_s^2 \langle P_0^2(t) \rangle . \tag{24}$$

In writing the second equality above we have invoked Parseval's theorem [2], which states that the area under the graph of the squared modulus of a given function is equal to the area under the graph of the squared modulus of the Fourier transform of that function.

Using Eqs. (23) and (24), one can now write the signal-to-shot-noise ratio as follows :

$$\boxed{\text{SNR} = 10 \log_{10} \left[\frac{\eta_s^2 \langle P_0^2(t) \rangle}{2e\eta_s \langle P_0(t) \rangle B} \right]} \tag{25}$$

Example 2 : Equivalent noise power (ENP) for a photodetector is usually defined as the incident light power which produces a signal amplitude equal to the noise amplitude. For shot noise, the ENP can be calculated from Eq. (25) as $2eB/\eta_s$. Thus for a typical value of $\eta_s = 0.5 \; A/W$, ENP for a shot-noise-limited detector is $6.4 \times 10^{-19} \; W/Hz$.

Dark-Current Noise : As mentioned in the preceding section, dark-current noise of photodiodes is closely related to the photon shot noise. Their similarity arises from the fact that dark-current electrons, which are thermally generated, are produced randomly and independently of each other. If the bulk of the semiconductor which comprises the photodiode is kept at a constant temperature, then the rate of generation of the dark-current electrons is constant. Denoting the average dark current by I_d, the corresponding noise spectral density (in $Amp/\sqrt{Hz}$) will be

$$i_{dark} = \sqrt{2eI_d} \ . \tag{26}$$

In practice the noises of the entire electronic circuitry (including the dark-current noise of the photodiodes) are lumped together and treated as a single component of the total system noise.

4. The Laser Noise : The laser light amplitude E is not constant, but varies randomly with time. Its fluctuations are rooted in the instabilities of the laser cavity which results in mode hopping and mode competition [3-5]. One can write the following expression for the amplitude of the light beam :

$$E(t) = E_0 \left[1 + \delta_e(t) \right] \exp (-i\omega t) \tag{27}$$

where $\delta_e(t)$ is a dimensionless, complex quantity with $|\delta_e(t)| \ll 1$ for all times t. Figure 2 is a diagram showing $1 + \delta_e(t)$ as the sum of two vectors in the complex plane. Assuming that the complex phase of $\delta_e(t)$ can assume all values between 0 and 2π, it is observed that $1 + \delta_e(t)$ is confined to a small disk centered at $(1,0)$ in the complex plane.

The laser power is proportional to the electric field intensity and is therefore given by :

$$P(t) \propto |E_0|^2 \left[1 + \delta_e(t) + \delta_e^*(t) + |\delta_e(t)|^2 \right] \simeq P_0 \left\{ 1 + 2 \, \text{Real} \left[\delta_e(t) \right] \right\}. \tag{28}$$

The rms fluctuations of the laser power are thus equal to $2P_0\Delta_e$ where

$$\Delta_e = \sqrt{ < \text{Real}^2 \left[\delta_e(t) \right] > }. \tag{29}$$

Unlike the spectra of shot noise and Johnson noise, the spectrum of $\delta_e(t)$ is not necessarily flat. In general, the frequency response of any measurement system has a finite range and a nonuniform magnitude, thus requiring that the spectral content of $\delta_e(t)$ be properly trimmed and adjusted, before using it in Eq. (29) to calculate the rms noise value.

When one measures the spectrum of the laser power fluctuations using a photodetector (i.e., intensity detection), one obtains a trace on the spectrum analyzer which, in addition to the desired spectrum, contains contributions from the shot noise and the thermal noise of the detection circuitry. The thermal noise, however, may be measured independently by observing the detector output when the beam is blocked, and the shot noise may be estimated from Eq. (23) using the average incident

light power P_0. It may also happen that the fluctuations of $\delta_e(t)$ have a limited frequency content, in which case the noise outside the range of frequencies of $\delta_e(t)$ is identified as the sum of shot noise and electronic noise. Since both the shot and thermal noises have flat spectra, one can then proceed to subtract their contributions from the total spectrum and obtain the spectrum of the laser power fluctuations[†].

Example 3 : Figure 3 shows the measured noise spectra at the output of the laser monitor in a typical experiment (see Fig. 1). The lower trace corresponds to the electronic noise which is monitored in the absence of the light beam, and the upper trace shows the total noise with an incident light power of $P_0 = 380\ \mu W$. The PIN photodiode/amplifier used for these measurements had a sensitivity of $\eta_s = 0.42\ A/W$ at the laser wavelength of 680 nm, and a gain (i.e., current to voltage conversion factor) of $G = 10^4\ V/A$. The electronic noise level read from Fig. 3 is -84 dBm. This is the power delivered to a 50 Ω resistor in a bandwidth of 30 kHz; thus the rms thermal noise voltage at the amplifier output is $v_{th} = 80\ nV/\sqrt{Hz}$, and the corresponding noise current at the output of the photodiode prior to amplification is $i_{th} = 8\ pA/\sqrt{Hz}$. The shot noise current density is calculated from Eq. (23) as follows :

$$i_{sh} = \sqrt{2e\ \eta_s\ P_0} = \sqrt{2 \times 1.6 \times 10^{-19} \times 0.42 \times 380 \times 10^{-6}} = 7.2\ pA/\sqrt{Hz}.$$

Since the total noise power in Fig. 3 is about 14 dB (i.e., a factor of 25) above the thermal noise level, we have

$$\frac{i_{th}^2 + i_{sh}^2 + i_{laser}^2}{i_{th}^2} = 25,$$

[†]Since the shot noise spectral level is proportional to P_0, whereas that of the laser power fluctuations is proportional to P_0^2, it is tempting to suggest that a plot of the total noise power versus P_0 should behave as $a + bP_0 + cP_0^2$, from which one can sort out the individual contributions. The problem with this approach, however, is that $\delta_e(t)$ itself may depend in an unknown manner on P_0, causing the argument to fail.

from which we find $i_{laser} = 38.5\ pA/\sqrt{Hz}$. This is the rms current fluctuation caused by the laser noise at the photodiode output (prior to amplification). The laser noise may be normalized by the average laser power and stated as a relative intensity noise (RIN), that is,

$$\text{RIN} = 20\ \log\ (i_{laser}/\eta_s P_0) = 20\ \log\ \frac{38.5 \times 10^{-12}}{0.42 \times 380 \times 10^{-6}} \simeq -132.5\ dB.$$

Since the laser noise spectrum in Fig. 3 is relatively flat through the frequency range $f = 0$ to $f = 10$ MHz, one can easily integrate the RIN over the entire 10 MHz bandwidth of the system and obtain the figure of -62.5 dB for the integrated RIN. Comparison with Eqs. (28) and (29) then shows that the rms value of *Real* $[\delta_e(t)]$, confined to a 10 MHz bandwidth, is $\Delta_e \simeq 4 \times 10^{-4}$.

Example 4 : The spectra shown in Fig. 4 correspond to the output of a laser monitor which is a low-noise, hybrid PIN photodiode/amplifier with a sensitivity of $\eta_s = 0.5\ A/W$ at $\lambda = 830$ nm [7]. The detector's current to voltage conversion factor is $G = 3.64 \times 10^4\ V/A$. The lower trace shows the spectrum of the detector output in the absence of light. The -88 dBm electronic noise level corresponds to $v_{th} = 51\ nV/\sqrt{Hz}$ at the amplifier output and to $i_{th} = 1.4\ pA/\sqrt{Hz}$ at its input. The upper trace was obtained when 39 μW of laser light was incident on the detector. From Eq. (23) the shot noise current density (prior to amplification) is found to be $i_{sh} = 2.5\ pA/\sqrt{Hz}$, thus

$$(i_{th}^2 + i_{sh}^2)/i_{th}^2 \simeq 4.2 = 6.2\ dB.$$

Therefore, the thermal-plus-shot noise level must be about 6.2 dB above the thermal noise level in Fig. 4. The remaining noise is due to fluctuations of the laser power, which may now be separated out. Let us approximate the frequency-dependence of the total noise density in Fig. 4 with a linear function as follows :

$$10\ \log\left[\frac{i_{th}^2 + i_{sh}^2 + i_{laser}^2}{i_{th}^2}\right] \simeq 23 - 1.3\ f \qquad\qquad (f\ \text{in MHz}).$$

This expression leads to the following frequency-dependence for the laser noise :

$$(i_{laser}/i_{th})^2 \simeq -4.2 + 200 \exp(-0.3 \, f) \qquad (f \text{ in MHz}).$$

The above function is now averaged over the frequency range from $f = 0$ to $f = 10$ MHz, yielding the average value of 59 for $(i_{laser}/i_{th})^2$. Thus the average noise current arising from the laser power fluctuations (within a 10 MHz bandwidth) is $i_{laser} \simeq 10.75 \, pA/\sqrt{Hz}$. Normalization by $\eta_s P_0$ yields an average RIN of -125.2 dB, and the rms value of the E-field fluctuations over the 10 MHz bandwidth of interest is $\Delta_e \simeq 8.7 \times 10^{-4}$.

5. Noise Due to Disk Surface Reflectivity Fluctuations and Depolarization : In the following analysis it will be assumed that the disk spins at a constant speed, and that the noise is measured on an erased track, that is, one with no reverse-magnetized domains. The effective light power incident on the disk surface is denoted by P_0, and the losses due to reflections from or transmissions through the various optical elements in the system are ignored. (If need be, however, such losses can easily be incorporated into the results later.) The three sources of noise considered here include : *i*) amplitude and phase variations of the X-polarized reflected light; *ii*) random depolarization of the incident (X-polarized) beam; and iii) amplitude and phase fluctuations of the magneto-optically generated component of polarization along Y [8-11]. The physical mechanisms responsible for these noises are described below.

For various reasons, there will be fluctuations in the effective reflectivity r_x for the X-component of polarization. First, the material composition and/or structure varies across the disk. Second, if there are grooves on the disk surface, their edge roughness is likely to scatter the light in a random fashion. Third, there are residual amounts of off-track and defocus errors that vary with time and, therefore, cause the reflectivity to fluctuate. Some of these noise sources are fixed on the disk and, consequently, their time-dependencies scale with the disk velocity; others, such as those due to mechanical vibrations or focus/track errors, are caused by fluctuations elsewhere in the system and do not scale with the velocity. In any event, assuming that these fluctuations are small, one writes :

$$r_x(t) = r_{xo}\left[1 + \delta_x(t)\right]; \quad |\delta_x| << 1 \tag{30}$$

where $\delta_x(t)$ is a small, dimensionless, complex coefficient, representing the fractional variations of r_x.

There exists the possibility of conversion of some of the X-polarized incident light into Y-polarized reflected light due to depolarization, as distinct from the magneto-optic conversion. This phenomenon is partly due to substrate-birefringence, but is also caused by the various scattering mechanisms at work on the disk surface. Perhaps the best way to characterize the depolarization contribution to noise is by defining a disk reflection coefficient r_{xy} as follows :

$$r_{xy}(t) = r_{xo}\, \delta_{xy}(t)\,; \qquad |\delta_{xy}| \ll 1 \qquad\qquad (31)$$

where, as before, $\delta_{xy}(t)$ is a small, dimensionless, complex coefficient.

Finally, there is the magneto-optic contribution to the Y-polarized reflected light. For a completely erased track, one may write the Y-component of the reflectivity as follows :

$$r_y(t) = r_{yo}\left[1 + \delta_y(t)\right]\,; \qquad |\delta_y| \ll 1\,. \qquad\qquad (32)$$

Some of the fluctuations in r_y originate from the structural/magnetic variations of the disk material along the length of the track, but there is also a correlation between fluctuations in r_y and those in r_x. For instance, if more X-polarized light is reflected, then less light will be available to interact with the magnetization of the material and produce the Y-polarized component. For the sake of simplicity, we shall ignore all possible correlations among δ_x, δ_{xy}, and δ_y, and treat these parameters as independent random variables.

The phase compensator in the data detection branch of the readout system of Fig. 1 eliminates the nominal ellipticity of the beam by bringing r_{xo} and r_{yo} in phase with each other. Consequently, we assume at the outset that r_{yo}/r_{xo} is real and, to emphasize its realness, we shall write it as $|r_{yo}/r_{xo}|$. The compensator will have no influence whatsoever on the noise coefficients δ_x and δ_y, and will modify δ_{xy} only by the addition of an irrelevant constant phase angle. The power incident on individual detectors is thus written as :

$$P_1,\, P_2 \propto \left| \frac{E_0}{\sqrt{2}} (1 + \delta_e) \left[\gamma\, r_{xo}\, (1 + \delta_x) \pm r_{xo}\, \delta_{xy} \pm r_{yo}\, (1 + \delta_y) \right] \right|^2$$

where the plus (minus) sign applies to the incident power P_1 (P_2) on detector #1 (#2). Expanding the above expression and ignoring the second order terms in the noise variables, we find the photocurrents S_1 and S_2 of the detectors as follows :

$$S_1, S_2 \simeq \frac{1}{2} \eta_s P_0 \left[\gamma \left| r_{xo} \right| \pm \left| r_{yo} \right| \right]^2$$

$$+ \eta_s P_0 \left| r_{xo} \right|^2 \left[\gamma \pm \left| \frac{r_{yo}}{r_{xo}} \right| \right] \text{ Real} \left[\gamma (\delta_e + \delta_x) \pm \delta_{xy} \pm \left| \frac{r_{yo}}{r_{xo}} \right| (\delta_e + \delta_y) \right] . \tag{33}$$

The sum of the two detector signals is thus given by

$$S_1 + S_2 \simeq \eta_s P_0 \gamma^2 \left| r_{xo} \right|^2 \left[1 + \left| r_{yo} / \gamma r_{xo} \right|^2 \right]$$

$$+ 2\eta_s P_0 \left| r_{xo} \right|^2 \left\{ \gamma^2 \text{ Real} \left[\delta_e + \delta_x \right] + \left| \frac{r_{yo}}{r_{xo}} \right| \text{ Real} \left[\delta_{xy} \right] + \left| \frac{r_{yo}}{r_{xo}} \right|^2 \text{ Real} \left[\delta_e + \delta_y \right] \right\} \tag{34}$$

The first term on the right-hand-side of Eq. (34) is the average photocurrent signal of the two detectors. The second term represents the fluctuations of this signal, and consists of three contributions : The contributions due to the laser noise δ_e and the noise in the X-component of reflectivity δ_x are proportional to γ^2. The second contribution comes from depolarization noise δ_{xy} and is proportional to $\left| r_{yo} / r_{xo} \right|$. Note that individual channels have a much larger noise component arising from depolarization, but in adding the two channels, much of this noise cancels out. The third contribution is a combination of the laser noise δ_e and the noise in the magneto-optic component of the reflected light δ_y; it is proportional to $\left| r_{yo} / r_{xo} \right|^2$. In practice, $\left| r_{yo} / r_{xo} \right|$ is usually much smaller than γ^2 and, therefore, the second and third contributions to the noise may be neglected. Under these circumstances the total fluctuations of the sum signal arise from electronic noise, shot noise, laser noise, and the r_x noise. Since all but the last of these fluctuations can be measured when the disk is stopped, the excess noise observed upon spinning the disk is attributed to the r_x contribution.

The output of the differential detection system is proportional to the difference of the two detector signals, namely,

$$S_1 - S_2 \simeq 2\eta_s P_0 \gamma \left| r_{xo} \right| \left| r_{yo} \right| \left\{ 1 + \text{Real} \left[2\delta_e + \delta_x + \delta_y \right] + \left| \frac{r_{xo}}{r_{yo}} \right| \text{Real} \left[\delta_{xy} \right] \right\} . \tag{35}$$

The first term on the right-hand-side of this equation is the magneto-optic signal, observed in the erased state of the disk. The second term is the combined contribution of the laser noise δ_ℓ and the reflectivity noises δ_x and δ_y; depolarization noise δ_{xy} constitutes the third term. Note that the depolarization term has a larger coefficient than the other noise term, and may therefore be the dominant noise in magneto-optical readout.

One observes that in going from the sum signal of Eq. (34) to the difference signal of Eq. (35), the contribution of $(\delta_\ell + \delta_x)$ is attenuated by a factor of $|r_{yo}/\gamma r_{xo}|$. The reason is that the laser noise and the r_x noise are identical in the two channels and, for a balanced system, they cancel out. The residual noise observed in this instance is due to the interference with the magneto-optic component, r_{yo}. The same thing, of course, happens to the r_y noise, but there the interference with r_x creates a term larger than the original r_y noise; that is why the coefficient of $(\delta_\ell + \delta_y)$ in the difference signal is larger than that in the sum signal by a factor of $|\gamma r_{xo}/r_{yo}|$. Similar considerations apply to the depolarization noise δ_{xy}.

The signals S_1 and S_2 of the individual detectors may themselves be written in terms of the sum and difference signals in the following way :

$$S_1, S_2 = \frac{1}{2}(S_1 + S_2) \pm \frac{1}{2}(S_1 - S_2) \tag{36}$$

It thus becomes clear that the sum signal is the common-mode signal, shared by the two detectors and rejected only by the differential amplifier. Practical differential amplifiers, unfortunately, have a finite common-mode-rejection-ratio (CMRR), and the noise accompanying the sum signal in Eq. (34) also appears at the output, albeit after a substantial attenuation. In the remainder of this section we shall assume that the differential amplifier has a large CMRR, and thus proceed to ignore the common-mode noise.

The rms values of the various fluctuating parameters (within the bandwidth of the system) are now defined as follows :

Appendix F

$$\Delta_x = \sqrt{< \text{Real}^2 \left[\delta_x(t)\right] >}$$

(37a)

$$\Delta_y = \sqrt{< \text{Real}^2 \left[\delta_y(t)\right] >}$$

(37b)

$$\Delta_{xy} = \sqrt{< \text{Real}^2 \left[\delta_{xy}(t)\right] >}$$

(37c)

The total signal and the rms noise (including thermal and shot noises but excluding the residual common-mode noise) at the differential output are thus written as

$$i_{signal} \simeq 2\, \eta_s\, P_0 \gamma\, |r_{xo}|\, |r_{yo}|$$

(38)

$$i_{noise}^2 \simeq \left\{ 2 i_{th}^2 + 2e\, \eta_s P_0 \gamma^2\, |r_{xo}|^2 \left[1 + |r_{yo}/\gamma r_{xo}|^2\right] \right\} B$$
$$+ \left(2\eta_s P_0 \gamma\, |r_{xo}|\, |r_{yo}|\right)^2 \left(4\Delta_e^2 + \Delta_x^2 + \Delta_y^2 + |r_{xo}/r_{yo}|^2\, \Delta_{xy}^2\right)$$

(39)

From a practical system design standpoint, there is an advantage in choosing γ as small as possible, so that the most light can get through to the disk during the writing process. However, Eqs. (38) and (39) indicate that γ cannot be made too small either, since in that eventuality the thermal noise becomes dominant and the overall signal-to-noise ratio (SNR) suffers. γ must therefore be large enough to bring the total noise level well above the level of the thermal noise. In the ideal case, when γ is sufficiently large to make the thermal noise negligible, the SNR becomes independent of γ and can be expressed as follows :

$$SNR_{ideal} \simeq \frac{2\eta_s P_0\, |r_{yo}|^2}{eB\left[1 + |r_{yo}/\gamma r_{xo}|^2\right] + 2\eta_s P_0\, |r_{yo}|^2 \left[4\Delta_e^2 + \Delta_x^2 + \Delta_y^2 + |r_{xo}/r_{yo}|^2\, \Delta_{xy}^2\right]}$$

(40)

Of course, the ideal SNR is never attained in practice, but it can be approached closely. From Eq. (39) the critical value γ_c of γ, at which the thermal noise strength equals the combined strength of all the other noises, is given by

$$\gamma_c^2 = \frac{i_{th}^2}{e\,\eta_s P_0\,|r_{xo}|^2\left\{1 + |r_{yo}/\gamma r_{xo}|^2 + 2\,(\eta_s/eB)\,P_0\,|r_{yo}|^2\left[4\Delta_e^2 + \Delta_x^2 + \Delta_y^2 + |r_{xo}/r_{yo}|^2\,\Delta_{xy}^2\right]\right\}} \quad (41)$$

When $\gamma = \gamma_c$, the SNR is only 3 dB below its ideal value; when $\gamma = 2\gamma_c$, the gap shrinks to 1 dB, and with $\gamma = 3\gamma_c$, the ideal SNR is only 0.5 dB away. Further increases of γ beyond these values are hardly justified; in fact, for large values of γ, the common-mode noise begins to appear in the differential output, causing the SNR to deteriorate.

According to Eq. (40), beyond the shot noise limit one is in a regime where the dominant noise is proportional to the signal; therefore, increasing the laser power P_0 does not enhance the SNR. In this regime, if the depolarization noise δ_{xy} happens to be an important contributor, then increasing r_{yo} will diminish the noise. On the other hand, if the laser noise δ_e and/or the reflectivity noises δ_x and δ_y are dominant, increases in r_{yo} will have no effect on the SNR. These are some of the issues to contemplate in optimizing the readout system.

Example 5 : Consider the readout system of Fig. 1, operating under the following conditions : laser wavelength $\lambda = 680$ nm, effective laser power incident on the disk $P_0 = 2$ mW, disk reflectivity $r_x = 0.5$, disk magneto-optic reflection coefficient $r_y = 0.005$, leakage parameter of the beam-splitter $\gamma = 0.4$, photodetector sensitivity $\eta_s = 0.42$ A/W, preamplifier conversion factor $G = 3.3 \times 10^4$ V/A, and differential amplifier's gain $= 13$. The laser noise for this system was analyzed in Example 3, and the rms fluctuations of the E-field were found to be $\Delta_e \simeq 4 \times 10^{-4}$.

Figure 5(a) shows the spectra of the differential amplifier's output voltage, measured with the light blocked from both detectors (lower trace), and with the light reaching the detectors while the disk was stopped (upper trace). The electronic noise level at -65 dBm is the sum of contributions

from the two detectors and the differential amplifier. Referred to individual photodiode currents (prior to amplification), this thermal noise has a density of $i_{th} \simeq 1.2 \ pA/\sqrt{Hz}$. The shot noise current density for the 40 μW of incident power on each photodiode is calculated as $i_{sh} \simeq 2.3 \ pA/\sqrt{Hz}$. This means that the thermal-plus-shot noise level is about 6.7 dB above the thermal noise, as is indeed the case in Fig. 5(a). Apparently, the laser noise does not contribute much to the upper trace in Fig. 5(a), in agreement with Eq. (39) which predicts a laser noise current density of 0.4 $pA/\sqrt{Hz}$ at the output of the differential amplifier. (The common-mode contribution of the laser noise, estimated from Eq. (34), is also negligible. Assuming the reasonable value of CMRR = 100, the common-mode laser noise appearing at the differential output is only about 0.04 $pA/\sqrt{Hz}$.)

Figure 5(b) shows two spectra of the differential amplifier's output with the disk spinning. The lower trace corresponds to an erased track, while the upper trace contains a recorded 8 MHz carrier signal. The erased track is about as noisy as the recorded one, leading one to believe that jitter and other signal fluctuations do not contribute much to the noise. Integrating the erased-state noise over the frequency range from $f = 0$ to $f = 10$ MHz, we obtain the figure of -30 dBm. This is the total noise power delivered to a 50 Ω resistor at the amplifier's output, and corresponds to an rms noise voltage of 7 mV. Dividing by the net gain of the system, the equivalent rms noise current is found to be 16.3 nA. After subtracting the contributions from thermal and shot noises, we find the remaining rms noise to be 11.5 nA which, according to Eq. (39), can arise from a small amount of depolarization noise ($\Delta_{xy} \simeq 0.7 \times 10^{-4}$). Of course, reflectivity fluctuations could as well be responsible for the observed noise, but the necessary values of Δ_x or Δ_y must be larger than Δ_{xy} by a factor of $|r_{xo}/r_{yo}| = 100$.

Finally, **Fig.** 5(c) shows the spectrum of the differential output with one of the two detectors blocked. Although the erased-track spectrum is not shown here, it is reasonable to neglect the noise associated with the signal (i.e., jitter and signal amplitude fluctuation noise). The integrated noise power within the 10 MHz bandwidth of the system is -30 dBm, corresponding to a preamplification rms noise current of 16.3 nA. Subtracting the thermal noise (of two detectors) and the shot noise (of one detector) from this figure, we find the remaining noise current to be 13.6 nA. According to Eq. (33), this noise is almost exclusively due to laser power fluctuations, thus ruling out the possibility

of a large r_x noise. One concludes, therefore, that the differential output noise (with neither detector

blocked) is due either to a small Δ_{xy} or a large Δ_y, but not a large Δ_x.

Example 6 : Consider the readout system of Fig. 1, operating under the following conditions : laser

wavelength λ = 830 nm, effective laser power incident on the disk P_0 = 2 mW, disk reflectivity

r_x = 0.4, disk magneto-optic reflection coefficient r_y = 0.004, leakage parameter of the beam-splitter

γ = 0.35, photodetector sensitivity η_s = 0.5 A/W, preamplifier conversion factor G = 3.3 × 10^4 V/A,

and differential amplifier gain = 18. The laser noise for this system was analyzed in Example 4, and

the rms fluctuations of the E-field were found to be $\Delta_e \simeq 8.7 \times 10^{-4}$.

Figure 6 shows the measured spectra of the differential amplifier's output voltage under various

circumstances. With the light blocked from both detectors the electronic noise level is at -62 dBm

(lower trace in Fig. 6(a)). Referred to individual photodiode currents (prior to amplification), this

thermal noise has a density of $i_{th} \simeq 1.2$ $pA/\sqrt{Hz}$. The shot noise current density for the 20 μW of

incident power on each photodiode is calculated as $i_{sh} \simeq 1.8$ $pA/\sqrt{Hz}$. This means that the thermal-

plus-shot noise level is about 5 dB above the thermal noise. (See the middle trace in Fig. 6(a) which

shows the output noise spectrum with light reaching both detectors while the disk is stopped.) The

laser noise contributes only 0.5 dB in this case since, according to Eq. (39), its current density is

0.6 $pA/\sqrt{Hz}$. (The common-mode contribution of the laser noise, estimated from Eq. (34), is

negligible : if CMRR = 100, the common-mode laser noise at the differential output is only about

0.1 $pA/\sqrt{Hz}$.)

The upper trace in Fig. 6(a) shows the spectrum of the differential output with the disk spinning

and the track containing a 4 MHz carrier signal. Assuming the erased track has the same level of

noise as the recorded one (i.e., ignoring jitter noise and other signal fluctuations) we integrate the

noise from f = 0 to f = 10 MHz and obtain the figure of -27 dBm. This is the noise power delivered

to a 50 Ω resistor at the amplifier's output, and corresponds to an rms noise voltage of 10 mV.

Dividing by the net gain of the system, the equivalent rms noise current is found to be 16.8 nA.

After subtracting the contributions of the thermal noise and the shot noise, we find the remaining rms

noise to be 13.7 nA which, according to Eq. (39), can arise from a small amount of depolarization

noise ($\Delta_{xy} \simeq 1.2 \times 10^{-4}$). Of course, reflectivity fluctuations could as well be responsible for the observed noise, but the necessary values of Δ_x or Δ_y must be larger than Δ_{xy} by a factor of $|r_{xo}/r_{yo}| \approx 100$.

Figure 6(*b*) shows the spectrum of the differential output with one of the two detectors blocked. Again, the erased-track spectrum is not shown here, but it is reasonable to neglect the noise associated with the signal. The integrated noise power within the 10 MHz bandwidth of the system is -24 dBm, corresponding to a preamplification rms noise current of 23.7 nA. Subtracting the thermal noise (of two detectors) and the shot noise (of one detector) from this figure, we find the remaining noise current to be 22.4 nA. According to Eq. (33), this noise arises from laser power fluctuations Δ_ℓ, reflectivity fluctuations Δ_x, and depolarization Δ_{xy}. Using the known values of Δ_ℓ and Δ_{xy} in Eq. (33), we find $\Delta_x = 6.6 \times 10^{-4}$. One concludes, therefore, that the output noise when neither detector is blocked is due either to a small Δ_{xy} or a large Δ_y, but not a large Δ_x.

6. Jitter and Signal-Amplitude Fluctuations : In this section we present computer simulation results pertaining to the noise arising from fluctuations of the information-carrying signal. Distinction will be made between jitter, which is caused by random variations of the zero-crossings of the signal waveform, and signal-amplitude-fluctuation noise. The basic waveform considered here is a 4 MHz, 50% duty-cycle carrier signal whose amplitude alternates periodically between the values of +1 and -1, transitions between the two levels of the signal being infinitely sharp. The power spectrum of this waveform was computed numerically, and the result is shown in Fig. 7. The (approximate) sampling intervals in the time and frequency domains were, respectively, 0.5 ns and 30 kHz, corresponding to a total number of samples Nmax = 65536. The spectrum contains the first and third harmonics of the waveform at 4 MHz and 12 MHz. With the unity power of the square-wave signal corresponding to 0 dB, the fundamental and the third harmonic power levels are at -0.912 dB and -10.455 dB, respectively. In Fig. 7 the spikes at frequencies other than 4 and 12 MHz are numerical noise due to truncation errors, their very small magnitudes attesting to the basic accuracy of the numerical routine.

Next, we introduced jitter in the transition times of the signal. A random number generator selected values in the interval $[-\Delta t, \Delta t]$ with uniform distribution. These random numbers were then added independently to individual transition times of the ideal signal, creating a waveform with jitter magnitude of Δt. As an example, Fig. 8 shows a section of the signal between $t = 0$ and $t = 2$ μs, with $\Delta t = 25$ ns of jitter. The computed power spectra of the resulting noisy signals are shown in Figs. 9(a)-(d) which correspond, respectively, to jitter magnitudes of $\Delta t = 3, 5, 15$ and 25 ns. (The spectral power densities are computed in a 30 kHz bandwidth.) Note that within the bandwidth of interest the spectra are relatively flat and that, understandably, their levels rise with the increasing magnitude of jitter.

Effects of amplitude fluctuations on the signal waveform and its power spectrum are shown in Fig. 10. Figure 10(a) is a section of a jitter-free waveform, exhibiting random amplitude variations in its upper half; the values of these signal amplitudes were chosen randomly and independently from the interval [0.85, 1.00] with a uniform probability distribution. The corresponding power spectrum in Fig. 10(b) shows a significant noise contribution only at low frequencies. A similar conclusion is

arrived at upon inspecting the spectrum of Fig. 10(c), which corresponds to a signal whose positive amplitude fluctuates within [0.70, 1.00] and has, in addition, a jitter noise component with $\Delta t = 3$ ns. Comparison with Fig. 9(a) clearly indicates that the high frequency noise is solely due to jitter, whereas at low frequencies the noise may be attributed to the amplitude fluctuations.

Finally, Fig. 11(a) shows a section of a signal waveform with positive amplitude fluctuations within [0.70, 1.00], negative amplitude fluctuations within [-1.00, -0.70], and jitter magnitude of $\Delta t = 3$ ns. The corresponding spectrum in Fig. 11(b) shares its general features with that in Fig. 10(c), but it has a larger noise content in the low frequency regime which is, of course, expected. The spectrum in Fig. 11(c) is obtained when the jitter magnitude is increased to $\Delta t = 15$ ns while amplitude fluctuations are maintained at their previous level. The noise in this instance is almost exclusively due to jitter, as a comparison with Fig. 9(c) indicates.

Effects of Finite Beam Size on Signal and Noise Spectra : Up to this point we have ignored the fact that the focused spot on the disk surface has a finite diameter. The effects of the finite spot size are readily incorporated into the preceding results if one ignores the diffraction effects. The signal at the output of the readout system is then obtained by convolving the intensity profile of the spot with the recorded pattern of information on the disk. For the sake of simplicity let us assume a Gaussian intensity distribution for the spot as follows :

$$I(x) = \frac{1}{\sqrt{\pi \rho^2}} \exp\left(-x^2/\rho^2\right) . \tag{42}$$

Here x is the spatial coordinate on the disk surface along the track, and ρ is a measure of the spot size (FWHM $= 1.66\,\rho$). The function in Eq. (42) is properly normalized so that the integrated spot intensity is unity. If the actual pattern of recorded data along the track is denoted by $\psi_0(x)$, and if v_0 is the disk velocity, then the output signal will be

$$\psi\,(v_0 t) = \int_{-\infty}^{\infty} I(x)\;\psi_0\,(x - v_0 t)\,dx\;. \tag{43}$$

The function $\psi(x)$, the result of convolution between $I(x)$ and $\psi_0(x)$, is scaled along the horizontal axis by the factor v_0 in order to yield the time dependence of the observed signal. Upon Fourier transformation, the convolution turns into the product of the Fourier transforms of the individual functions, that is,

$$\mathcal{F}\left\{\psi\,(v_0 t)\right\} = v_0\,\mathcal{F}\left\{I\,(v_0 t)\right\}\,\mathcal{F}\left\{\psi_0\,(v_0 t)\right\}. \tag{44}$$

The transform of the Gaussian function is readily calculated as follows :

$$v_0\,\mathcal{F}\left\{I\,(v_0 t)\right\} = \exp\left\{-\,(\pi\rho/v_0)^2\,f^2\right\}. \tag{45}$$

If the spectra of $\psi_0\,(v_0 t)$ and $\psi\,(v_0 t)$ are denoted by $\mathcal{S}_{\psi_0}(f)$ and $\mathcal{S}_\psi(f)$, respectively, we will have

$$\boxed{\mathcal{S}_\psi(f) = \exp\left\{-\,2\,(\pi\rho/v_0)^2\,f^2\right\}\,\mathcal{S}_{\psi_0}(f)} \tag{46}$$

Equation (46) shows that the spectrum of the signal (including jitter and amplitude noise) is attenuated by a multiplicative factor that is the Fourier transform of the spot intensity distribution. In the literature, this effect is usually attributed to the *Modulation Transfer Function* (MTF) of the optical readout system. The frequency at which the spectrum is attenuated by a factor of 2 is a measure of the width of the MTF. According to this definition, the width of the Gaussian function in Eq. (46) is approximately equal to $v_0/5\rho$.

Example 7 : In Fig. 5(*b*) the recorded carrier is read from the disk at the constant velocity of $v_0 = 14\ m/s$. Assuming a Gaussian profile for the focused spot with FWHM = 1 μm (i.e.,

$\rho = 0.6 \ \mu m$), we find an MTF attenuation of 10 dB at $f = 8$ MHz. Similarly, in Fig. 6 where $v_0 = 10 \ m/s$ and $\rho = 0.7 \ \mu m$, the attenuation of the 4 MHz carrier is found from Eq. (46) to be 6.7 dB.

Of the various noises discussed in the present chapter, the spectra of the electronic, shot, and laser noise are obviously unaffected by the MTF. The spectrum of the disk noise, on the other hand, is attenuated in a manner similar to that of the information signal as described by Eq. (46). An example of this phenomenon may be seen in Fig. 12, where the spectrum of an erased track is shown for three different disk velocities [12]. In each case, the tail of the trace corresponds to thermal + shot + laser noise, which is velocity-independent. The low frequency magnitudes of the spectral density functions drop by 3 dB each time the velocity is doubled. This reflects the fact that the noise power is constant; in other words, when the velocity is doubled (causing the spectrum to stretch over a range of frequencies twice as large) the magnitudes of the spectral density drop by a factor of 2 (i.e., 3 dB) in order to maintain the total (integrated) power. If one assumes that the underlying sources of disk noise have flat spectra, then the curves of Fig. 12 are simply plots of the MTF.

Example 8 : In Fig. 12 the curve corresponding to $v_0 = 6$ m/s drops by about 12 dB between f = 0 and f = 4 MHz. Assuming that the curve represents the actual MTF of the system and that the MTF has the Gaussian form of Eq. (46), we find $\rho = 0.56 \ \mu m$, corresponding to FWHM = 0.93 μm.

PROBLEMS

9.1) In deriving Eq. (19) from Eq. (18) several steps were left out. Describe the missing steps and fill the gaps in the derivation.

9.2) Photomultiplier tubes (or avalanche photodiodes) multiply photo-induced electrons (or electron-hole pairs) and output G electrons for every captured photon. In general, G is not the same for all photons; instead, it should be considered a random variable with average $\langle G \rangle$ and square-average $\langle G^2 \rangle$. The multiplication process is rapid enough to be assumed instantaneous, and the value of G for a given photon is independent of that for any other photon. Assuming an incident laser beam with power $P_0(t)$, determine the spectra of signal and shot noise at the photomultiplier output.

9.3) Equation (33) was derived from the equation immediately preceding it, but the details of derivation were left out. Examine the approximations involved in this derivation and the conditions under which the second-order terms in δ_e, δ_x, δ_y and δ_{xy} may be ignored. Pay special attention to those remaining terms that contain r_{yo}, since in practice the magnitudes of $|r_{yo}/r_{xo}|$ and $|r_{yo}/\gamma r_{xo}|$ are likely to be comparable to δ_e, δ_x, etc.

9.4) Obtain the first few terms in the Fourier series representation of a periodic square-wave function such as the one whose spectrum is shown in Fig. 7. Assume that the function has frequency f_0 with 50% duty cycle, and that its amplitude is confined to the values of +1 and -1. Show that the first and third harmonics of the waveform have power levels of -0.912 dB and -10.455 dB, respectively, as the numerically computed spectrum in Fig. 7 indicates. (The numerical results are based on the following formula :

$$\mathcal{S}_{\psi}(m) = 2 \left| \frac{1}{Nmax} \sum_{n=0}^{Nmax-1} \psi(n) \exp\left[-\frac{i\,2\pi mn}{Nmax} \right] \right|^2$$

where the function $\psi(t)$ is uniformly sampled at times $t = n\,\Delta t$, its power spectrum $\mathcal{S}_{\psi}(f)$ is sampled (also uniformly) at frequencies $f = m\,\Delta f$, the total number of samples is Nmax, and the various parameters are related by the equality $\Delta t\,\Delta f = 1/Nmax$.)

9.5)   Figure 12 shows three traces of the noise spectral density, obtained from the same erased track at three different disk velocities. According to Eq. (46) the Modulation Transfer Function (MTF) should not affect the low-frequency end of the spectrum, yet the DC noise level in the figure drops by about 3 dB for each doubling of the velocity. Clearly, the spectrum $\mathcal{S}_{\psi_0}(f)$ of the signal itself is responsible for the observed behavior. Explain this phenomenon on the basis of the definition of the spectral density function in Eq. (16).

References

1. J. Smith, *Modern Communication Circuits*, McGraw-Hill, New York, 1986.

2. A. Papoulis, *Probability, Random Variables, and Stochastic Processes*, 2nd edition, McGraw-Hill, New York, 1984.

3. A. Arimotó, M. Ojima, N. Chinone, A. Oishi, T. Gotoh, and N. Ohnuki, "Optimum conditions for the high frequency noise reduction method in optical videodisc players", Applied Optics 25, *pp*1398-1403 (1986).

4. M. Ojima, A. Arimoto, N. Chinone, T. Gotoh, and K. Aiki, "Diode laser noise at video frequencies in optical videodisc players", Applied Optics **25**, *pp*1404-1410 (1986).

5. G. A. Acket, D. Lenstra, A. J. Den Boef, and B. H. Verbeek, "Influence of feedback intensity on longitudinal mode properties and optical noise in index-guided semiconductor lasers", J. Quant. Elect. QE-20, *pp*1163-1169 (1984).

6. A. G. Dewey, "Optimizing signal to noise ratio from a magneto-optic head", paper EO8.2, presented at the meeting of the Optical Society of America, Boston, Massachusetts, November 1990.

7. A. G. Dewey, "Optimizing the noise performance of a magneto-optic read channel", SPIE Vol.1078, pp279-286 (1989).

8. J. W. Beck, "Noise considerations in optical beam recording", Applied Optics 9, *pp*2559-2564 (1970).

9. J. P. J. Heemskerk, "Noise in a video disk system : experiments with an (AlGa)As laser", Applied Optics 17, *pp*2007-2012 (1978).

10. F. Inoue, A. Maeda, A. Itoh, and K. Kawanishi, "The medium noise reduction by intensity dividing readout in the magneto-optical memories", IEEE Trans. Magnet. 21, *pp*1629-1631 (1985).

11. D. Treves and D. S. Bloomberg, "Signal, noise, and codes in optical memories", Optical Engineering 25, *pp*881-891 (1986).

12. A. G. Dewey, "Measurement and modeling of optical disk noise", SPIE Vol.695, pp72-78 (1986).

Appendix F

Figure Captions

Fig.1   Schematic diagram of a magneto-optical readout system. In the forward path the leaky PBS provides a fraction γ^2 of the X-polarized light to the monitor of laser power. In the return path, 100% of the magneto-optically generated Y-component of polarization plus the fraction γ^2 of the returning X-polarized light are deflected towards the differential detection module.

Fig.2   Complex plane diagram showing the locus of $1+\delta_e(t)$, where $\delta_e(t)$ is a small complex quantity whose phase can assume arbitrary values in the interval $[0, 2\pi]$. The radius of the circle which is the upper bound on the magnitude of $\delta_e(t)$ is exaggerated.

Fig.3   Spectrum of the combined electronic + shot + laser noise as well as that of the electronic noise alone at the output of a laser power monitor [6]. The operating wavelength is $\lambda = 680$ nm and the incident light power level is 380 μW.

Fig.4   Spectrum of the combined electronic + shot + laser noise as well as that of the electronic noise alone at the output of a laser power monitor [7]. The operating wavelength is $\lambda = 830$ nm and the incident light power level is 39 μW. Since the spikes on the upper trace were generated by the electronic circuitry within the laser power supply, they were ignored in the noise analysis.

Fig.5   Measured noise spectra at the differential output of a magneto-optical readout system [6]. The operating wavelength and the light power incident on the disk were $\lambda = 680$ nm and $P_0 = 2$mW, respectively. Other system parameters are given in the text (see Example 5). In (a) the disk was stopped. In (b) the spectrum of an erased track shows little deviation from that of a recorded track (carrier frequency = 8 MHz). The spectrum in (c) was obtained with the light blocked from one of the detectors.

Fig.6   Measured noise spectra at the differential output of a magneto-optical readout system [7].
The operating wavelength and the light power incident on the disk were $\lambda = 830$ nm and
$P_0 = 2$mW, respectively. Other system parameters are given in the text (see Example 6).
The traces in (a) were obtained with the light blocked from both detectors (lower trace),
with the disk stopped but the light allowed to reach the detectors (middle trace), and with
the disk spinning and the light reaching both detectors (upper trace). The track under
consideration was recorded with a 4 MHz carrier signal. The spectrum in (b) is similar to
the upper trace in (a), but the light in this case was blocked from one of the detectors.

Fig.7   Computed power spectrum of a 4 MHz, 50% duty cycle, square-wave signal in the absence
of jitter and other signal fluctuations. A total of 65536 samples were used in this fast
Fourier transform (FFT) computation. The exact duration of the signal waveform was
33.25 μs, which is an integer multiple of the carrier period (0.25 μs). The approximate
values of the sampling intervals in time and frequency are, therefore, 0.5 ns and 30 kHz,
respectively. (The exact values of the sampling intervals are slightly different from those
quoted above; these are adjusted to fulfill two requirements : i) the duration of the signal
in time is an integer multiple of the carrier period, ii) the total number of samples is an
integer power of 2.)

Fig.8   Section of a square-wave signal in the time interval [0, 2 μs], with jitter magnitude
$\Delta t = 25$ ns. A random number generator is used to select the deviation of each zero-
crossing point from its nominal position. The deviations are uniformly distributed in the
interval [-Δt, Δt], and the random number corresponding to any given point is
independent of that for any other point.

Fig.9   Spectra of square-wave signals (such as the one shown in Fig. 8) with different amounts of
random jitter. The noise density shown here is computed within a 30 kHz bandwidth. (a)
$\Delta t = 3$ ns, (b) $\Delta t = 5$ ns, (c) $\Delta t = 15$ ns, (d) $\Delta t = 25$ ns.

Appendix F

Fig.10   (*a*) Section of a square-wave signal in the time interval [0, 5 μs]. The waveform is free

from jitter, but its positive amplitude fluctuates randomly within the interval [0.85, 1.00].

(*b*) Spectrum of the signal in (*a*), showing that the noise appears only at low frequencies.

(*c*) Spectrum of a signal waveform with $\Delta t = 3$ ns of jitter in addition to positive

amplitude fluctuations in the interval [0.70, 1.00].

Fig.11   (*a*) Section of a square-wave signal in the time interval [0, 5 μs]. The waveform has

$\Delta t = 3$ ns of jitter, its positive amplitude fluctuates randomly within the interval

[0.70, 1.00], while its negative amplitude fluctuations are confined to the interval

[-1.00,-0.70]. (*b*) Spectrum of the signal in (*a*). (*c*) Spectrum of the same signal when

jitter is increased to $\Delta t = 15$ ns.

Fig.12   Measured noise spectra from an erased track on a magneto-optical disk [12]. The traces

are obtained from the same track under identical conditions with the exception that the

disk velocity is different for different traces. The velocities corresponding to these

measurements are $v_0 = 3$ *m/s*, 6 *m/s*, and 12 *m/s*.
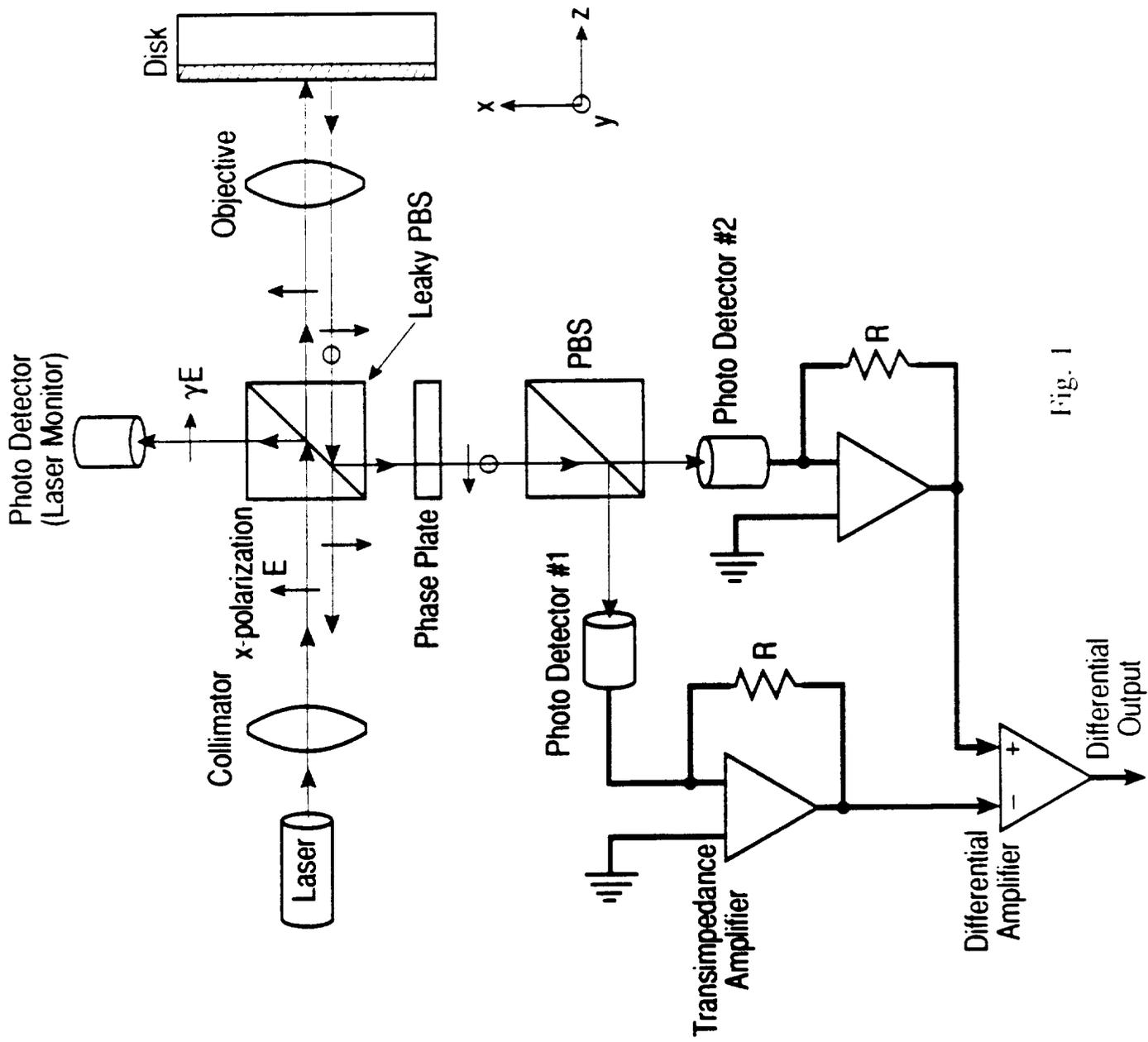
Fig. 1
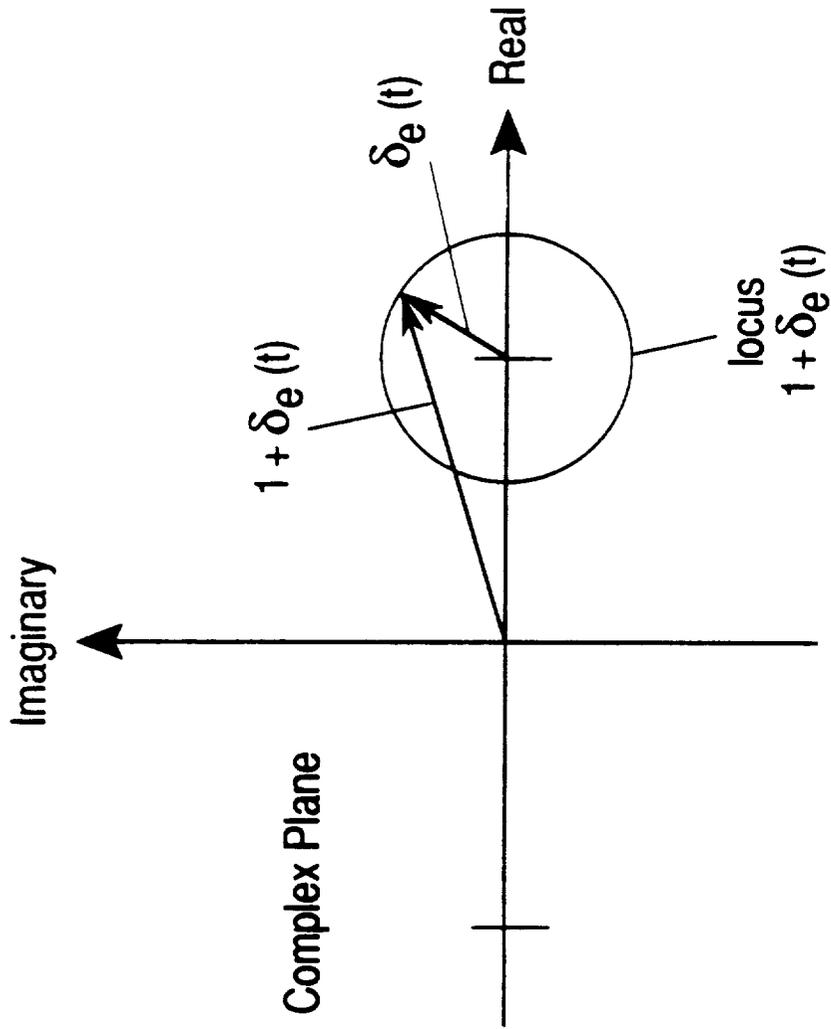
Fig. 2
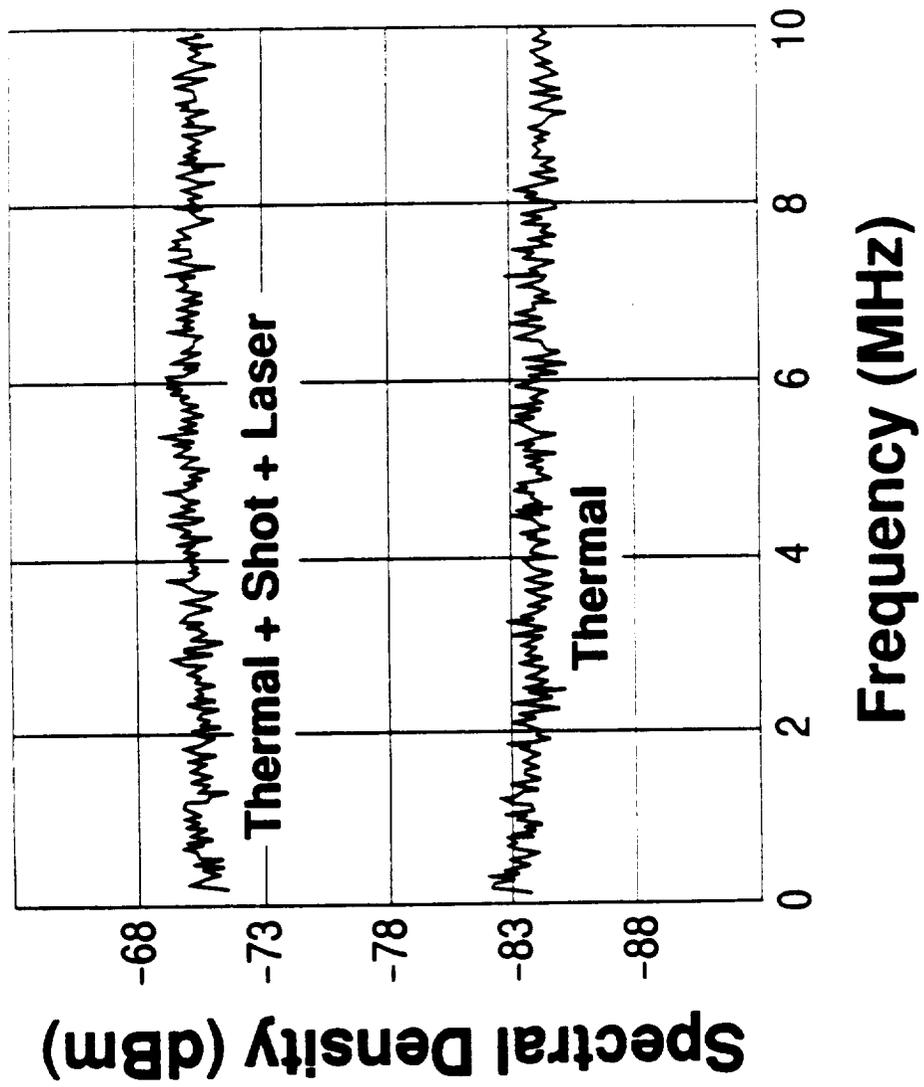
Fig. 3
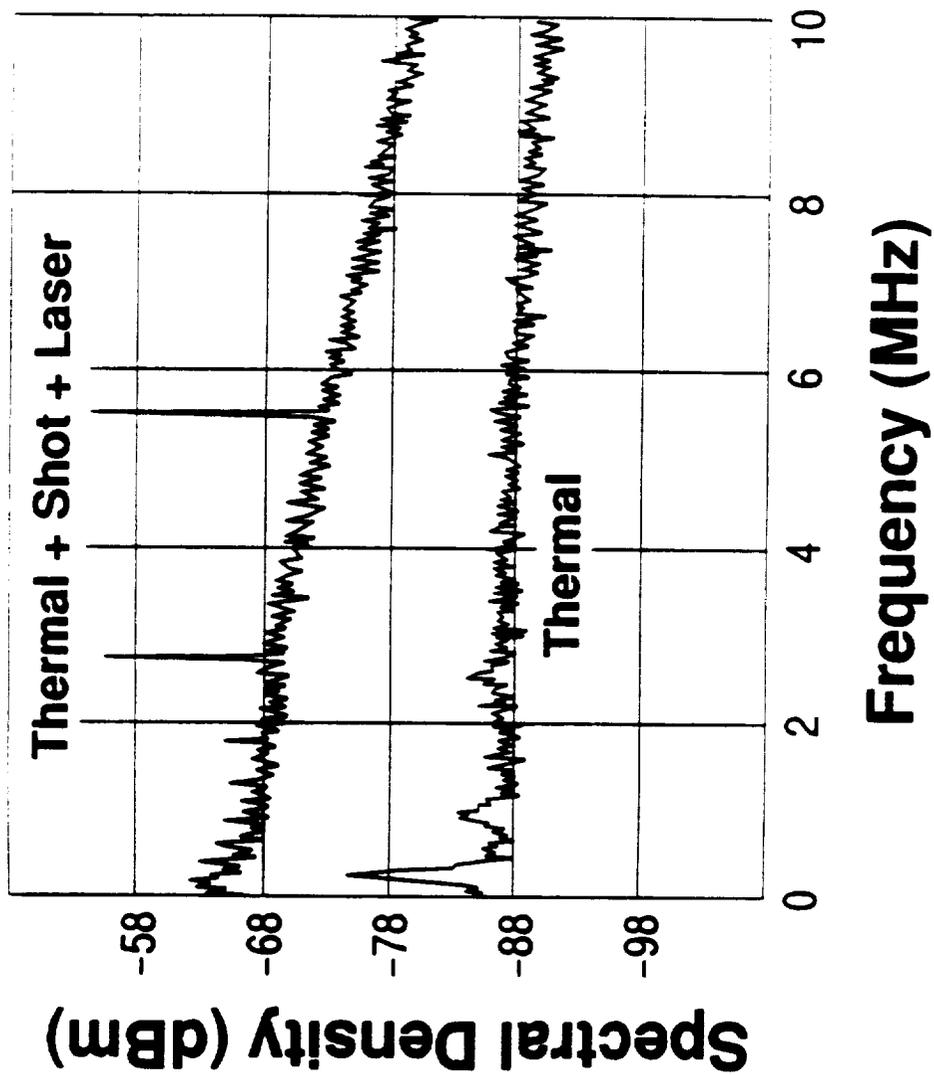
Fig. 4
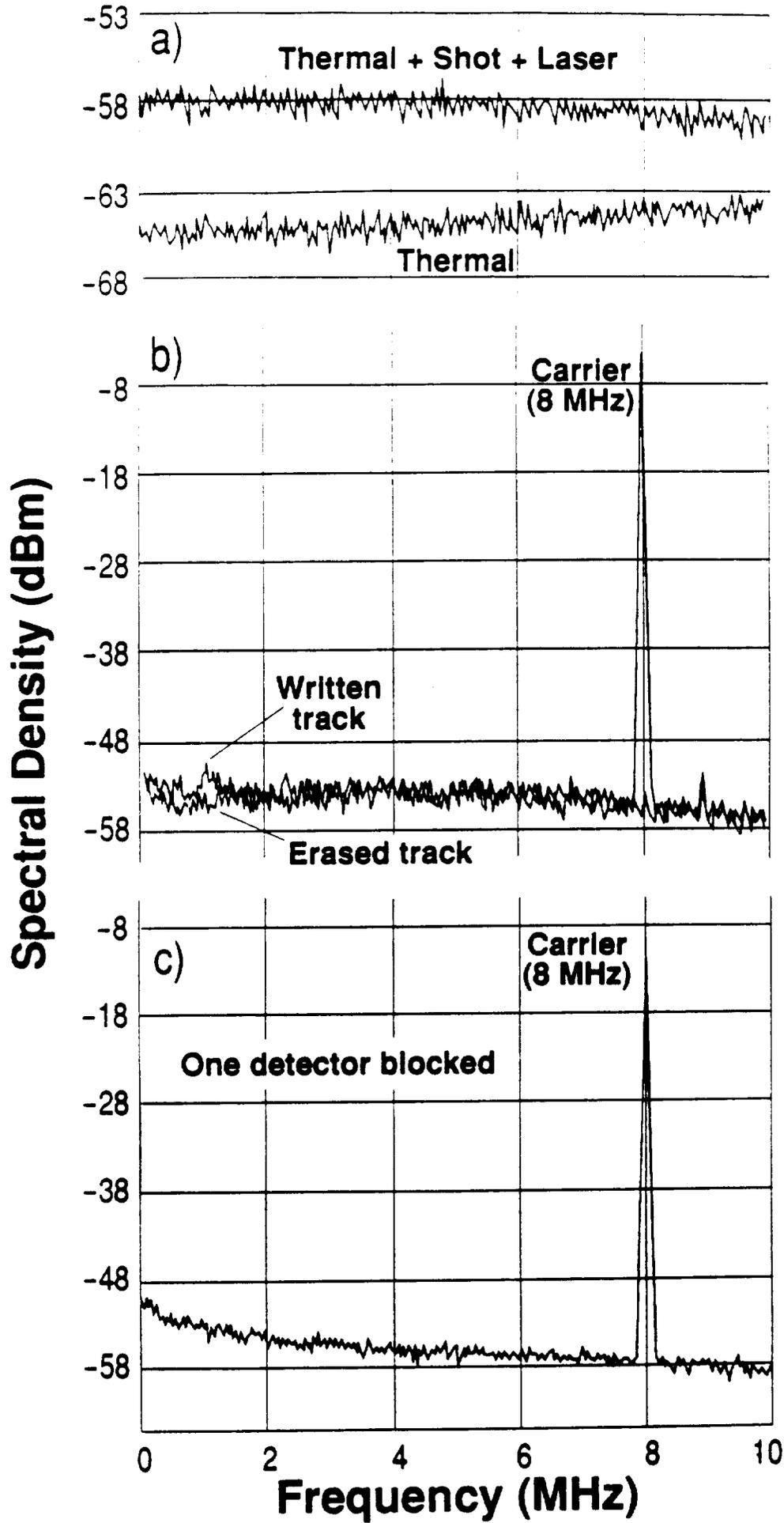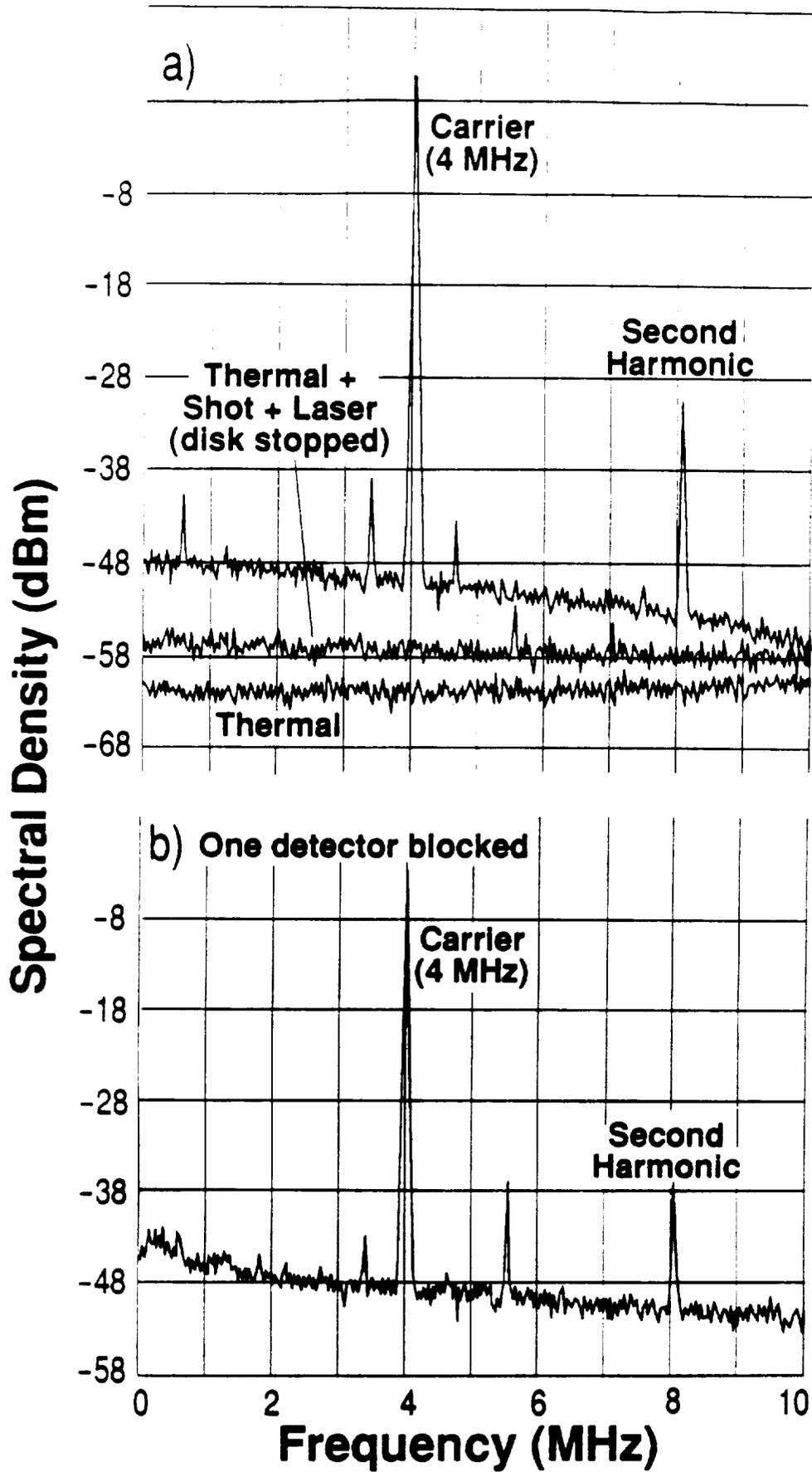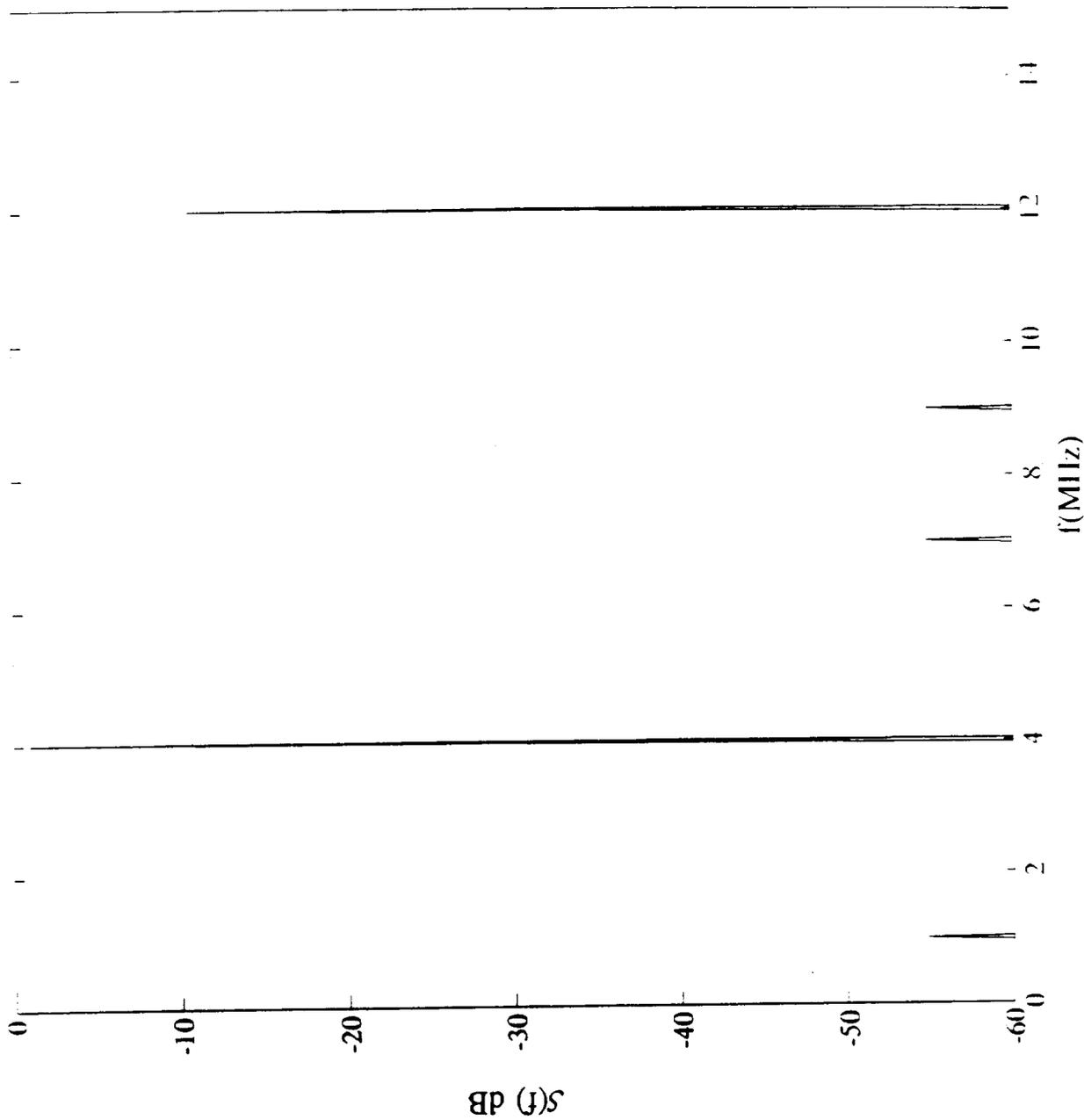
a)

-53

-58 Thermal + Shot + Laser

-63

-68 Thermal

b)

-8 Carrier (8 MHz)

-18

-28

-38

-48 Written track

-58 Erased track

c)

-8 Carrier (8 MHz)

-18 One detector blocked

-28

-38

-48

-58

Spectral Density (dBm)

0   2   4   6   8   10

Frequency (MHz)

Fig. 5

Fig. 6

Fig. 7

Appendix F

Fig. 8

(a)

Fig. 9

Fig. 9

Fig. 9

(c)

Fig. 9

(a)

Fig. 10

Fig. 10

(c)

Fig. 10

Appendix F

(a)

Fig. 11

(b)

Fig. 11

Appendix F

(c)

Fig. 11

Fig. 12

N92-14909
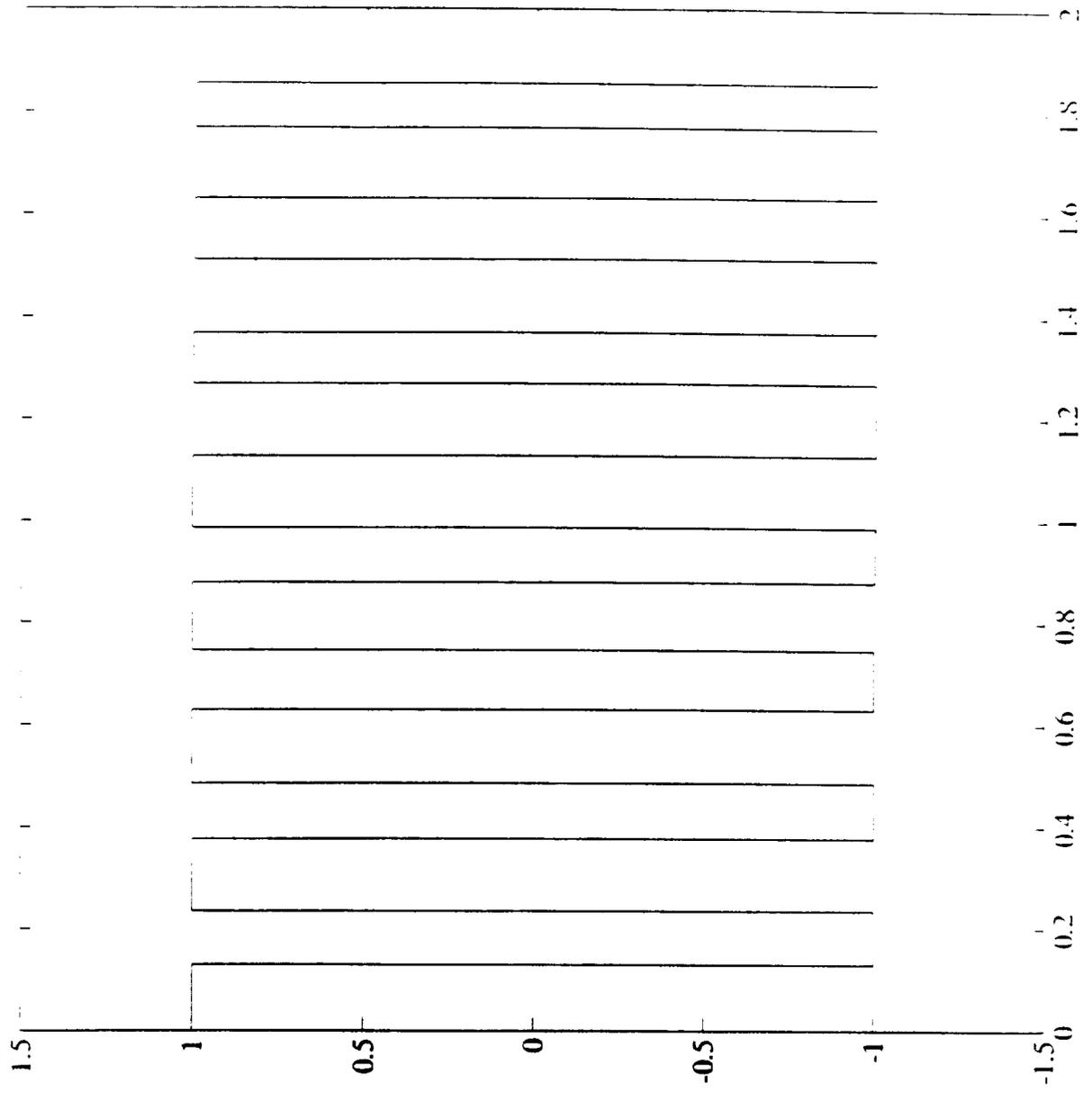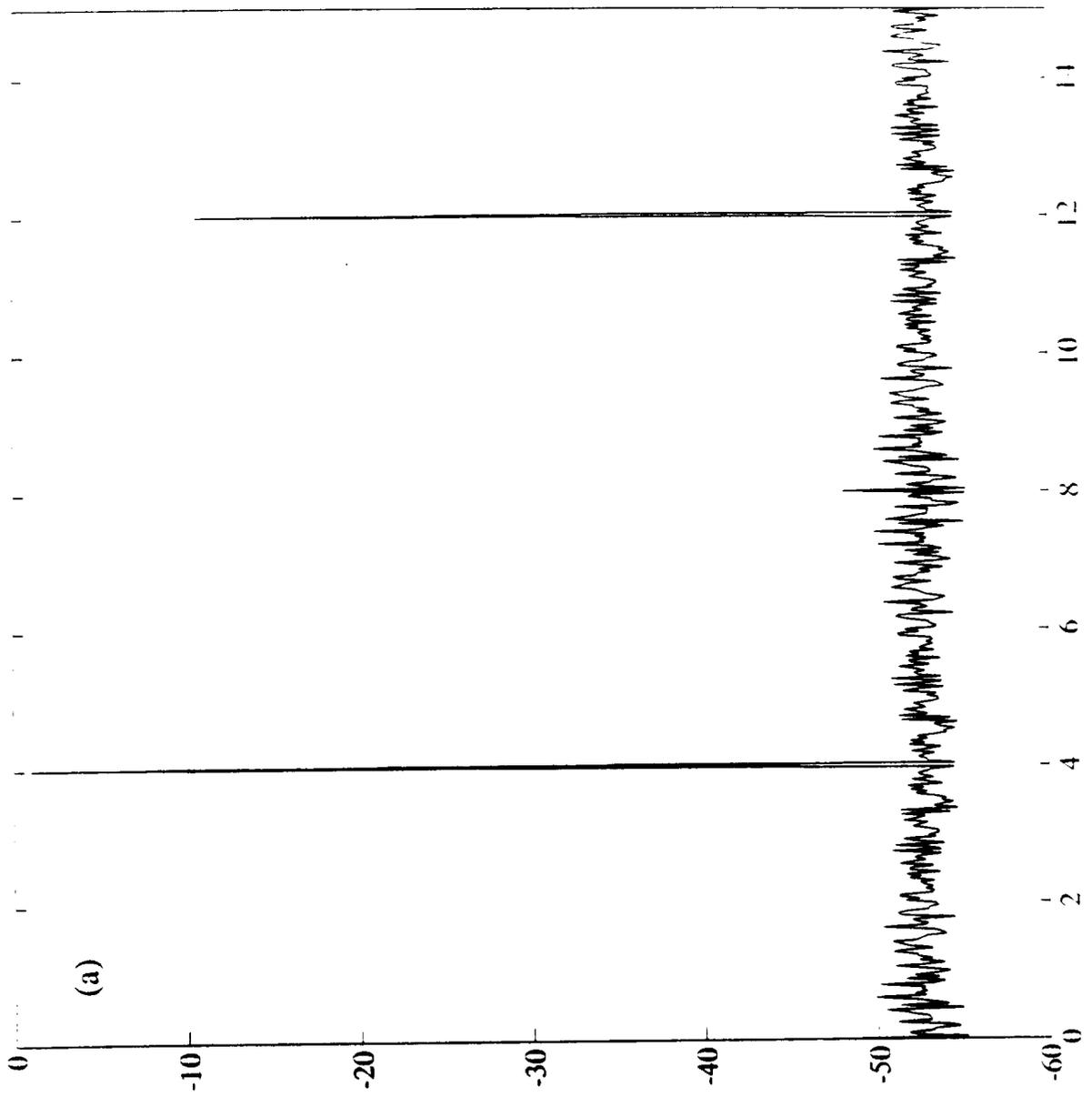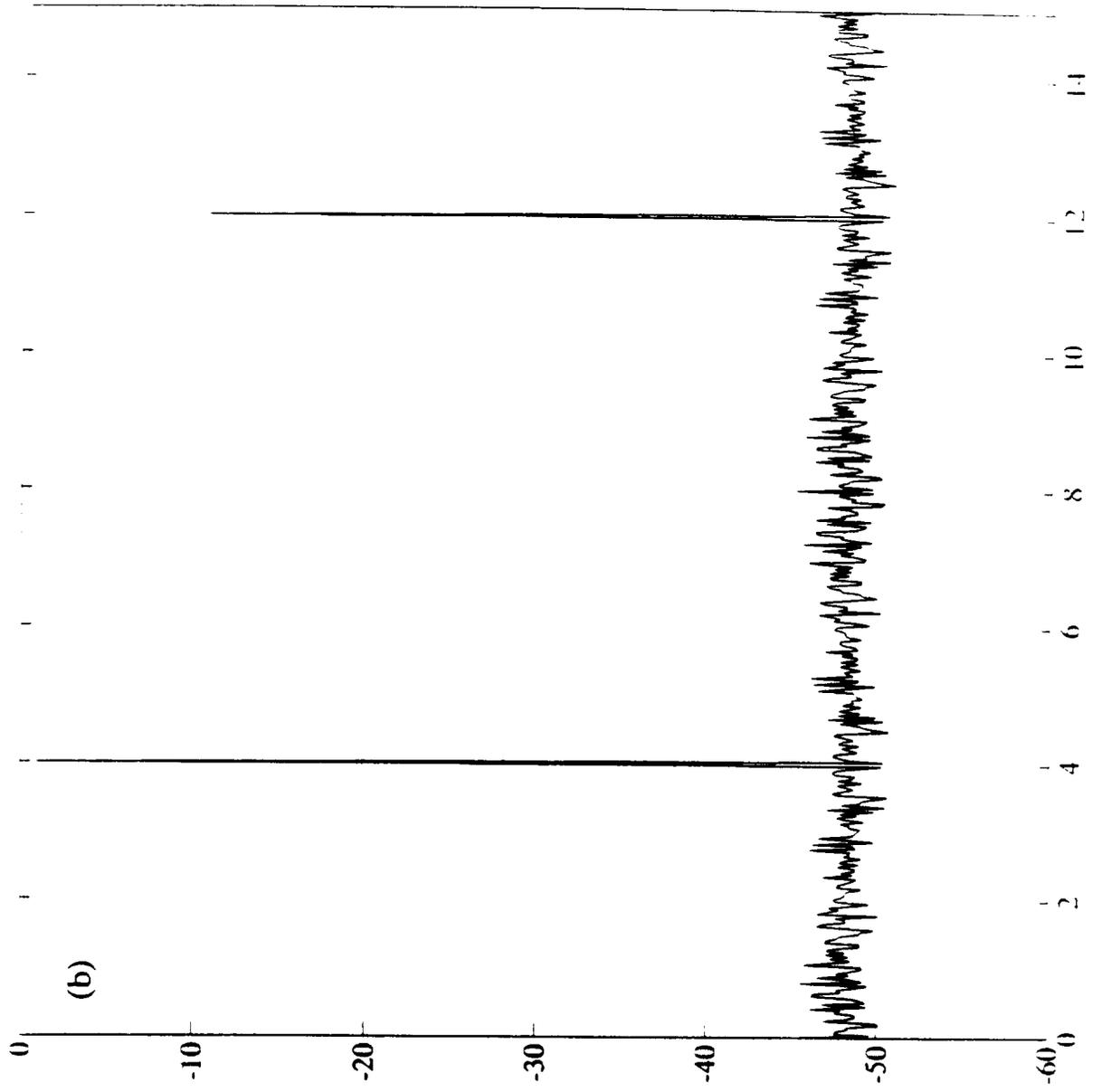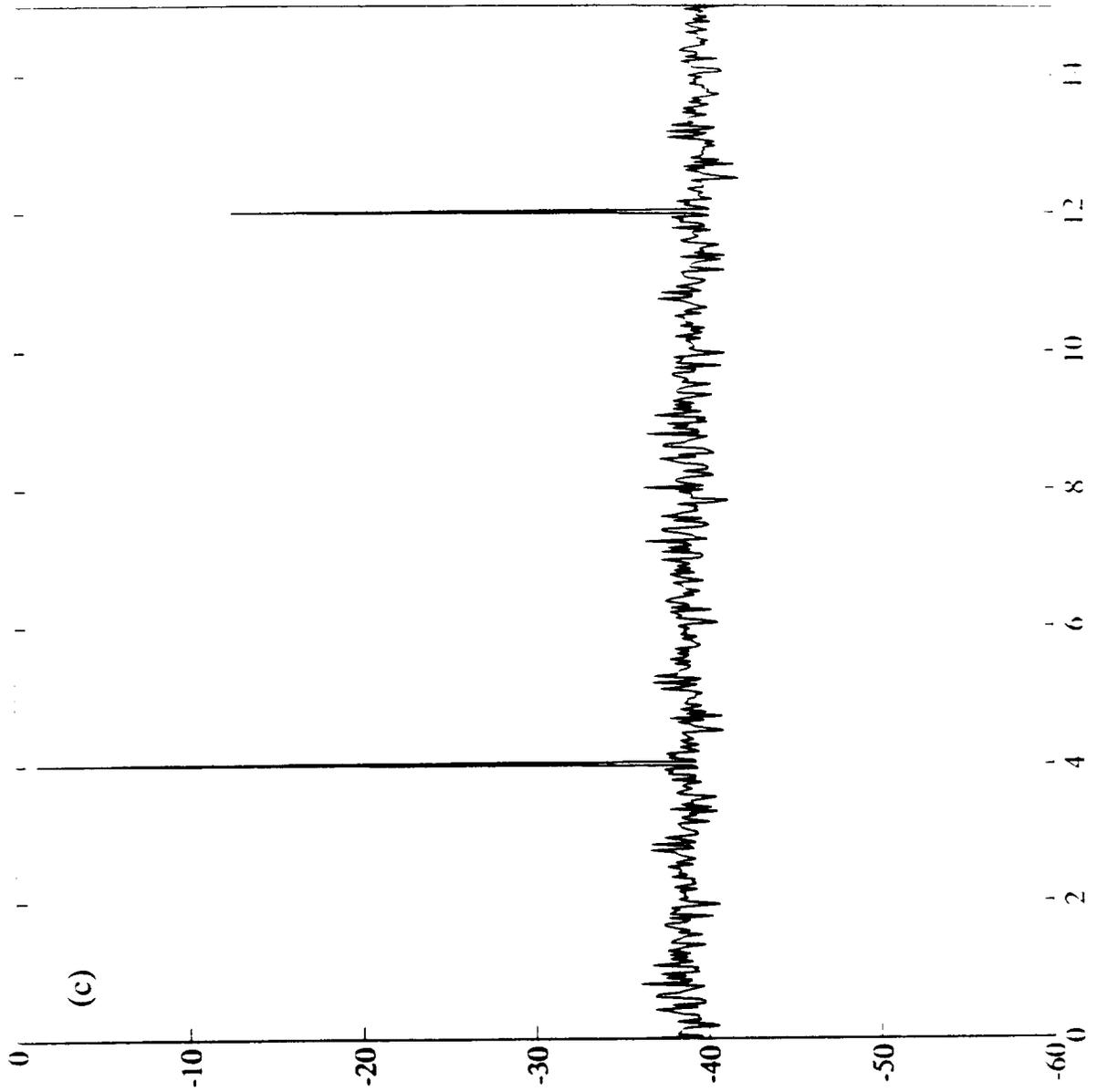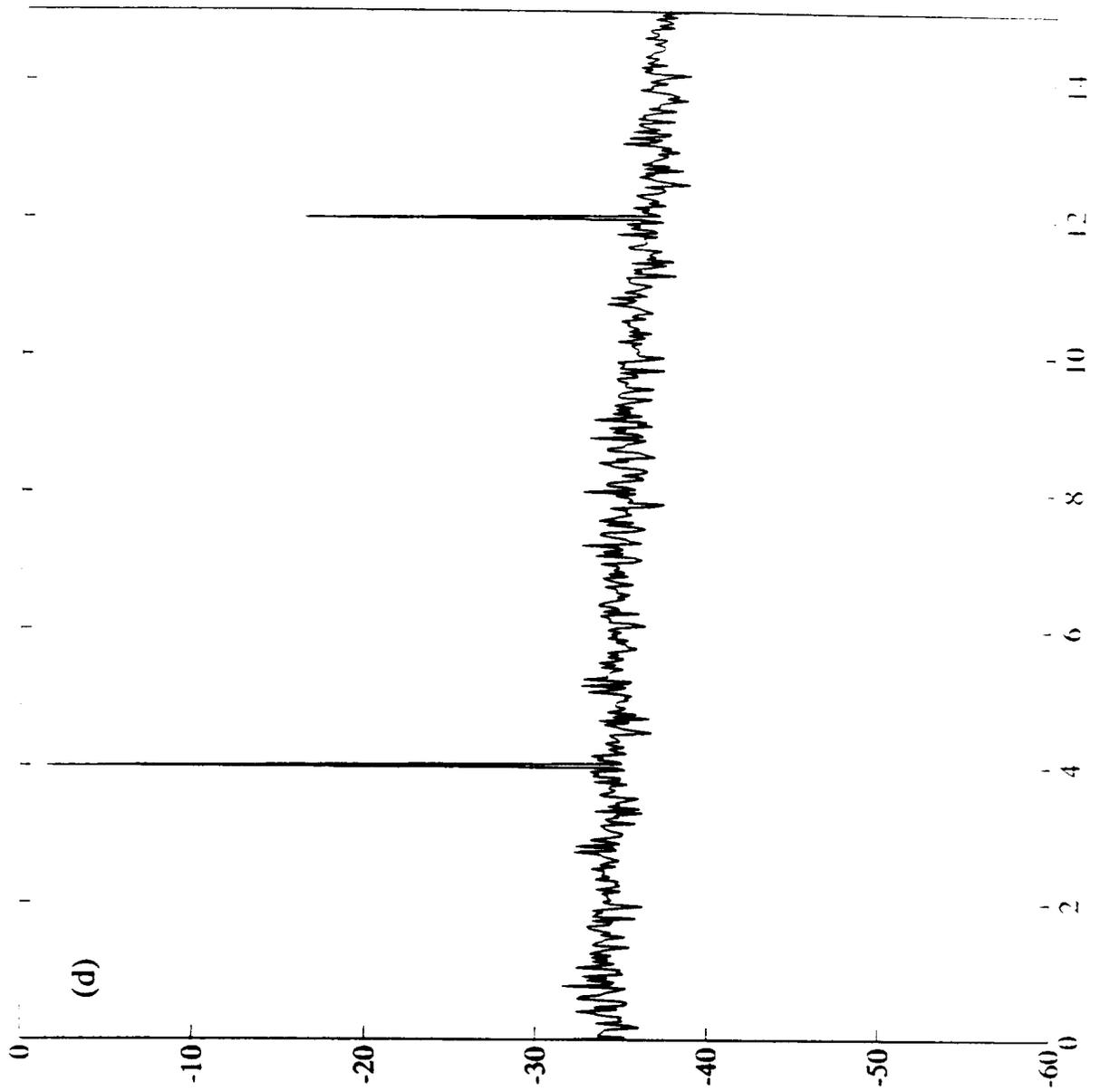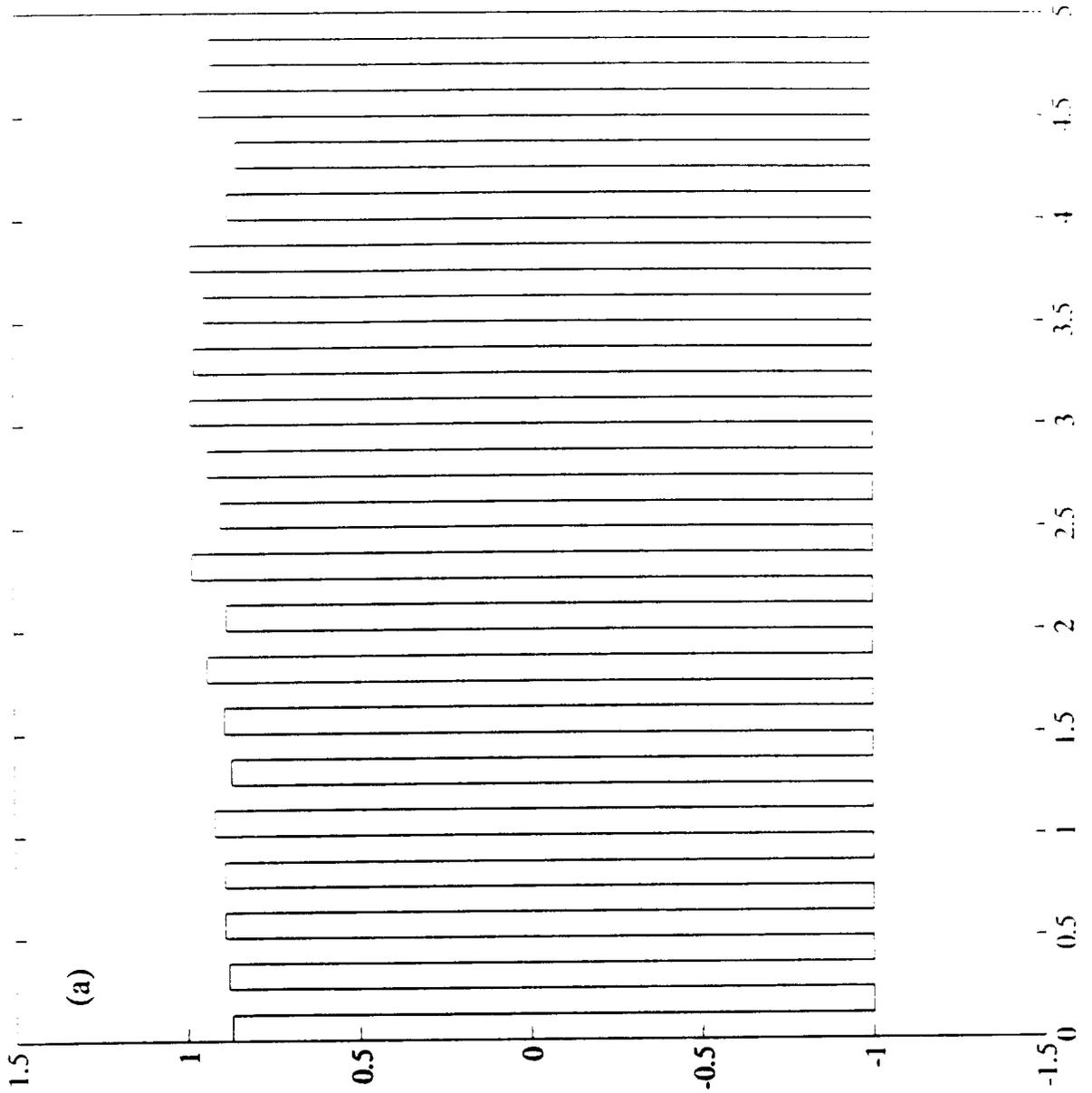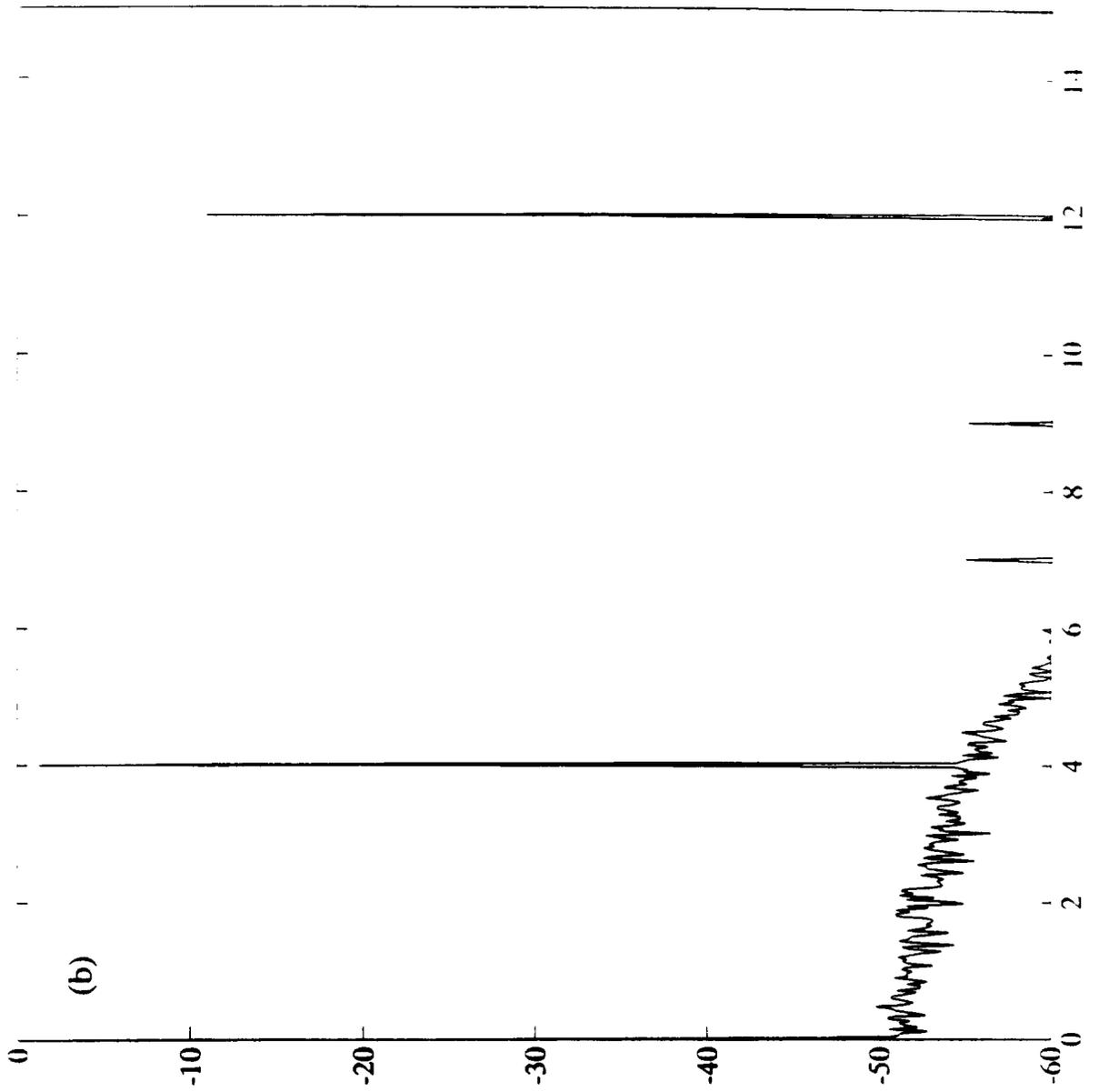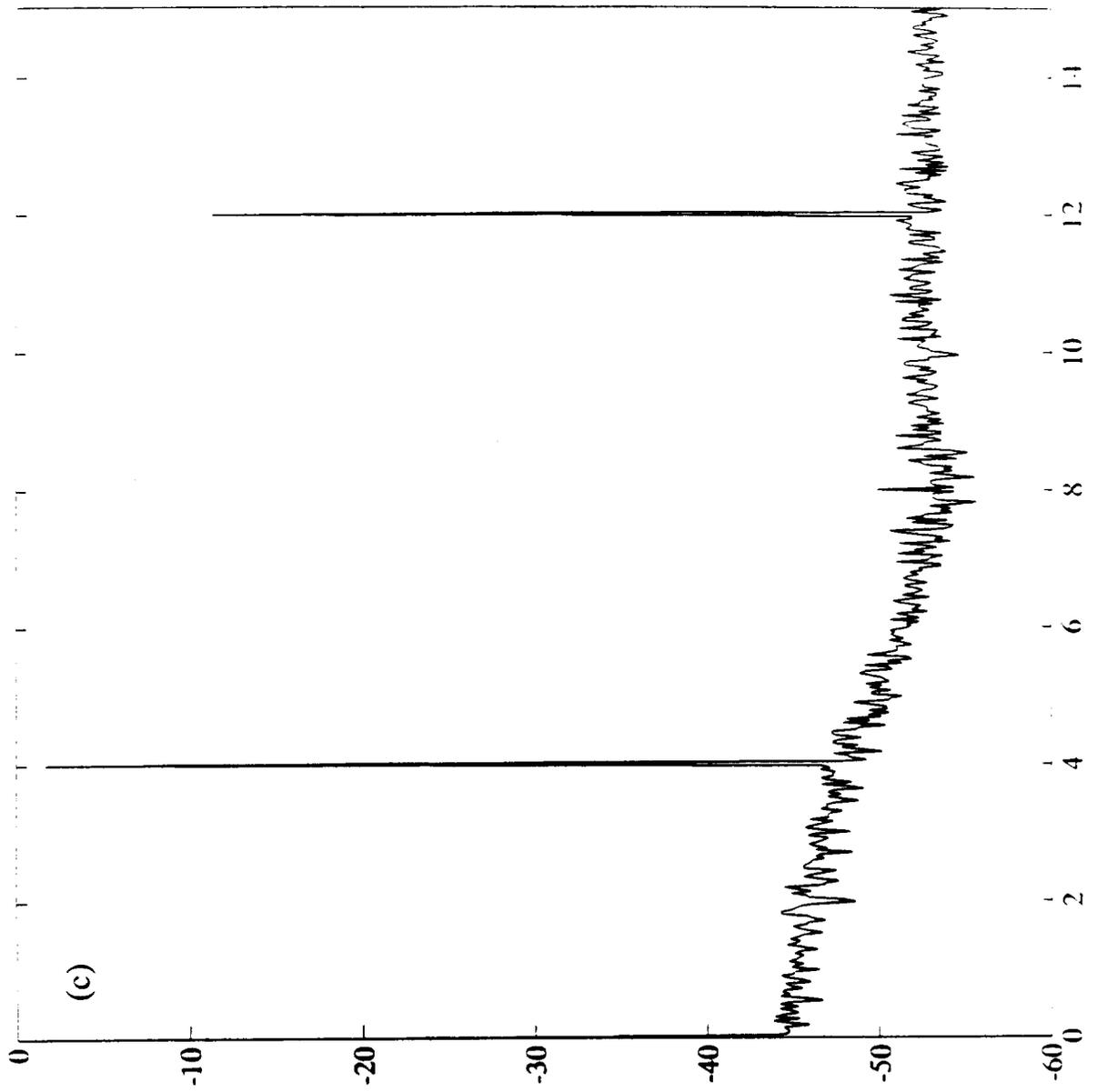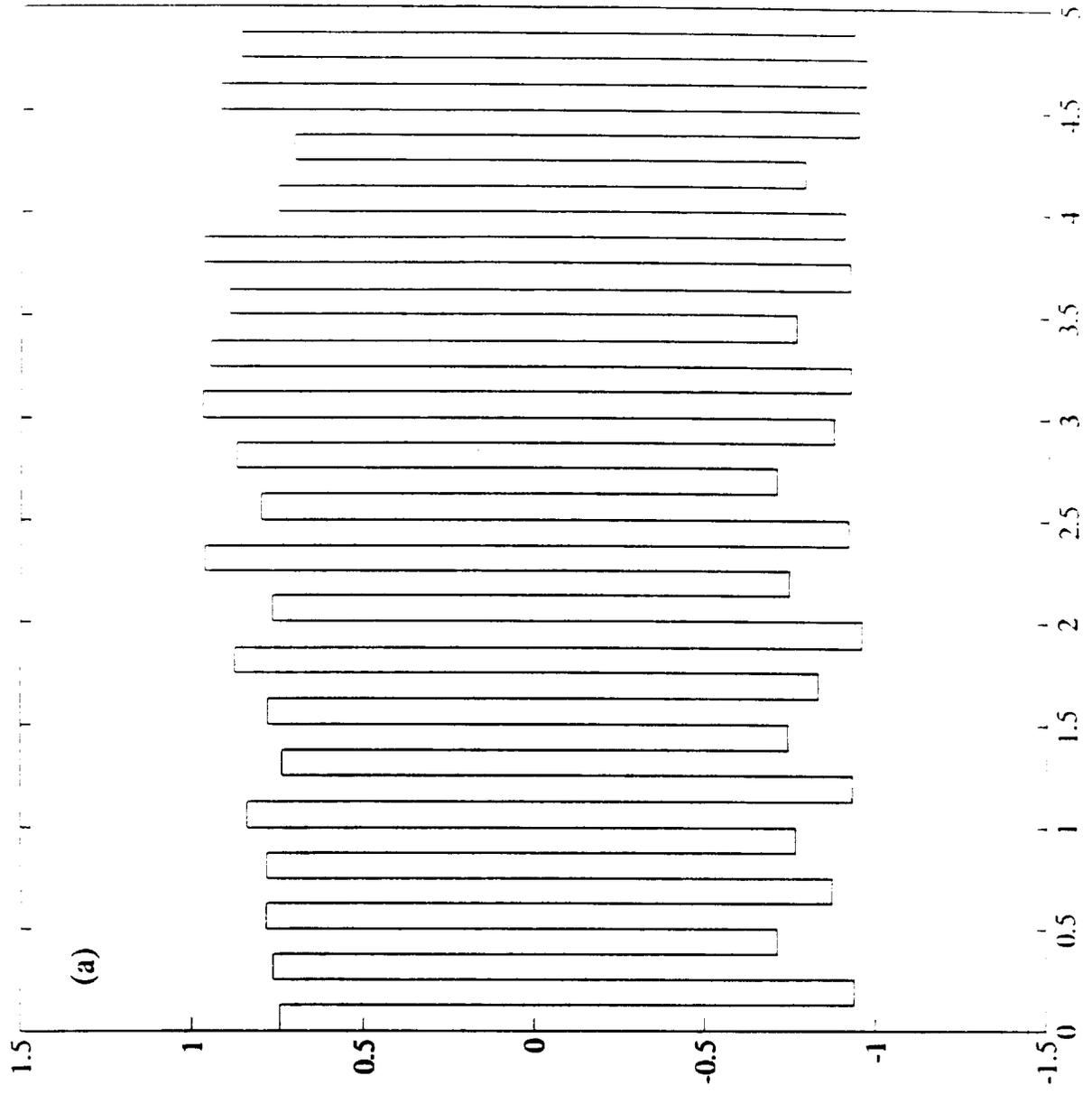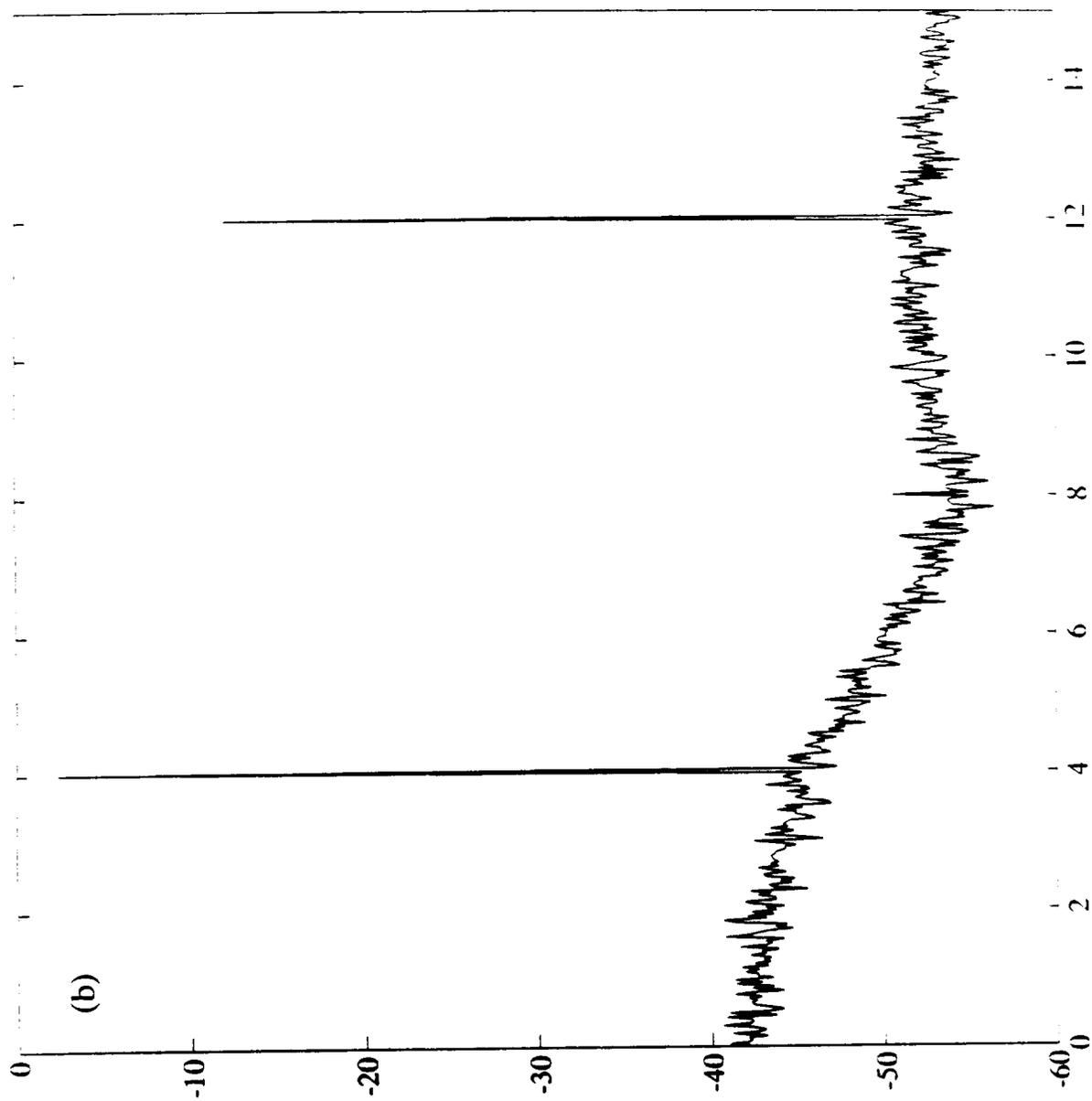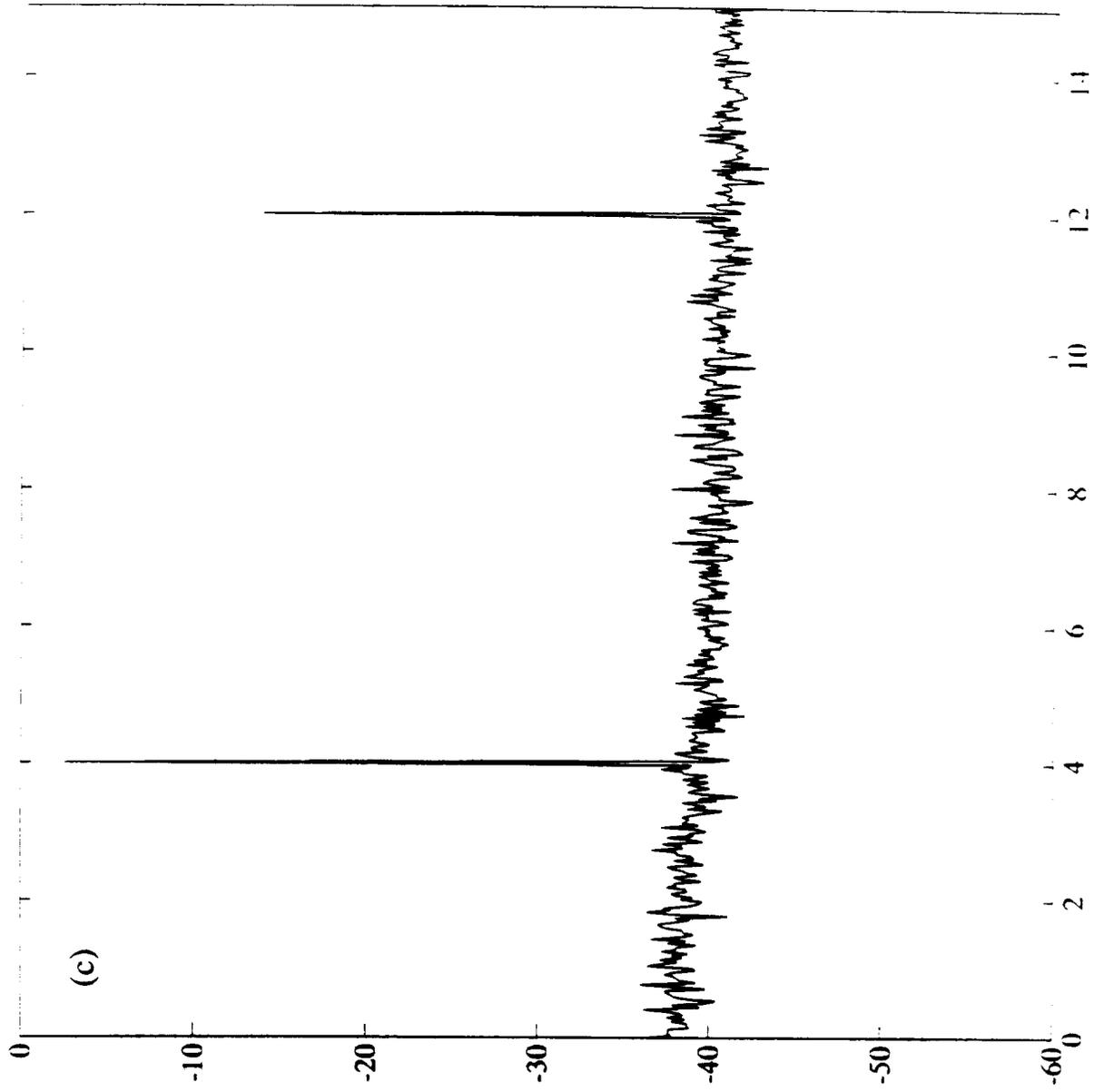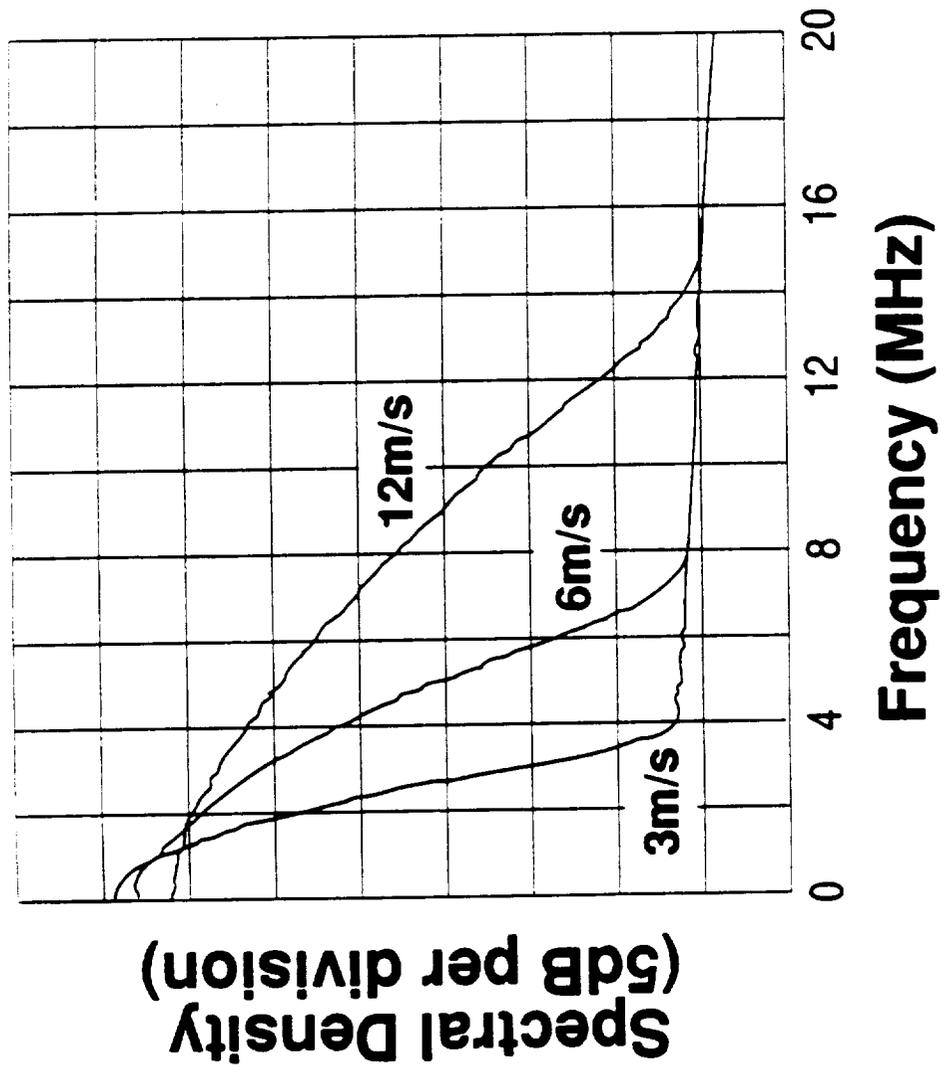
Differential Spot-Size Focus Servo

T.D. Milster, M.S. Wang, F.F. Froehlich, J.L. Kann, J.P. Treptau, and K.E. Erwin

Optical Sciences Center, University of Arizona, Tucson, Arizona, 85721

Abstract

We describe performance of a differential spot-size (wax-wane) focus servo. Cross talk from the tracks are analyzed in the single detector and differential focus circuits. Magnitude of the cross talk is reduced by a factor of three in the differential circuit. A false FES signal is present when the spot crosses sector marks at an angle.

2. Introduction

There are several techniques that can be used for focus-error detection in an optical data storage device. Astigmatic, knife-edge, critical-angle prism, pupil obscuration, and spot-size detection are common techniques (1)(2)(3). These methods sense the focus error by manipulating reflected light from the disk and creating an electrical focus-error signal (FES) with sectioned detectors. If a continuously pregrooved disk is used, the reflected light also contains diffracted orders that are used to provide a tracking-error signal (TES). It is difficult to completely separate the focus-error information from the tracking-error information, regardless of the focus-error detection method. The residual amount of TES observed in the FES is called cross talk. Other kinds of pattern noise, such as diffraction from sector marks, beam motion, and partial obscuration, can also lead to false FES signals. Prikryl (4) has modeled the sensitivity of several focus-error detection methods to sources of cross talk. Cohen (1) and Stahl (5) have modeled cross talk sensitivity of astigmatic focus-error detection. In this paper, we discuss the characteristics of a differential spot-size measurement technique, which has better cross-talk rejection than the single-detector spot-size measurement technique. Similar differential techniques have been presented in the literature (6), but they have not been analyzed with respect to cross talk.

Our differential spot-size technique is illustrated in Figure 1. Reflected light from the objective lens is focused through a polarizing beam splitter onto two quadrant detectors. Detector 1 is slightly inside focus, and detector 2 is slightly beyond focus. Representations of spot sizes through focus are sketched in Figure 2. For the in-focus condition, the spots are approximately the same size, but they are displaced slightly from the center of the detector. Displacement on detector 1 is opposite from the displacement on detector 2. As the disk moves outside of focus (farther away from the objective lens), the spot on detector 1 becomes smaller, and the spot on detector 2 becomes larger. As the disk moves inside of focus (closer to the objective lens), the spot on detector 1 becomes larger, and the spot on detector 2 becomes smaller. An error signal is generated from :
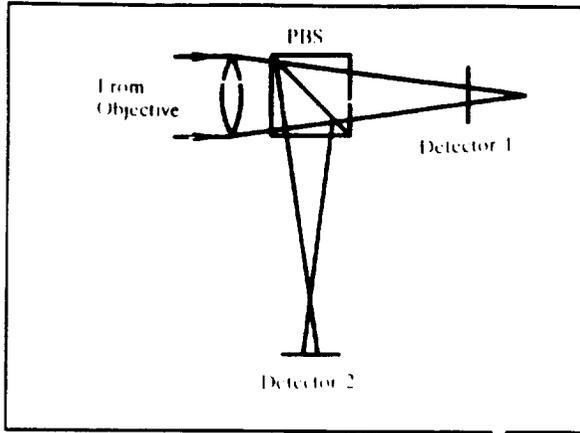
Figure 1. Detector optics layout for the differential spot size technique.
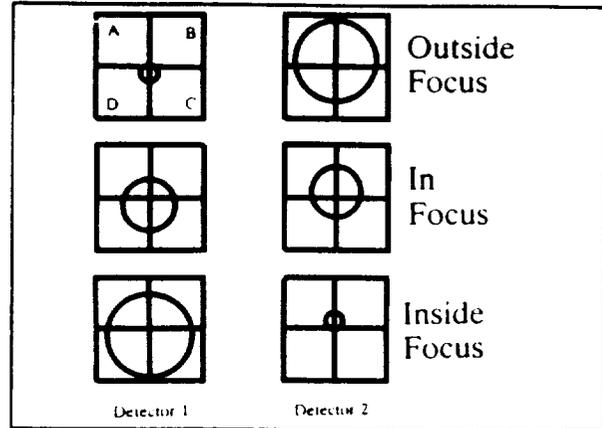
Figure 2. Spot shapes on the quad detectors for three different focus conditions.

$$\epsilon_1 = \frac{2(A + B) - (C + D)}{A + B + C + D}$$

$$\epsilon_2 = \frac{(A + B) - 2(C + D)}{A + B + C + D}$$

$$\epsilon = \epsilon_1 - \epsilon_2 \quad ,$$

[1]

where A, B, C, and D are detector voltages, ϵ_1 and ϵ_2 are FES signals for detectors 1 and 2, and ϵ is the differential FES. This method can also be considered as a differential wax-wane focus scheme. We subtract the combined quadrant signals from each detector to generate the magneto-optic read-back signal.

The following paragraphs describe modeling and experiment used to evaluate the differential spot-size technique.

3. Modeling

Our model is a scalar diffraction implementation of the servo path from the disk to the detectors. We use a Fresnel approximation to describe the propagation from disk to objective lens and from detector lens to detectors. The A, B, C, and D signals are found by integrating the squared absolute value of the amplitude over detector quadrants.

An important consideration for servo design is gain, G, expressed in volts per micron. If one assumes a uniform beam, an expression for G in spot-size focus detection is given by

$$G = \frac{\Delta e}{\Delta z}$$

$$= G_g \times \frac{0.976}{l} \times \left(\frac{f_{det}}{f_o}\right)^2 \quad ,$$

Table I

|	Single spot size servo	Differential spot size servo
Gain (measured)	0.36V/μm	0.71V/μm
Gain (calculated)	0.37V/μm	0.74V/μm
Residual FES (p-p)	0.14V	0.085V
Crosstalk (p-p)	0.38μm	0.12μm
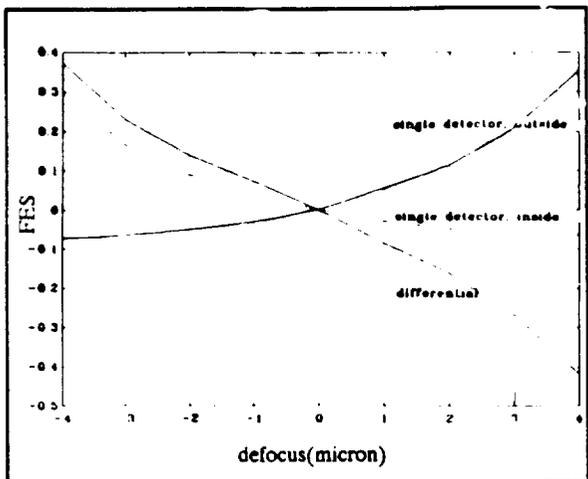
Figure 3.   Calculated FES curves for single detector and differential circuits.
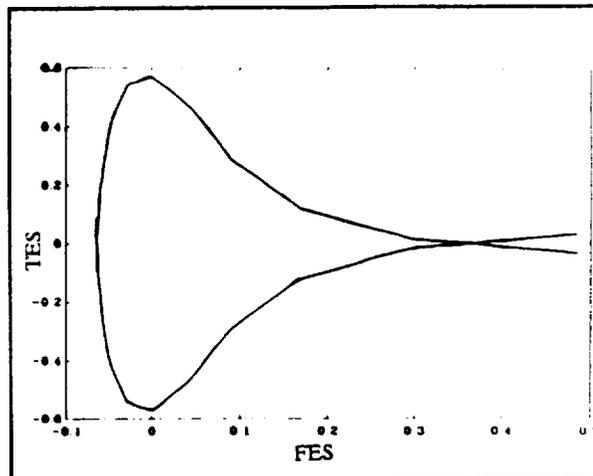
Figure 4.   Calculated Lissajous envelope for the single-detector circuit.

where G_E is electronic gain (5), l is distance from detector to nominal focus (11 mm), f_{det} is focal length of the detector lens (124 mm), f_o is focal length of the objective lens (4.3 mm), and Δz is disk displacement. Our calculated G is 0.37 V/μm, which corresponds well to the measured value of 0.36 V/μm. Gain for the differential spot-size focus technique is twice G, or 0.74 V/μm. The measured differential gain is 0.71 V/μm. Table I summarizes these results.

Figure 3 displays FES versus defocus for both detectors individually and the differential FES. Single-detector FES is a nonlinear function of position. The differential FES is more linear.


Figure 5.   Calculated Lissajous envelope for the differential circuit.

We studied the interaction of focus and tracking signals by calculating the envelope of the Lissajous pattern formed between the FES and the TES. Figure 4 displays the Lissajous pattern for the single-detector case. Due to nonlinear gain of the FES, the TES signal approaches zero rapidly as the system goes out of focus in one direction. In the opposite focus direction, the TES falls off more slowly. The envelope of the differential FES is displayed in Figure 5, which is nearly symmetrical around best focus.

4. Experimental Procedure and Results

The measurement of cross talk on the FES (focus error signal) requires knowledge of the focus servo gain and the peak-to-peak voltage fluctuation of the FES as a result of track crossings. The servo gain is measured on the linear region of the open-loop FES. The actuator-to-disk spacing is varied by translating the optical head with a micrometer screw, and the change in open-loop FES voltage at a fixed time reference is noted. The time

Milster

3
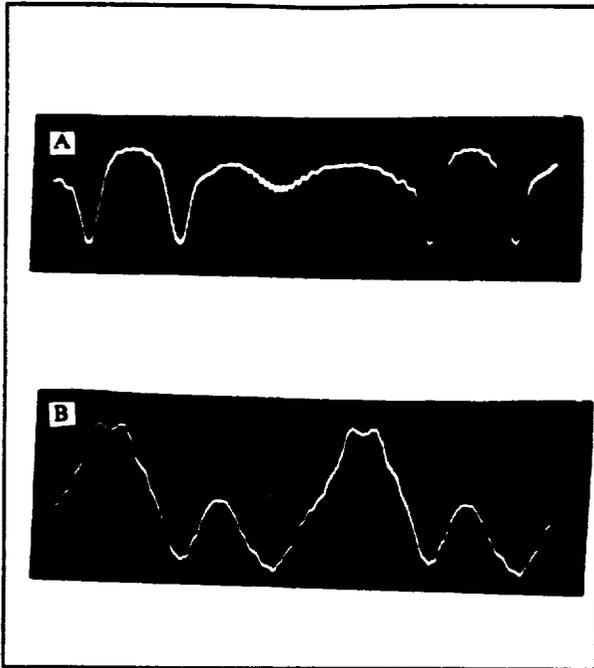
Figure 6.   Open loop FES signals. A: single detector, B: differential circuit. X: 10ms/div, Y: 5V/div.

Figure 7.   Lissajous patterns. A: single-detector X=1V/div, B: differential circuit X=2V/div. X: FES , Y: TES 1V/div.

reference is established relative to the synch pulse from the disk spindle. The gain is then computed as the change in open-loop FES voltage for a given displacement of the actuator and is expressed in volts per micron. The peak-to-peak voltage fluctuation of the FES is measured directly on an oscilloscope with the focus servo locked and the tracking servo unlocked. The peak-to-peak cross talk is then calculated by

$$\text{Cross talk (um}_{pp}) = \frac{\text{FES Voltage (Vpp)}}{\text{Servo Gain (V/um)}}$$

We made most measurements on a glass substrate magneto-optic disk spinning at 1800 rpm. Figure 6 displays the open-loop FES signals for the single-detector and differential circuits. Figure 7 displays the Lissajous patterns for single-detector and differential circuits. The single-detector Lissajous pattern consists of nominally straight lines with small oscillations. Vertical lines correspond to small values of cross talk (7). The nonlinearity of the gains corresponds to the envelope predicted in Figure 4. At this time we have no


Figure 8.   Open-loop TES servo signals from the differential circuit. A: differential FES, Y=0.1V/div. B: TES, Y=2 V/div. X=2ms/div.

*Milster*   4
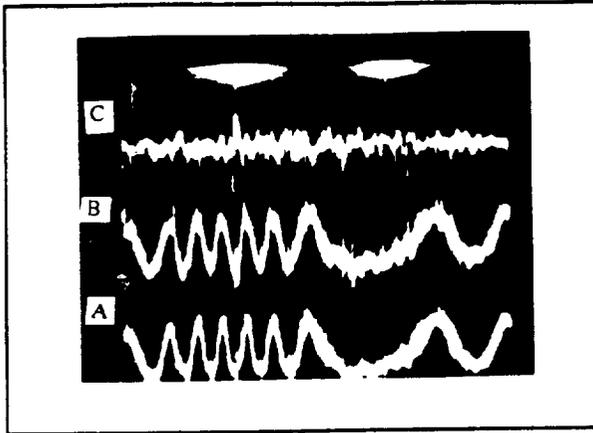
Figure 9.   Cancellation of cross talk for the differential spot size technique. A: detector 1, B: detector 2, C: differential circuit.   X=1 ms/div, Y=0.1 V/div.
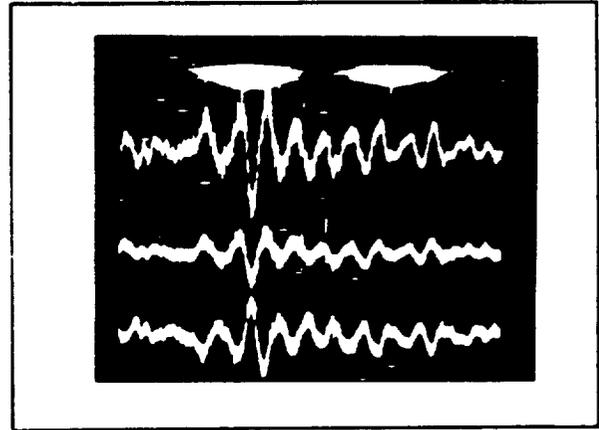
Figure 10.   False FES due to diffraction from the sector marks.

explanation for the oscillations or the skew of the pattern.   The differential-detector Lissajous pattern is more symmetric, but there is still some asymmetry due to a small imbalance in the gains.   The lines making up the pattern are nearly vertical, and there are no observable oscillations.

Oscilloscope traces of servo error signals for the single-detector spot size technique are shown in Figure 8.   The lower trace is the open-loop TES (tracking error signal), and the upper trace is the closed-loop FES showing cross talk.   The cross talk was minimized by rotational and lateral alignment of the quad detector.   The cross talk was found to be 0.38 μm_{pp}.

The improved cross talk performance for the differential spot size technique is illustrated in Figure 9.   The lower two traces are individual FES signals from quad detectors 1 and 2.   Track crossings are in phase on these signals.   The upper trace is the differential FES, which shows cancellation of the track crossings.   The residual cross talk was 0.12 μm_{pp}, which is a factor of three improvement over the single-detector technique.

In the course of measuring the cross talk for the differential technique on a plastic disk, we discovered an FES signal generated by sector marks.   This excitation yields the focus servo response shown in Figure 10.   The response acted like a true focus error, thus the individual FES signals are out-of-phase, and the response is doubled in the differential FES.   We believe that this response is due to diffraction as the spot crosses the sector mark.

5. Conclusions

We have analyzed a differential spot-size (wax-wane) focus error technique for sensitivity to cross talk from track crossings.   The single-detector circuit exhibited cross talk of 0.38μm_{pp}.   The differential circuit exhibited cross talk of 0.12μm_{pp}, which is approximately a factor of three improvement.   An undesired signal was discovered as the spot crosses a sector mark.   It is believed that diffraction from the sector mark causes a false FES signal. We are investigating how to minimize this effect.

6. References

1. D. K. Cohen, "Analysis of methods for detecting focus error in optical data storage systems," Ph.D. Dissertation, University of Arizona, Tucson, Arizona (1987).

2. M. Irie, T. Fujita, M. Shinoda, and M. Kondo, "Focus sensing characteristics of the pupil obscuration method for continuously grooved disks," *Proc. Int. Symp. on Optical Memory, 1987 Japanese Journal of Applied Physics*, vol. 26, pp.183-186 (1987) supplement 26-4.

3. M. Yamamoto, A. Watabe, and H. Ukita, " Optical Pregroove dimensions: design considerations," *Appl. Opt.*, vol 25, 22, pp. 4031-4034 (1986).

4. I. Prikryl, "Optical servo cross talk," *SPIE 1078 Optical Data Storage Topical Meeting*, pp. 244-255 (1989).

5. R.P. Stahl, "Modeling optical feedtrough of track crossings into the focus error signal in an optical storage device," Master's Report, Department of Optical Sciences, University of Arizona, Tucson, Arizona (1990).

6. M. Oka, A. Fukumoto, K. Osato, and S. Kubota, "A new focus servo method for magneto-optical disk systems," *Proc. of the Int. Symp. on Optical Memory, 1987, Japanese Journal of Applied Physics*, vol. 26, pp. 187-190 (1987) supplement 26-4.

7. S.L. Grove, K.W. Getreuer, and D.L. Schell, "Lissajous analysis of focus cross talk in optical disk systems," to be published in SPIE Proceedings 1499.

N92-14910

Measurement of Laser Spot Quality

T.D. Milster, Optical Sciences Center, University of Arizona, Tucson, Arizona 85721
J.P. Treptau, Optical Sciences Center, University of Arizona, Tucson, Arizona 85721

Abstract

Several ways of measuring spot quality are compared. We examine in detail various figures of merit such as full-width-at-half maximum (FWHM), full-width-at-$1/e^2$ maximum, Strehl ratio, and encircled energy. Our application is optical data storage, but results can be applied to other areas like space communications and high-energy lasers. We found that the optimum figure of merit in many cases is Strehl ratio.

Introduction

There are several methods useful for measuring laser spot quality, such as interferometry, CCD cameras, and knife-edge scanners. Interferometric methods commonly use a lens to recollimate the light, as shown in Figure 1a. Measurements are highly precise with better than $\lambda/100$ wavefront variation. However, there are certain difficulties involved in using an interferometer. The numerical aperture (NA) of the collecting optics must be greater than the NA of the beam. The collection optics may introduce aberrations into the beam. Also, it is tedious to align the interferometer. In some situations, the physical size of the interferometer is not convenient. CCD cameras avoid some of the alignment problems associated with interferometers. As shown in Figure 1b, a laser spot can be focused directly onto the CCD array. However, the sampling of the spot is limited by the pixel size, which is typically about 10μm by 10 μm. Spot diameters of less than several hundred microns are difficult to measure accurately with a CCD. An auxiliary lens can be placed between the spot and the CCD, as shown in Figure 1c, but the NA of the collection optics must be greater than the NA of the beam. The alignment must also be done very carefully, and the optics must be carefully considered. For example, Bobroff et al. have constructed, with some difficulty, a very high quality system for measuring spots from lithographic lenses (1). A third option for measuring spot quality is to use a knife-edge scanner. The spot profile is estimated by scanning an opaque edge through the spot, as shown in Figure 1d. A detector records transmitted power versus time. The derivative of the knife-edge scan with respect to time, $\delta i/\delta t$, is the line scan of the spot, which is an estimate of the spot profile. The line scan is equivalent to scanning an infinitely thin slit, as shown in Figure 2. The slit integrates irradiance in the y direction. Therefore, the line scan is not exactly equivalent to the true spot profile. However, because of its small size
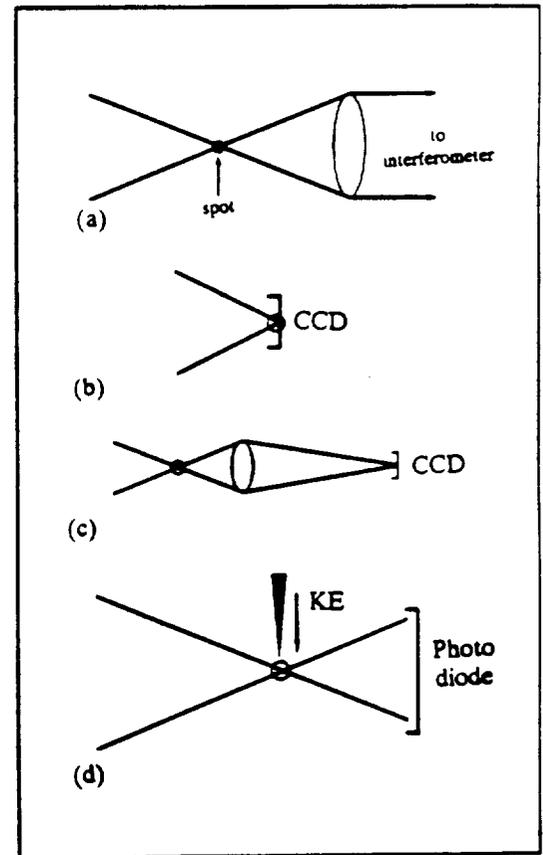
Figure 1.   Measurement methods: (a) interferometric; (b) CCD direct; (c) CCD with aux. lens; (d) knife-edge scanner.

and direct output, the knife-edge
technique is very convenient in the laboratory.

We can understand differences between the
knife-edge scan and the true spot profile by analyzing
the spot irradiance distribution in Figure 3a. Various
amounts of aberration add to yield a wavefront standard
deviation , σ, of $\sigma = 0.077$, which is just at the
diffraction limit. The spot is slightly elongated in a
diagonal direction, which is most easily observed in the
5% irradiance contour level. The true spot profile and
the knife-edge scan ($\delta i/\delta t$) are shown in Figure 3b.
Since the knife-edge scan integrates the spot
distribution in one direction, it indicates a wider profile
than the true spot.

Each measurement method can produce various
figures of merit for the spot. The standard deviation of
the wavefront, σ, can be found from interferometric
data. The full-width-at-half maximum (FWHM) is
shown in Figure 4a. The full-width-at-$1/e^2$ maximum
(FW$1/e^2$) is shown in Figure 4b. The Strehl ratio is
defined as the ratio of the maximum irradiance of the
aberrated spot to the maximum irradiance of an
unaberrated spot, as shown in Figure 4c. Encircled
energy is defined as the ratio of the power delivered in

Figure 2.   The derivative of the knife-
edge scan is equivalent to scanning an
infinitely thin slit across the spot. (a) slit
scan; (b) $\delta i/\delta t$.

a circular area surrounding the maximum of the aberrated spot to power in the same area around the
maximum of the unaberrated spot, as shown in Figure 4d.

Our application is measuring sub-micron spot profiles for optical data storage devices. The
NA is typically between 0.45 and 0.60. Wavelengths are in the range of 780nm to 830nm. Spot sizes
are typically too small for direct CCD measurements. Interferometric methods are commonly used

(a)   (b)

Figure 3.   (a) An aberrated spot that shows an asymmetric irradiance profile is analyzed. The
value $\sigma = 0.077$ is near the diffraction limit; (b) Differences between the knife-edge scan through
the spot and the true spot profile are shown.

to test collimated light beams in the optical path, but they are not used for testing the focussed spot. Instead, some form of knife-edge scanner is used. Modified CCD devices are of questionable utility due to the large NA. Size and quality of the focused spot is very important because small spots yield high data densities. Historically, FWHM has been used as a metric for spot quality.

Other applications use similar figures of merit. In high-energy laser work and space-laser communications, the full width of the far-field divergence angle is typically used. The motivation is to deliver as much energy as possible to the receiver. However, it is often the case that a substantial amount of energy falls outside of the central peak.

This paper addresses differences between various figures of merit for measuring beams with small amounts of aberration. We consider only spherical, coma, and astigmatic aberrations. We restrict our attention to beams that are near or under Marechal's criterion for diffraction-limited performance (2), that is $\sigma \leq 1/14$ waves. For larger amounts of aberration, some figures of merit become difficult to interpret. For example, it would be very difficult to determine FWHM for Figure 5, which illustrates a spot aberrated with 0.8 wave of coma, 0.8 wave of astigmatism, and 1.6 waves of spherical. Piston, tilt, and defocus have been added to minimize wavefront variance. This brings the spot into best possible focus. Our results are based on a computer simulation.

Figure 4. Various figures of merit. (a) FWHM; (b) FW1/e2; (c) Strehl ratio = I_{ab}/I_o; (d) encircled energy = P_{ab}/P_o.

Simulation

We analyze an optical data storage system that focuses light from a laser diode to a disk medium. An illustration of the optical path is shown in Figure 6. The laser diode has different divergence angles in the parallel and perpendicular directions with respect to the junction. Circularization optics are used after a collimator to make the beam more uniform. A partially-polarizing beam splitter is used to direct the reflected light from the disk to data and servo detectors. The stop is located at the objective lens, which focuses light on the disk. Our system parameters include NA = 0.55, f_o = 4.0 mm, and λ = 780 nm. The amplitude distribution in the pupil is Lorentzian in the direction perpendicular to the junction and Gaussian in the direction parallel to the junction. The widths of the amplitude distribution were adjusted for the best tradeoff between power throughput and spot size (3). The unaberrated FWHM is approximately 0.9μm in

Figure 5. 0.8 wave coma, 0.8 wave astigmatism, and 1.6 waves spherical at best focus.

the direction perpendicular to the junction and 0.87μm in the direction parallel to the junction. Random amounts of aberration were added to the pupil for each trial, and the proper amount of piston, tilt, and defocus were added in order to bring the spot into best focus. Standard deviation

of the wavefront was kept between the limits: $0 \leq \sigma \leq 0.10$. Random parameters included spherical, coma, coma rotation angle, astigmatism, and astigmatism rotation angle. The diffracted spot was calculated with scalar diffraction theory. Figures of merit were calculated for each trial, and the results are plotted versus standard deviation of the wavefront. We calculate figures of merit for both the true spot profile and the knife-edge scan.
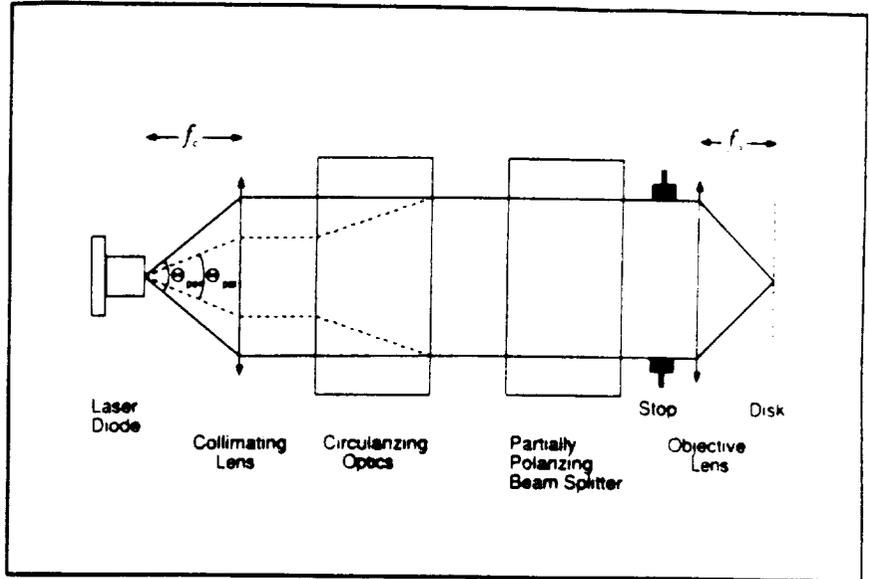
Figure 6.   MO storage device (laser to disk).

Results

Figure 7 displays results for FWHM. For low values of σ, the FWHM in x and y directions (perpendicular and parallel to the junction, respectively) are not equal. This is due to Gaussian/Lorentzian filling of the aperture. Also, the knife-edge scan is not equivalent to the true spot profile. This is because of the line-scan integration. As σ is increased, FWHM does not increase noticeably. Near the diffraction limit, $\sigma \approx 0.07$, FWHM starts fluctuating significantly, which indicates a poor correlation between FWHM and σ. As σ is increased beyond the diffraction limit, the four different measures are very dependent on the amount and rotation angle of the aberration.

The fact that width measurements are not very sensitive to small amounts of aberration may be understood by examining the difference between aberrated and unaberrated spots. Figure 8 displays an aberrated spot with 0.955 waves of spherical and the appropriate amount of defocus. The difference is also displayed, which shows that energy is taken from the central lobe and placed in the outer rings. The difference function passes through zero at the first dark ring. Therefore, the width of the central lobe is constrained. Any changes
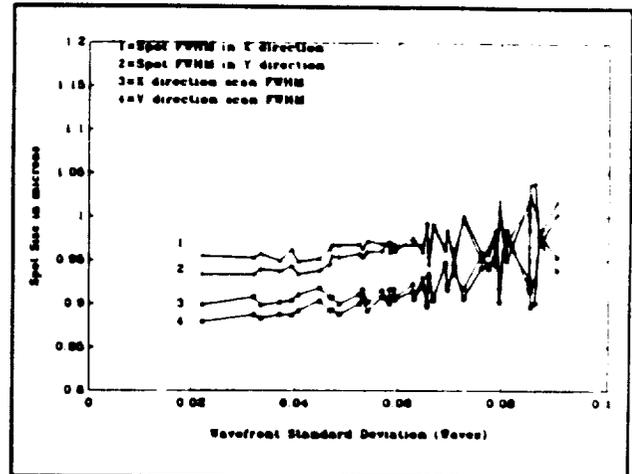

Figure 7.   FWHM from the computed spot and knife-edge scans.
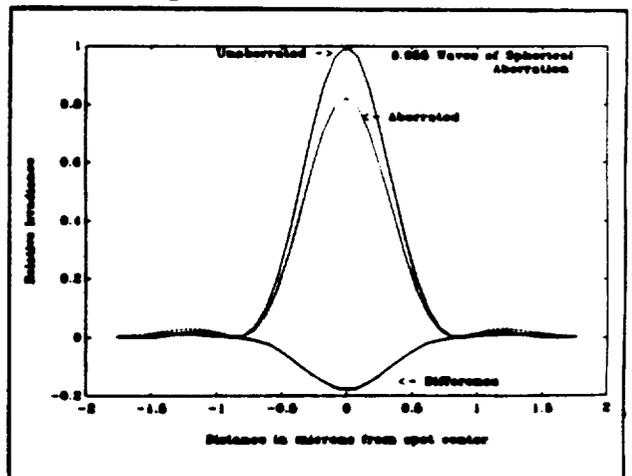
Figure 8.   Aberration contribution to the spot profile with 0.955 wave of spherical and the appropriate amount of defocus.
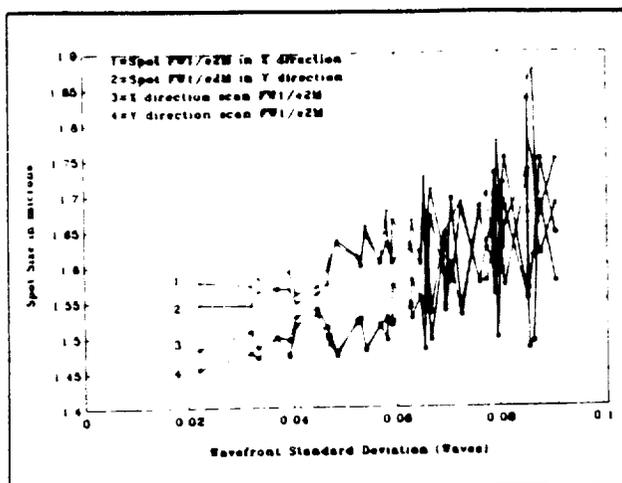
Figure 9.   FW1/e2 from the computed spot and knife-edge scans.
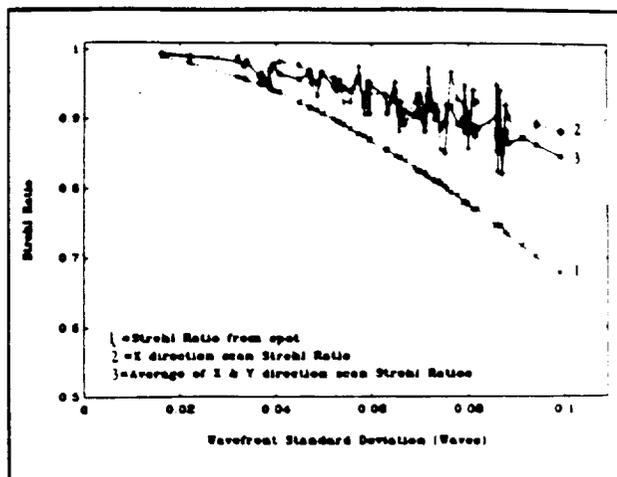
Figure 10.   Comparison of Strehl ratio from computed spot and knife-edge scans.

in width of the central lobe are secondary effects. Similar results are obtained with other aberrations.

Figure 9 displays results for $FW1/e^2$. Differences between spot and knife-edge scan are observed at low values of σ, which are due to integration of the line scan. Differences also are observed between x and y profiles, which are due to Gaussian/Lorentzian filling of the aperture. As σ increases, $FW1/e^2$ generally increases, but it quickly becomes poorly correlated with σ. The $FW1/e^2$ is very sensitive to the kinds of aberrations present and their orientations.

Figure 10 displays results for Strehl ratio. The Strehl ratio for the spot followed Marechal's relationship (2), that is, SR = 1 - $(2\pi/\lambda)^2\sigma^2$. Fluctuations in Strehl ratio for the spot measurement are very small. Strehl ratio for the knife-edge scan in the x direction fluctuates considerably. Strehl ratio for the

Figure 11.   Encircled energy: average of scans and 0.25μm diameter spot pinhole.

knife-edge scan in the y direction (not shown) also fluctuates considerably. A smoother curve is generated by taking the average of x and y scans. The average decreases with increasing σ, which indicates a reasonable figure of merit.

Figure 11 displays results for encircled energy. As with the Strehl ratio results, a comparatively smooth curve is generated by taking an average of the x and y scans. The averages for 2μm, 1μm and 0.5μm effective widths from the knife-edge scans are shown. The encircled energy for a 0.25 micron diameter pinhole over the spot is also shown. The noise-like variations in encircled energy versus σ are approximately equivalent for the data shown. The average of the 0.25μm

knife-edge scan is comparable to the average Strehl-ratio data of Figure 10. This suggests that an adequate integration range around the central peak is about 100% x $0.25/0.9$ = 28% of the unaberrated spot FWHM.

Conclusions

We have illustrated several important points about measurement of laser spot quality. First, results from knife-edge scans and actual spot profiles differ due to the integration of the differentiated knife-edge signal. Secondly, width measurements are not adequate (by themselves) to describe spot quality. This is because width of the central lobe is constrained by pupil filling for small amounts of aberration, and, for large amounts of aberration, width measurements are difficult to interpret. Thirdly, the most sensitive measure of spot quality for many applications is the Strehl ratio. The Strehl ratio is difficult to measure directly, but it may be approximated by averaging the encircled energy found from x and y scans of a knife-edge scanner. The integration range should be no more than about 28% of the unaberrated spot FWHM.

References

1.   N. Bobroff, P. Fadi, A.E. Rosenbluth, and D.S. Goodman, "Bench evaluation of lithographic lenses from measurements of the point spread function," *Proc SPIE 922*, pp. 376-386, 1988.

2.   M. Born and E. Wolf, Principles of Optics, 6th ed., Pergammon Press, New York, p 469 (1986).

3.   H.M. Haskal, "Laser recording with truncated Gaussian beams," Appl. Opt., vol. 18 no 13, pp. 2143-2146 (1979).

N92-14911

Laser Beam Modeling in Optical Storage Systems

J.P. Treptau, Optical Sciences Center, University of Arizona, Tucson, AZ, 85721
T.D. Milster, Optical Sciences Center, University of Arizona, Tucson, AZ, 85721
D.G. Flagello, T.J. Watson Research Center, IBM, Yorktown Heights, NY, 10598

Abstract

A computer model has been developed that simulates light propagating through an optical data storage system. This paper will discuss a model of a laser beam that originates at a laser diode, propagates through an optical system, interacts with a optical disk, reflects back from the optical disk into the system, and propagates to data and servo detectors.

Introduction

The field of optical data storage technology has rapidly advanced in the recent past. Several different types of optical disks have been developed, each with different capabilities and different methods of storing information. One form of optical disk used for data storage is the CD-ROM, which is a read only device. The write-once read-many (WORM) medium was developed after the CD-ROM, and it has the increased functionality of allowing the user to write information to the disk. A drawback of WORM devices is that they are not erasable. Most recently, the erasable optical disk has been developed, which has the full functionality of magnetic disk media, in that data may be written, read back, and erased from the disk if desired. This paper will discuss a system model of an erasable optical disk system. A number of system models analyzing various components of an optical disk system have already been completed (1)(2)(3). In contrast to those models, this model is a complete, end-to-end system model instead of an analysis that deals with only specific components of an optical data storage system.

There are several types of erasable optical disks, each with a different technique to write, read, and erase data. The most common type of erasable media is magneto-optic. The read operation in magneto-optic media accomplished through polarization modulation. Light incident on the disk is reflected, and the reflected light has its polarization rotated due to the data pattern on the disk. The polarization rotation of the reflected light is known as the polar Kerr effect (4). The system model discussed in this paper will consider the disk to be an erasable, magneto-optic medium.

Modeling the Laser Beam

The source of light in a magneto-optic (M-O) disk system is a laser diode. A physical optics analysis is accomplished through modeling the amplitude and phase of the laser beam's electric field. Beam propagation is simulated through the use of Fresnel diffraction calculations (5). In this model, a scalar diffraction approach is used. A vector diffraction analysis is certainly valid, but it is very computationally expensive. In the system model, the beam is represented by a matrix of complex values, where each matrix element represents a different sample point in the wavefront. The complex values represent the amplitude and phase of the wavefront at a given point. Fresnel diffraction calculations are computed through the use of Fast Fourier Transforms.

Consideration must be given to the type of beam a laser diode generates. Among others, there are two characteristics of a typical laser diode used for optical data storage that are discussed. A diagram for a typical laser diode is shown in Figure 1. The cavity is rectangular in shape, which causes

the far-field pattern of the beam to have an elliptical shape. This necessitates, as far as optical data storage is concerned, circularizing optics in the system. Secondly, the cavity is index guided perpendicular to the diode junction, and gain guided parallel to the junction. This has three effects on the emitted beam: (1) The far-field intensity pattern has a Lorentzian profile in the direction perpendicular to the junction (6); (2) The far-field intensity pattern has a Gaussian profile in the direction parallel to the junction (7); and (3) the beam contains astigmatism (7).
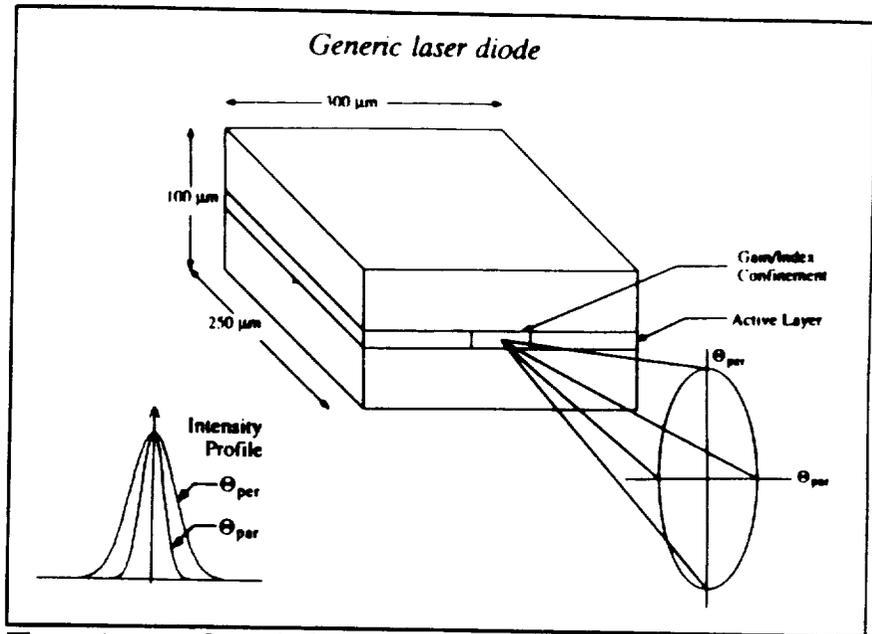
Figure 1   Generic Laser Diode

Modeling the Optical System

The laser beam propagates from the diode and eventually is incident on the entrance pupil of the optical system. A geometrical optics analysis of the system is a valid method of characterizing the optical system. Ray-trace calculations may be performed in order to quantify aberrations in the system. Figure 2 shows a portion of a generic M-O optical data storage system. The light from the diode is collimated, circularized, focused down to a spot on the disk, and the reflected light containing information is delivered to data and servo detectors. The following paragraphs describe a method of modeling the entrance pupil to exit pupil mapping of the optical system.

The wavefront is propagated to the entrance pupil of the system with scalar diffraction. The optical system maps the wavefront incident on the entrance pupil to the exit pupil of the system. Then, the wavefront is propagated to the disk with scalar diffraction. This modeling of the pupil to pupil mapping is accomplished in a two pronged approach as shown in Figure 3.
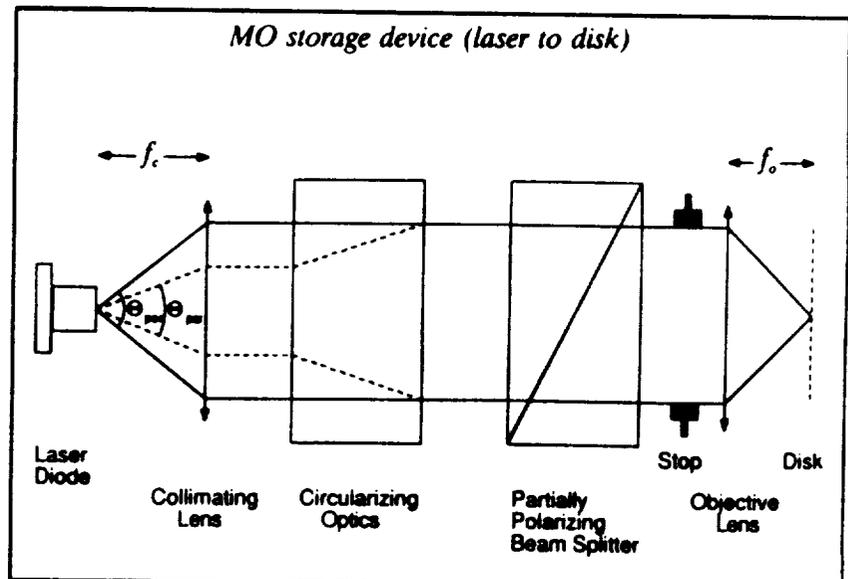
Figure 2   Schematic of an Optical System for M-O Data Storage

To begin, we compute the ideal diffraction mapping of the entrance pupil to the exit pupil. We calculate a paraxial system quantifier, the ABCD matrix. An ABCD matrix is developed for all the elements in the system, and the resulting system ABCD matrix is simply the product of all component matrices:
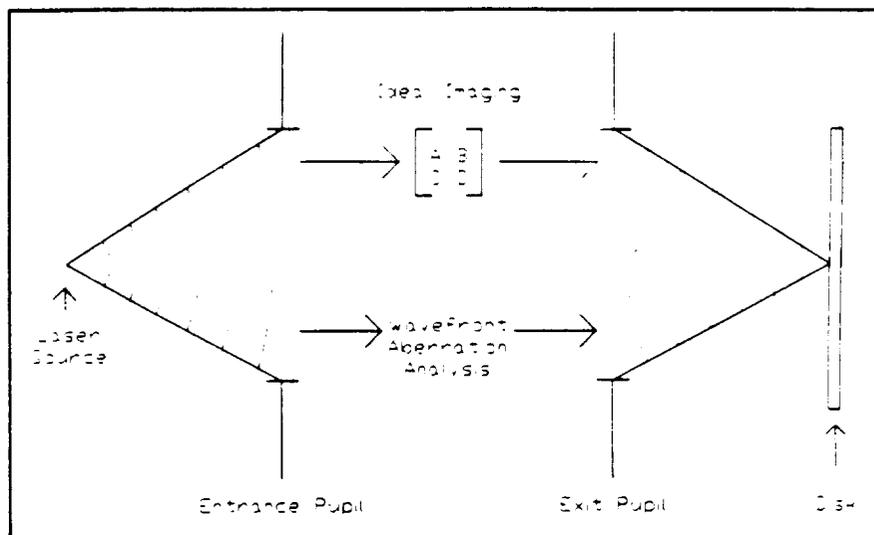
Figure 3   Diagram of Entrance Pupil to Exit Pupil mapping technique

$$ABCD_{system} = \prod_{n=1}^{i} ABCD_n \qquad .$$

In the above equation, the optical system has i elements. Once the system ABCD matrix has been found, that information is placed into the Huygens' integral for wave propagation (8). In the following equation, x_1 = entrance pupil plane, x_2 = exit pupil plane, and $\bar{u}_i(x_i)$ is the wavefront at the given plane. Computation of the integral will map the wavefront from entrance to exit pupil, that is,

$$\bar{u}_2(x_2) = e^{-jkL} \cdot \int\int \bar{K}(x_2,x_1)\bar{u}_1(x_1)dx_1 \qquad .$$

The Huygens' kernel in one transverse dimension is given by:

$$\bar{K}(x_2,x_1) = \sqrt{\frac{j}{B\lambda_o}}\exp\left[-j\frac{\pi}{B\lambda_o}(Ax_1^2-2x_1x_2+Dx_2^2)\right] \qquad .$$

The aberrations in the optical system must now be considered. To compute the aberrations, a ray-trace of the system is performed. An ideal lens may be placed at the exit pupil, and that lens will focus the rays to an image plane. At the arbitrary image plane, the two-dimensional transverse ray fan is calculated. If that ray fan is integrated, the result is the optical path difference (OPD) in the exit pupil due to the aberrations in the system.

The ideal diffraction imaging wavefront and the OPD in the exit pupil due to aberrations are combined to give the total exit pupil wavefront. This is simply the addition of the two component phase fronts. The OPD due to aberrations, plus the ideal diffraction phase front equals the exit pupil phase front. The amplitude of the beam at the exit pupil is given by the ideal diffraction propagation of the amplitude of the E-field incident on the entrance pupil.

The wavefront that is now at the exit pupil is propagated to the optical disk using scalar diffraction calculations. The light interacts with the disk, and it is reflected from the disk back into the optical system. The reflected light propagates to detectors where the data is converted into an electrical signal.

Modeling Disk Interaction

Jones calculus is utilized in the analysis of the disk-laser beam interaction (2). The following column vector represents an arbitrary E-field, where E_x and E_y symbolize two orthogonal polarization components:

$$E = \begin{pmatrix} E_x \\ E_y \end{pmatrix} \quad .$$

E_x and E_y are the matrices of complex values that model the wavefront. The light that is incident on the disk is linearly polarized, and the direction of polarization is defined as the x direction. The following column vector represents the incident light:

$$E_i = \begin{pmatrix} E_x \\ 0 \end{pmatrix} \quad .$$

This light interacts with the disk. The disk may be described using the following Jones matrix:

$$D = \bar{r} \begin{pmatrix} 1 & \kappa e^{i\delta} \\ \kappa e^{i\delta} & -1 \end{pmatrix} \quad ,$$

where $\bar{r}$ is the bulk reflectivity of the medium, κ is a matrix which contains information about the tangent of the Kerr angle at sampled positions on the disk, and δ is the phase shift between the x and y components on reflection from the medium (2). The reflected light is the product of the disk matrix and the incident light:

$$E_r = D \cdot E_i = \bar{r} \begin{pmatrix} 1 & \kappa e^{i\delta} \\ \kappa e^{i\delta} & -1 \end{pmatrix} \begin{pmatrix} E_x \\ 0 \end{pmatrix} = \bar{r} \begin{pmatrix} E_x \\ \kappa E_x e^{i\delta} \end{pmatrix} \quad .$$

κ contains the information about the data marks on the disk. Marks, which correspond to logical ones have a value equal to +tan(Kerr angle). Spaces between the marks, which correspond to logical zeros, have a value equal to -tan(Kerr angle). Figure 4 graphically depicts the matrix elements in a sample κ matrix.

The two polarization components in the reflected field are separately propagated back through the optical system using of Fresnel diffraction calculations. The methods described in the sections above are used to model propagation of the reflected light back through the system to data and servo detectors, which convert the information contained in the reflected beam into an electrical signal.

Implementation

This model is implemented on a 386 computer, running at 25 MHz. The modeling environment is the MATLAB programming language. MATLAB is an interactive mathematics programming environment that allows a user to perform a variety of calculations, including those necessary for the scalar diffraction model of the light propagating through the system.
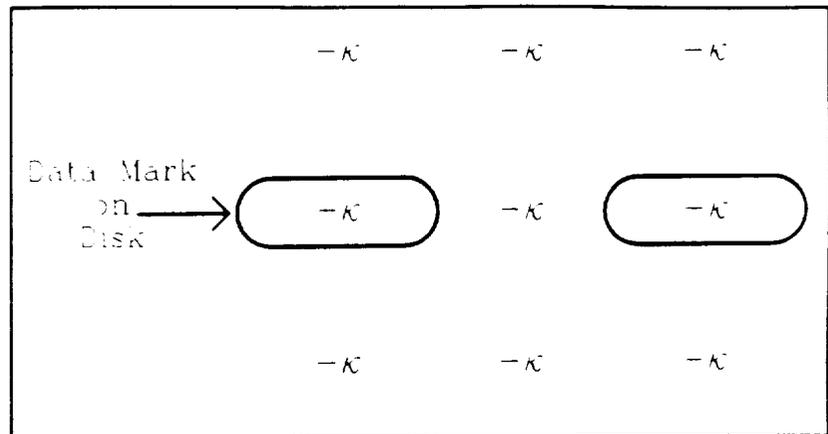
Figure 4   Example of a κ matrix

Conclusion

Light that travels through an optical data storage system can be modeled using the techniques discussed above. We can treat the modeling of light differently according to the functional subsystems interacting with the light. As discussed above, these subsystems are the laser diode, the optical system, and the optical disk. The model of the laser beam in the system is a combined physical optics analysis and geometrical optics analysis. The model uses Fresnel diffraction calculations and ray-trace calculations in order to simulate the propagation of the laser beam through the system.

Acknowledgements

The authors wish to thank Ken Moore of the Optical Sciences Center for suggesting the combination of ray-trace and diffraction calculations necessary to find the exit pupil wavefront. This work was supported by NASA grant no. NGT-50579.

References

1.   M. Mansuripur, "Certain computational aspects of vector diffraction problems", *JOSA A v. 6, no. 5* (1989)

2.   T. Milster, T. Gardner, "Modeling of a magneto-optic read path", *Proc. SPIE v. 899* (1988)

3.   C. Perlov, H. Birecki, "Modeling the magneto-optic recording process", *JJAP v. 28* (1989)

4.   A.B. Marchant, *Optical recording: a technical overview*, Addison-Wesley Inc. (1990)

5.   J.W. Goodman, *Introduction to Fourier Optics*, McGraw-Hill Inc. (1968)

6.   W.P. Dumke, "The angular beam divergence in double-heterojunction lasers with very thin active regions", *IEEE Journal of Quantum Electronics v. QE-11, no. 7* (1975)

7.   D.D. Cook, F.R. Nash, "Gain-induced guiding and astigmatic output of GaAs lasers", *Journal of Applied Physics v. 46, no. 4* (1975)

8.   A.E. Siegman, *Lasers*, University Science Books (1986)

N92-14912

Micro-optic lens for data storage

T.D. Milster, R.M. Trusty, M.S. Wang, F.F. Froehlich, and J.K. Erwin
Optical Sciences Center, University of Arizona, Tucson, Arizona 85721

Abstract

We describe a new type of microlens for data storage applications that has improved off-axis performance. The lens consists of a micro-Fresnel pattern on a curved substrate. The radius of the substrate is equal to the focal length of the lens. If the pattern and substrate are thin, the combination satisfies the Abbe sine condition. Therefore, the lens is free of coma. We analyze a 0.5 numerical aperture, 0.50 mm focal length lens in detail. A 0.16 numerical aperture lens was fabricated holographically, and results are presented.

2. Introduction

There are several types of microlenses commonly used in optical data storage systems. The most common are molded glass and molded plastic lenses. Molded optics weigh less than conventional multiple-element designs. Typical apertures are 3.5 mm to 4.5 mm in diameter, and numerical apertures (NAs) range from 0.45 to 0.55. For optical data storage applications, the smallest molded microlenses commercially available have an entrance pupil diameter of 3.0 mm (1). There are at least two reasons to use smaller optics. If a smaller microlens is used as an objective lens, the same number of disks can fit into a smaller stack height, and volumetric storage density will increase. Secondly, if all hardware dimensions scale linearly with optics size, a reduction in lens size by some factor will allow a reduction in moving mass by that factor to the third power, since mass scales with volume. The result will be an improvement in access time.

A serious problem observed with microlens components is a limited field of view. For applications like multiple beams and galvanometric tracking servos, the spatial area that must be in focus on the disk encompasses many track widths. The required focal area does not change as the objective lens focal length becomes smaller, which implies that the angular field of view increases, as shown in Figure 1. For example, consider a system that must focus over ± 30 tracks with a 0.5 numerical aperture (NA) lens. A diffraction-limited lens with a focal length of 4.5 mm requires a ±0.61° angular field. A lens with a 1.0 mm focal length would require a ±2.8° angular field. The limiting aberration in these systems is coma. Coma is also the limiting aberration in waveguides using focused grating couplers (2). In this paper, we outline a technique that eliminates coma and dramatically improves off-axis
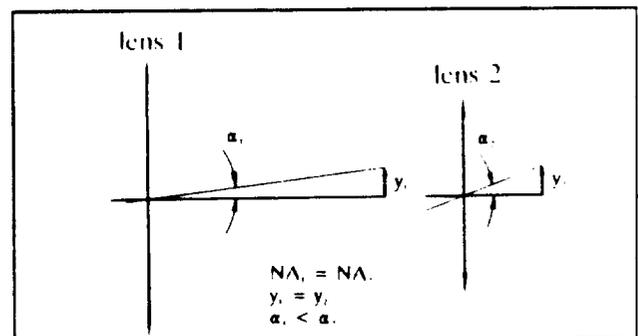
Figure 1.   Angular field increases with smaller lenses.

MILSTER

performance of these devices. A 160 μm
diameter 0.16 NA microlens has been
fabricated.

3. Microlens properties

There are several microlens techniques
which have been proposed. These include
graded-index lenses (3), holographic lenses
and zone plates (4), and micro-Fresnel lenses
(MFLs) (5). Each of these techniques has the
potential for very small apertures (~100 μm)
and high NA (0.5). Graded-index lenses
depend on the refraction of light rays.
Holographic lenses and zone plates utilize
diffraction properties. In the MFL, the center

Figure 2.   Planar MFL illuminated at
angle α.

portion acts like a refractive element, and the edges (where the zone spacing is on the order
of a wavelength) act like a diffractive element. The advantage of the Fresnel lens is that it
does not become significantly thicker and heavier as the NA increases. We now examine
the focal properties of very small (< 1 mm) focal length MFLs.

Off-axis performance of planar Fresnel lenses has been described by Young (6).
Consider the geometry of Figure 2, where a planar MFL is illuminated with a plane wave
at angle α. The radius of the nth zone is given by r_n. Coma, astigmatism and field
curvature aberrations are described by: $W_{131} = \alpha r_n^3/2\lambda f^2$, $W_{222} = \alpha^2 r_n^2/2\lambda f$, and
$W_{220} = \alpha^2 r_n^2/4\lambda f$, respectively. These aberrations are plotted as a function of field angle, α,
in Figure 3 for the following parameters: $f = 1.0$ mm, NA = 0.50 and $\lambda = 0.785$ μm. This
lens cannot be used at more than a 0.13° field without coma contributing λ/4 departure
(Rayleigh limit) to the ideal wavefront. If the coma could be eliminated, the limiting
aberration is astigmatism, which does not cross the Rayleigh limit until α ≈ 2.1°. A factor
of 16 improvement in the field angle would be realized.

Coma can be eliminated by forcing the MFL to satisfy the classical Abbe sine
condition (7). One way to satisfy the
Abbe sine condition is make the zonal
focal lengths equal when the lens is
used at infinite conjugates. As shown in
Figure 4, a planar MFL converts an
incident plane-wave phase distribution
into a converging spherical wave. The
zonal focal lengths, f_{zn}, increase with
radius. To become compatible with the
Abbe sine condition, the optical power
of the element can be placed on a
spherical surface (8), as shown in
Figure 5. The zonal focal lengths are
now equal, and the Abbe sine condition
is satisfied. A simple extension of
Young's treatment verifies that coma is
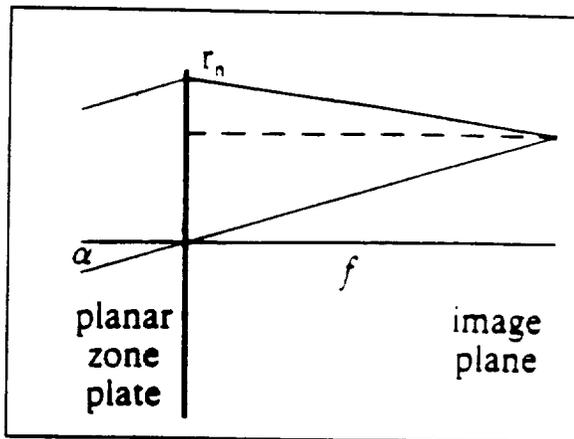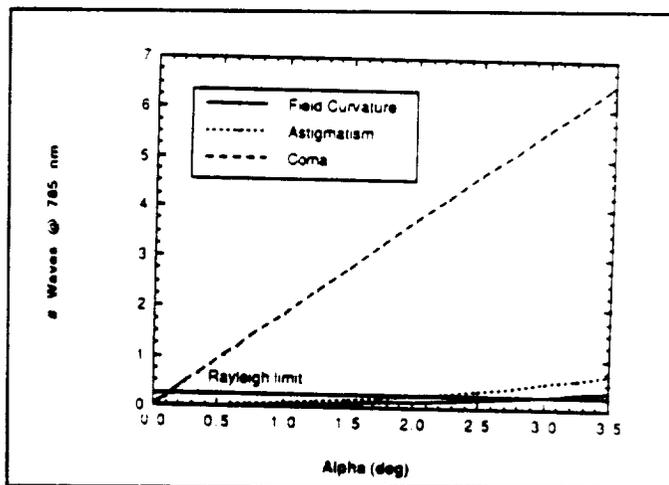
Figure 3.   Off-axis aberrations of a 0.50 NA
$f = 1.0$ mm planar MFL.
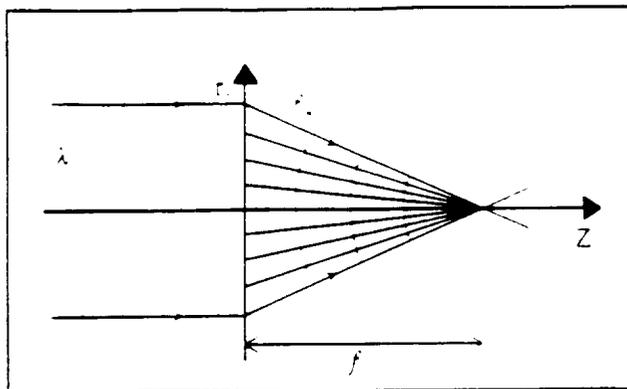
Figure 4. Planar-substrate MFL. Zonal focal lengths, f_{zn}, are not equal.
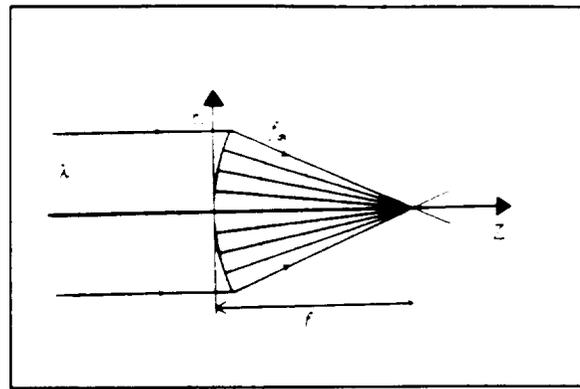
Figure 5. Curved-substrate MFL. Zonal focal lengths, f_{zn}, are equal.

eliminated. Delano (9) has also shown that coma is zero in this type of design.

In our treatment we neglect effects of the disk cover plate. Spherical aberration introduced by the cover plate can be corrected by modifying the MFL pattern on either the flat or curved-substrate designs. Coma due to the cover plate is small compared to coma from the flat MFL if a thin cover plate is used.

So far we have discussed properties of MFLs with the exact phase distribution required to form a converging spherical wave. The index variation is similar to a blazed and chirped diffraction grating. Blazing increases the diffraction efficiency of the MFL. Theoretically, 100% diffraction efficiency can be obtained with proper blazing (10). For the planar geometry of Figure 4, the required phase distribution is

$$\psi_n(r_n) = -\frac{2\pi}{\lambda}\left[f - \sqrt{f^2 + r_n^2}\right] + n\pi \quad . \tag{1}$$

For the curved geometry of Figure 5, the analogous expression to Equation 1 is

$$\psi_n(r_n) = -\frac{2\pi}{\lambda}\left[f - \sqrt{f^2 - r^2}\right] + n\pi \quad . \tag{2}$$

It is not necessary to form the exact phase distribution of Equation 1 or Equation 2 in order to evaluate the optical performance of the lens. Instead, a rectangular profile can be used at modulo π phase shifts. The result is a binary-type MFL with a lower diffraction efficiency but identical optical properties. The binary-type MFLs are desirable in the initial part of the work because they are easier to fabricate.

4. Experiment

To date, our efforts have focused on making a micro Fresnel lens on a curved substrate. The necessary substrate must be a thin spherical shell of the proper radius and high optical quality. We modify microspheres made for laser fusion research, which have the necessary characteristics. The microspheres are available with radii in the 500 μm -
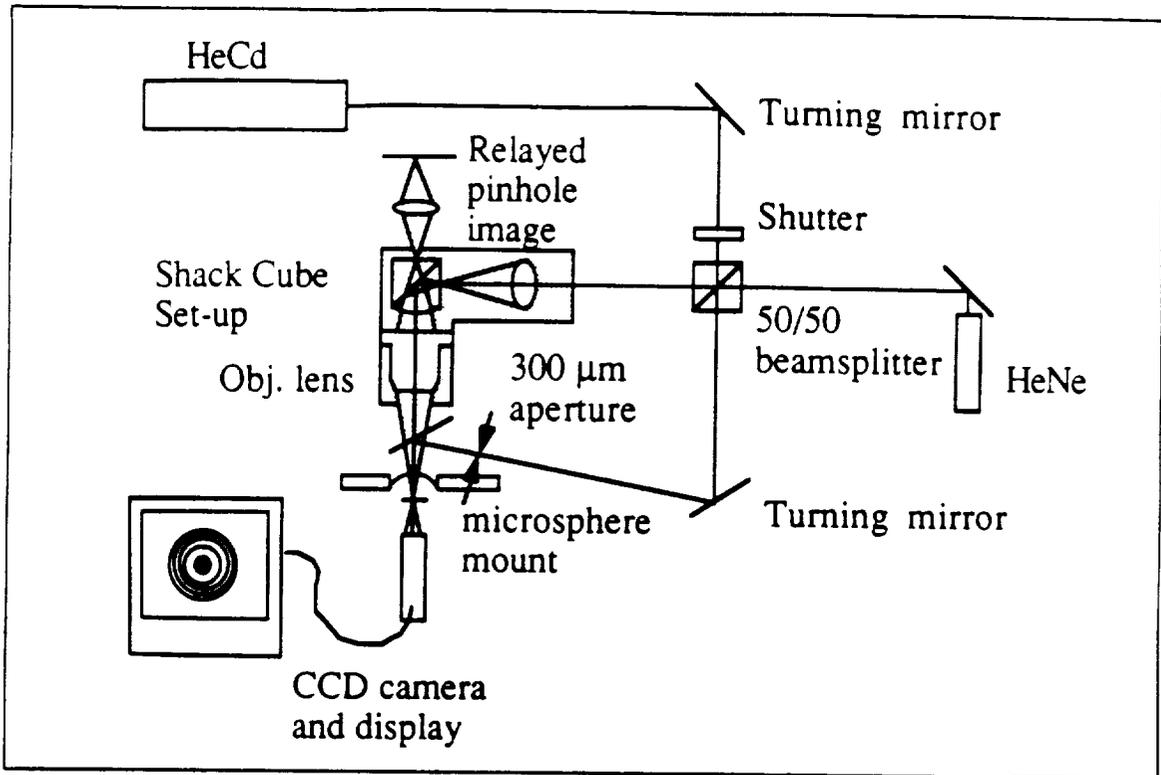
Figure 6.   Experimental setup for exposing the hologram.

1000 μm range.   The shells are 1 μm to 3 μm thick.   We have measured quality of two microspheres using a ZYGO interferometer.   Initial tests have shown that the parallelism between the inner and outer surfaces is better than a fraction of a fringe.   The wavefront quality of the surfaces varies dramatically.   One sphere tested with the ZYGO was of sufficient quality to use as a substrate, and the other was not.   We visually inspect the surface before each attempt at making a lens.

Our construction procedure consists of making a holographic exposure from a converging beam and a planar wavefront. A modified Mach-Zehnder arrangement was used, which is similar in principle to one described by Nishihara and Suhara (11).   The experimental setup is shown in Figure 6.   A HeCd laser was used to expose the photoresist, and a HeNe laser was used for alignment.   Both lasers were aligned to be coaxial.   A shutter controlled light from the HeCd laser.   One arm of the interferometer passed through a Shack-cube beam splitter that provided the object point for a finite-conjugate objective lens. The objective lens was focused at the center of curvature of the microsphere.   The second arm of the interferometer was reflected off a turning mirror and a pellicle beam splitter to provide the plane-wave component for the hologram.   Fringes were observed by a CCD camera behind the microsphere mount.   Reflections off the microsphere that passed back through the Shack cube were used to align the substrate axially and transversely.   After aligning with the HeNe laser, the substrate was translated axially the proper distance to compensate for focal shift caused by the blue HeCd laser.

Tolerance of the construction process is an important part of this study.   We used CODEV, an optical design program, to study tolerances for f = 0.50 mm, NA = 0.50 and λ = 0.442 μm.   Transverse displacement and axial defocus errors during the construction process
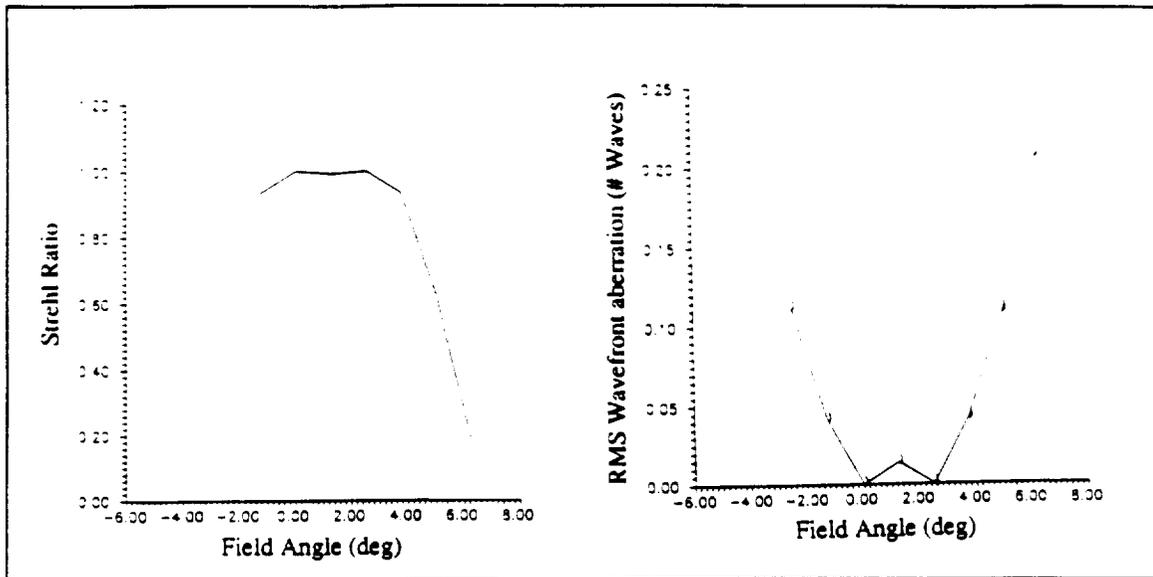
Figure 7.   Strehl ratio and rms wavefront error for an 11μm transverse alignment error.

were studied. The Strehl ratio and rms wavefront error are displayed in Figure 7 for an 11 μm transverse alignment error. The useful field angle is ±2.6° centered about 1.3°. The rms wavefront aberration indicates that there are two fields angles for which aberration is essentially zero. Figure 8 displays astigmatic line images versus field angle. Since there is no coma in this system, the line image plot is a good indicator of how the device would actually perform. There are two points in the field where the astigmatism is zero. This indicates that the system behaves with binodal astigmatism. The transverse displacement can be compensated by tilting the lens to the appropriate bias angle. Strehl ratio and
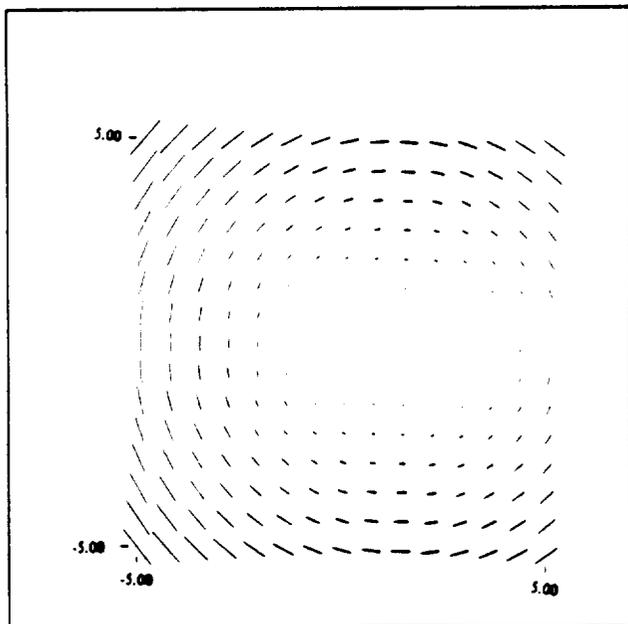
Figure 8.   Astigmatic line images versus field angle.
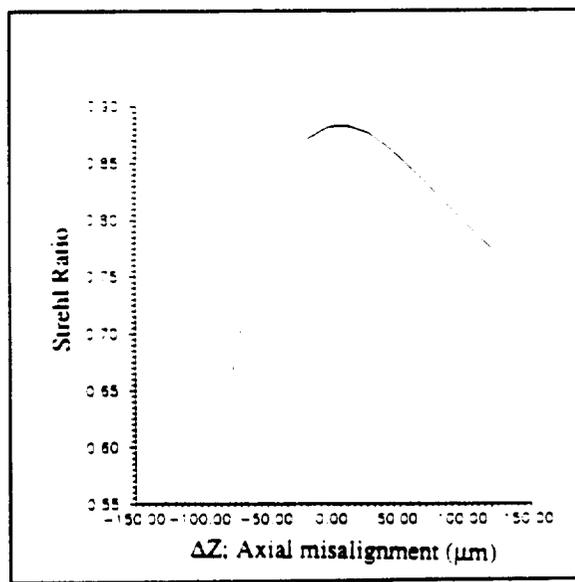
Figure 9.   Strehl ratio versus axial alignment error.

MILSTER
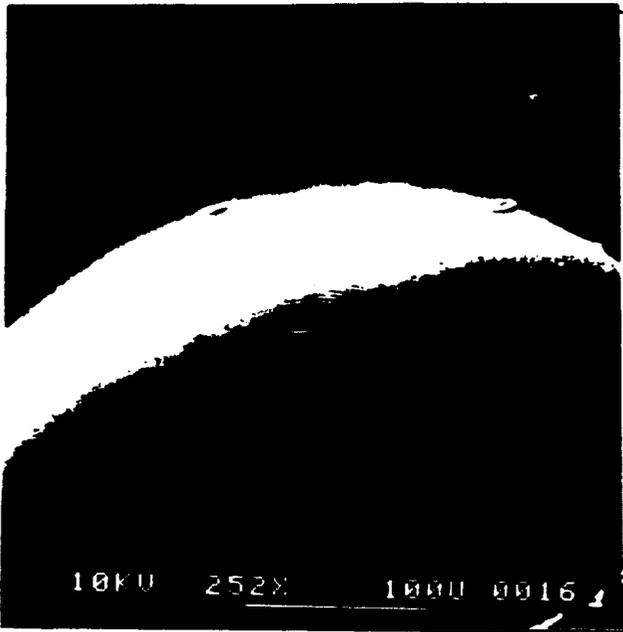
Figure 10.   SEM photograph of a microlens exposed on a curved substrate.
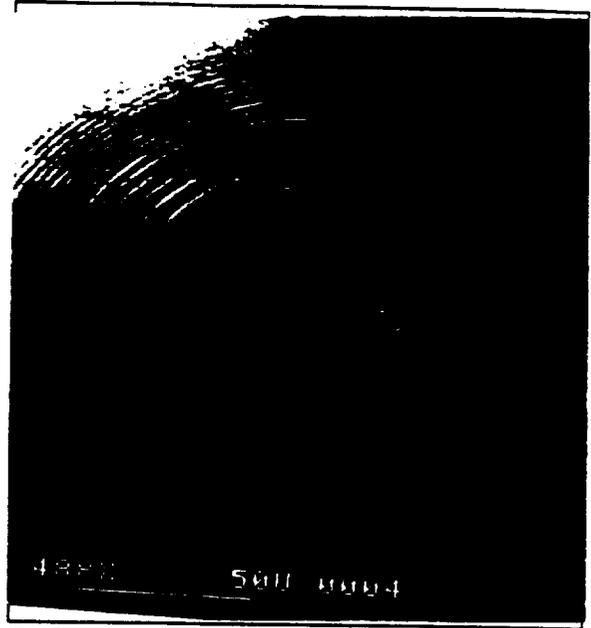
Figure 11.   Enlargement of the central portion of Figure 10.

versus axial alignment error is shown in Figure 9. The allowable defocus is in the range of ±30 μm, which is quite easy to control.

5. Results

A standard photoresist solution was used to coat a microsphere. The microsphere was cut in half and mounted on a holder. Figure 10 shows an SEM photograph of a microlens that has been exposed on the curved surface. We were only able to expose a 0.16 NA lens due to a conflict between the finite working distance of the objective lens and the pellicle beam splitter. Figure 11 shows the same lens under higher magnification. A rough appearance is observed in the holographic pattern.

We tried to test the optical quality of the microlens, but, due to the large amount of scatter, strong zero-order beam, and small size, we were not able to get consistent results. We did test diffraction efficiency and lens NA, which were 11.8% and 0.16, respectively.

6. Conclusions

We have shown that, in order for micro optics to be used effectively in advanced data storage systems, off-axis aberrations must be considered. One solution for improving off-axis performance is to curve the substrate of a MFL so that its radius of curvature is equal to its focal length. This satisfies the Abbe sine condition, and effectively eliminates coma. We tried a proof-of-principle experiment in which a microsphere substrate was coated with photoresist and exposed in a modified Mach-Zehnder interferometer. We were successful in exposing a 0.16 NA photoresist pattern. The pattern was mottled, so we were not able to test the lens quality due to scattering and physical constraints. The holographic method was instructive, but the NA is limited to rather low values (<0.20). Our group is pursuing

MILSTER

other methods of writing the patterns, which include electron-beam writing and binary optics.

7. Acknowledgements

8. References

1. Corning, Inc., commercial literature describing model 350160 aspheric lens.

2. G.L. Lawrence and P.J. Cronkite, "Waveguide grating with broad spectral response using gradient-effective index," University of Arizona patent disclosure submitted June 6, 1988.

3. K. Iga, Y. Kokuban, M. Oikawa, *Fundamentals of Microoptics,* Academic Press, New York, 1984.

4. G.T. Sincerbox, "Miniature optics for optical recording, " *Proceedings of the SPIE*, vol. 935, Gradient-Index Optics and Miniature Optics, pp. 63-76 (1988).

5. H. Nishihara and T. Suhara, "Micro Fresnel Lenses," in *Progress in Optics Vol XXIV,* E. Wolf, ed., North-Holland Physics Publishing, New York, pp. 3-36 (1987)

6. M. Young, "Zone plates and their aberrations," JOSA, vol. 62, No. 8, pp. 972-976 (1972)

7. R. Kingslake, *Lens Design Fundamentals,* Academic Press, Inc., San Diego, p. 158 (1978)

8. W.T. Welford, "Aplanatic hologram lenses on spherical surfaces," Opt. Com., vol. 9, no. 3, p. 268-269 (1973).

9. E. Delano, "Primary aberrations of meniscus Fresnel lenses," JOSA, vol. 66, No. 12, pp 1317-1320 (1976).

10. H. Dammann, "Blazed Synthetic Phase-Only Holograms," Optik, vol 31, pp. 95-104 (1970)

11. N. Nishihara and T. Suhara, "Micro Fresnel lenses," Progress in Optics V XXIV, E. Wolf, editor, North-Holland Physics Publishing, New York, pp. 3-35 (1987).

Use of Rigorous Vector Coupled-Wave Theory for Designing and Tolerancing Surface-Relief Diffractive Components for Magneto-Optical Heads

Charles W. Haggans and Raymond K. Kostuk

Optical Sciences Center
University of Arizona
Tucson, Arizona 85721

ABSTRACT

A rigorous coupled-wave model is presented, experimentally validated, and used for tolerancing surface-relief diffractive elements. Applications of this model in the design and tolerancing of components for magneto-optical (M-O) data storage heads are investigated.

1. INTRODUCTION

Surface-relief lithographically generated diffractive elements show promise for M-O data storage head applications due to their polarization selectivity, planar geometry, high diffraction efficiency, and manufacturability. However, previous application of surface-relief diffractive elements to M-O storage systems has been limited due to the lack of a suitable description for their polarization properties.

A model for describing these properties is presented in this paper. A general rigorous vector coupled-wave model for the calculation of the diffraction efficiency and the polarization properties of surface-relief gratings is described and validated with experimental measurements. The accuracy of the model is then analyzed. The presentation concludes with examples showing how the model can be used in the design and tolerancing of components for M-O head applications.

2. RIGOROUS COUPLED WAVE MODEL

The formalism used in this model is an extension of Moharam and Gaylord's rigorous coupled-wave analysis for volume grating diffraction.[1,2]. In this treatment, an arbitrary surface-relief profile is approximated by slicing the profile into a number of equal thickness slabs. Coupled-wave equations are then generated for the field in each slab and are solved using a state-variables method. The complex amplitudes of the reflected and transmitted diffracted orders are then generated by matching boundary conditions.

All fields are treated as vector quantities in this model. A vector approach enables the calculation of the polariation properties of diffracted beams when cross-coupling between the polarization states takes place. This condition exists when the grating vector is not in the plane of incidence. Polarization cross-coupling is a vector effect that cannot be treated using scalar approaches. Vector analysis also allows for the treatment of arbitrary incident and output polarizations.

The state of incident elliptical polarization is specified by the s and p amplitude ratio angle (α) (defined in Figure 1) and the s and p phase difference (δ). In this figure, a and b are the major and minor axis lengths for the vibrational ellipse of the incident electric vector. a_1 and a_2 are the maximum field strengths in the p and s directions, and ψ is the angle of rotation of the major axis of the ellipse from the

p axis.   An additional angle (χ) is used to represent the angular ratio of the major to minor axes of the ellipse.   These parameters are related by the trigonometric relations[3]:

$$\cos |\delta| = \frac{\tan 2|\psi|}{\tan 2|\alpha|} \qquad\qquad \sin |\delta| = \frac{ab}{a_1b_1} \qquad\qquad (1)-(2)$$

$$\sin |\delta| = \frac{\sin 2|\chi|}{\sin 2|\alpha|} \qquad\qquad \tan |\alpha| = \frac{a_2}{a_1} \qquad\qquad (3)-(4)$$

$$\tan |\chi| = \frac{b}{a}. \qquad\qquad\qquad (5)$$

The output polarization parameters determined by the model are the s and p amplitude ratio angle (α) and the s and p phase difference angle (δ) for all reflected and transmitted orders.   From these two parameters, the rotation angle of the polarization ellipse (ψ) can be calculated.   In the conical diffraction case, the s and p directions are different for each diffracted order.   These directions are defined with respect to the plane containing the propagation vector for that order and the grating vector.

The model is implemented in MATLAB, an interpreted matrix manipulation language.   Runs are currently made on a 33MHz/386 personal computer and a VAX 8650.   Typical run times are 3 seconds per data point for a single step grating (nt=1 and ns=9) and 5 minutes per data point for a ten step grating (nt=10 and ns=9).

3. EXPERIMENTAL VALIDATION OF THE MODEL

Model predictions were compared to experimental measurements made in our laboratory and to the published results of two other research groups.   The diffraction efficiency and polarization properties of a trapezoidal profile photoresist grating were measured in our laboratory.   This grating was fabricated holographically in Shipley 1811 photoresist.   The substrate was a microscope slide.   Measurements were made in reflection with an absorbing layer index-matched to the back surface of the substrate to eliminate Fresnel reflections from that surface.   The incident beam was linearly polarized at a 45° angle to the s and p axes.   The experimental reflected diffraction efficiency (η) was defined as the measured power diffracted into the +1st reflected order divided by the measured incident power.

The polarization rotation angles ψ and χ were measured by both a direct and an indirect method.   In the direct method, a linear polarizer was used to measure ψ.   When the transmission axis of the polarizer was aligned with the major axis of the polarization ellipse, the maximum power was transmitted.   For this condition, ψ was the angle between the polarizer transmission axis and the p axis.

χ was measured using a linear polarizer and a quarter-wave plate.   The fast axis of the quarter-wave plate was aligned with the major axis of the ellipse.   This eliminated the 90° phase difference between the linear polarization components along the b and a axes, giving linearly polarized light.   The plane defined by the linear polarization was rotated an angle χ from the major axis of the ellipse.   This angle was measured using a linear polarizer as described above.

In the indirect method, the magnitudes of ψ and χ were calculated from four power measurements.   The measured powers were proportional to $|a_1|^2$, $|a_2|^2$, $|a|^2$, and $|b|^2$. $|a_1|^2$ and $|a_2|^2$ are proportional to the power transmitted by a linear polarizer aligned with the p and s axes.   Similarly, powers proportional to $|a|^2$ and $|b|^2$ are measured for a polarizer aligned with the major and minor axes. $|\psi|$, $|\chi|$, $|\delta|$, and $|\alpha|$ were then calculated using equations (1)-(5).

These two methods for characterizing the output elliptical polarization state complement each other. The transmission axis of a single linear polarizer must be accurately aligned in the indirect power measurement method. In the direct measurements, both a linear polarizer and the fast axis of a quarter-wave plate must be accurately positioned. Thus, the indirect method give $|\psi|$ and $|\chi|$ more precisely than direct measurements. The direct measurement of ψ and χ gives the sense of rotation of the angles. This is useful because the sign of δ is the same as the sign of χ. [3]

The geometrical and physical properties of the grating were determined for input into the model. The grating period was determined optically to be .429 ± .0005 μm. This value was obtained by retroreflecting the +1st diffracted order onto the incident beam. The angle of rotation of the grating to achieve this condition (θ) gives the grating period according to:

$$\Lambda = \frac{\lambda}{2\sin\theta}. \tag{6}$$

In this relation, Λ is the grating period and λ is the wavelength of the incident light. This value was then used to calibrate the Scanning Electron Micrograph (SEM) (Figure 2). The grating depth was estimated from this photo to be .22 ± .01 μm. A 10 step approximation to the grating profile was made by averaging the profiles of the six visible grating ridges and 11 coupled waves were retained in the analysis. The index of refraction of the substrate was measured to be 1.51 using a Brewster's angle technique, and the published Shipley photoresist index of refraction is 1.64 at .6328 μm.

Figures 3 through 5 compare the experimental and calculated values of diffraction efficiency, α, and $|\delta|$ for the +1st reflected order diffracted by this grating. To obtain the best fit to the experimental data, iterations were made over the uncertainty range of the grating depth and grating profile measurements. Figure 3 shows diffraction efficiency (η) versus angle of incidence, Figure 4 shows +1st order polarization ratio angle (α) versus angle of incidence, and Figure 5 shows the phase difference magnitude ($|\delta|$) versus angle of incidence. Good agreement was obtained for all parameters.

Our model predictions were compared to published experimental results from a study of the antireflection properties of short period gratings.[4] In this work, Enger and Case fabricated gratings etched in fused quartz substrates with periods short enough to supress all propagating diffraction orders. They observed significant phase differences between the s and p polarizations of the zeroth order transmitted beam. Figure 6 shows the best fit to their experimental measurements and our model calculations of phase difference as a function of grating depth for gratings of approximately triangular profile. The physical parameters of their grating no.8 were used as input for our model. This grating has a period of .31 μm, the refractive index of the quartz substrate is 1.46, and measurements were made at a wavelength of .6328 μm. An 8 step profile approximation was used and 9 coupled-waves were retained in the analysis. Nearly exact agreement was obtained over a 1 μm range of depths.

Finally, a comparison was made to work originally performed by Moharam, et. al.[5] and later by Nakata and Koshiba[6]. Coupled wave (C-W) and boundary-element (B-E) theory were used respectively in these studies to calculate the transmitted diffraction efficiency of high aspect ratio photoresist gratings. The diffraction efficiency of two gratings was measured for s and p polarized light by the original authors. The s and p component diffraction efficiencies for grating no.8 were calculated using our model. This grating has a period of .458 μm, a refractive index of 1.64, a depth of .59 μm, and an undercut profile.

Figure 7 shows the experimental measurements and the calculations of the three models for the diffraction efficiency of s polarized light as a function of angle of incidence. Figure 8 is the corresponding plot for p polarization. Our calculations deviated from the measured data in the manner of the previous studies for s polarization for angles of incidence between 15° and 25°. The B-E model provides the best fit to the measured data for large angles of incidence. However, our calculations

tend to agree with experiment better than the previous C-W model predictions. For p polarization, our model provided a better fit to the experimental data for large angles of incidence than either of the two previous models. However, it exhibited increased deviations from experiment from 25° to 40°.

Because the parameters input to the previous C-W model are not known, it is not possible to determine the cause of the poor agreement between the two models. The rigorous coupled-wave formalism used in our model reduces to the scalar coupled-wave formalism used in the previous C-W model. Thus, we assume that differences in the predictions of the two models occur because of differences in the approximation of the grating profile.

4. ACCURACY OF MODEL PREDICTIONS

Three factors determine the accuracy of the model in predicting experimental measurements: The accuracy of measurement of the physical properties of the grating, the precision with which the grating profile is approximated, and the numerical precision of the model.

For exact reproduction of the experimental measurements, the grating profile must be exactly characterized. Some physical parameters such as the grating period, the angle of incidence, and the refractive indices can be accurately determined. However, the grating depth and the grating profile are difficult to characterize. Measurement of these two parameters is limited by the irregularity of the grating ridges and by lack of contrast of the SEM photograph.

The precision of the approximation of the grating profile is determined by the number of slabs (nt) used in the approximation. The numerical precision of the model is determined by the number of coupled waves (ns) retained in the analysis. For perfect grating characterization, each output parameter converges to a constant value as nt and ns are increased.

The effects of inaccurate profile determination and insufficient numerical precision are readily observable from Figures 9 and 10. Figure 9 shows the calculated reflected +1st order diffraction efficiency versus ns for 5, 8, 10, and 12 approximations to the profile of Figure 2 for an incidence angle of 35°. Figure 10 is a similar plot for the reflected s and p phase difference. In these figures, the curves for nt=8 and nt=12 converge to efficiency values that are larger than those for the nt=5 and nt=10 curves. If the shapes of the curves changed as nt increased, the precision of the approximation of the profile would be in question. For this situation, increasing nt would cause a convergence in profile shape. However, the similar shape of the curves indicates that error in duty cycle measurement is responsible for the different efficiencies at convergence. This source of error limits the accuracy of the comparison to experiment to approximately 5 degrees for the phase difference angle and .5% for the diffraction efficiency for the grating of Figure 2.

The convergence of the curves in Figures 9 and 10 indicates that the numerical precision of the predictions increases as ns increases. The phase difference curves of Figure 10 can be observed to converge slower than the diffraction efficiency curves of Figure 9. This indicates that diffraction efficiency is less sensitive to the numerical precision of the model. Thus, the phase difference is a better indicator of the level of model precision.

These figures show that the precision of the profile approximation and the numerical precision of the model are satisfactory for this grating for coarse profile approximations and a small number of retained orders. This is evident from the similarity of the curve shapes and the rapid convergence of each curve. Sufficient precision for small values of ns and nt is computationally advantageous because the execution time of the model increases rapidly as these parameters increase.

5. APPLICATION TO MANUFACTURING TOLERANCE ANALYSIS

This model demonstrates that small errors in the fabrication of surface-relief gratings (depth, period, etc.) can cause substantial deviations from designed performance. These deviations are especially important as the grating period decreases and for high aspect ratio gratings.

The impact of manufacturing errors can be quantified by the comparison of calculated diffraction efficiencies over a hypothetical range of grating parameter values. Figure 11 shows theoretical first order diffraction efficiency curves for a two step approximation to a trapezoidal grating for three closely spaced grating periods (1.0, 1.1, and 1.2 μm). This figure shows that a .2 μm change in the grating period can cause as much as a 30% change in the diffraction efficiency. Since an optimistic tolerance in the fabrication of grating structures using lithographic techniques is of this order, it can be seen that manufacturing tolerances limit the performance of high spatial frequency lithographically generated gratings.

6. APPLICATION TO POLARIZING ELEMENT DESIGN

A unique aspect of this model is its three-dimensional efficiency surface generation module. This module can be used as an aid in designing complex elements. The output of this module is a three-dimensional plot of diffraction efficiency versus two grating parameters (i.e., grating period and grating depth, duty cycle and wavelength, etc.). Using this module, design points can be generated from a wide range of input parameters in a single run.

An example of the utility of this module is the design of rectangular profile polarization selective and nonselective elements. Figure 12 shows the diffraction efficiency for the 1st transmitted order as a function of grating depth and period for s and p polarizations for a square profile grating. Note that point B exhibits high s and low p efficiency, giving a design point for a polarization selective element for leaky beamsplitting applications. Figure 13 is the indicated cross-section of this surface in the .45 μm grating period plane. Alternatively, point A shows high s and p diffraction efficiency into the 1st transmitted order, forming a polarization nonselective element. Figure 14 shows the indicated cross-section in the .6 μm grating period plane.

7. CONCLUSION

A model for calculating the diffraction efficiency and polarization properties of surface-relief diffractive structures has been presented. Three examples of the validity of this model's predictions have been given. Use of the model for tolerancing and design of diffractive components has been presented.

8. ACKNOWLEDGEMENTS

9. REFERENCES

1.   M.G. Moharam and T.K. Gaylord, "Three Dimensional Coupled Wave Analysis of Planar-Grating Diffraction," J. Opt. Soc. Am., Vol. 73, 1105-1112 (1983).

2.   M.G. Moharam and T.K. Gaylord, "Diffraction Analysis of Dielectric Surface Relief Gratings," J. Opt. Soc. Am., Vol.   72, 1385-1392 (1982).

3.   M. Born and E. Wolf, Principles of Optics, 6th ed., Pergamon Press, Oxford, 1980.

4.   R.C. Enger and S.K. Case, "Optical Elements With Ultrahigh Spatial Frequency Surface Corrugations," Appl. Opt., Vol. 22, 3220-3228 (1983).

5.   M.G. Moharam, T.K. Gaylord, G.T. Sincerbox, H. Werlich, and B.Yung, "Diffraction Characteristics of Photoresist Surface-Relief Gratings," Appl. Opt., Vol. 23, 3214-3220 (1984).

6.   Y. Nakata and M. Koshiba, "Boundary-Element Analysis of Plane-Wave Diffraction from Groove-Type Dielectric and Metallic Gratings, "J. Opt. Soc. Am., Vol. 7, ..34-1502 (1990).
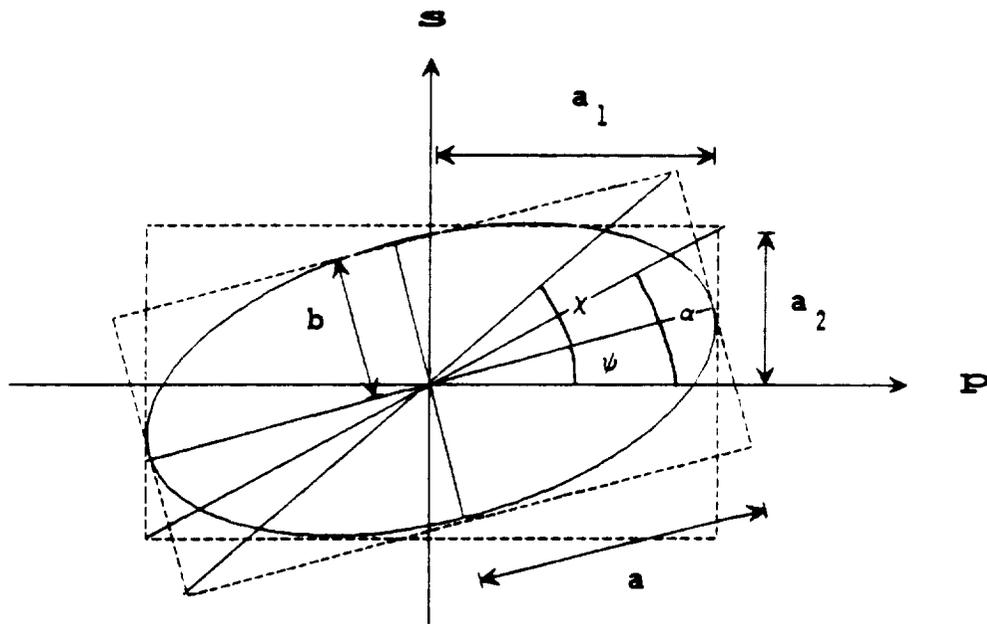
Fig. 1. Vibrational ellipse of the electric field
for elliptical polarization.
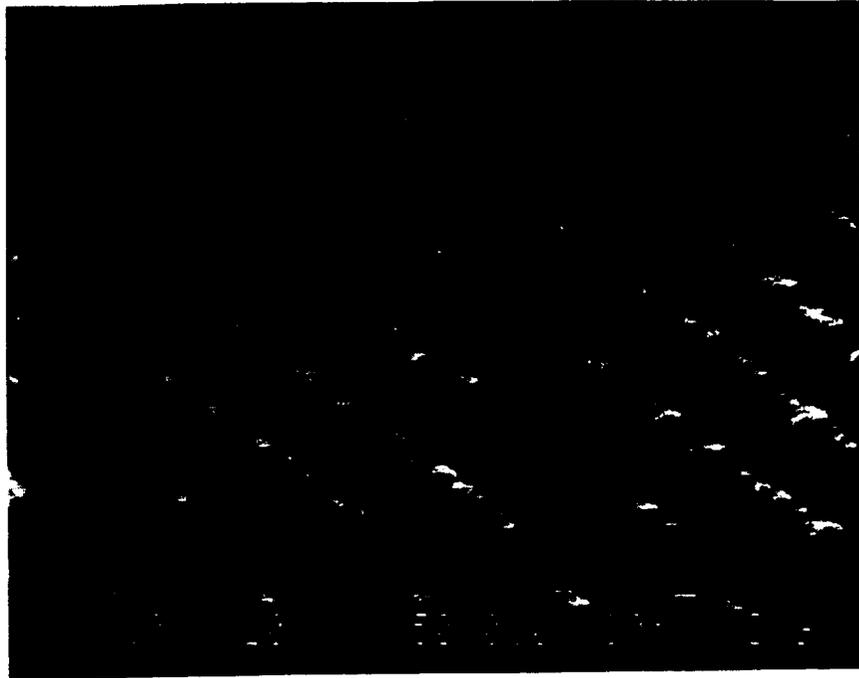
Fig. 2. Scanning electron micrograph of the
photoresist grating measured in our laboratory.
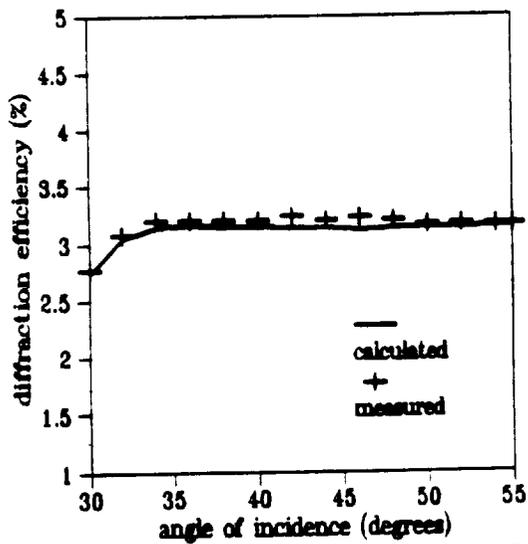
Fig. 3. +1st reflected order D.E.
for the grating in Fig. 2.
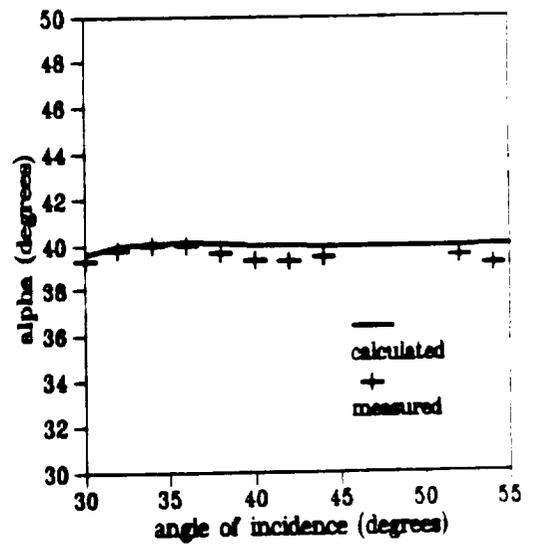
Fig. 4. +1st order polarization ratio
angle for the grating in Fig. 2.
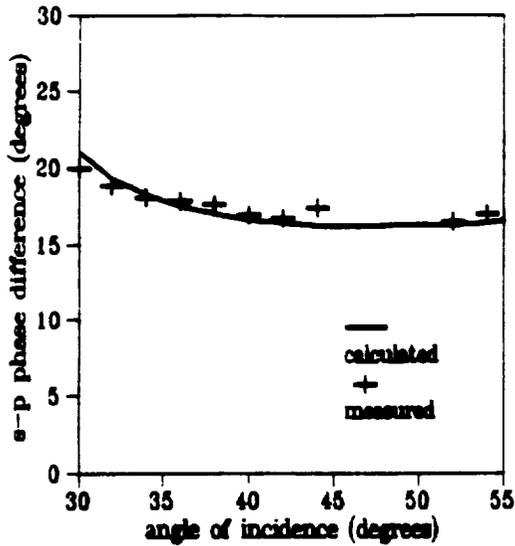
Fig. 5. +1st reflected order s-p phase difference for the grating in Fig. 2.
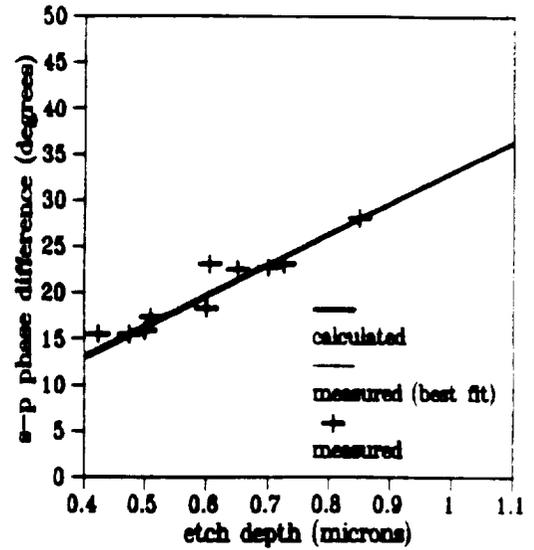
Fig. 6. Phase difference vs. etch depth for grating 8 from reference 4.
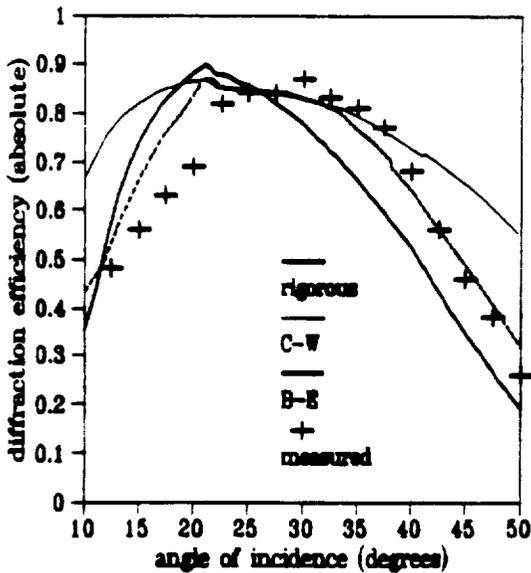
Fig. 7. Transmitted D.E. of grating 8 of reference 6 for s polarization.
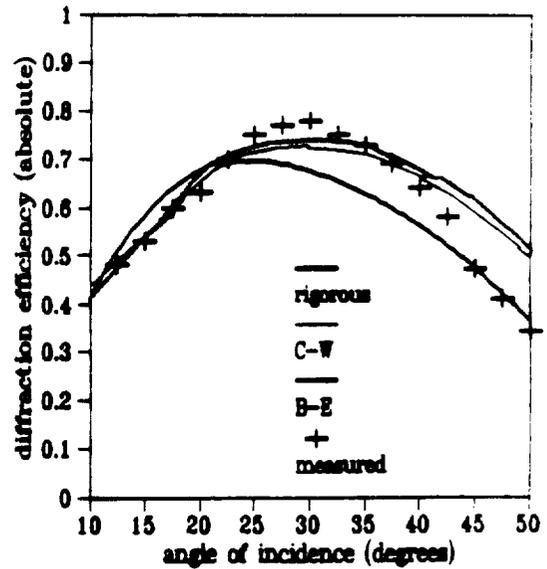
Fig.8. Transmitted D.E. of grating 8 of reference 6 for p polarization.
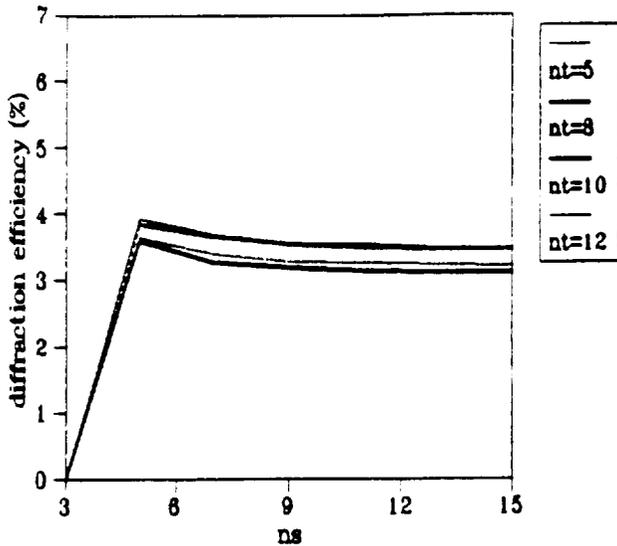
Fig. 9. Reflected +1st order DE vs. ns
calculated for the grating in Figure 2.
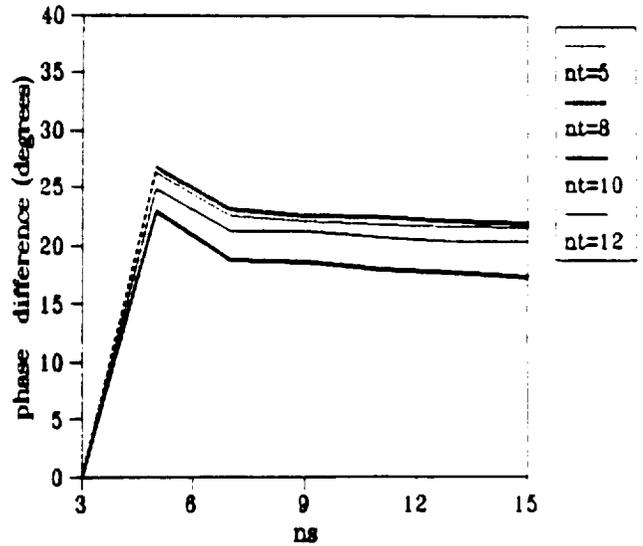
Fig. 10. Reflected phase difference vs.
ns calculated for the grating in Fig.2.
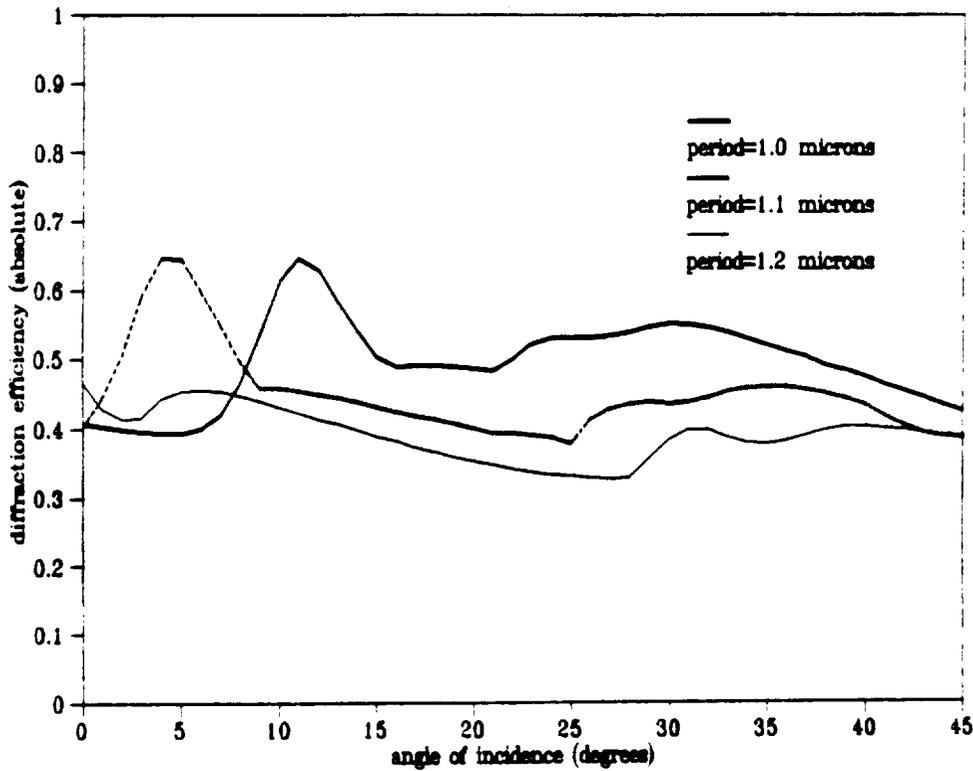
Fig. 11. +1st transmitted order diffraction efficiency for s polarization vs. angle
of incidence for a two slab photoresist grating (n=1.64) of .55 micron depth on a
glass substrate (n=1.51) at a wavelength of .6328 microns. The duty cycles of
the two slabs are 23.8% and 38.1% respectively, and the first slab is positioned
on the second slab to give even symmetry in the grating profile.

Appendix K
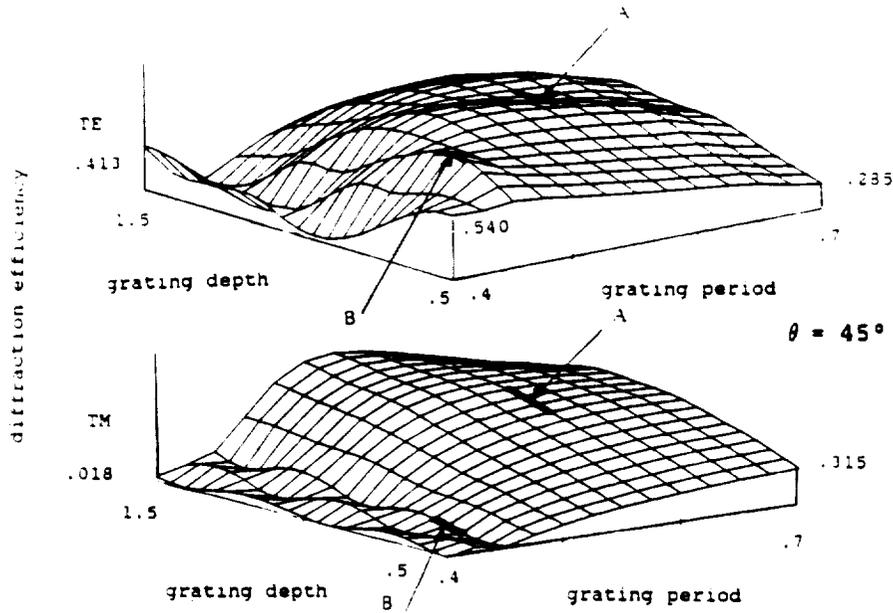
Fig. 12. +1st transmitted order diffraction efficiency for s and p polarizations vs. grating depth and period for a rectangular profile photoresist grating (n=1.68) at a wavelength of .780 microns. The duty cycle of the grating is 60%.
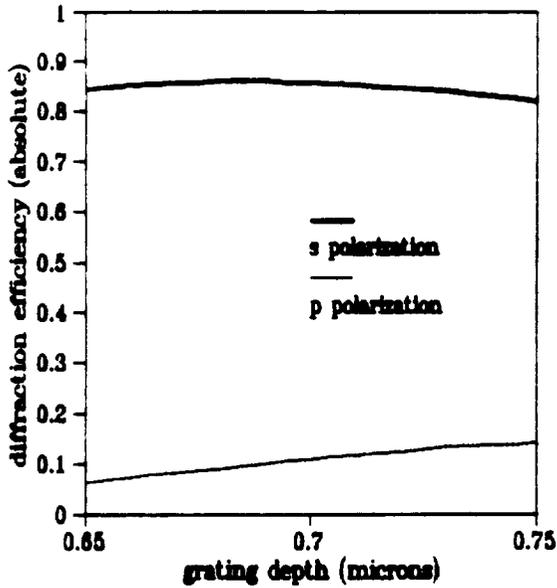
Fig. 13. Cross-sectional profile B of
Fig.12 for grating period=.45 microns.
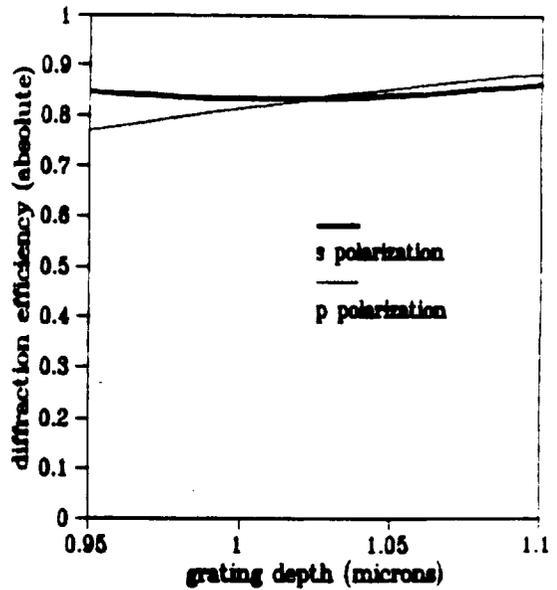
Fig. 14. Cross-sectional profile A of
Fig.12 for grating period=.6 microns.

N92-14914

Practical Design Considerations and Performance Characteristics of High Numerical Aperture Holographic Lenses

Raymond K. Kostuk

Electrical and Computer Engineering Department, and Optical Sciences Center, University of Arizona Tucson, AZ. 85721, USA

ABSTRACT

The diffraction efficiency of interferometrically formed holographic lenses is influenced by the recording geometry and properties of the recording material. Variations in efficiency increase when attempting to make high numerical aperture elements. In this presentation the factors which influence the diffraction efficiency of high numerical aperture holographic lenses are examined.

1. Introduction

Many factors influence the diffraction efficiency of holographic lenses. These include changes in the visibility of interfering fields across the hologram aperture due to intensity and polarization variations, changes in the average refractive index and thickness of the recording material between exposure and processing steps, and variation of the interbeam angle over the aperture of the hologram. Considering high efficiency phase gratings, these effects physically alter the refractive index modulation at different locations across the aperture.

In order to analyze the influence of these factors, high numerical aperture (0.54 N.A.) holographic objectives were formed in bleached silver halide emulsions using a reversal bleach process. The total efficiency of this lens was 43% compared to a planar grating efficiency of 47% formed with two collimated beams and similar geometrical conditions. The efficiencies of higher diffraction orders for both s- and p- polarized reconstruction beams are mapped across the aperture, and related to the interbeam angles of the construction beams at different locations. Although several evaluations of high N.A. lenses have previously been made[1-3], these investigations only considered a section of the lens containing the grating vector (K) which was illuminated with light polarized perpendicular to this plane. This paper provides experimental results for the efficiency of the grating with different K vector and reconstruction field polarization orientations.

2. Characterization of Holograms formed in Bleached Silver Halide Emulsions

Holograms for this evaluation were formed in Agfa 8E75HD silver halide emulsions exposed with 632.8 nm illumination, and processed with an Ilford reversal chemistry (SP678C developer/SP679C bleach). This material was chosen because its properties have been well characterized, and because processing is relatively simple and provides consistent results.

Although the efficiency is less than that obtained for dichromated gelatin and some photopolymers, many of the same factors affecting silver halide holograms will also appear in gratings formed in other materials.

The efficiency as a function of exposure for a series of unslanted and slanted planar gratings processed with the reversal chemistry are shown in Figures 1 and 2. (The diffraction efficiency for this analysis is equal to the power in a particular order divided by the incident power.) An interbeam angle of $40°$ was used for both cases, and the slanted grating formed with one beam at normal incidence to the emulsion and the second at $40°$ to the normal in air. (This geometry corresponds to the interfering rays at the center of the focusing holographic lens.) Maximum efficiency for the unslanted grating occurs when the hologram is illuminated at the construction angle. However, for the slanted grating, the maximum diffraction efficiency occurs at a different angle from that used during construction. Figure 2 shows that their is about a 10% change in absolute diffraction efficiency (20% relative) near the optimum exposure for this process. This results from changes in the emulsion thickness which effectively rotates the grating plane, and a change in the average refractive index further detunes the grating from peak efficiency at the construction angle. A reversal bleach removes the exposed silver halide crystals which were converted to silver during development[4]. This mechanism reduces both the emulsion thickness and average refractive index producing a drop in efficiency. This same mechanism however, also reduces the negative effects of scatter and noise gratings, and gives reasonably high diffraction efficiency. Since the thickness and average refractive index change could be quantified, the reversal bleach process was used for this evaluation. Measurement of an emulsion exposed with 115 $\mu J/cm^2$ showed an average refractive index change from 1.64 to 1.60, and a thickness reduction from 5.0 μm to 4.5 μm.

3. Factors Affecting the Efficiency of Focusing HOEs

Consider the construction geometry for a holographic lens shown in Fig. 3. In this arrangement an on-axis spherical beam interferes with an off-axis collimated reference beam. The polarization of the reference field is along the y-axis. The spherical beam is formed by focusing collimated beam with its field polarized along the y-axis. The polarization of this beam has a different orientation for each ray illuminating the aperture. Therefore, as the NA of the element increases there will be a larger difference between the polarization vectors of the spherical and reference beams. High numerical aperture elements accentuate this difference and make it necessary to consider vector effects both during construction and reconstrucion.

The configuration of Figure 3 provides a relatively large interbeam angle over much of the grating aperture. This reduces the grating period, increases the overall efficiency, and tends to equalize the efficiency of s- and p- diffracted light[5]. Another advantage of this arrangement is that non-diffracted light in the zero order does not overlap with the focusing beam during reconstruction which would reduce the signal-to-noise level in the region of focus. In addition, the off-axis geometry can also be used to help circularize the reconstruction beam.

In order to analyze the varying efficiency of this hologram a localized planar grating approximation is made at discrete points across the aperture[3]. At the lens center the corresponding planar grating has an interbeam angle of $40°$ with both fields polarized in the y direction. Plots of the experimental diffraction efficiency vs. reconstruction angle for the central region of a 0.54 NA focusing element and for a hologram formed with two collimated fields are illustrated in Figures 4 and 5 respectively. These holograms were made using the same exposing and processing conditions and show reasonably good correspondence in maximum efficiency, however there is an angular displacement indicating that the probe beam diameter(1mm) may have exceeded the limit for the local plane grating approximation.

The efficiency of a volume hologram depends on the visibility of the interfering fields and the exposure level at the film plane. When the emulsion response is linear, this dependence can be approximated[7] by the relation

$$\eta = SE_0V \quad .$$

where S is a film sensitivity factor, E_0 is the average film exposure, and V is the visibility of the interfering fields within the emulsion. The film sensitivity factor will depend on the particular type of emulsion and processing chemistry. The exposure will vary across the aperture of the focusing element due to changes in the path lengths between the center and edge of the aperture for the expanding spherical beam, and changes in the fresnel coefficients. These differences affect the beam ratio (R) which in turn influence the visibility since

$$V = \frac{2R^{1/2}cos(\Omega)}{(1 + R)} \quad ,$$

with Ω the relative orientation of the polarizations of the interfering fields.

Combining these factors and calculating the ratio of the efficiency at the edge of the hologram aperture relative to the center shows (Fig.6) that the expected fall-off for a 0.55 NA element illuminated with an s-polarized reconstruction beam is about 15%, and 25% with a p-polarized beam.

As stated earlier, these calculations assume that η varies linearly with exposure. This is a good assumption for dichromated gelatin and many photopolymers, however materials such as silver halide tend to saturate after reaching a maximum value (Figure 1). This can be used to advantage by exposing the emulsion beyond the linear range of the film. Since the efficiency does not change rapidly with exposure in this region, variations of η across the aperture can be reduced. (It is assumed that nonlinearities in the refractive index modulation were small since measurements showed that very little power went into higher diffraction orders.)

For a highly linear responding material the slope of the efficiency vs exposure can be reduced by using a thinner emulsion. Exposing the emulsion at level slightly above the first η maximum will then keep the total efficiency high over a relatively large exposure range.

Other factors which influence the diffraction efficiency of high numerical aperture HOEs are differences in emulsion thickness and average refractive index between the exposure and post process phase of hologram recording. The effects of these variations on the diffraction efficiency for the slanted planar grating described earlier corresponding to the local grating at the center of the focusing HOE were determined using coupled wave analysis[3] and are illustrated in Figures 7 and 8. As indicated a change in emulsion thickness produces significant displacement and reduction in the efficiency, however a change in the average refractive index of 0.06 results in only a small displacement of the curve (i.e. $2°$). Values for the average refractive index and thickness change for emulsions processed with the reversal bleach presented in the previous section indicate that the change in average refractive index is not significant, however the thickness change will produce a major shift in the efficiency performance.

The numerical values in **Figure 3** show the normalized coordinates in the x direction and the corresponding interbeam angles $\Delta\theta_{inter}$ for a 0.55 NA lens. These angles can then be used to compute the appropriate grating vector and diffraction efficiency for local planar gratings. For emulsions on the order of 5 μm thick, average refractive index of 1.6, and index modulation of 0.05, the volume grating conditions will not be satisfied across the aperture. This will give rise to higher diffraction orders which extract power from the desired order.

4. Fabrication and Evaluation of High N.A. Holographic Lenses

Holographic lenses were formed with a spherical beam produced with a 0.55 N.A. long working distance microscope objective and a collimated reference beam at $40°$ to the surface normal of the emulsion. A beam ratio of 1 at the center of the exposed area was obtained by placing a mask with a small diameter aperture in the film plane and then measuring the power in each beam. The film was then exposed with 115 $\mu J/cm^2$ of 632.8nm illumination from a HeNe laser as mentioned in Section 1, and processed with a standard Ilford reversal chemistry. This exposure level was beyond the linear range of the film/process combination (Figure 1), and was expected to improve uniformity in the efficiency over the aperture of the HOE.

After processing the hologram was illuminated with the conjugate of the planar reference beam. A mask with a 1 mm aperture was mounted on an x-y translational stage to probe the efficiency at different locations in the aperture. Both s- and p- polarized light was used to illuminate discrete positions along the x- and y-axes of the hologram. The results of these measurements are shown in Figures 9-12. The smallest interbeam angle exists at the x = -1.0 positions on the x-axis efficiency plots. The +1 and -1 diffraction orders are equal at this coordinate indicating that the grating acts like a thin sinusoidal grating. There are several weaker diffraction orders (R_o, T(-2), and R(-1)) not shown on these figures for clarity which account for an additional 15% of the incident illumination at the x = -1 position. In each case the efficiency of the primary order also decreases near the edge of the aperture with the largest interbeam angle. It is not exactly clear if this drop is a result of a decrease in exposure or is due to an overcoupling effect. From Figures 1 and 2 it can be seen that a slanted grating does not saturate in the same manner as an unslanted

one. This effect would be accentuated near the edge of the hologram aperture where the interbeam angle in air is close to 73°. Given these limitations however, the total s- and p-efficiencies over the complete aperture were 43.1 and 41.7% respectively. A corresponding planar grating formed with a normally incident beam and a second beam at 40° to the emulsion normal had an s-polarized reconstruction beam efficiency of 47%. Using this as a reference for the maximum efficiency obtainable with this film and process chemistry, the focusing element efficiency is approximately 92% of the possible planar grating efficiency.

Acknowledgements

5. References

1. C. Kojima, K. Miyahara, K. Hasegawa, T. Otobe, and H. Ooki, "In-Line Holographic Lenses of High Numerical Aperture," Japan. J. Appl. Phys., 20, Supplement 20-1, 199-204 (1980).

2. R.R.A. Syms and L. Solymar, "Higher diffraction orders in on-axis holographic lenses," Appl. Opt., 21, 3263-3268 (1982).

3. R.R.A. Syms and L. Solymar, "Experimental and theoretical evaluation of the efficiency of an off-axis volume holographic lens," Appl. Phys. B 32, 165-173 (1983).

4. G. Saxby, **Practical Holography**, Prentice Hall, p.73, (1988).

5. A.B. O'Connor and R.K. Kostuk, "Polarization properties of high numerical aperture holographic objectives," OSA Topical Meeting on Optical Data Storage, Los Angeles, CA. 17-19 Jan. 1989, Technical Digest p.95-97.

6. R.R.A. Syms and L. Solymar, "Localized one-dimensional theory for volume holograms," Opt. Quant. Electron., Vol. 13, 415-419 (1981).

7. L.H. Lin, "Method of characterizing hologram-recording materials," J.Opt. Soc. Am., Vol. 61, 203-208 (1971).

8. H. Kogelnik, "Coupled wave theory for thick hologram gratings," Bell Syst. Tech. J., Vol. 48, 2909-2947 (1969).
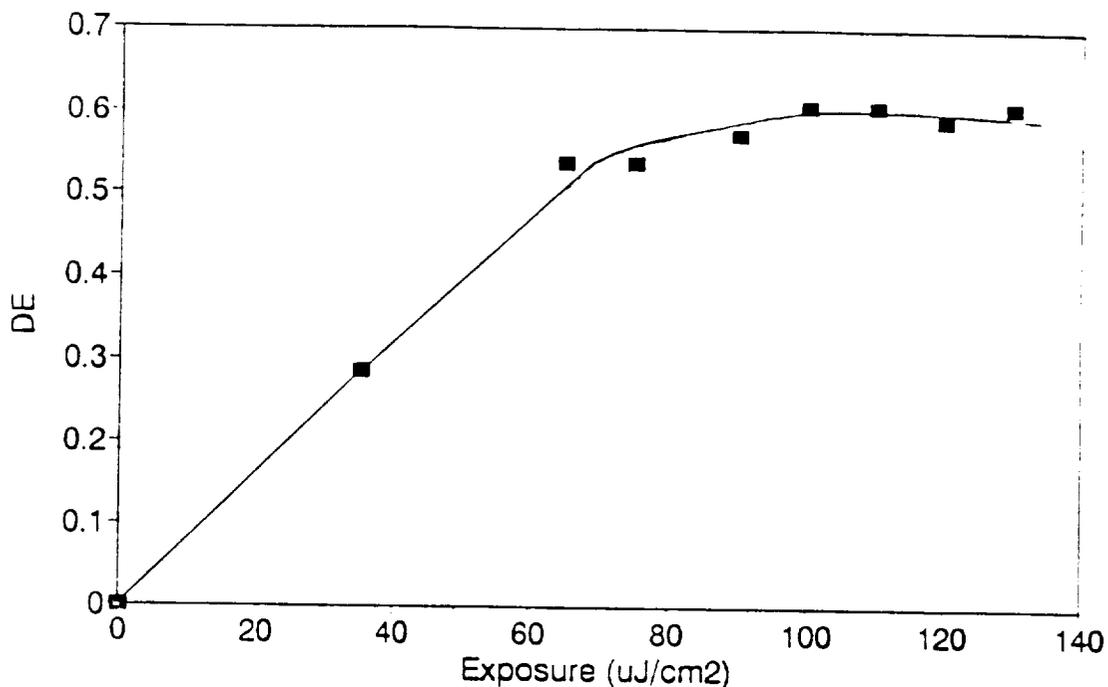
Figure 1. Diffraction efficiency vs. exposure for Agfa 8E75HD emulsions processed with Ilford SP678C developer and SP679C reversal bleach. Grating planes are normal to the emulsion surface, and was formed with two collimated beams having a 40° interbeam angle in air.
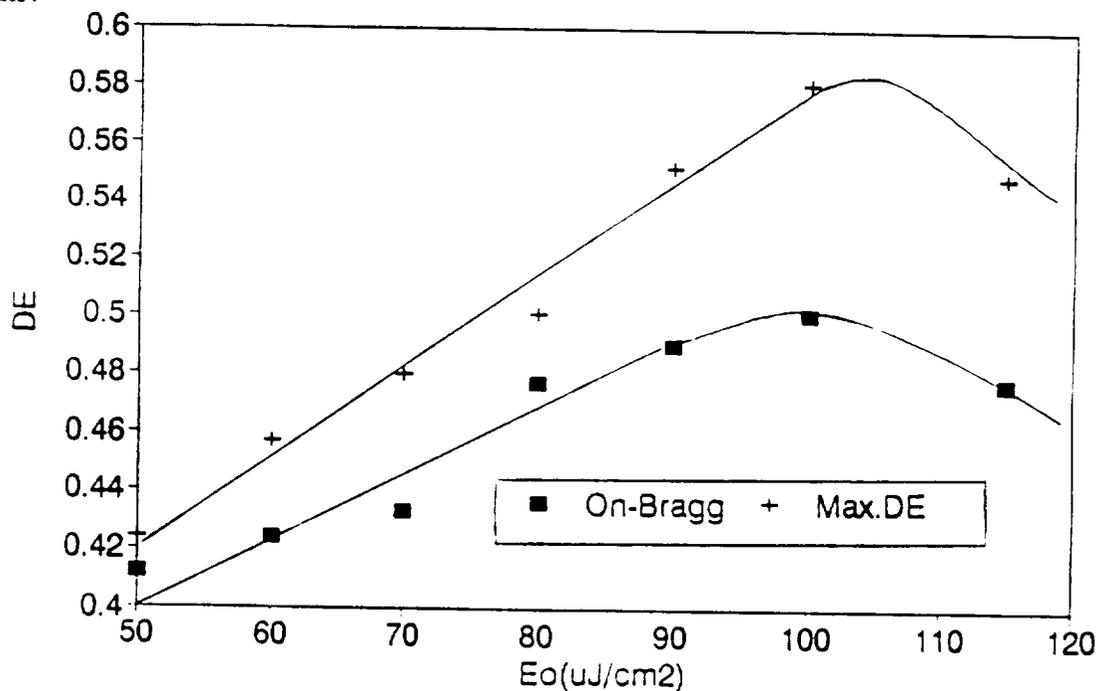
Figure 2. Diffraction efficiency vs. exposure for a planar grating formed in Agfa 8E75HD emulsions processed with Ilford SP678C developer and SP679C bleach. The slanted grating was formed with one beam normal to the emulsion surface and the second at 40° to the normal in air. The upper curve shows maximum efficiency obtained by rotating the grating, and the second is reconstructed at the formation angle.
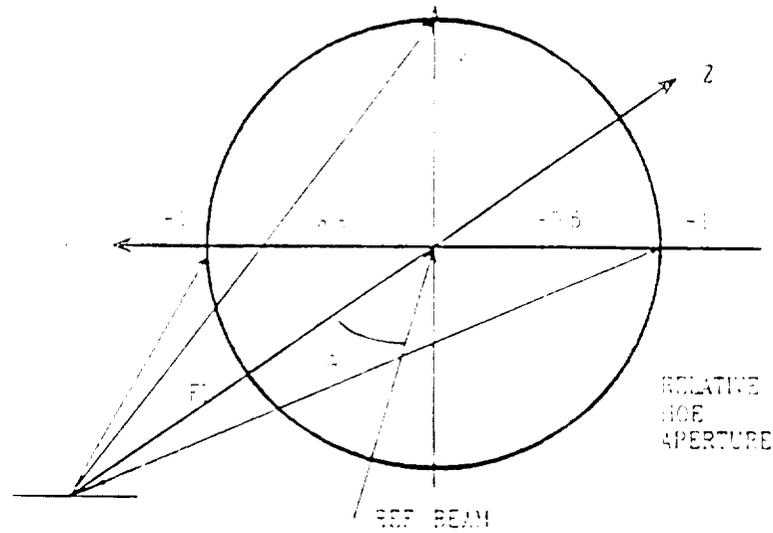
X(D/2)	Δθ_inter
-1.00	~ ~
-0.75	14.3°
-0.5	22.2°
-0.25	30.9°
0.00	40.0°
0.25	49.1°
0.50	57.8°
0.75	65.7°
1.00	72.7°

Figure 3. Construction geometry for a high N.A. lens formed with an on-axis spherical and an off-axis collimated reference wave. Also shown are different interbeam angles (in air) which exist along the x-axis.
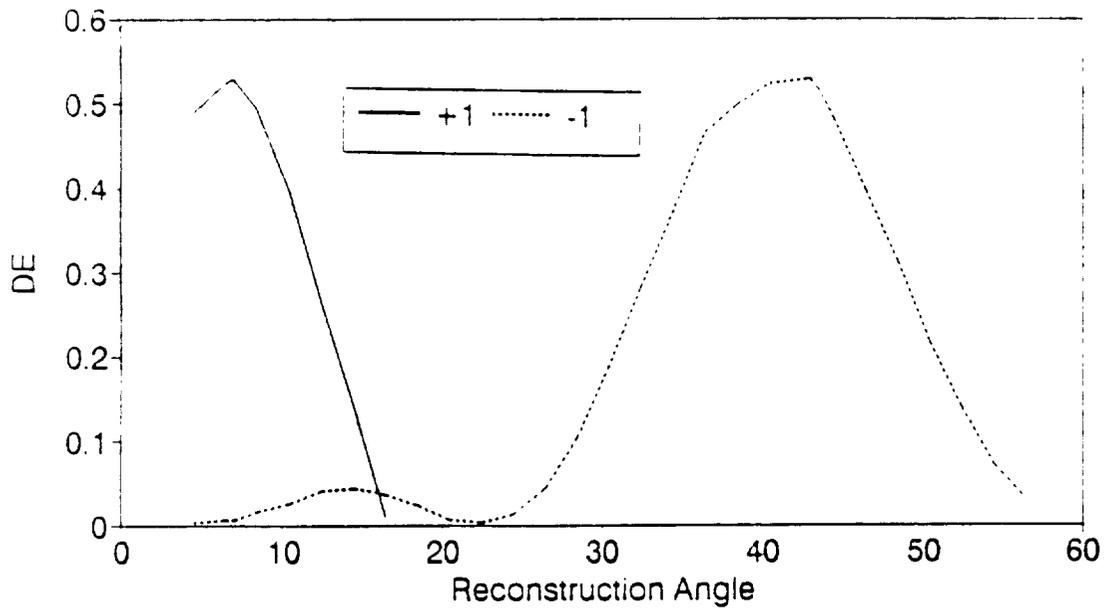
Figure 4. Diffraction efficiency vs. reconstruction angle at the center of the 0.54 N.A. focusing HOE.
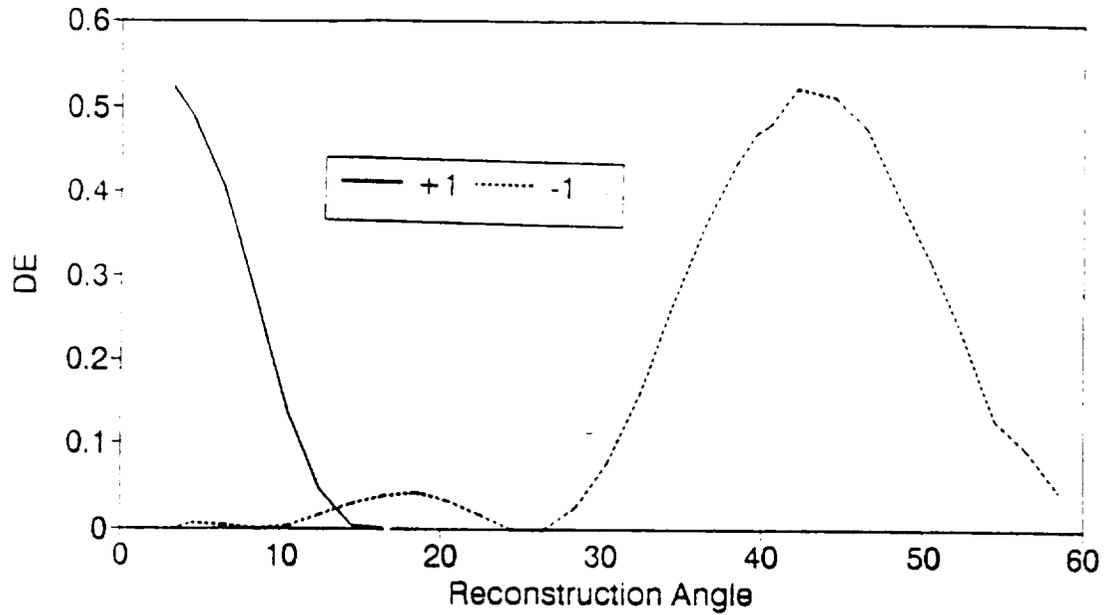
Figure 5. Diffraction efficiency vs. reconstruction angle for a planar grating corresponding to the local planar grating at the center of the 0.54 N.A. focusing HOE.
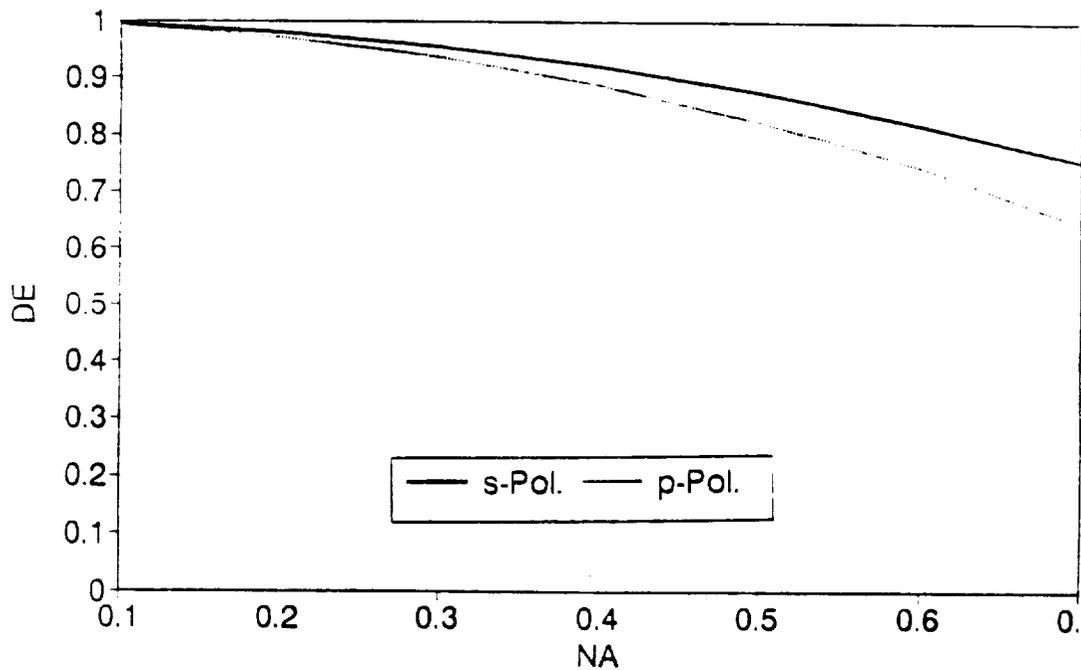
Figure 6. Drop in diffraction efficiency with N.A. resulting from exposure variation, polarization mismatch, and different Fresnel coefficients across the aperture. A linear dependence on exposure and visibility is assumed.
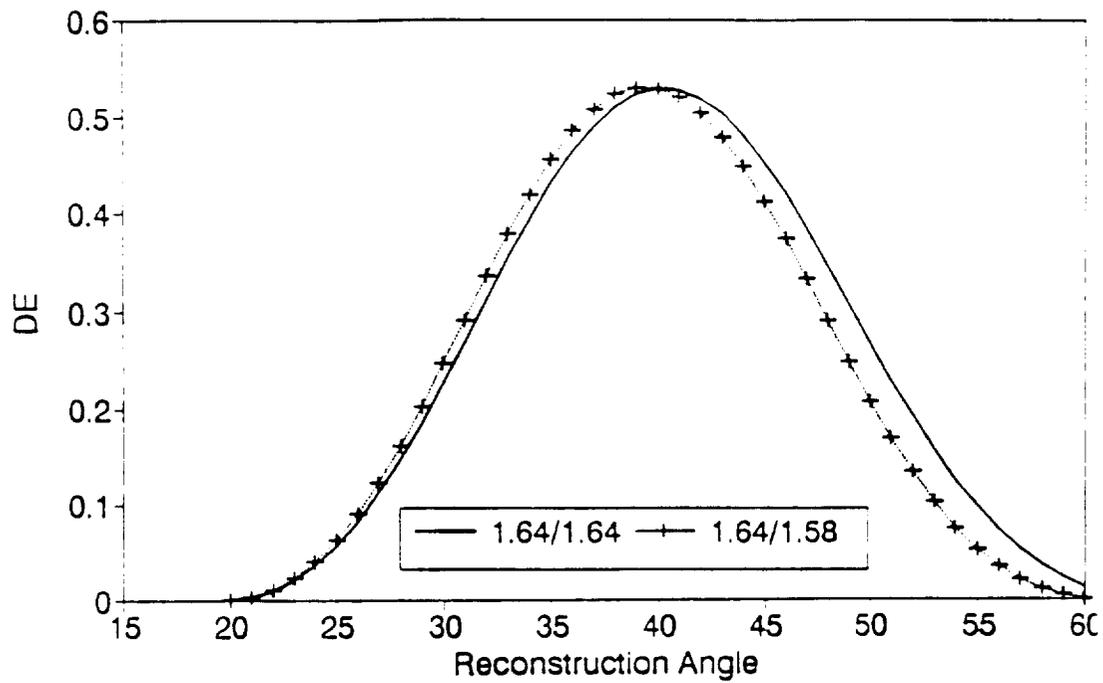
Figure 7. Diffraction efficiency vs. reconstruction angle for a planar grating formed and reconstructed with the same average refractive index, and with a change of 0.06 in index.
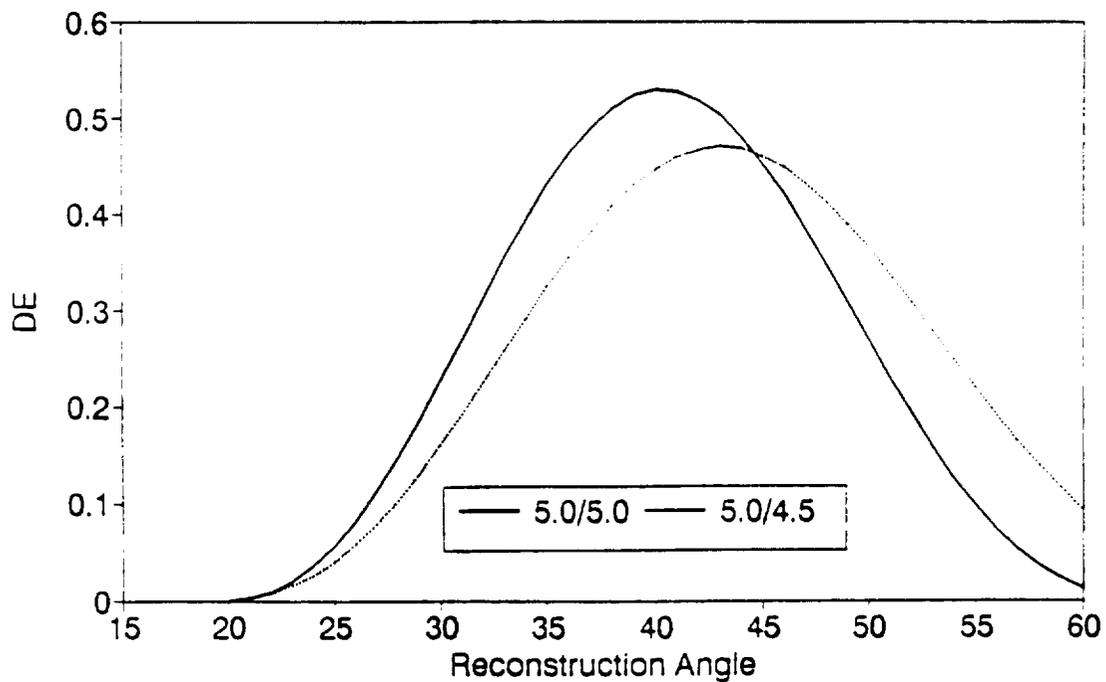
Figure 8. Diffraction efficiency vs. reconstruction angle for a planar grating formed and reconstructed with the same average refractive index, and with a change of 0.06 in index.
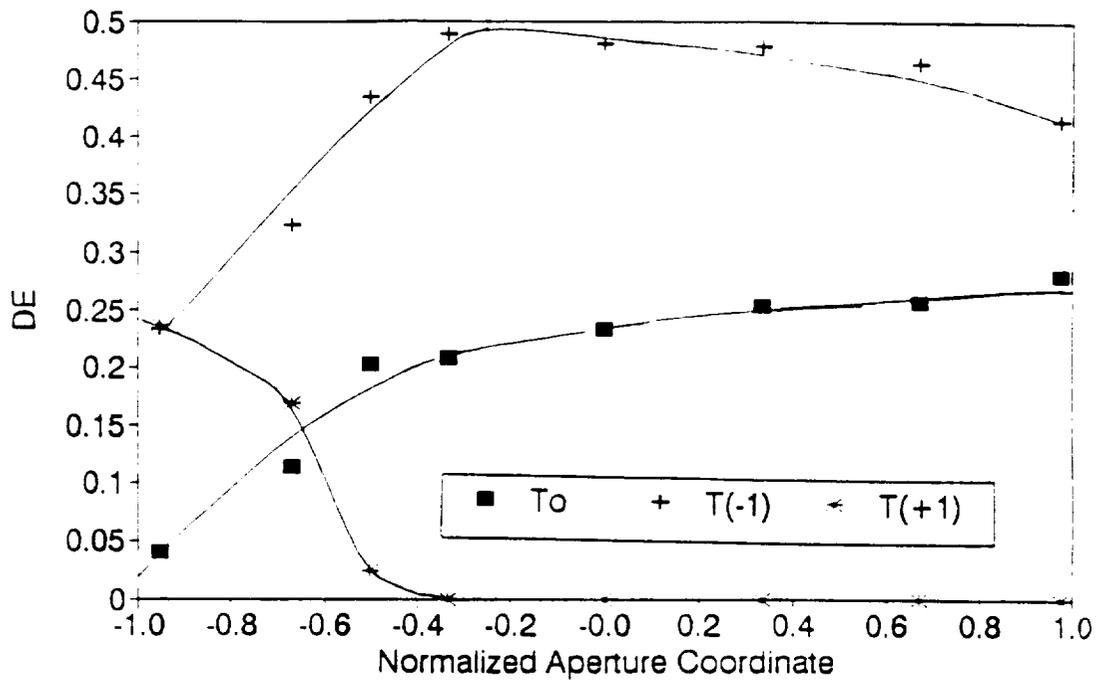
Figure 9. Measured diffraction efficiency across the x-axis of a 0.54 N.A. HOE reconstructed with s-polarized light.
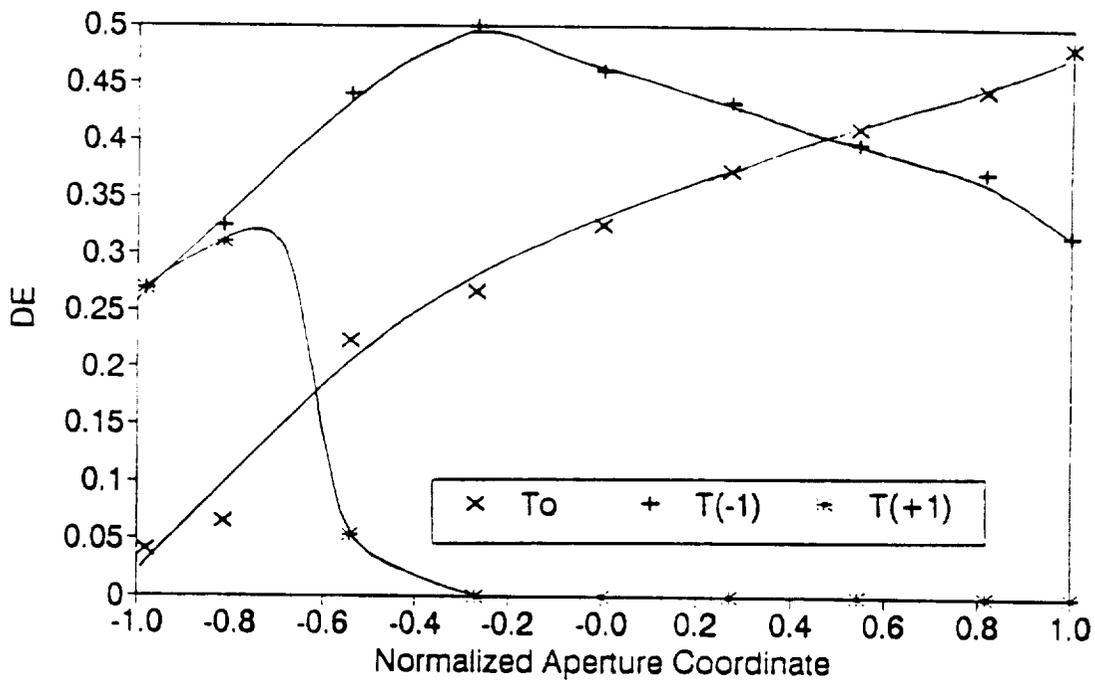
Figure 10. Measured diffraction efficiency across the x-axis of a 0.54 N.A. HOE reconstructed with p-polarized light.
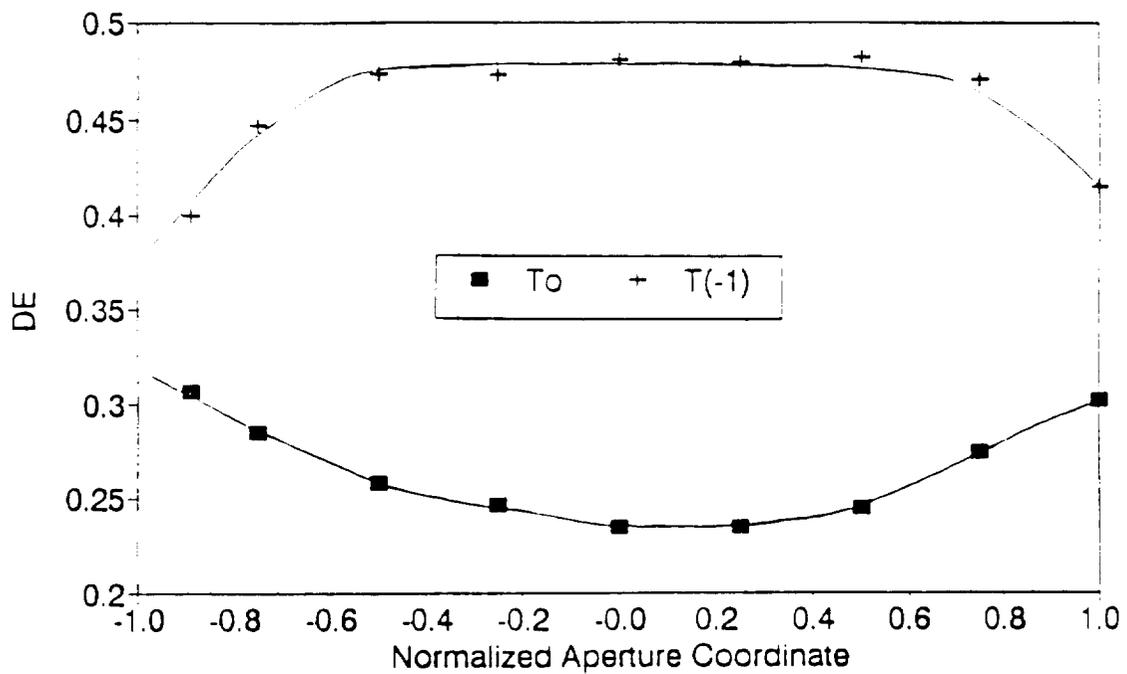
Figure 11. Measured diffraction efficiency across the y-axis of a 0.54 N.A. HOE reconstructed with s-polarized light.
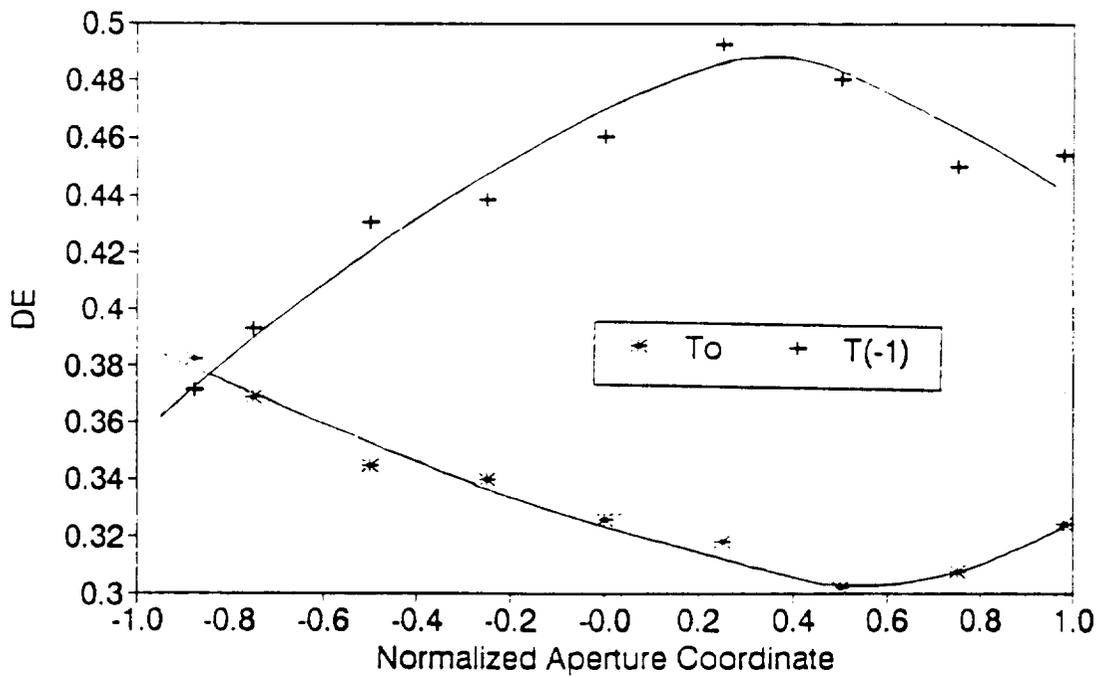
Figure 12. Measured diffraction efficiency across the y-axis of a 0.54 N.A. HOE reconstructed with s-polarized light.

Appendix L

Effects of beam focusing on the efficiency of planar waveguide grating couplers

Lifeng Li and Mool C. Gupta

Results of a theoretical and experimental investigation into the variation of coupling efficiency with coupling angle are presented for various beam focusing conditions for an integrated optical grating coupler. This investigation shows that the acceptance angle of the grating coupler can be broadened, within a relatively large range and with a relatively small loss of coupling efficiency, by focusing the incident laser beam.

Key words: Integrated optics, grating couplers

I. Introduction

Diffraction gratings play an important role in integrated optics: they are used to couple light into waveguides; to focus, deflect, and split beams; and to filter light spectrally (as in distributed feedback lasers).[1,2] Grating couplers are not only durable, they can be fabricated through planar photolithographic techniques.

A distinctive feature of a periodic grating coupler is that its coupling efficiency is high only if the incident beam falls within a narrow range of coupling angles.[3] In many cases this feature can be used to some advantage. For some applications, however, it is desirable to render the coupling efficiency less sensitive to the coupling angle. One way to achieve this is by focusing the incident beam. A focused beam can be considered a bundle of rays with a range of angular components. When this angular range covers the optimum coupling angle, a portion of the bundle will be coupled into the waveguide and the remainder will not. Thus, the curve of coupling efficiency vs coupling angle will be broadened, but its peak height will be lowered.

Even though grating couplers are widely used in integrated optics, and even though the theory of grating couplers is well understood, to our knowledge little detailed study has been done on the angular dependence of the coupling efficiency for focused beams. In this paper we report the results of our theoretical and experimental investigation into the variation with coupling angle of the coupling efficiency for an integrated optical grating coupler. Various focused beam conditions were explored in our investigation. The important question we address is how great an angular broadening can be achieved for a given loss of peak efficiency.

II. Theory

The analysis of a grating coupler requires two calculations: (1) the calculation of the effective index and leakage factor of the corrugated waveguide, and (2) the calculation of the coupling efficiency. For the first calculation we use Maystre's integral method.[4] For the second calculation we use the method developed by Neviere et al.[5-8] This method consists of three steps. First, an incident beam of finite width is represented by a superposition of plane waves. Second, the response of the grating coupler for a plane wave in the vicinity of the waveguide resonance is represented by a complex pole. Third, the total response of the coupler to the finite beam is given by the superposition of its response to plane waves. Neviere et al.[7] considered only the case in which the incident angle is phase matched with the grating coupler, and the incident beam has no phase variation other than that of a plane wavefront. In our work we considered the general case. By allowing an arbitrary incident angle and arbitrary phase variation, we studied the angular dependence and defocus dependence of the device's coupling characteristics. Throughout this paper we assume that $l \gg 1/\alpha'$, where l is the grating length and α' is the leakage factor defined below. This condition is well satisfied by the grating couplers used in our experiment.

Following the analysis in Refs. 7 and 8, one can

Lifeng Li is with University of Arizona, Optical Sciences Center, Tucson, Arizona 85721, and Mool Gupta is with Eastman Kodak Company, Research Laboratories, Rochester, New York 14650-2017.

OPTICAL PAGE IS
OF POOR QUALITY

224 *Appendix M*

derive the following expression for the coupling effi-
ciency for a lossless, infinitely long grating coupler:

$$\eta(x) = \frac{\cdots}{\cdots} \qquad \cdots m K \cdots \qquad$$

$$\cdots R \cdots \cdots \cdots \cdots \qquad (1)$$

where x is the position along the grating and y is
measured along the normal to the waveguide; $k_o = 2\pi/\lambda$, with λ the wavelength in a vacuum; n is the refractive
index of the incident medium; $C(y) = 1$ for TE, and
$C(y) = 1/\epsilon$ for TM, with ϵ the dielectric constant, and C_i
is $C(y)$ in the incident medium; $\alpha = k_o N_{eff}$, with N_{eff} the
effective index of the guided mode; $K = 2\pi/d$, with d
the grating period; m is the diffraction order which gets
coupled into the waveguide; v_m is the mth order field
amplitude excited by an incident plane wave on reso-
nance; and $q(x)$ gives the incident beam profile, nor-
malized such that $\int |q|^2 dt = 1$, with t perpendicular to
the beam axis.

The variables defined above are properties of the
grating coupler and of the incident beam. The inter-
action between the coupler and the incident beam is
described completely by the function $r(x)$, which can
be stated in three equivalent forms:

$$\frac{dr(x)}{dx} + i(\alpha_o - \alpha)r(x) = q(x), \qquad (2)$$

$$r(x) = -i \int p(\xi) \frac{1}{\xi + \alpha_o - \alpha_p} \exp(i\xi x) d\xi, \qquad (3)$$

$$r(x) = \int q(x') H(x - x') \exp[i(\alpha_o - \alpha_p)(x - x')] dx'. \qquad (4)$$

where $p(\xi)$ is the Fourier transform of $q(x)$; $\alpha_o = nk_o$
$\sin\theta_o$ is the center spatial frequency of $p(\xi)$; θ_o is the
incident angle; $\alpha_p = nk_o \sin\theta_R + i\alpha'$ is the complex pole
of the waveguide grating structure; θ_R is the resonance
coupling angle; α' is the leakage factor; and $H(x - x') =$
1 if $x - x' > 0$ and $H(x - x') = 0$ if $x - x' < 0$. Equation
(2) is probably the most useful for a numerical compu-
tation of $r(x)$, but Eqs. (3) and (4) are more useful for
an intuitive understanding of the dependence of $r(x)$
on the incident angle or beam size (angular width) of
the incident beam. We define several terms to simpli-
fy our discussion. $\Theta \equiv \theta_o - \theta_R$, the angular detuning.
We define the full width at half maximum of the η vs Θ
curve, the apparent acceptance angle (or, simply, the
acceptance angle) of the grating coupler, and denote
this by $\Delta\theta_a$. Clearly, $\Delta\theta_a$ depends both on the grating
coupler and on the incident beam. It can be shown[5]
that, as the incident beam becomes a plane wave, $\Delta\theta_a$
tends to its lowest value $\Delta\theta_i = 2 \text{Im}[\alpha_p]/(nk_o \cos\theta_R)$,
which is the full width at half-maximum of the Lorent-
zian profile $1/|\xi + \alpha_o - \alpha_p|^2$. We call $\Delta\theta_i$ the intrinsic
acceptance angle of the grating coupler.

The angular dependence of $\eta(x)$ is contained in the
function $r(x)$. When $\Theta = 0$, $r(x)$ as given by Eq. (4) is a
convolution of the incident beam profile and an expo-
nential decay function. When $\Theta \neq 0$, an oscillatory
function is superimposed on the exponential decay
function; therefore, the coupling efficiency decreases.
In Eq. (3), $r(x)$ is given by an overlapping integral of
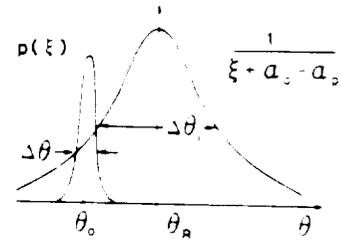
(a)
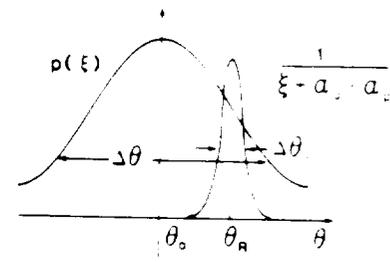
(b)

Fig. 1. Two limiting cases for the overlap integral given in Eq. (3). (a) $\Delta\theta \ll \Delta\theta_i$ and (b) $\Delta\theta \gg \Delta\theta_i$.

$p(\xi)$ and $1/(\xi + \alpha_o - \alpha_p) \exp(i\xi x)$. When $\Theta = 0$, the
peaks of the two functions coincide, and the maximum
coupling efficiency is achieved. A nonzero detuning
implies a shift in the two peaks and a decrease in
efficiency. When Θ changes, the two curves move
relative to each other. If the angular width of incident
beam $\Delta\theta$ is $\ll \Delta\theta_i$, the Lorentzian is probed by the
incident beam; if $\Delta\theta$ is $\gg \Delta\theta_i$, the incident beam is
probed by the Lorentzian (Fig. 1). In other words, the
apparent acceptance angle approaches the intrinsic
acceptance angle as $\Delta\theta$ tends to zero, and it approaches
$\Delta\theta$ as the latter becomes $\gg \Delta\theta_i$.

Now let us consider a Gaussian beam, as depicted in
Fig. 2. Once the wavelength and polarization are
known, a Gaussian beam is specified completely by its
beam waist ω_0 or its angular width $\Delta\theta$. These two
quantities are related by $\Delta\theta = \tan^{-1}(\lambda/\pi\omega_0)$. For our
purposes it is more convenient to use the angular
width. To specify the position of a Gaussian beam
relative to a grating coupler we need three parameters:
incident angle θ_o, lateral offset x_o, and defocus z_o. The
lateral offset is defined as the distance between the
beam axis and the edge of the grating. The defocus is
defined as the distance between the beam's center on
the grating to the beam waist, as shown in Fig. 2. We
consider only the angular dependence, and we set $z_o = 0$. We consider the influence of defocus on the cou-
pling efficiency at a later time.

III. Experimental Procedures

The optical waveguide was prepared by e-beam de-
position[9,10] of a Corning 7059 glass film onto a quartz
substrate with refractive index 1.46. The thin film

20 December 1990 / Vol. 29, No. 36 / APPLIED OPTICS   5321
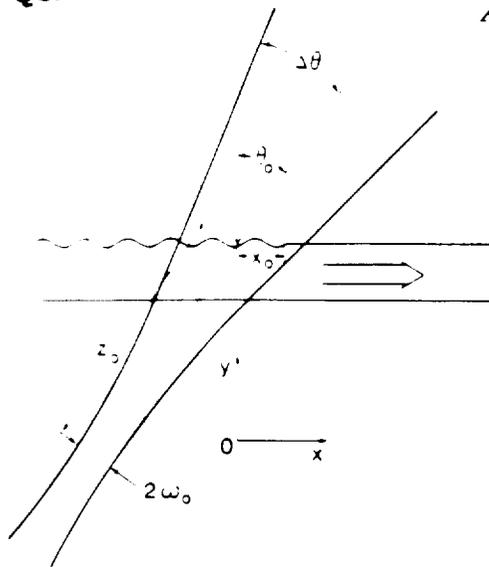
Fig. 2. Geometric configuration for optical coupling of a Gaussian beam by a grating coupler.

Fig. 3. Theoretical coupling efficiency vs coupling angle for four different Gaussian beam angular widths.

was 0.6 μm thick, its refractive index was 1.50, and its optical loss was 1 dB/cm. The waveguide cover is air. For TE polarization this waveguide supports only the lowest order guided mode. A surface relief grating was etched into the film at the air–film interface. The grating was fabricated by the holographic technique. A 0.22-μm thick photoresist (Shipley 1400 series) thin film was spin coated onto the quartz substrate. The resist was exposed with interference fringes 0.38 μm apart (using a He–Cd laser with a wavelength of 0.4416 μm). The exposed grating pattern was then developed, with an *in situ* monitoring technique.[11] The relief pattern was transferred to the 7059 glass waveguide by reactive ion beam etching with a C_2F_6 gas. The ion beam etch rate for the film was found to be 15 nm/min at an ion beam current density of 1 mA/cm². The shape of the grating rulings was rectangular. From a comparison of the measured and theoretically calculated diffraction efficiencies at several incident angles, we estimated that the grating groove had a depth of 0.17 μm. Two gratings, each 5 mm long, were etched ~2 cm apart on a single sample, one grating to be used as the input coupler and the other as the output coupler.

The angular measurements were taken by mounting the grating coupler on a rotation stage with a 0.001° resolution. Intensities of the transmitted, reflected, and throughput beams were measured with silicon detectors. The detector for the reflected signal had a large receiving area, so that the reflected beam would remain on the detector during the entire measurement process. The coupling efficiency measurements were performed with a polarized He–Ne laser with a Gaussian beam profile. The laser beam was expanded and nearly collimated, so that its angular halfwidth was 0.0085°, corresponding to a 2.7-mm diam beam waist. To obtain other angular widths, convex lenses of vari-

ous focal lengths were inserted after the beam expander. For all the measurements reported here, the input grating coupler was positioned at the beam waist and the laser beam was TE polarized with respect to the grating coupler.
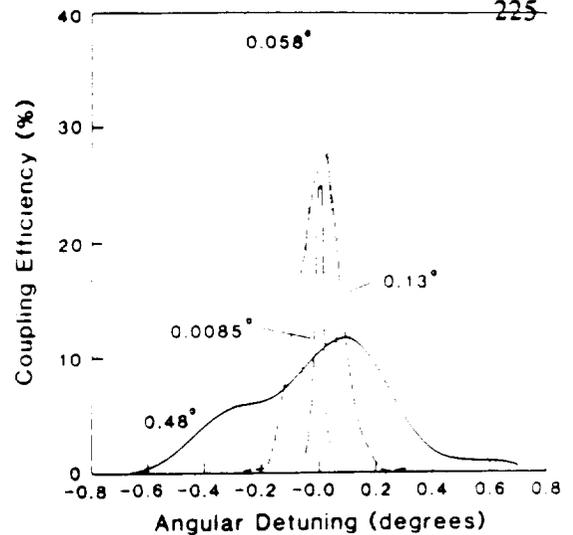
Each focused beam experiment proceeded as follows: First, the optimum coupling condition was located iteratively by adjusting the lateral offset and the coupling angle, so that the sum of the transmitted and reflected intensities was minimized. Once the optimum condition was obtained, the lateral offset was fixed for the remainder of the measurement, and the coupling angle was referred to as the zero angular detuning. At the beginning of the measurement sequence, the grating was rotated to a negative detuning value at which the coupling efficiency was sufficiently low. The grating was then rotated, in small increments, in the positive direction until the coupling efficiency was sufficiently low at a positive detuning value. The transmitted and reflected light intensities were measured at each angular position, from which the coupling efficiency was calculated.

IV. Results

In Fig. 3, four theoretical curves for coupling efficiency vs angular detuning are plotted. For each curve the angular width of the incident beam is indicated.

Experimental data for variations in the coupling efficiency with coupling angle for four focused beam conditions are shown in Figs. 4-7. The percentage transmission, reflection, and throughput data were obtained. The throughput, that is, the light outcoupled by the second grating, is given in arbitrary units but is directly proportional to the coupling efficiency. The experimental coupling efficiencies were calculated by subtracting the percentage transmission and reflection from one hundred. We expect these coupling efficiency values to be somewhat higher than the actual values, because absorption and scattering are not taken into
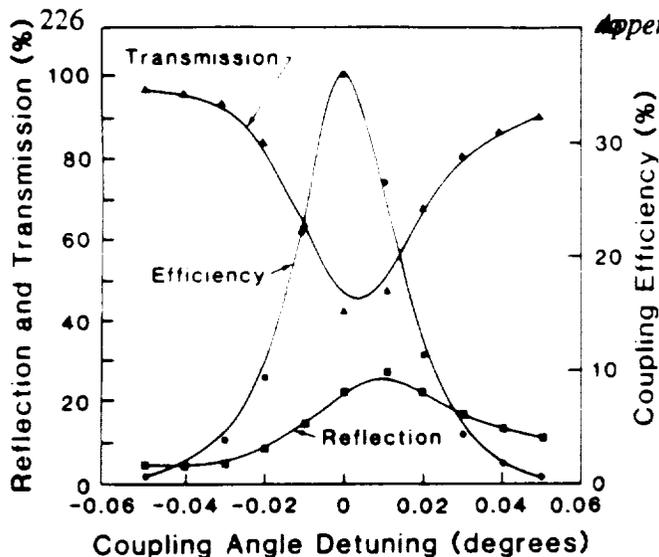
Fig. 4. Experimental data of percentage transmission, reflection, and coupling efficiency vs angular detuning for a Gaussian beam of 0.0085° angular width.

(a)
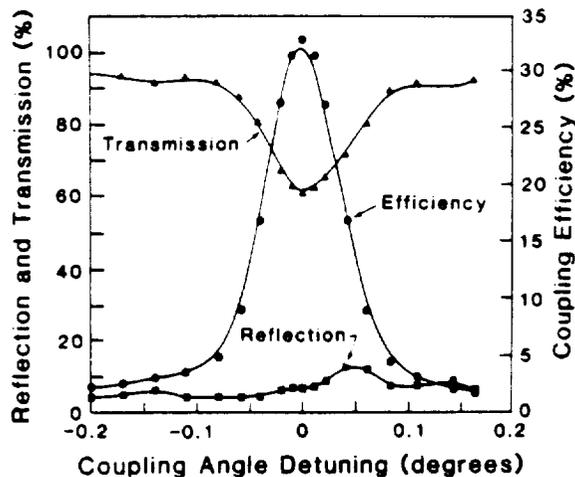
Fig. 5. Experimental data of percentage transmission, reflection, and coupling efficiency vs angular detuning for a Gaussian beam of 0.058° angular width.

(b)

Fig. 6. Experimental data of (a) percentage transmission, reflection, and coupling efficiency, and (b) outcoupled power vs angular detuning for a Gaussian beam of 0.13° angular width.

account. However, for a study of the angular dependence of the coupling efficiency, this definition suffices.

The experimental values of the transmission, reflection, and coupling efficiency for a Gaussian beam with a 0.0085° angular width are shown in Fig. 4. These values indicate an increase in the transmitted signal and a decrease in the reflected signal as the incident angle is detuned. In addition, the angular position between the transmission minimum and the reflection maximum is shifted. The acceptance angle, measured from the efficiency curve, is 0.029°. Although the peak value of the experimental curve is greater than the theoretical value given in Fig. 3, the acceptance angles measured from both curves agree well.

The experimental data and the theoretical efficiency curves for Gaussian beams with angular widths of

0.058° and 0.13° are shown in Figs. 5 and 6(a), respectively. The shapes of these curves are similar to that of the curve shown in Fig. 4. Note that, although the peak efficiency values are comparable with that in Fig. 4, the apparent acceptance angles have increased to 0.085° and 0.15°, respectively. There is good agreement between the experimental and theoretical curves. The variation in the coupling efficiency with coupling angle, as measured with the outcoupled beam from the second grating, is illustrated in Fig. 6(b). The measured throughput signal curve agrees well with the measured efficiency curve, but the throughput signal has a much higher signal-to-noise ratio.

The experimental transmission, reflection, and coupling efficiency data for a Gaussian beam with a 0.48° angular width are shown in Fig. 7(a). For this case, the

(a)

Fig. 8. Experimental and theoretical acceptance angle (squares and solid line) and coupling efficiency (triangles and long-dashed line) vs Gaussian beam angular width.

(b)
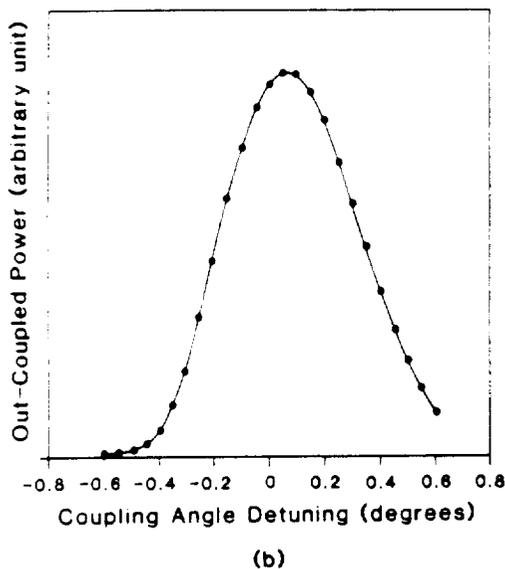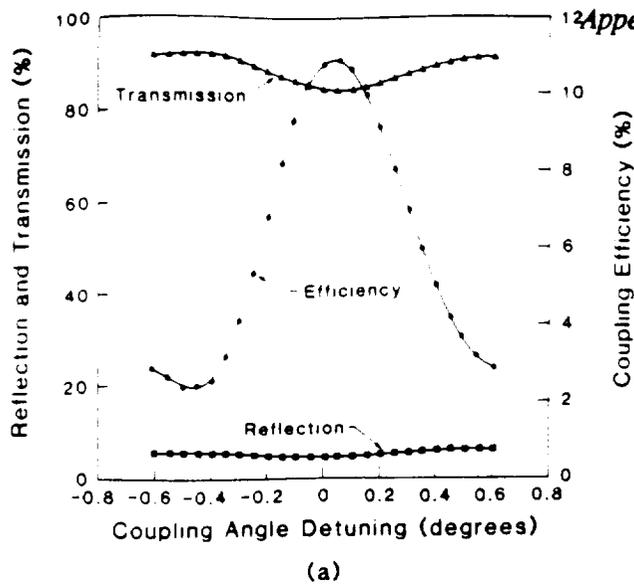
Fig. 7. Experimental data of (a) percentage transmission, reflection, and coupling efficiency, and (b) outcoupled power vs angular detuning for a Gaussian beam of 0.48° angular width.

acceptance angle rises to 0.57° and the peak efficiency falls to 11%. The apparent acceptance angle is about twenty times and the peak efficiency about two-thirds that for the beam of 0.0085° angular width. The rise in efficiency around −0.4° detuning arises from substrate mode coupling. A simple calculation shows that, for the grating coupler used in the measurements, the onset coupling angle for the substrate mode is about −0.4° from the optimum coupling angle for the guided mode. Thus, as the coupling angle is detuned in the negative direction, a portion of the input beam is coupled into the substrate. Because of the way we define coupling efficiency, this substrate coupling effect appears in the efficiency curve. No such effect is seen in the beam outcoupled by the second grating [see

Fig. 7(b)]. Likewise, this effect did not appear in our earlier experiments because the acceptance angles were well under 0.4°. It is not known why the shoulder on the left of the theoretical efficiency curve does not appear on the experimental curve. Despite the difference in the shapes of the experimental and theoretical efficiency curves, the acceptance angles measured from these two curves are nearly equal.

V. Discussion and Conclusions

The experimental results and theoretical calculations for the four focused beams are presented in Fig. 8. The horizontal axis is taken as the angular halfwidth of the incident Gaussian beam at $1/e^2$. All the curves and data points share this axis. Curve 1 represents the theoretical coupling efficiency and curve 2 the theoretical apparent acceptance angle; the triangles and squares are the respective experimental points. The arrow indicates the position of the intrinsic acceptance angle $\Delta\theta_i$ of the grating coupler on the vertical axis. Curve 3 shows the calculated relationship between the full width at half-maximum and the halfwidth at $1/e^2$ maximum for a Gaussian beam. As indicated in Sec. II, as the angular width of the incident beam decreases, the apparent acceptance angle of the grating coupler approaches the intrinsic acceptance angle. Furthermore, as the angular width of the incident beam increases, the apparent acceptance angle approaches the width of the incident beam. Also, at the maximum coupling efficiency, the apparent acceptance angle is about twice the width of the incident beam. Except for two efficiency data points, the experimental data and the theoretical curves are in good agreement.

Note that, in Fig. 8, the coupling efficiency is plotted on a linear scale, while the acceptance angle is plotted on a logarithmic scale. It can be seen that, for a small

loss of efficiency, the acceptance angle can be enlarged several times by using a more tightly focused beam. For example, to achieve the 42% maximum coupling efficiency, one must use a Gaussian beam with a 0.03° angular halfwidth, for which the apparent acceptance angle is ~0.06°. If one is content with a 30% coupling efficiency (~25% less than the maximum value) and wishes to double the acceptance angle, one can do so by focusing the incident beam to an angular halfwidth of 0.1°.

The asymptotic behavior of curve 2 at the lower end suggests that the intrinsic acceptance angle can be probed by a sufficiently collimated beam. Because the intrinsic acceptance angle is directly proportional to the leakage factor for the grating coupler, one could easily measure the leakage factor.

Summarizing, we have conducted a theoretical and experimental study of the angular dependence of the coupling efficiency for a planar waveguide grating coupler. Our results show that, by appropriately focusing the incident Gaussian beam, the acceptance angle of the coupler can be greatly increased with only a small decrease in the maximum coupling efficiency. We also show good agreement between theoretical calculations and experimental measurements. This study allows one to estimate the acceptance angle and coupling efficiency for a grating coupler with a focused incident beam. These findings are useful in applications where the angular tolerance of waveguide coupling is an important issue.

References

1. A. Yariv and M. Nakamura, "Periodic Structures for Integrated Optics," IEEE J. Quantum Electron. **QE-13**, 233-253 (1977).
2. T. Suhara and H. Nishihara, "Integrated Optics Components and Devices Using Periodic Structures," IEEE J. Quantum Electron. **QE-22**, 845-867 (1986).
3. K. Ogawa, W. S. C. Chang, B. L. Sopori, and F. J. Rosenbaum, "A Theoretical Analysis of Etched Grating Couplers for Integrated Optics," IEEE J. Quantum Electron. **QE-9**, 29-42 (1973).
4. D. Maystre, "Integral Methods," in *Electromagnetic Theory of Gratings*, R. Petit, Ed. (Springer-Verlag, Berlin, 1980), pp. 63-100.
5. M. Neviere, R. Petit, and M. Cadilhac, "About the Theory of Optical Grating Coupler-Waveguide Systems," Opt. Commun. **8**, 113-117 (1973).
6. M. Neviere, P. Vincent, R. Petit, and M. Cadilhac, "Systematic Study of Resonances of Holographic Thin Film Couplers," Opt. Commun. **9**, 48-53 (1973).
7. M. Neviere, P. Vincent, R. Petit, and M. Cadilhac, "Determination of the Coupling Coefficient of a Holographic Thin Film Coupler," Opt. Commun. **9**, 240-245 (1973).
8. M. Neviere, "The Homogeneous Problem," in *Electromagnetic Theory of Gratings*, R. Petit, Ed. (Springer-Verlag, Berlin, 1980), pp. 123-157.
9. M. C. Gupta and T. A. Strasser, "Electron-Beam-Deposited Corning 7059 Glass Thin Films for Waveguides," Proc. Soc. Photo-Opt. Instrum. Eng. **993**, 44-45 (1988).
10. M. C. Gupta, "Low-Optical-Loss Glass Thin Films," Appl. Opt. **29**, 4310-4314 (1990).
11. L. Li, M. Xu, G. I. Stegeman, and C. T. Collin, "Fabrication of Photoresist Masks for Submicrometer Surface Relief Gratings," Proc. Soc. Photo-Opt. Instrum. Eng. **835**, 72-82 (1987).

Appendix N

Jitter Model and Signal Processing Techniques
for Pulse Width Modulation Optical Recording

Max. M.-K. Liu
Department of Electrical and Computer Engineering
University of Arizona
Tucson, AZ 85721

ABSTRACT

This paper discusses a jitter model and signal processing techniques for data recovery in Pulse Width Modulation (PWM) optical recording. In PWM, information is stored through modulating sizes of sequential marks alternating in magnetic polarization or in material structure. Jitter, defined as the deviation from the original mark size in the time domain, will result in error detection if it is excessively large. This paper takes a new approach in data recovery by first using a high speed counter clock to convert time-marks to amplitude-marks, and uses signal processing techniques to minimize jitter according to the jitter model. The signal processing techniques include motor speed and intersymbol interference equalization, differential and additive detection, and differential and additive modulation.

1   Introduction

Optical data storage is built upon many disciplines. Through the applications of these disciplines, storage densities and access speeds have been improved significantly [1]. In addition to the results that have provided shorter wavelength laser diodes, lighter optical heads, and better understanding of media, the use of signal processing techniques is also important in extracting information from noisy signals. As a result, this paper will study how data can be modulated, equalized, detected, and demodulated to achieve higher density storage.

Background

Since the magneto-optical (M-O) and phase change media have only two different polarizations or states, information can be stored only through modulating marks alternating in polarization or state. In this paper, pulse width modulation (PWM) is considered where marks of variable size according to the input signal are recorded.

In detecting a readback signal, the peak detection technique is commonly used [2][3]. That is, a signal of peaks at mark boundaries is first generated by a differentiator if necessary. To recover the original signal, a time window is used to decide whether a peak falls into it or not. The time window is generally derived from the readback signal by a phase lock loop (PLL) [4].

Approach of This Paper

In this paper, a different approach is taken in recovering the original signal. First, mark boundaries are detected by methods such as the peak detection method described above. In the second step, instead of using the time window method, a high speed counter clock is used to quantize the mark size between two adjacent mark boundaries, as depicted in Figure 1. The counter output generates an integer number proportional to the time mark. In other words, this quantization step transforms the readback signal from time marks to amplitude marks, and signal processing techniques are subsequently used.

There are two important advantages of this quantization approach. First, it converts a time-mark signal to an amplitude-mark signal. As a result of this conversion, time domain noise (jitter) is at the same time converted to amplitude domain noise, which allows us to perform signal processing in the amplitude domain. Another advantage of this approach is it provides a flexible and integrated implementation of various equalization, detection, and demodulation algorithms. This will become clear in the subsequent discussion.

One disadvantage of this approach is the added quantization error in the quantization step. However, if the clock is fast enough, this quantization error is negligible. For example, if the clock's period is one nsec and mark sizes are multiples of 100 nsec, we have a signal to noise ratio $SNR = 10 log_{10}(\frac{100}{1}) = 50 \ s \ db$ (for calculation, see [5] for example).

Jitter, defined[2] as the total deviation away from the original mark size by all possible causes, is the time domain noise, similar to the amplitude noise in an amplitude modulated signal. There are various sources that contribute to the total jitter. This paper will establish a jitter model that translates all jitter sources into the total jitter, and study how the jitter can be reduced by signal processing.
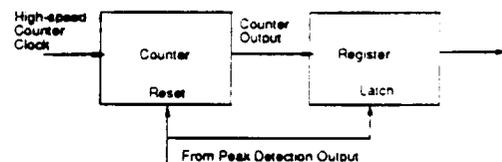
Figure 1: Quantization of Time Marks to Amplitude Marks

2   Jitter Model

This section describes a jitter model based on which equalization, detection, and modulation techniques are described in the following sections. Although the model is not yet completely verified experimentally, it is formulated according to recent experiment and simulation studies [6]-[8].

---

[1] If we assume the disk linear velocity is 4 m/sec, this 100 nsec time unit corresponds to 400 nm mark unit. For a system using (2,7) RLL code, the minimum mark size is 1.2 μm. If we compare this with a typical diffraction limit at 1 μm, this 100 nsec is a reasonable assumption.

[2] In optical recording, since there are many sources causing mark size deviation, jitter is also defined differently. For example, in peak detection, the deviation of a mark boundary is called peak shift [3], and jitter is one of the causes due to random noise. In this paper, for simplicity, jitter is the total result of all deviation causes, and each cause will be described in detail in the jitter model.

2.1 Write Process Jitter Model

In the write process, modulated input data to a disk drive is in a sequence of time marks: $\ldots T_{j-1}, T_j, T_{j+1} \ldots$ where T_j is the time duration of mark j. We can define $t_j = \sum_{i=1}^{j-1} T_i$ to be the starting time of mark j.

When the input signal is recorded onto a disk, the spatial mark size W_j^w written corresponding to time mark T_j is

$$W_j^w = T_j V_w - \delta_j^w - \delta_{j+1}^w + T_j \Delta V_w, \qquad (2.1)$$

if the disk is rotating at a nominal linear constant velocity V_w plus velocity jitter ΔV_w. In the equation, δ_j^w is the jitter at the left hand side of the mark, δ_{j+1}^w is at the right hand side, and δ_j^w is positive if it makes W_j smaller. Figure 2.

In Case of No Jitter
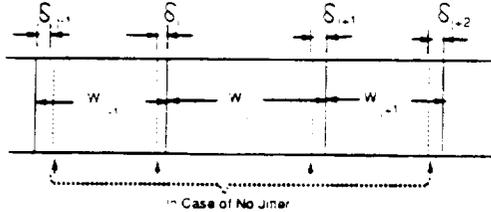
Figure 2: Mark Size and Associated Jitter

In Eq. (2.1), each δ_j^w is due to three different jitter sources.

$$\delta_j^w = \delta_{1,j}^w + \delta_{2,j}^w + \delta_{3,j}^w, \qquad (2.2)$$

where

$\delta_{1,j}^w$: Jitter due to random noise such as electronic noise and magnetic medium property fluctuation or defects. This first type of jitter is called noise jitter and often simply called jitter. This jitter has no correlation with the input signal and is independent of adjacent jitter of the same kind.

$\delta_{2,j}^w$: Jitter due to laser power and/or beam width fluctuation, or other similar mechanisms. This kind of jitter is called bit shift jitter. This jitter is shifted in different direction at the rising and falling edges of a mark in erase-and-write optical recording systems, where marks are "written" or "burned" only with even indexes. That is, the jitter sequence ($\delta_{2,j-1}^w$, $\delta_{2,j}^w$, $\delta_{2,j+1}^w$) will be alternating in sign. The magnitude of this jitter in general should be slowly varying and has strong correlation with adjacent ones.

$\delta_{3,j}^w$: Jitter due to intersymbol interference (ISI). This jitter is a function $f(\ldots, T_{j-1}, T_j, T_{j+1} \ldots)$ of adjacent time marks. This function can be linear or non-linear of time mark sizes T_j's. Physically, when a mark is being written, the longer the mark, the more heat is accumulated on the media, which results in this mark size dependent jitter.

2.2 Read Process Jitter Model

In the read process, the spatial mark size that is being read back can be similarly expressed as:

$$W_j^r = W_j^w - \delta_j^r + \delta_{j+1}^r, \qquad (2.3)$$

where each jitter component has its similar counterpart described in the write process. Specifically,

$\delta_{1,j}^r$: Noise jitter due to random receiver noise

$\delta_{2,j}^r$: Peak shift jitter due to laser beam width fluctuation in the read process.

$\delta_{3,j}^r$: ISI jitter in the read process. Physically this ISI jitter is due to the convolution of the laser beam width with a written mark size. The time mark read out will depend on the mark size recorded.

Including the motor speed jitter, we have $T_j^r = (W_j^r/V_r)(1 - \Delta V_r/V_r)$. Therefore, from Eqs. (2.1) and (2.3), we have:

$$T_j^r = (\frac{V_w}{V_r})T_j + (\frac{V_w}{V_r} \cdot \frac{\Delta v}{v})T_j - \frac{1}{V_r}\sum_{i=1}^{3}(\delta_{i,j} - \delta_{i,j+1}) \qquad (2.4)$$

where $(\Delta v/v) = (-\Delta V_r/V_r) + (\Delta V_w/V_w)$ and $\delta_{1,j} = \delta_{1,j}^w - \delta_{1,j}^r = \delta_{laser,j} + \delta_{media,j} + \delta_{receiver,j}$, $\delta_{2,j} = \delta_{2,j}^w + \delta_{2,j}^r$, and $\delta_{3,j} = \delta_{3,j}^w + \delta_{3,j}^r$. For convenience, we call $\delta_{1,j}$ the noise jitter, $\delta_{2,j}$ the bit shift jitter, and $\delta_{3,j}$ the ISI jitter.

3 Equalization Techniques

The objective of equalization discussed in this section is to restore the original mark size T_j from T_j^r.

(i). Write Velocity Jitter Correction

The term $T_j \Delta V_w$ in Eq. (2.1) is the jitter caused by velocity fluctuation and is proportional to T_j. In time-window-based peak detection systems where mark sizes are not quantized, this T_j-proportional jitter is not important since it can be compensated easily by a phase lock loop (PLL) in the read process. However, when time marks are quantized and converted into amplitude marks, it is more difficult to use a PLL. In the following we explain how velocity fluctuation can be compensated by using the servo voltage in the disk drive.

A circuit that removes motor speed jitter is depicted in Fig. 3. In the figure, a voltage signal $v(t)$ that is proportional to the linear velocity of the disk with respect to the laser head is sent to an integrator. If the integrator is reset to zero at time t_j, the voltage output $U_j(t_{j+1})$ of the integrator equals the spatial mark W_j at time t_{j+1}, and the comparator output changes from "0" to "1". This transition will reset the integrator, change the JK Flip-Flop state from on to off, and turn off the laser diode. Similar operation repeats from time t_{j+1} to t_{j+2}.
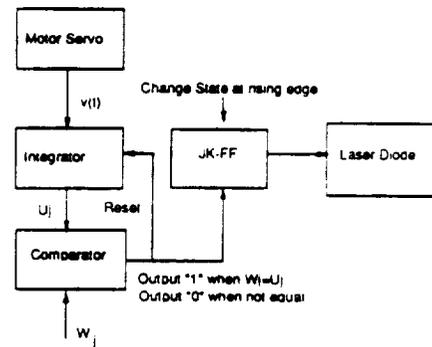

Figure 3: Circuit for Write Process Compensation

With this compensation, the mark size written becomes:

$$\{W_j^w = \{W_j - \delta_j^1 - \delta_{j-1}^2$$

(ii). Read Process Equalization

The equalization in the receiver consists of two steps as shown in Figure 4. The first step is to reduce the ISI jitter $\delta_{1,j}$. The way to reduce ISI is to subtract each T_j^r by an amount of $\delta_{1,j}^r$, $\delta_{1,j}$, where $\delta_{1,j}^r = f_i(\cdots, T_{j-1}^r, T_j^r, T_{j+1}^r, \cdots)$ and $f_i(\cdot)$ is the pre-known ISI function. $\delta_{1,j}^r$ cannot be exactly equal to $\delta_{1,j}$ because we use T_j^r instead of T_j to estimate the ISI jitter. Better estimation can be obtained by using decision feedback equalization (DFE).

Neglecting the second order effect $(\delta_{3,j} - \delta_{3,j}^r)$ and combining Eqs. (2.4) and (3.1), we have:

$$T_j^{r,1} \approx (\frac{V_w}{V_r})T_j(1 - \frac{\Delta V_r}{V_r}) - (\frac{1}{V_r})\sum_{i=1}^{2}(\delta_{i,j} - \delta_{i,j+1}) \qquad (3.2)$$

The second step is to correct the motor speed jitter in the read process. To accomplish this, we also use the motor servo voltage signal to estimate the quantity $\Delta V_r/V_r$, based on which, we have:

$$T_j^{r,2} \approx (\frac{V_w}{V_r})T_j - (\frac{1}{V_r})\sum_{i=1}^{2}(\delta_{i,j} - \delta_{i,j+1}) \qquad (3.3)$$

After these two steps, jitter that is left includes only $\delta_{1,j}$ and $\delta_{2,j}$. The first one is purely random and has no correlation with adjacent ones. The second one is slowly varying and alternating in sign as a function of j. Instead of equalizing this second jitter directly, the following detection techniques are used to make correct detection insensitive to this jitter.
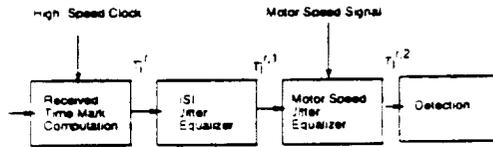

Figure 4: Block Diagram in Receiver Equalization and Detection

4   Detection Techniques

The first method to recover the original mark size T_j from $T_j^{r,2}$ is called the Differential Interleaving Detection (DID). If we subtract $T_{j+2}^{r,2}$ from $T_j^{r,2}$, the difference is:

$$\Delta T_j = (T_j^{r,2} - T_{j+2}^{r,2}) \approx (\frac{V_w}{V_r})(T_j - T_{j+2}) - \frac{1}{V_r}(\delta_{1,j} - \delta_{1,j+2} - \delta_{1,j+1} + \delta_{1,j+3}),$$

$$(4.1)$$

where the term: $\delta_{2,j} - \delta_{2,j+2} - \delta_{2,j+1} + \delta_{2,j+3}$ is of second order and maybe neglected because of the strong positive correlation between $(\delta_{2,j}, \delta_{2,j+2})$ and $(\delta_{2,j+1}, \delta_{2,j+3})$.

ΔT_j in Eq. (4.1) has only the random jitter. Comparing this with Eq. (3.3), this technique has a 3db power penalty. However, we may use maximum likelihood sequence detection (MLSD) to detect each ΔT_j in a sequence of $(\cdots, \Delta T_{j-2}, \Delta T_j, \Delta T_{j+2}, \cdots)$ to avoid this penalty. With this differential interleaving method, if the first two mark sizes T_1 and T_2 are predefined, subsequent T_j's can all be obtained from the differential terms.

In the case that the T_j's are modulated according to the input data, straightforward detection may have an error propagation problem. To solve this, a post-modulation method called Differential Interleaving Modulation (DIM) can be used as described in the next section.

The second method to recover the original mark sizes recorded is called the Additive Interleaving Detection (AID). This method first adds the two adjacent mark sizes read. That is:

$$\Xi T_j \stackrel{def}{=} T_j^{r,2} + T_{j+1}^{r,2} \approx (\frac{V_w}{V_r})(T_j + T_{j+1}) - \frac{1}{V_r}(-\delta_{2,j} + \delta_{2,j+2})$$

$$(4.2)$$

Again, the term $\delta_{2,j} - \delta_{2,j+2}$ is of second order and neglected.

From the detected $(\cdots, \Xi T_{j-1}, \Xi T_j, \Xi T_{j+1}, \cdots)$, the T_j can all be recovered if the first T_1 is predefined. This method has the same error propagation problem as DID. If written marks are modulated according to ΞT_j instead of T_j, the problem is completely removed, and this post-modulation is called Additive Interleaving Modulation (AIM).

5   Modulation Techniques

For a given modulation code that translates an input message into a sequence of mark sizes S_j, the objective of the postmodulation DIM or AIM is to translate S_j into T_j so that at the detection either ΔT_j or ΞT_j can be used directly to recover the original S_j without any error propagation. Without loss of generality, $V_r = V_w$ is assumed in the following discussion.

(i). Differential Interleaving Modulation

For a given modulation code, assume each mark generated satisfies the following condition:

$$0 < S_{min} \leq S_j \leq S_{max}. \qquad (5.1)$$

For DIM, we first define the initial values T_1 and T_2, and subsequent T_j's after T_1 and T_2 are obtained as follows:

$$T_{j+2} = \begin{cases} T_j + S_j, & \text{if } T_j + S_j \leq T_{max} \\ T_j + S_j - T_{max} + T_{min} - 1, & \text{if } T_j + S_j > T_{max}, \end{cases}$$

$$(5.2)$$

where $0 < T_{min} \leq T_j \leq T_{max}$ for each j.

To make the modulation rule self-consistent when $T_j = T_{max}$ and $S_j = S_{max}$, from the second part of Eq. (5.2), we need:

$$S_{max} + T_{min} - 1 \leq T_{max} \text{ or } T_{max} - T_{min} \leq S_{max} - 1. \qquad (5.3)$$

By subtracting T_j on both sides of Eq. (5.2), we have:

$$-\Delta T_j = T_{j+2} - T_j = \begin{cases} S_j, & \text{if } T_j + S_j \leq T_{max} \\ S_j - T_{max} + T_{min} - 1, & \text{if } T_j + S_j > T_{max} \end{cases}$$

We note that if $T_j + S_j \leq T_{max}$ is true in recording, $-\Delta T_j = T_{j+2} - T_j = S_j \geq S_{min}$, and if $T_j + S_j > T_{max}$ is true in recording, by Eq. (5.3), $-\Delta T_j = T_{j+2} - T_j = S_j - T_{max} + T_{min} - 1 \leq 0$. Therefore:

$$-\Delta T_j = T_{j+2} - T_j = \begin{cases} S_j, & \text{if } -\Delta T_j \geq S_{min} \\ S_j - T_{max} + T_{min} - 1, & \text{if } -\Delta T_j \leq 0. \end{cases}$$

As a result, the differential pre-demodulation rule is:

232

$$S_j^* = \begin{cases} -\Delta T_j^* & \text{if } -\Delta T_j^* \geq S_{min} \\ -\Delta T_j^* + T_{max} - T_{min} + \epsilon & \text{if } -\Delta T_j^* < \end{cases} \quad (5.4)$$

and the original S_j can be recovered by simple threshold detection from S_j^*. Here we see the condition in Eq. (5.3) also provides the error detection capability when $0 < -\Delta T_j^* < S_{min}$ happens.

(iii). Additive Interleaving Modulation

Assume the given modulation code and the past AIM code follow the same condition in Eq. (5.1). The AIM rule is described as follows

$$S_{j+1}^* = \begin{cases} S_j - T_j + T_{min} & \text{if } S_j - T_j \geq 0 \\ S_j - T_j + T_{max} - S_{min} & \text{if } S_j - T_j < 0 \end{cases} \quad (5.5)$$

This definition makes sure $T_j \geq T_{min}$. To make sure $T_j \leq T_{max}$, we need the following two additional conditions. Substituting $T_j = T_{min}$ and $S_j = S_{max}$ in the first part of Eq. (5.5), we need

$$S_{max} - T_{min} + T_{min} = S_{max} \leq T_{max}. \quad (5.6)$$

Substituting $(S_j - T_j)$ with -1 in the second part of Eq. (5.5), we need

$$-1 - T_{min} + T_{max} - S_{min} \leq T_{max}, \text{ or } T_{min} \leq S_{min} + 1 \quad (5.7)$$

In addition, to know whether $S_j - T_j \geq 0$ or $S_j - T_j < 0$ is true in recording to select the right equation from Eq. (5.5) for data recovery, we should have another condition for T_{min} and T_{max}. Note that when $S_j - T_j < 0$ is true, we have: $\min(T_j + T_{j+1}) = \min(S_j + T_{max} + T_{min} - S_{min}) = T_{max} + T_{min}$, and when $S_j - T_j \geq 0$ is true, $\max(T_j + T_{j+1}) = \max(S_j + T_{min}) = S_{max} + T_{min}$. Therefore, condition (5.6) should be modified as:

$$T_{max} > S_{max} \quad (5.8)$$

As a result, with the two conditions (5.7) and (5.8), we can have the following AIM demodulation rule

$$S_j^* = \begin{cases} \Sigma T_j^* - T_{min} & \text{if } \Sigma T_j^* \leq S_{max} + T_{min} \\ \Sigma T_j^* - (T_{min} + T_{max} - S_{min}) & \text{if } \Sigma T_j^* \geq T_{min} + T_{max} \end{cases} \quad (5.9)$$

Again, if $S_{max} + T_{min} < \Sigma T_j^* < T_{min} + T_{max}$, errors can be detected

6 Simulation Examples

This section examines how data recovery is improved by using the signal processing techniques discussed earlier. To have a quantitative performance evaluation, we use the mark error rate (MER) as the criterion, which is defined as the ratio of the number of misdetected marks to the total number of input marks.

In the following subsections, we first describe three different sets of the statistical parameters that are used in the computer simulation programs. These three sets are used to describe three different jitter scenarios. Next, we describe five different detection methods based on which MER is calculated. In simulation, each MER is obtained at a given signal to noise ratio (SNR), where SNR is defined as.

$$SNR \equiv \frac{\text{Unit Mark Size}}{\text{RMS Jitter of } \epsilon} = \frac{(\Delta T)V_r}{\sqrt{\sigma_{laser}^2 + \sigma_{media}^2 + \sigma_{receiver}^2}}$$

where ΔT is the unit of time. From this definition, we see that SNR here only includes noise jitter. At the end, we will discuss the simulation results.

6.1 Statistical Parameters

In simulation, time mark sizes are $i\Delta T$, where ΔT is chosen to be 100 nsec, and i is uniformly distributed between 3 and 8 (similar to the (2,7) code but not exactly). The disk linear velocity is set at 4.0 m/sec in the both write and read process. For simplicity, the velocity flucuation in the write process is assumed to be zero in all simulation cases (or assuming the velocity correction can be done perfectly). Three different sets of parameters are selected to cover the following scenarios:

1. **All velocity jitter, bit shift jitter, and ISI are significant.**

In this scenario, read velocity fluctuation range is set to be ± 0.4 m/sec, or 10% of the mean velocity. Velocity is maintained to be slowly varying within a time mark period.

Bit shift jitter (δ_2, δ_1) is set to have a mean shift 200 nm to represent approximately 20% of the laser beam width (assuming the diffraction limit is 1 μm), and the fluctuation of the shift is ± 60 nm, or approximately $\pm 6\%$ of the laser beam width. The bit shift jitter is also maintained to be slowly varying in a time mark period.

ISI jitter is assumed to be essentially a linear function of the time mark written. The proportional constant is chosen to be 0.05 in this scenario. The detection performance is shown in Figure 5.

2. **Only bit shift jitter is significant.**

In this scenario, velocity jitter is set to zero, and the ISI jitter is reduced from 0.05 in scenario 1 to 0.02. Other parameters are the same as those in scenario 1. The detection performance is shown in Figure 6.

3. **Only ISI is significant.**

In this scenario, velocity jitter is set to zero, and the bit shift jitter is reduced from ± 60 nm in scenario 1 to ± 10 nm, or $\pm 1\%$ of the laser beam width. Other parameters are maintained to be the same as in scenario 1. The detection performance is shown in Figure 7.

6.2 Detection Methods

Five detection methods are used in simulation. They are

1. **Basic Detection.**

The basic detection method is based on threshold detection and uses no equalization other than compensating the average bit shift term $\bar{\delta}_2$. That is, for each detected mark size, T_j^*, we subtract $2\bar{\delta}_2/V_r$ if j is even and add the same amount if j is odd.

2. **Basic Detection plus ISI Equalization.**

In addition to the average bit shift compensation, this second detection method equalizes the ISI jitter.

3. **Basic Detection plus ISI and Velocity Equalization.**

In addition to the basic detection and ISI equalization, this detection method equalizes velocity fluctuation.

4. **Differential Detection plus ISI and Velocity Equalization.**

This detection method equalizes ISI and velocity fluctuation, but it does not cancel bit shift jitter in the rudimentary way of method 1. Instead, it uses the better differential detection method
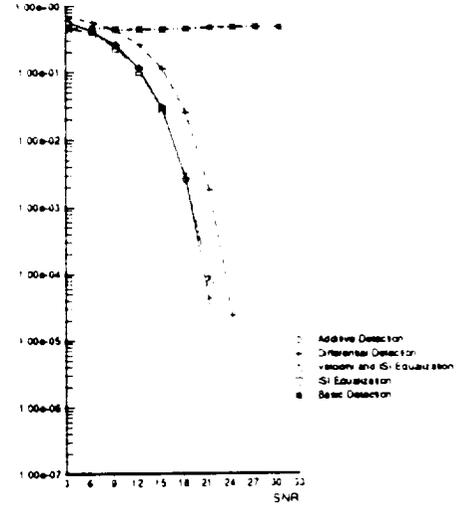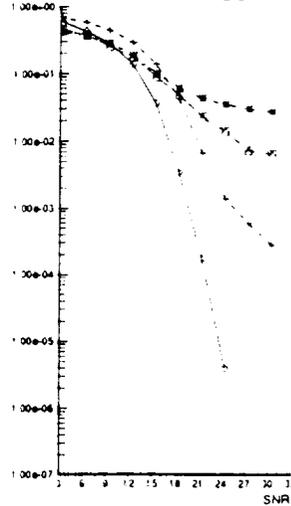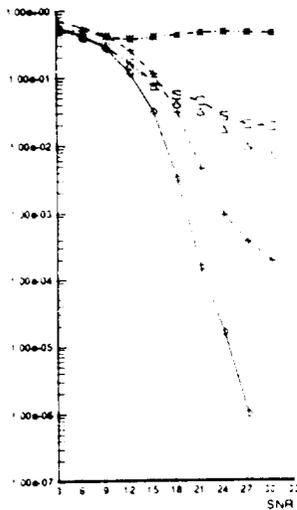
Figure 5: Mark Error Rate of scenario 1   Figure 6: Mark Error Rate of scenario 2   Figure 7: Mark Error Rate of scenario 3

(DID) to cancel the jitter.

5. Additive Detection plus ISI and Velocity Equlization.

This detection method is almost the same as the last method except it uses additive detection rather than differential detection described in section 4.

6.3 Discussion

From the results, we may make the following observations.

1. The basic detection method is not an effective detection method if the noise jitter is dominated by other jitter. As shown in Figures 5 to 7, MER can not be effectively improved by increasing SNR. This indicates the importance of equalization.

2. Methods 2 and 3 perform almost the same if velocity fluctuation does not exist. These two methods perform equally as well as the DID and AID methods when gaussian noise dominates ($SNR < 12$) (even better than DID).

3. Differential detection performs better than the first three detection methods, and is approximately 3 db poorer than additive detection. This is what we predicted before. But interestingly, when SNR is greater than 25 db, DID reaches an error floor if bit shift jitter is significant (see Figures 5,6). We do not see the similar floor when only ISI jitter is important (Figure 7). This error floor is likely due to the second order jitter effect that we have neglected, and this effect does not appear in the case of AID. When noise jitter dominates ($SNR < 12$ in Figures 5-7), DID is not better than the other methods because of the extra 3db penalty.

4. Additive detection performs better in all cases, especially when all sources of jitter are important or when bit shift jitter is not negligible (see Figures 5-7).

7 Conclusions

This paper has introduced a jitter model and a quantization approach, based on which signal processing techniques in equal-

ization, detection, and modulation were used to obtain better data recovery. From the simulation examples illustrated, we found that additive detection plus velocity and ISI equalizations performed best. Its smaller SNR to obtain the same mark error rate implies smaller sizes can be recovered and consequently a higher density can be achieved.

8 Acknowledgement

The author would like to thank M. Mansuripur and R. Hajjar of the Optical Sciences Center of the University of Arizona, David Cheng and Roger Wood of IBM, and the anonymous reviewers for their valuable help and input to this paper.

References
[1] Alan B. Marchant, *Optical Recording. A Technical Overview*, Addision Wesley, 1990.

[2] Roger Wood, "Magnetic and Optical Storage Systems: Opportunities for Communications Technology", pp. 1605-1612. Proceeding of ICC, 1989.

[3] Dennis G. Howe, "Signal-to-noise ratio (SNR) for reliable data recording", SPIE Vol. 695, Optical Mass Data Storage II, pp. 255-261, 1986.

[4] H. Burkhardt, "Phase Detection with Run-Length-Limited Codes", IBM Technical Disclosure Bulletin, Vol. 24, No. 1B, p. 683, June 1981.

[5] B. P. Lathi, Chapter 3 of *Modern Digital and Analog Communication Systems*, 2nd Ed., Holt, Rinehart, and Winston, 1989.

[6] David C. Cheng, Private Communications. IBM Research Division, San Jose.

[7] T. W. McDaniel, "Simulation of bit jitter in magneto-optic recording", J. of Appl. Phys., April 1988, pp. 3859-3861.

[8] Max M.-K. Liu, "Experiments for Future High Density Optical Data Storage", Paper presented in Optical Data Storage meeting, University of Arizona, Tucson, Apr. 1990.

Appendix N

Appendix to Self-Study
ODSC Sunset Review

PAPERS IN REFEREED JOURNALS

Neal Armstrong (Chemistry)

"Quantitation of Auger and X-Ray Photoelectron Spectroscopies: A Straight Forward Procedure for Most Spectroscopies, Complex Sample Matrix and Instrumental Parameters Make Quantitation of Surface Electron Spectroscopies a Real Challenge," with K.W. Nebesny and B.L. Maschhoff, Anal. Chem., 61, 469A (1989).

"Oxide Formation on Rare Earth/Transition Metal Thin Films," with Paul A. Lee, Kurt F. Stork, and Brian L. Maschhoff, "Materials for Magneto-optic Data Storage", Takao Suzuki, Clifford Robinson and Charles Falco, eds., Materials Research Society, Vol. 150, p. 227 (1989).

"Thin Oxide Layers on Clean Iron Surfaces: Formation in Vacuum and Characterization by Photoelectron Spectroscopy and Electrochemical Reactions of Probe Molecules at the Oxide/Electrolyte Interface," with B.L. Maschhoff, Langmuir, in press.

"Oxide Formation on Fe and Ti Thin Films and on Fe Thin Films Modified with Ultrathin Layers of Ti," with Paul A. Lee, Kurt F. Stork, Brian L. Maschhoff, and Ken W. Nebesny, Surface and Interface Analysis, in press.

"Oxide Formation on Rare Earth/Transition Metal and Bimetallic Transition Metal Thin Films: Modeling the Effect of Fourth Element Modifiers on O_2 and H_2O Surface Chemistries," with Paul A. Lee, J. Magnetism & Magnetic Materials, in press.

"Challenges to Quantitation in AES and XPS: Systems of Electrochemical Interest," with K.W. Nebesny, P.A. Lee, K.F. Stork, B.L. Maschhoff, J.W. Pankow, and T.S. Patterson, J. Electrochem. Soc., in press.

Charles M. Falco (Physics)

Competing Interactions in Metallic Superlattices
Charles M. Falco, J. L. Makous, J. A. Bell, W. R. Bennett, R. Zanoni, G. I. Stegeman and C. T. Seaton in, Competing Interactions and Microstructures - Statics and Dynamics, R. LeSar, A. Bishop and R. Heffner, eds. (Springer-Verlag, 1988), p. 139

Brillouin Scattering from Collective Spin Waves in Magnetic Superlattices
B. Hillebrands, A. Boufelfel, Charles M. Falco, P. Baumgart, G. Güntherodt, E. Zirngiebl and J. D. Thompson J. Appl. Phys. 63, 3880 (1988)

Magnetic and Structural Characterization of Copper/Cobalt Multilayers Craig D. England, Wayne R. Bennett and Charles M. Falco of Appl. Phys. 64, 5757 (1988)

Appendix   Sunset Review: Self-Study   A-2

Determination of Effective Optical Constants of Magnetic Multilayers
    M. N. Deeter, D. Sarid, C. D. England, W. R. Bennett and Charles M. Falco Appl. Phys. Lett.
54, 2059 (1989)

Materials for Magneto-Optic Data Storage
    C. J. Robinson, T. Suzuki and C. M. Falco, editors Materials Research Society, Pittsburgh,
1989

Structural and Magnetic Properties of Ti/Co Multilayers
    Robert Van Leeuwen, Craig D. England, John R. Dutcher, Charles M. Falco and Wayne R.
Bennett. J. Appl. Phys. 67, 4910 (1990)

NMR Studies of Compositionally Modulated Co/Cu Thin Films
    K. Le Dang, P. Veillet, W. R. Bennett, D. C. Person and Charles M. Falco J. of Physics F -
Metals Physics - IN PRESS

X-ray Characterization of Magnetic Multilayers and Superlattices
    Charles M. Falco, J. M. Slaughter and Brad N. Engel in, Nanostructured Magnetic Materials,
G. Hadjipanyis and G. Prinz, eds. (Plenum, New York, IN PRESS)

Structural and Magnetic Properties of Epitaxial Co/Pd Superlattices
    Brad N. Engel, Craig D. England, Masafumi Nakada, Robert Van Leeuwen and Charles M.
Falco in, Nanostructured Magnetic Materials, G. Hadjipanyis and G. Prinz, eds. (Plenum, New York,
IN PRESS)

Magnetic Properties of Metallic Multilayers and Superlattices
    Charles M. Falco and Brad N. Engel Physica B - IN PRESS

Structural and Magnetic Ordering at Interfaces of Metallic Superlattices
    Charles M. Falco and Brad N. Engel in, Ordering at Surfaces and Interfaces, A. Yoshimori,
T. Shinjo and H. Watanabe, eds. (Springer Verlag, Berlin, IN PRESS)

Magnetic Properties of Pd/Co Multilayers
    W. R. Bennett, C. D. England, D. C. Person and Charles M. Falco J. Appl. Phys. - IN PRESS

Magnetic Properties of Epitaxial Co/Pd Superlattices
    Brad N. Engel, Craig D. England, Robert Van Leeuwen, Masafumi Nakada and Charles M.
Falco J. Appl. Phys. - SUBMITTED

Preparation and Structural Characterization of Epitaxial Co/Pd (111) Superlattices
    Craig D. England, Brad N. Engel and Charles M. Falco J. Appl. Phys. - SUBMITTED

Ursula J. Gibson

    Kenneth D. Cornett, Ursula J. Gibson, "Detection of Micrometer-sized Pinholes in Specularly
Reflecting Films", Rev. Sci. Instrum., v.598(1988), p. 1341.

Raymond K. Kostuk (ECE)

Wang, L. and Kostuk, R.K., "Direct Formation of Planar Holograms and Noise Gratings at 820nm in Bleached Silver-Halide Emulsions," Opt. Lett. 14, 919-921 (1989).

Kostuk, R.K., Kato, M. and Huang, Y.-T., "Polarization properties of substrate-mode holograms "Appl. Opt., 29, 3848-3854 (1990).

Kostuk, R.K., "Factorial optimization of bleach constituents for silver-halide holograms," accepted for publication in Applied Optics.

George N. Lawrence

Cronkite, P. and G. Lawrence, "Aberration Minimization of Focusing Grating Coupler under wavelength shift," Appl. Opt., Vol. 27, No. 4, 679-683 (1988).

Lawrence, G. and P. Cronkite, "Physical optics analysis of the focusing grating coupler optical data head," Appl. Opt., Vol. 27 No. 4, 672-678 (1988).

G. Lawrence, "Optical Design of Holographic Optical Elements," Optics News 26, p26, June, 1988.

G. Lawrence and S-H Hwang, "Beam propagation in GRIN Media," submitted to Appl. Opt.

G. Lawrence, K. Moore, and P. Cronkite, "Rotationally symmetric construction optics for a waveguide focusing grating," submitted to Appl. Opt. 23.

S. Eckhardt and G. Lawrence, "Non-Fresnel diffraction behavior in thick refractive elements observed by Talbot imaging," submitted to Appl. Opt.

John A. Leavitt - (Physics)

J. A. Leavitt, "Ion Beam Analysis with a 6 MV Van de Graaff," Nucl. Instr. Meth. B 24/25, 717 (1987).

L. C. McIntyre, Jr., J. A. Leavitt, B. Dezfouly-Arjomandy, and J. Oder, "Depth Profiling of Phosphorus using Resonances in the $^{31}P(\alpha,p)34S$ Reaction," Nucl. Instr. Meth. B 35, 446 (1988).

J. A. Leavitt, L. C. McIntyre, Jr., P. Stoss, M. D. Ashbaugh, B. Dezfouly-Arjomandy, M. F. Hinedi, and G. Van Zijll, "Backscattering Spectrometry with ^{4}He, ^{12}C, ^{14}N, ^{40}Ar, and ^{84}Kr Analysis Beams with Energies 1.5 to 5.0 MeV," Nucl. Instr. Meth. B 35, 333 (1988).

J. A. Leavitt, L. C. McIntyre, Jr., M. D. Ashbaugh, B. Dezfouly-Arjomandy, and J. G. Oder, "Characterization of Optical Coatings with Backscattering Spectrometry," Appl. Opt. 28, 2762 (1989).

J. A. Leavitt, L. C. McIntyre, Jr., J. G. Oder, P. Stoss, M. D. Ashbaugh, B. Dezfouly-Arjomandy, Z. Lin, and Z. M. Yang, "Cross-Sections for 170° Backscattering of ^{4}He from Carbon for ^{4}He energies between 1.8 and 5.0 MeV," Nucl. Instr. Meth. B 40/41, 776 (1989).

J. A. Leavitt, L. C. McIntyre, Jr., M. D. Ashbaugh, J. G. Oder, Z. Lin, and B. Dezfouly-Arjomandy, "Cross-Sections for 170.5° Backscattering of ^{4}He from oxygen for ^{4}He Energies between 1.8 and 5.0 MeV," Nucl. Instr. Meth. B 44, 260 (1990).

L. C. McIntyre, Jr., J. A. Leavitt, M. D. Ashbaugh, B. Dezfouly-Arjomandy, Z. Lin, J. Oder, R. F. C. Farrow, and S. S. P. Parkin, "Detection and Depth Profiling of ^{19}F using Resonances in the ^{19}F(α,p)^{22}Ne Reaction," Nucl. Sci. Tech. (China) 1, 56 (1990).

Lifeng Li

Lifeng Li and Mool C. Gupta, "The Effects of Beam Focusing on the Efficiency of Planar Waveguide Grating Couplers," Appl. Opt. 29, 5320-5325(1990).

Mool C. Gupta and Lifeng Li, "Achromatic Compensation of Integrated Optical Grating Couplers," accepted for publication in Appl. Opt.

Mool C. Gupta and Lifeng Li, "The Effects of Beam Defocusing on the Efficiency of Planar Waveguide Grating Couplers," accepted for publication in Appl. Opt.

H. Angus Macleod

K. Balasubramanian and H. A. Macleod, "Performance calculations for multilayer thin-film structures containing a magneto-optical film" (abstract), J. Opt. Soc. Am. A 3 28 (1987).

K. Balasubramanian, A. S. Marathay, and H. A. Macleod, "Modeling magnetooptical thin-film media for optical data storage," Thin Solid Films, 164, 391-403 (1988).

M. Mansuripur

J. Calkins, M. F. Ruane, and M. Mansuripur, "A system for measurement of domain wall motion in amorphous rare earth-transition metal alloys" (contributed), presented at the 4th joint MMM-Intermag Conference, Vancouver, Canada, July 1988. Published in IEEE Trans. Mag. 24, 2314 (1988).

R. E. Uber and M. Mansuripur, "Magneto-optical measurement of anisotropy energy constant(s) for amorphous RE-TM alloys" (contributed), presented at the 4th joint MMM-Intermag Conference, Vancouver, Canada, July 1988. Published in IEEE Trans. Mag. 24, 2461 (1988).

M. Mansuripur, "Magnetization reversal dynamics in the media of magneto-optical recording," J. Appl. Phys. 63, 5809 (1988).

M. Mansuripur and R. Giles, "Demagnetizing field computation for dynamic simulation of the magnetization reversal process," IEEE Trans. Magnet. 24, 2326 (1988).

M. Mansuripur and T. W. McDaniel, "Magnetization reversal dynamics in magneto-optic media" (invited), presented at the conference on Magnetism and Magnetic Materials (MMM), Chicago, Illinois, November 1987. Published in J. Appl. Phys. 63, 3831 (1988).

Hajjar and M. Mansuripur, "Mean-field analysis of ternary and quaternary rare earth-transition metal alloys for thermomagnetic recording" (contributed), presented at the Intermag '89 Conference, Washington, D.C., March 1989. Published in IEEE Trans. Magnet. 25, 4021 (1989).

M. Mansuripur, "Demagnetizing field computation for thin films: Extension to the hexagonal lattice," J. Appl. Phys. 66, 3731 (1989).

M. Mansuripur, "On the self magnetostatic energy of jagged domain walls," J. Appl. Phys. 66, 3727 (1989).

M. Mansuripur, "Computation of fields and forces in magnetic force microscopy," IEEE Trans Magnet. 25, 3467 (1989).

M. Mansuripur, "Certain computational aspects of vector diffraction problems," J. Opt. Soc. Am. A 6, 786 (1989).

M. Mansuripur, "Detecting transition regions in magneto-optical disk systems," Appl. Phys. Lett. 55, 716 (1989).

M. Mansuripur, "Domain wall energy in the media of magneto-optical recording," J. Appl. Phys. 66, 6175 (1989).

M. Mansuripur, F. Zhou, and J. K. Erwin, "Measuring the wavelength dependence of magneto-optical Kerr (or Faraday) rotation and ellipticity: a technique," Appl. Opt. 29, 1308 (1990).

M. Mansuripur, "Analysis of multilayer thin film structures containing magneto-optic and anisotropic media at oblique incidence using 2 x 2 matrices," J. Appl. Phys. 67, 6466-6475 (1990).

M. Mansuripur and R. Giles, "Simulation of the magnetization reversal dynamics on the Connection Machine," *Computers in Physics* 4, 291-302, (1990).

R.A. Hajjar, F.L. Zhou and M. Mansuripur, "Magneto-optical measurement of anisotropy energy constants on amorphous rare earth-transition metal alloys", J. Appl. Phys. 67, 5328-5330 (1990).

R. Giles and M. Mansuripur, "Possible sources of coercivity in thin films of amorphous rare earth-transition metal alloys", to appear in *Computers in Physics*, March 1990.

M. Mansuripur, "Computation of electron diffraction patterns in Lorentz electron microscopy f thin magnetic films", to appear in J. Appl. Phys., February 1990.

R. Hajjar, M. Mansuripur, and H.-P. D. Shieh, "Measurements of the magnetoresistance effect in magneto-optical recording media," submitted to J. Appl. Phys. (1990).

M. Mansuripur, R. Giles and G. Patterson, "Coercivity of domain wall motion in thin films of amorphous rare earth-transition metal alloys," (invited), to appear in J. Magnet. Soc. Japan (1991).

M. Mansuripur, "Effects of high-numerical-aperture focusing on the state of polarization in optical and magneto-optical data storage systems," submitted to *Applied Optics* (1990).

Hong Fu, M. Mansuripur, and P. Meystre, "A generic source of perpendicular anisotropy in amorphous rare earth-transition metal films," submitted to Phys. Rev. Lett. (1990).

B. E. Bernacki and M. Mansuripur, "Characterization of magneto-optical recording media in terms of domain boundary jaggedness," to appear in J. Appl. Phys. (1991).

M. Mansuripur, "Enumerative modulation coding with arbitrary constraints and post-modulation error correction coding for data storage systems," submitted to IEEE Transactions on Information Theory (1990).

R. Giles, P. Alexopoulos and M. Mansuripur, "Micromagnetics of thin film media for magneticrecording", submitted to **Computers in Physics**, 1990.

M. Mansuripur and Hong Fu, "Direct overwrite in magneto-optical recording using circularly polarized microwaves", submitted to *Appl. Phys. Lett.*, 1990.

M. Mansuripur, R. Giles and G. Patterson, "Possible sources of coercivity in thin films of amorphous rare earth-transition metal alloys," (contributed), presented at the 35th Annual Conference on Magnetism and Magnetic Materials (MMM), San Diego, California, Oct. 29-Nov.1, 1990. To be published in J. Appl. Phys. (1991).

M. Mansuripur, "Computation of electron diffraction patterns in Lorentz electron microscopy of thin magnetic films," (contributed), presented at the 35th Annual Conference on Magnetism and Magnetic Materials (MMM), San Diego, California, Oct. 29-Nov.1, 1990. To be published in J. Appl. Phys. (1991).

R. Giles and M. Mansuripur, "Micromagnetics of thin film CoX media for longitudinal magnetic recording," (contributed), presented at the 35th Annual Conference on Magnetism and Magnetic Materials (MMM), San Diego, California, Oct. 29-Nov.1, 1990. To be published in J. Appl. Phys. (1991).

R. Hajjar, M. Mansuripur, and H.-P. D. Shieh, "Measurements of the anomalous magnetoresistance effect in magneto-optical recording media," (contributed), presented at the 35th Annual Conference on Magnetism and Magnetic Materials (MMM), San Diego, California, Oct. 29-Nov.1, 1990. To be published in J. Appl. Phys. (1991).

F. L. Zhou, J. K. Erwin, and M. Mansuripur, "Spectral measurements of the magneto-optical Kerr rotation and ellipticity in the media of optical recording," (contributed), presented at the 35th Annual Conference on Magnetism and Magnetic Materials (MMM), San Diego, California, Oct. 29-Nov.1, 1990. To be published in J. Appl. Phys. (1991).

Appendix   Sunset Review: Self-Study   A-7

Pierre Meystre

C. M. Savage, F.Marquis, M. D. Watson, and P. Meystre, "Direct overwrite in magneto-optical recording," Appl. Phys.Lett. 52 1277 (1988)

C. M. Savage, M. D. Watson, and P. Meystre, "Modeling magneto-optical domain erasure without cylindrical symmetry," J. Appl. Phys. 66, 1789 (1989)

M. D. Watson and P. Meystre, "Direct overwrite without inititalization in a bilayer magneto optical disk," Appl. Phys. Lett 56, 2249 (1990)

P. Meystre and H. Fu, "Magnetooptic Direct Overwrite by Adiabatic Following, submitted to Appl. Phys. Lett.

M. Mansuripur, H. Fu, and P. Meystre, "Direct Overwrite in Magetooptical Recording Using Circularly Polarized Microwaves, submitted to Appl. Phys. Lett.

H. Fu, M. Mansuripur, and P. Meystre, "Generic Source of Perpendicular Anisotropy in Rare earth-transition-metal Films, submitted to Phys. Rev. Lett.

Tom D. Milster

F.F. Froehlich, M.S. Wang and T.D. Milster, "A technique for simultaneous alignment and collimation of a laser diode in an optical data storage head," submitted to *Appl. Opt.*

Dror Sarid

Merritt N. Deeter and Dror Sarid, "Effects of incident angle on read-out in magnetooptic storage media," Appl. Optics 27, 713 (1988).

Merritt N. Deeter, Jeffery T. Ingle and Dror Sarid: "Jones-Matrix Analysis of Incident-Angle Effects in Storage media" Appl. Opt. 28, 335 (1988).

Merritt N Deeter and Dror Sarid, "Determination of optical constants by angle-scanning reflectometry," Appl. Opt., (in Press, 1989).

Merritt N. Deeter, Dror Sarid, C. D. England, W. R. Bennett and Charles M. Falco, "Determination of Effective Optical Constants of Magnetic Multilayers," Appl. Opt. (in Press, 1989).

Dror Sarid, Douglas Iams, Volker Weissenberger and L. Stephen Bell, "Compact Scanning Force Microscope Using a Diode Laser," Opt. Lett. 28 335 (1988).

Dror Sarid, Volker Weissenberger, Douglas A. Iams and Jeffrey T. Ingle, "Theory of the laser diode interaction in a scanning force microscope," IEEE J. Quant. Electron. 7257, 1968 (1989).

Douglas Iams, Jeffery Ingle, Josef Ploetz, L. Stephen Bell and Dror Sarid, "Performance of a Scanning Force Microscopy using a Laser Diode" J. Vac. Sci. Tech, (Accepted) (1989).

Appendix   Sunset Review: Self-Study   A-8

Laura A. Weller-Brophy

L. A. Weller-Brophy and D. G. Hall, "Local normal mode analysis of guided mode interactions with waveguide gratings," J. Lightwave Tech. 6, 1069-1082 (1988).

L. A. Weller-Brophy and D. G. Hall, "Statistical analysis of waveguide gratings using Rouard's method," Appl. Opt. 27, 963-966 (1988).

C. Martijn de Sterke, J. E. Sipe, and L. A. Weller-Brophy, "Electromagnetic Stark ladders in waveguide geometries," accepted for publication in Applied Physics Letters, 1991.

W. E. Torruellas, L. A. Weller-Brophy, R. Zanoni, G. I. Stegeman, Z. Osborne, and B. J. J. Zelinski, "Third harmonic generation measurement of nonlinearities in SiO_2-TiO_2 sol-gel films,". Accepted for publication in Applies Physics Letters, 1991.

R. L. Roncone, L. A. Weller-Brophy, L. Weisenbach, and B. J. J. Zelinski, "Embossed gratings in sol-gel waveguides: Pre-emboss heat treatment effects." Accepted for publication in J. Non-Crystalline Solids, 1991.

L. A. Weller-Brophy, "The Principles and Applications of Waveguide Gratings," accepted for publication in *Applied Optics and Optical Engineering,* Volume 11, July, 1989.

PAPERS IN PROCEEDINGS
and/or
DIGESTS OF NATIONAL/INTERNATIONAL MEETINGS

James J. Burke

P. Hu and J. Burke, "Optical data storage technology and opportunities," Proceedings of 1987 International Symposium on VLSI Technology, Systems, and Applications, May 13-15, 1987, Taipei, Taiwan, R.O.C. (Invited).

J. Burke and P. Hu, "The Optical Data Storage Center," Eighth IEEE Symposium on Mass Storage Systems, May 11-14, Tucson, Arizona (Invited).

R. R. Shannon, J. J. Burke, and P. Y. Hu, "Research activities at the Optical Data Storage Center," Technical Digest, International Symposium on Optical Memory 1987, September 16-18, 1987, Tokyo (Invited).

Appendix   Sunset Review: Self-Study   A-9

Charles M. Falco (Physics)

Magnetic Properties and Structural Characterization of Fe/Tb Multilayers
     Wayne R. Bennett, Donald C. Person and Charles M. Falco Topical Meeting on Optical Data Storage, Technical Digest Series 10, 127 (Optical Society of America, 1987)

Sputtering and Molecular Beam Epitaxy (MBE) Deposition of Magneto-Optical Materials
     Charles M. Falco, Brad N. Engel, Craig D. England and Robert A. Van Leeuwen Proc. of the Materials Research Society 150, 73 (1989)

Magneto-Optic Properties of Cu/Co and Pd/Co Multilayers
     Craig D. England, Don C. Person, Wayne R. Bennett, Wolfgang Reim and Charles M. Falco Proc. of the Materials Research Society 150, 103 (1989)

Magnetic and Magneto-Optical Properties of Interfaces and Superlattices
     Brad N. Engel and Charles M. Falco Materials Research Society Bulletin 15, 34 (1990)

Evidence for Collective Exchange Modes in Co/Pd Multilayers Observed by Brillouin Light Scattering
     B. Hillebrands, J. V. Harzer, R. L. Stamps, G. Güntherodt, C. D. England and Charles M. Falco Proc. of the Materials Research Society - IN PRESS

Magnetic Properties and Structural Characterization of Fe/Tb Multilayers
     Wayne R. Bennett, Donald C. Person and Charles M. Falco Topical Meeting on Optical Data Storage, Technical Digest Series 10, 127 (Optical Society of America, 1987)

Magnetic and Magneto-Optical Properties of Interfaces and Superlattices
     Brad N. Engel and Charles M. Falco Materials Research Society Bulletin 15, 34 (1990)

Sputtering and Molecular Beam Epitaxy (MBE) Deposition of Magneto-Optical Materials
     Charles M. Falco, Brad N. Engel, Craig D. England and Robert A. Van Leeuwen Proc. of the Materials Research Society 150, 73 (1989)

Magneto-Optic Properties of Cu/Co and Pd/Co Multilayers
     Craig D. England, Don C. Person, Wayne R. Bennett, Wolfgang Reim and Charles M. Falco Proc. of the Materials Research Society 150, 103 (1989)

Evidence for Collective Exchange Modes in Co/Pd Multilayers Observed by Brillouin Light Scattering
     B. Hillebrands, J. V. Harzer, R. L. Stamps, G. Güntherodt, C. D. England and Charles M. Falco Proc. of the Materials Research Society - IN PRESS

Appendix   Sunset Review: Self-Study   A-10

Ursula J. Gibson

Kenneth D. Cornett, Ursula J. Gibson, Anthony P. Taylor, "Ion-Assisted Deposition of Protective Overlayers for Magneto-Optic Data Storage," Mat. Res. Soc. Symp. Proc., v.128 (1989), p.495.

A. P. Taylor, K. D. Cornett, U. J. Gibson, and T. K. Hatwar, "Metallic Diffusion Barriers for MO Media", Mat. Res. Soc. Symp. Proc., v152 (1989).

Ray Kostuk - (ECE)

Kostuk, R.K., "Holographic Applications for Data Storage,"*Conf. Digest Topical Meeting on Optical Data Storage* Vancouver, BC, Canada, March 1990.

A.B. O'Connor and R.K. Kostuk, "Polarization properties of high numerical aperture holographic objectives," *OSA Technical Digest on Optical Data Storage*, Jan.17-19, 1989, Los Angeles, CA., Vol. 1, 94-97.

Haggans, C. and Kostuk, R.K.,"Use of rigorous vector coupled wave theory in design and tolerancing studies of arbitrary profile surface-relief diffractive components for magneto-optical heads," to be presented at the IEEE LEOS/OSA Topical Meeting on Optical Data Storage at Boulder, CO, February 25-27, 1991.

George Lawrence

Lawrence, G. and P. Cronkite, "Physical optics analysis of the focusing grating coupler optical data head," Fourth Topical Meeting, Optical Data Storage, March 1987.

Cronkite, P. and G. Lawrence, "Optical Design Principles for Chirped Grating Optical Data Head," Fourth Topical Meeting, Optical Data Storage, March 1987.

Cronkite, P. and G. Lawrence, "Optical Design of an HOE Grating Coupler for Optical Data Storage," SPIE Proc., Vol. 818 p221 (1987).

Lawrence, G., "Design of Holographic Construction Optics for Focusing Grating Optical Readout Heads," International Symposium on Optical Memory, Tokyo, Japan (1987).

P. Cronkite and G. Lawrence, "Design of High-Numerical Aperture Holographic Gratings for Integrated Optics Readout Heads," SPIE Vol. 883, p. 188 (1988).

G. Lawrence, M. Wang, S-H Hwang, "Optical Performance of a Waveguide Grating Imaging Device," SPIE Vol. 965-06 (1988).

S. Eckhardt, G. Lawrence, J. Burke, "Diffractive and Aberration Effects of Propagation through a Refractive Surface," OE'Lase, Jan. 1989 1045-28.

G. Lawrence and P. Cronkite, "Practical Design Methods for Holographic Construction of Waveguide Focusing Grating Couplers," OE Lase '89 Jan. 1989, 1051-20.

G. Lawrence, "Polarization Modeling in Physical Optics Analysis," SPIE 33rd Annual Symposium, August, 1989 1166-08.

S-H Hwang and G. Lawrence, "Physical Optics Analysis of Gradient Index Optics", SPIE 33rd Annual Symposium, August, 1989 1168-40.

G. Lawrence and P. Cronkite, "Rotationally Symmetric Holographic Construction Optics for Waveguide Grating Couplers," SPIE 33rd Annual Symposium, August, 1989.

G. Lawrence and K. Moore, "Design methods for Gradient Index waveguide gratings," submitted to the International Lens Design Conference 1990.

John A. Leavitt

J. A. Leavitt, L. C. McIntyre, Jr., M. D. Ashbaugh, and J. G. Oder, "Characterization of Optical Coatings with Backscattering Spectrometry," Optical Interference Coatings, 1988 Technical Digest Series, Vol. 6 (Opt. Soc. Am., Washington, DC, 1988), pp. 10-13.

L. C. McIntyre, Jr., M. D. Ashbaugh, and J. A. Leavitt, "Limits on the Accuracy of Stoichiometry Determined by Rutherford Backscattering Using Computer Peak Fitting," MRS Symposium Proc. 93, 401 (1987).

J. A. Leavitt and L. C. McIntyre, Jr., "High Energy ⁴He Backscattering," in High Energy and Heavy Ion Beams in Materials Analysis, eds. J. R. Tesmer, C. J. Maggiore, M. Nastasi, J. C. Barbour, and J. W. Mayer (Materials Research Society, Pittsburgh, 1990), pp. 129-138.

Lifeng Li

Lifeng Li, Mai Xu, G. I. Stegeman, and C. T. Colin, "Fabrication of Photoresist Masks for Submicrometer Surface Relief Gratings," Proc. SPIE 835, 72-82(1987).

Lifeng Li, James J. Burke, George I. Stegeman, and Colin T. Seaton, "Design Technique for Guided-Wave Gratings," J. Opt. Soc. Am. A4, No.13, P18(1987).

Shiow-Hwei Hwang, Qian Gong, Lifeng Li, and George Lawrence, "Polarization Properties of Waveguide Focusing Grating Couplers," in OSA Annual Meeting Technical Digest 1990, Vol.15 of the OSA Technical Digest Series (Optical Society of America, Washington, D.C.,1990), pp 85.

Lifeng Li, Qian Gong, George Lawrence, and James J. Burke, "Polarization Properties of Planar Dielectric Waveguide Grating Couplers," in OSA Annual Meeting Technical Digest 1990, Vol.15 of the OSA Technical Digest Series (Optical Society of America, Washington, D.C.,1990), pp 85.

H. Angus Macleod

K. Balasubramanian and H. A. Macleod, "Normal incidence performance of multilayer thin-film structures containing a magneto-optical film," Proc. SPIE 678, 192-201 (1986).

K. Balasubramanian, A. S. Marathay, and H. A. Macleod. "Design technique for anisotropic multilayer thin-film systems," presented at the 1987 Annual Meeting of the Optical Society of America, Rochester, New York.

K. Balasubramanian, A. S. Marathay, and H. A. Macleod, "Anisotropic effects in thin film multilayers," presented at the 7th International Conference of Thin Films (ICTF-7) New Delhi, December 1987.

Y. Mao, H. A. Macleod, and K. Balasubramanian, "Optical constant determination of magneto-optical thin film using surface plasmon resonance phenomenon," Optical Interference Coatings Topical Meeting, Tucson, Arizona, 1988.

M. Mansuripur

Mansuripur, "Magneto-optical recording in thin amorphous films of rare earth-transition metal alloys" (invited), presented at the 34th National Vacuum Symposium of the American Vacuum Society, Anaheim, California, November 1987. Summary abstract published in J. Vac. Sci. Technol. A 6, 1864 (1988).

M . Mansuripur and C. Pons, "Diffraction modeling of optical path for magneto-optical disk systems" (invited), presented at the meeting of the Society of Photo Instrumentation Engineers (SPIE), Los Angeles, California, January 1988. Published in Proc. SPIE 899, 56 (1988).

J. Hartman, M. Lind and M. Mansuripur, "Read channel optical modeling for a bump forming dye-polymer optical data storage medium" (contributed), presented at the OSA/SPIE meeting on Optical Data Storage, Los Angeles, CA, January 1989. Published in Proc. SPIE 1078, 308-323 (1989).

M. Mansuripur and R. Giles, "Magnetizaion reversal dynamics and the mechanism of coercivity in amorphous RE-TM alloys" (contributed), presented at the International Symposium on Optical Memory (ISOM), Kobe, Japan, September 1989. Extended abstract published in the Conference Proceedings.

P. Meystre

M. D. Watson, C. M. Savage, and P. Meystre, "Direct Overwrite in Magneto-optical recording," Technical Digest OSA annual meeting, MQ1 (1988).

P. Meystre, C. M. Savage, and M. D. Watson, "Modeling thermomagnetic direct overwrite," Modeling workshop, Tucson, AZ, March 1988 (not refereed)

Appendix Sunset Review: Self-Study A-13

M. D. Watson and P. Meystre, "Direct overwrite on a performatted bilayer magneto-optical disk," Proc. SPIE Topical Meeting on Optical Data Storage, Vancouver Canada, Jan. 1990

M. D. Watson and P. Meystre, "Modeling direct-overwrite without cylindrical symmetry," Magneto-optics workshop, Tucson, AZ, Jan 1991 (not refereed)

Tom D. Milster

T.D. Milster and T.S. Gardner, "Modeling of a Magneto-Optic Read Path," SPIE 0-E/LASE, 1988, also *Proc. SPIE 899*, 61-66, 1988.

T.D. Milster, "Characteristics of phase-compensation techniques in magneto-optical read-back systems," SPIE OE-LASE '89, San Diego, 1989, also *Proc. SPIE 1166*, pp. 355-365, 1989.

T.D. Milster, M. K. Benedict and R. P. Stahl, "Laser diode requirements for magneto-optical storage devices," IEEE/LEOS Topical Meeting on Optical Data Storage, March 5-7, 1990, Vancouver, also *Proc. SPIE 1316*, pp. 143-149, 1990.

T.D. Milster and J.P. Treptau, "Testing methodology and standardization for optical disks," ISOS '90, Chongqing, China, 1990.

J.P. Treptau, T.D. Milster and D.G. Flagello, "Laser beam modeling in optical storage systems," OE LASE '91, Los Angeles, to be published in SPIE #1415, 1991.

T.D. Milster and J.P. Treptau, "Measurement of laser spot quality," OE LASE '91, Los Angeles, to be published in SPIE #1415, 1991.

George Ian Allan Stegeman (CREOL)

L. Li, Mie Xu, G. I. Stegeman, and C. T. Seaton, "Fabrication of photoresist masks for submicron surface relief gratings," in Proceedings of SPIE Conference on *Integrated Optical Circuit Engineering V* edited by M. A. Mentzer, Proc. SPIE 835, 72-82 (1987)

Q. Gong, G. Assanto, R. Zanoni, G. I. Stegeman, R. Burzynski and . N. Prasad, "Efficient grating coupling and optical characterization of poly-4BCMU waveguides," SPIE, in press

K. B. Rochford, R. Zanoni, Q. Gong, W. E. Torruellas and G. I Stegeman, "Waveguide channels and gratings in polydiacetylene films using photo-induced bleaching," SPIE, in press

Laura Weller-Brophy

L. A. Weller-Brophy, "Local Normal Mode Analysis of Waveguide Grating Couplers," Annual Meeting of Optical Society of America, Santa Clara, California, October 1988.

R. L. Roncone, L. A. Weller-Brophy, and B. J. J. Zelinski, "The embossing of surface corrugation gratings on dielectric waveguides" *Proceedings for the 4th International Conference on Ultrastructure Processing of Ceramics, Glasses, and Composites,* Wiley and Sons, New York, 1990.

G. W. Dale, H. H. Fox, B. J. J. Zelinski, and L. A. Weller-Brophy," Sol-Gel synthesis of thin films for use as planar waveguides," *Proceedings for the 4th International Conference on Ultrastructure Processing of Ceramics, Glasses, and Composites,* Wiley and Sons, New York, 1990.

L. Weisenbach, T. L. Davis, B. J. J. Zelinski, R. L. Roncone, and L. A. Weller-Brophy, "Processing of SiO$_2$-TiO$_2$ Thin Film Waveguides," *The Materials Research Society Symposium Proceedings,* **180**, 377-382 (1990)

L. A. Weller-Brophy, B. J. J. Zelinski, and D. P. Birnie III, Materials challenges in integrated optical recording heads," MRS Bulletin, pp. 25-30 (April 1990).

Brian J. J. Zelinski

"Sol-Gel Synthesis of Thin Films for use as Planar Waveguides", G.W. Dale, H.H. Fox, Brian J.J. Zelinski and Laura Weller-Brophy, presented at the Fourth International Conference on Ultrastructure Processing of Ceramics, Glasses and Composites, Tucson, AZ, February, 1989.

"Sol-Gel Synthesis of Planar Optical Waveguides and Integrated Components", Ronald L. Roncone, Laura Weller-Brophy and Brian J.J. Zelinski, presented at the Fourth International Conference on Ultrastructure Processing of Ceramics, Glasses and Composites, Tucson, AZ, February, 1989.

"The Influence of Pre-processing upon Embossed Grating Depth and Shape," Ronald L. Roncone, Laura A. Weller-Brophy, Brian J.J. Zelinski, presented at the Better Ceramics Through Chemistry IV symposium of the Materials Research Society Spring Meeting, San Francisco, California, April, 1990.

"Shrinkage Behavior of SiO$_2$-TiO$_2$ Thin Film Waveguides, Lori Weisenbach, Teri Davis, Brian J.J. Zelinski, Ronald L. Roncone and Laura A. Weller-Brophy, presented at the Better Ceramics Through Chemistry IV symposium of the Materials Research Society Spring Meeting, San Francisco, California, April, 1990.

"TEM Investigation of Sol-Gel Coatings," L. Weisenbach, D.L. Klein, B.D. Fabes and Brian J.J. Zelinski, presented at the Better Ceramics Through Chemistry IV symposium of the Materials Research Society Spring Meeting, San Francisco, California, April, 1990.

"Third Harmonic Generation Measurements of Nonlinearities in SiO$_2$-TiO$_2$ Sol-Gel Films," W.E. Torruellas, L.A. Weller-Brophy, R. Zanoni, G.I. Stegeman, Z. Osborne, B.J.J. Zelinski, presented at NLO'90, Hawaii, July, 1990.

"Materials Challenges in Integrated Optical Recording Heads," L.A. Weller-Brophy, B.J.J. Zelinski, D. Birnie III, *MRS Bulletin,* 15, 25-30, 1990.

"Processing Behavior of SiO_2-TiO_2 Thin Film Waveguides," L. Weisenbach, T.L. Davis, Brian J.J. Zelinski, R.L. Roncone and L.A. Weller-Brophy, *Mat. Res. Soc. Symp. Proc.*, 180, 1990.

"Sol-Gel Synthesis of Thin Films for use as Planar Waveguides", G.W. Dale, H.H. Fox, Brian J.J. Zelinski and Laura Weller-Brophy, *Mat. Res. Soc. Symp. Proc.*, 180, 1990.

"Sol-Gel Synthesis of Planar Optical Waveguides and Integrated Components", Ronald L. Roncone, Laura Weller-Brophy and Brian J.J. Zelinski, accepted for publication in the proceedings of the Fourth International Conference on Ultrastructure Processing of Ceramics, Glasses and Composites, Tucson, AZ, February, 1989.

UNPUBLISHED ORAL PRESENTATIONS

U. J. Gibson

"An XPS Study of Reactions and Diffusion Behavior of Several Thin Overlayers on TbFeCo", International Metallurgical Coatings Conference, Spring 1989, San Diego, CA.

Modification of Zirconium Fluoride Thin Films for Integrated Optical Devices", Optical Society of America, Fall 1989, Orlando, FL.

"Reactive IAD of ZrOF for GRIN Integrated Optics", Ceramics and Advanced Materials, Joint Meeting of the New Mexico Section of the American Ceramic Society and the New Mexico Section of the Materials Research Society, October 5, 1990, Sante Fe, New Mexico.

Ray Kostuk (ECE)

Kostuk, R.K., "Effects of Bleach Constituents on the Performance of Silver-halide Holograms," *Proc. of 1990 SPIE Meeting on Optics, Electro-optics and Laser Application in Science and Engineering*, Los Angeles, CA, January 1990.

Kostuk, R.K., "Practical design considerations and performance characteristics of high numerical aperture holographic lenses," SPIE Electronic Imaging Science and Technology, 24 Feb.-1 Mar. 1991, San Jose, CA.

Appendix   Sunset Review: Self-Study   A-16

George Lawrence

G. Lawrence, "Combining Geometrical and Diffraction Theory in Optical Calculations," Invited Paper, WE1, OSA Annual Meeting, Oct., 1989.

G. Lawrence, "Compensation of aberrations due to wavelength shift in waveguide grating couplers by gradient-index methods", TuLL3, Opt. Soc. of Am. annual meeting, Oct. 1989.

Kenneth D. Cornett, George Lawrence, Ursula J. Gibson, "Fabrication of Large Gradient-Index Profiles in Thin Film Waveguides", FS1, Opt. Soc. of Am. annual meeting, Oct. 1989.

John A. Leavitt

J. A. Leavitt, " MeV Ion Beam Analysis," National Technical University Research Seminar video tape, Oct. 27, 1987, available from Microcampus, University of Arizona.

J. A. Leavitt, L. C. McIntyre, Jr., J. G. Oder, P. Stoss, M. D. Ashbaugh, and B. Dezfouly-Arjomandy, "Cross Sections for 170° Backscattering of ^{4}He from C, N, O, F, Mg, Al, and Si for ^{4}He Energies between 1.8 and 5.0 MeV," BAPS 33, 1730 (1988).

J. A. Leavitt, L. C. McIntyre, Jr., "High Energy and Heavy Ion Backscattering," Workshop on High Energy and Heavy Ion Beams in Materials Analysis, Albuquerque, NM, June 14-17, 1989, one hour invited talk.

J. M. Molarius, E. Kolawa, K. Moishita, J. L. Tandon, J. A. Leavitt, and M.-A. Micolet, "Encapulants for Thermal Annealing of GaAs," Spring 1989 Meeting of the Electrochemical Society, Los Angles, CA, May 7-12, 1989.

J. A. Leavitt and L. C. McIntyre, Jr., "Non-Rutherford ^{4}He Cross Sections for Ion Beam Analysis," Bull. Am. Phys. Soc. 35, 1695 (1990).

J. A. Leavitt, L. C. McIntyre, Jr., M. D. Ashbaugh, B. Dezfouly-Arjomandy, and Z. Lin, "MeV Ion Beam Analysis with ^{4}He Beams," Materials Characterization Symposium, Tucson, AZ, March 12-13, 1990.

L. C. McIntyre, Jr., J. A. Leavitt, B. Dezfouly-Arjomandy, Z. Lin, and M. D. Ashbaugh, Materials Characterization Symposium, Tucson, AZ, March 12-13, 1990.

B. Dezfouly-Arjomandy, Z. Lin, J. A. Leavitt, and L. C. McIntyre, Jr., "Depth Profiling Hydrogen in Materials with MeV ^{15}N Beams," Materials Characterization Symposium, Tucson, AZ, March 12-13, 1990.

Z. Lin, L. C. McIntyre, Jr., M. D. Ashbaugh, B. Dezfouly-Arjomandy, and J. A. Leavitt, "Calculation of Non-Rutherford Cross Sections for Backscattering of ^{4}He from ^{16}O for ^{4}He Energies from 1.5 to 5.0 MeV," March 12-13, 1990.

Appendix   Sunset Review: Self-Study   A-17

M. Mansuripur

M. Mansuripur, "Optical disk data storage," invited talk at the monthly meeting of the New England Section of the Optical Society of America, Lexington, Massachusetts, September 1987.

M. Mansuripur, "New developments in magneto-optics research," invited talk at the Research Laboratories, Eastman Kodak Company, October 1987.

M. Mansuripur, "Optical disk data storage," invited talk at the New England Section of the IEEE Magnetics Society, Lexington, Massachusetts, December 1987.

M. Mansuripur, "Erasable optical disk data storage," invited talk at the Research Division, Raytheon Corp., Lexington, Massachusetts, February 1988.

M. Mansuripur, "Optical disk data storage," invited talk at the Illinois Institute of Technology, Chicago, Illinois, November 1987.

M. Mansuripur and R. Giles, "Magnetization reversal dynamics in RE-TM alloys," invited talk at the IBM Almaden Research Center, San Jose, California, January 1988.

M. Mansuripur, "Magnetization reversal dynamics in the media of optical recording," invited talk at Komag Corp., Milpitas, California, January 1988.

M. Mansuripur, "Magnetization reversal dynamics in magneto-optic media," (invited) presented at the meeting of the American Physical Society, New Orleans, Louisiana, March 1988.

M. Mansuripur and R. Giles, "Demagnetizing field computation for dynamic simulation of the magnitization reversal process" (contributed), presented at the 4th joint MMM-Intermag Conference, Vancouver, Canada, July 1988.

M. Mansuripur, "Erasable magneto-optical disk data storage," invited talk at the symposium on Space Flight Data Storage Technology, Jet Propulsion Laboratory, Pasadena, California, July 1988.

M. Mansuripur, "Analysis of demagnetizing field, domain wall structure and zigzag boundaries by the Fourier transform technique" (invited), presented at the 2nd Topical Workshop on Magneto-Optical Recording Technology, Hidden Valley resort, Somerset, PA, October 10-12, 1988.

M. Mansuripur, "Modeling media and systems of optical data storage," invited talk at the storage research centers faculty meeting at IBM's General Products Division, San Jose, California, Dec. 7-9, 1988.

M. Mansuripur, "Analysis of demagnetizing field by the Fourier transform technique," invited talk at the IBM's T.J. Watson Research Laboratory, Yorktown Heights, NY, December 1988.

M. Mansuripur, "Overview of magneto-optical data storage" (invited) workshop on micromagnetics for magnetic recording, Center for Magnetic Recording Research (CMRR), University of California at San Diego, Feb. 8-10, 1989.

M. Mansuripur, "Computation of fields and forces in magnetic force microscopy" (contributed), presented at the Intermag '89 Conference, Washington, D.C., March 1989.

M. Mansuripur, "Amorphous rare earth-transition metal alloys for erasable optical data storage," invited talk at the 8th Annual Symposium of the Arizona Chapter of American Vacuum Society, Tucson, Arizona, April 6-7, 1989.

M. Mansuripur, "Erasable Optical Data Storage: Challenges and Opportunities," invited talk at the magnetic recording seminar series, IBM General Products Division, San Jose, California, November 1989.

M. Mansuripur, "Erasable optical data storage," presented at the Hewlett-Packard Laboratories, Palo Alto, California, November 1989.

M. Mansuripur and R. Giles, "Simulation of magnetization reversal dynamics on the Connection Machine" (invited), presented at the 34th Annual Conference on Magnetism and Magnetic Materials (MMM), Boston, Massachusetts, November 1989.

R. Hajjar, F. Zhou, and M. Mansuripur, "Magneto-optical measurement of anisotropy energy constants on amorphous RE-TM alloys," (contributed), presented at the 34th Annual Conference on Magnetism and Magnetic Materials (MMM), Boston, Massachusetts, November 1989.

R. Giles, R. Kotiuga, F. Humphrey and M. Mansuripur, "Parallel micromagnetic simulations on the Connection Machine" (contributed), presented at the 4th SIAM Conference on Parallel Processing for Scientific Computing, Chicago, Illinois, December 1989.

M. Mansuripur, "Computer modeling of magnetization reversal dynamics in magnetic and magneto-optical media", presented at Philips Research Laboratories, Eindhoven, The Netherlands, January 1990.

M. Mansuripur, "Progress in modeling of optical data storage media and systems," invited talk at the storage research centers faculty meeting at IBM's General Products Division, San Jose, California, January 11-12, 1990.

M. Mansuripur, "Computer modeling of optical storage media and systems" invited presentation at the OSA/SPIE/LEOS topical meeting on Optical Data Storage, Vancouver, Canada, March 1990.

R. Keys, D. Miller, J. W. Goodman, J. Malinson and M. Mansuripur (panelists), "Issues in Optical Technologies: Switching, Logic, and Storage"; evening panel discussion held at the Conference on Lasers and Electro-Optics (CLEO), Anaheim, California, May 1990.

B. Bernacki and M. Mansuripur, "Observation of domain wall behavior in the presence of submicrometer defects and substrate structures in the media of magneto-optical recording", (contributed), presented at the Conference on Lasers and Electro-Optics (CLEO), Anaheim, California, May 1990.

M. Mansuripur, "Critical issues in optical recording", (invited), Sixth Interdisciplinary Laser Conference, Minneapolis, Minnesota, September 16-19, 1990.

M. Mansuripur, "Physics of magneto-optical recording and readout processes," (invited), presented at the Annual Meeting of the Optical Society of America, Joint OSA/LEOS Session on Optical Storage, Boston, Massachusetts, November 1990.

M. Mansuripur and R. Giles, "Dynamics of magnetization reversal in amorphous films of RE-TM alloys," (invited), to be presented at the Magneto-Optical Recording International Symposium (MORIS), Japan (1991).

B. E. Bernacki and M. Mansuripur, "Characterization of magneto-optical recording media in terms of domain boundary jaggedness," (contributed), presented at the 35th Annual Conference on Magnetism and Magnetic Materials (MMM), San Diego, California, Oct. 29-Nov.1, 1990.

M. Mansuripur and R. Giles, "Characterization, modeling and dynamic simulation of the micromagnetic behavior in the media of erasable optical data storage", invited talk at the IBM T.J. Watson Research Center, Yorktown Heights, New York, November 1990.

INVENTION DISCLOSURES

George N. Lawrence

G. Lawrence, "Sub-scale, visible holographic fabrication of waveguide grating," Invention Disclosure, University of Arizona, 1988.

G. Lawrence, "Concentric waveguide focusing grating," Invention Disclosure, University of Arizona, 1988.

G. Lawrence, "Self-focusing, line narrowed, waveguide grating optical head," Invention Disclosure, University of Arizona, 1988.

G. Lawrence, "Holographic construction optics for waveguide grating," Invention Disclosure, University of Arizona, 1988.

G. Lawrence and S-H Hwang, "Waveguide grating with broad spectral response using gradient effective index," Invention Disclosure, University of Arizona, 1988.

Appendix   Sunset Review: Self-Study   A-20

Pierre Meystre

Direct Overwrite by Adiabatic Following (1990)

Tom D. Milster

L. A. Weller-Brophy and T. D. Milster, "Multi-layer integrated read/write head for magnetooptic data storage," UA1016

PATENTS

B. Fitingof and M. Mansuripur, "Method and Apparatus for Implementing Post-Modulation Error Correction Coding Scheme", application pending.

M. Mansuripur, "Direct Overwrite on Magneto-Optical Media Using Circularly Polarized Microwaves", application pending.

THESES AND DISSERTATIONS

1985 - 1990

BALASUBRAMANIAN, KUNJITHAPATHAM, 1988. Dissertation. Director: Macleod
  Structural Inhomogeneity and Anisotropy in Optical Filters and Thin Films; Applications to Optical Storage Media

BUSECK, DAVID A., 1987. Thesis. Director: Koliopou..s
  Simultaneous Acquisition Phase-Shifting Interferometry

BUSHROE, FREDERICK N., 1989. Thesis. Director: Burke
  An Optical Head for a Magneto-Optic Disk Test System

COHEN, DONALD KENNETH, 1987. Dissertation. Director: Wyant
  Analysis of Methods for Detecting Focus Error in Optical Data Storage Systems

CORNETT, KENNETH D., 1990. Dissertation. Director: Gibson
  Optical, Chemical and Protective Properties of Thin Films Produced by Ion-Assisted Deposition.

CRONKITE, PATRICK J., 1988. Thesis. Director: Lawrence
Design Method for Focusing Grating Coupler Using Holographic Optical Elements

DEETER, MERRITT NORTON, 1988. Dissertation. Director: Sarid
Applications of the Smith Model of Magnetooptical Effects to Investigations of Magnetic and Magnetooptical Recording Media

DEVORE, SCOTT L., 1988. Dissertation. Director: Wyant
Analysis and Measurement of Optical Disk Drive Functions

ECKHARDT, STEPHEN KARL, 1990. Dissertation. Director: Burke
Beam Propagation and Shift-Variant Optics

GARDNER, TIMOTHY STUART, 1989. M.S. without thesis. Director: Burke

GUNNARSSON, GUNNAR HANS, 1987. Thesis. Director: Koliopoulos
Multilevel Readout for CD-ROM Storage

IAMS, DOUGLAS ALLAN, 1988. Thesis. Director: Sarid
Magnetic Samples Using Optical Detection Methods

INGLE, JEFFERY T., 1989. Thesis. Director: Sarid
Applications of Scanning Force Microscopy to Magnetic and Electronic Media

KELLEY, MURRAY F., 1989. Thesis. Director: Gibson
Scanning Tunneling Microscope Characterization of Nickel Thin Film Nucleation and Growth

LI, LIFENG, 1988. Dissertation. Director: Stegeman
Application of Diffraction Grating Theory to Analysis and Fabrication of Waveguide Gratings

O'CONNOR, ARTHUR BRUCE, 1989. Thesis. Director: Kostuk
Polarization Properties of High Numerical Aperture Holographic Optical Elements

PHYSICS DEPARTMENT:

DON PERSON, 1988. No Thesis. No Dissertation. Director: Falco

BIJAN DEZFOULY-ARJOMANDY, 1990. Dissertation. Director: Leavitt
Hydrogen Depth Profiling Using the 6.385 MEV Resonance in the $^1H(^{15}N,\alpha\gamma)^{12}C$ Nuclear Reaction

ANTHONY P. TAYLOR, 1988. Thesis. Director: Gibson
Terbium Iron Cobalt Diffusion Barrier Studies

Appendix   Sunset Review: Self-Study   A-22

CHEMISTRY:

STORK, KURT FORREST, 1990. Thesis. Director: Armstrong
   Surface Chemistries of Oxygen and Water on Titanium-iron bimetallic systems

. . .